DETERMINATION OF RESIDUAL STRESS BASED ON THE ESTIMATION OF EIGENSTRAIN

A DISSERTATION
SUBMITTED TO THE DEPARTMENT OF MECHANICAL ENGINEERING
AND THE COMMITTEE ON GRADUATE STUDIES
OF STANFORD UNIVERSITY
IN PARTIAL FULFILLMENT OF THE REQUIREMENTS
FOR THE DEGREE OF
DOCTOR OF PHILOSOPHY

Michael R. Hill

August 1996

© Copyright 1996 by Michael R. Hill
All Rights Reserved

I certify that I have read this dissertation and that in my opinion it is fully adequate, in scope and quality, as a dissertation for the degree of Doctor of Philosophy.

Drew V. Nelson
(Principal Advisor)

I certify that I have read this dissertation and that in my opinion it is fully adequate, in scope and quality, as a dissertation for the degree of Doctor of Philosophy.

Sheri D. Sheppard
(Co-Principal Advisor)

I certify that I have read this dissertation and that in my opinion it is fully adequate, in scope and quality, as a dissertation for the degree of Doctor of Philosophy.

Dennis R. Carter

Approved for the University Committee on Graduate Studies:

Abstract

For aging welded structures subjected to cyclic loading, the process of re-certification seeks to determine the amount of time the structure can remain safely in service. Inspection of older structures often reveals weld defects buried deep within the welded joint. Lifetime assessment is then performed, assuming crack growth will initiate from these buried defects. Residual stress in the vicinity of the defect is a necessary component of the lifetime assessment. The objective of this thesis is to investigate and develop sectioning-based methods for residual stress determination in thick welded plates.

This thesis includes a lengthy review of techniques critical for lifetime assessment of welded structures. Experimental evidence indicates that current methods for including weld residual stress in linear elastic crack growth prediction provide reasonable accuracy when residual stresses are known. Several methods for finding residual stress in thick welded plates have been presented in the literature, and these are also reviewed.

Residual stress in a defective weld may be different from that in a sound weld. Further, the difference in stress between sound and defective joints may not be well predicted by linear superposition, which merely accounts for traction-free defect surfaces, since the development of residual stress is a non-linear process. To investigate the coupling of residual stress and weld defects, a welding process was developed by which a buried defect of pre-determined size, shape, and orientation was introduced. Residual stress existing in defective welded plates could then potentially be compared to sound welds made under similar conditions. However, the task of uncovering these residual stresses is a difficult one. The remainder of the thesis is devoted to the investigation and verification of techniques for finding subsurface weld residual stress.

The finite element method was found to be a useful technique for the comparison of residual stress measurement methods. Simulation of competing sectioning techniques revealed that the eigenstrain method (or inherent strain method), recently developed by Ueda, provided the most accurate estimates of residual stress within the welded joint. Experimental results further demonstrated that the principal assumptions of this relatively new technique are well-founded. Even though the eigenstrain method is attractive, its complexity and need for a large experimental effort have hindered its adoption. In response to these concerns, the localized eigenstrain method was developed in this thesis. This technique retains the benefits of the eigenstrain method while reducing the effort required to produce estimates of residual stress near the weld bead.

Several conclusions regarding the eigenstrain method are made in this thesis based on numerical simulation. To provide physical verification of the eigenstrain approach, residual stress was investigated within a swage-autofrettaged tube. Stress estimates provided by the eigenstrain method were compared to an elastic-plastic simulation of the swage process. Limitations of both the eigenstrain method and the elastic-plastic simulation are revealed, but both produce comparable results.

Acknowledgments

I could never have accomplished this task without the help of so many generous people.

This entire body of work is dedicated to my loving wife and constant companion, Jeanine. Her understanding and encouragement gave me the strength to persevere under difficult circumstances. Likewise, she was always a happy participant in the small celebrations along the way.

My co-advisors, Professors Drew Nelson and Sheri Sheppard, assisted me greatly from the time I arrived at Stanford, five years ago. By no means overbearing, they offered the encouragement to facilitate progress on the project and the leeway which allowed me to own it. Their hours spent reviewing the thesis, and those of Professor Dennis Carter, are sincerely appreciated.

My entire family, as well as Jeanine's, was involved in this project. Parents and grandparents, brothers and sisters, uncles, aunts, and cousins, each has offered some contribution to my soul, every bit of which was required to complete this thesis.

Constant interaction with many friends, at Stanford and elsewhere, helped me to maintain my perspective. Special thanks are due to Kristin Burns, Victor Ellis, Paul and Susie Graven, the Hawken-Widmann family, Emily Parmacek, the Rioux family, Herb Ruprecht, Andy Shrader, the Soll family, Jim and Angela Stewart, and the Worth family. I sincerely apologize to the others I have insulted by omitting.

The division between friends and colleagues has been mostly absent during my time at Stanford. However, the following have offered commiseration and, in some cases, technical expertise in addition to friendship: Lori Bassman, Jesse Dorogusker, Ginger

Giddings, Craig Lawrence, Dr. Marjo van der Meulen, Dr. Borjana Mikić, Jamey Nielsen, Mike Strange, Dr. Jim Widmann, Dr. Ron Worth, and Dr. Steve Zuniga.

NASA Ames Research Center funded this research, through both monetary sponsorship and access to laboratory facilities. Several people at NASA were involved in formulating this collaborative effort, including Dr. Tina Panontin and Roy Hampton. In addition, several others at NASA were helpful, including Bill Bird, Chris Chen, Dan Dittman, Jim Govorko, Howard Meche, Frank Pichay, Jr., and John Segretto.

During my time at Stanford, I benefited from contact with several professors as they executed the duty of the University, as described in the *Founding Grant of The Leland Stanford Junior University*, “to qualify students for personal success and direct usefulness in life.” Among those who were especially influential are Professors Rolf Faste, Huajian Gao, Tom Kenny, Ilan Kroo, Bill Nix, Bernie Roth, Doug Wilde, and the late Juan Simo.

I would also like to give my thanks to Professors Paul Wirsching and Skip Perkins at the University of Arizona, where I earned my Bachelors and Masters degrees. Without their example I would not be where I am today. Go ’Cats!

Table of Contents

Abstract . . . .**iv**

Acknowledgments . . . . **vi**

Table of Contents . . . . **viii**

List of Figures . . . . **xiii**

List of Tables . . . . **xxii**

1. Introduction **1**

- 1.1 Background 3
  - 1.1.1 Welds as the site for failure initiation 3
  - 1.1.2 Fatigue in the weld region 3
  - 1.1.3 Scope of the current research 4
- 1.2 Factors influencing crack growth in the weld region 4
  - 1.2.1 Elements of prediction of fatigue crack propagation 4
  - 1.2.2 Residual stress and crack growth 8
  - 1.2.3 Material and microstructure variation 11
- 1.3 Analysis methods for crack growth in the weld region 12
  - 1.3.1 Determination of crack growth parameters 12
  - 1.3.2 Superposition of residual stress on applied loading 14
    - 1.3.2.1 Weight functions 14
    - 1.3.2.2 Computational techniques 25
- 1.4 Determination of residual stress 27
  - 1.4.1 Techniques for surface stress 29

1.4.1.1 Hole drilling 29
1.4.1.2 Ultrasonic testing 29
1.4.1.3 X-ray diffraction (XRD) 30
1.4.2 Techniques for subsurface stress 31
1.4.3 Computational simulation 31
1.5 Experiments on crack propagation in residual stress fields 32
1.5.1 Residual stress due to welding 32
1.5.2 Residual stress due to heat treatment 39
1.5.3 Residual stress due to localized plastic deformation 41
1.6 Influences of internal weld defects 44
1.6.1 Early experimental data 44
1.6.1.1 Results in an S-N format 45
1.6.1.2 Reassessment of early data using fracture mechanics 48
1.6.2 Effect of defects on the formation of residual stress 50
1.6.2.1 Simulation of the thermal elasto-plastic problem 52
1.6.2.2 Experimentation 53
1.7 Summary 53
1.8 Contributions of this thesis, a road map 55
1.9 Figures 56

2. Fabrication of Defective Welds 85

2.1 Description of the desired defect 85
2.2 Trials on thin plates 87
2.3 Trials on thick plates 90
2.4 Defective welds produced 92
2.5 Summary 92

3. Methods for Triaxial Residual Stress Estimation 97

3.1 Methods to be compared 98
3.1.1 Method proposed by Gunnert (1961) 98

3.1.2 Method proposed by Rosenthal and Norton (1945) 101
3.1.3 Slotting methods 102
3.1.4 Method proposed by Ueda (1975) 104
3.2 Numerical application of the methods 111
3.2.1 Baseline residual stress state 111
3.2.2 Technique used to compare the methods 113
3.2.3 Simulation of the Rosenthal and Norton method 113
3.2.4 Simulation of Ueda’s method 114
3.3 Results 114
3.4 Investigation of Ueda’s assumption 116
3.5 Comparison of the methods 117
3.6 Testing to verify numerical results 119
3.7 Conclusions 120

4. Exposition of the Eigenstrain Method 122

4.1 Description of the eigenstrain method 123
4.1.1 Stress as a function of eigenstrain 123
4.1.2 Reduction to a linear system 124
4.1.3 Application of the eigenstrain method to a long welded joint 129
4.2 Model problem to examine the method 130
4.2.1 Definition of geometry and assumed eigenstrain distribution 131
4.2.2 FEA solution to the model problem 133
4.3 Solution for eigenstrain 135
4.3.1 Finding cross-sectional eigenstrain 137
4.3.2 Finding longitudinal eigenstrain 138
4.3.3 Results of the eigenstrain method 139
4.4 Discussion 141

5. Implementation of the Eigenstrain Method 146

5.1 Description of the experiments 146

5.2 Choice of surface stress measurement method 147
5.3 Measurement of block to slice stress release 148
5.4 Measurement of stress in the slice 148

6. Evaluation of the Eigenstrain Method 156
6.1 Development of a test specimen 157
6.2 Fabrication of the test specimen 163
6.3 Measurement of residual stress 165
    6.3.1 Development of an axisymmetric eigenstrain method 165
    6.3.2 Experimental execution of the axisymmetric eigenstrain method 170
6.4 Computation of residual stress 173
    6.4.1 Matching the analysis to measured data 174
    6.4.2 Residual stress prediction 176
    6.4.3 Numerical verification of the axisymmetric eigenstrain method 178
6.5 Comparison of measured and computed stress 181
6.6 Conclusions 189

7. Localization of the Eigenstrain Method 191
7.1 A one-dimensional example 192
    7.1.1 Localized eigenstrain method applied to the strip 196
    7.1.2 Effect of dice size on stress release 202
7.2 Generalization to three dimensions 205
    7.2.1 Model problem to illustrate the method 206
    7.2.2 Division of eigenstrain into ε^*_A and ε^*_B 208
    7.2.3 Scheme for interpolation of ε^*_B 210
    7.2.4 Scheme for interpolation of ε^*_A 212
    7.2.5 Interpolation for longitudinal eigenstrain, ε^*_{zz} 216
7.3 Results of the localized eigenstrain method 221

8. Conclusions 224

8.1 Summary of the thesis 224

8.2 Directions for future research 226

References 229

List of Figures

Page

Figure 1.1 – Commonly encountered weld defects (Gray, 1975) 57

Figure 1.2 – Crack growth retardation following a peak overload (Kanninen, 1985) 57

Figure 1.3 – Idealized residual stress in a butt welded plate (Baldwin, 1949) 58

Figure 1.4 – Experimentally obtained residual stress through the thickness of a butt welded plate (Masubuchi, 1980) 58

Figure 1.5 – Experimentally obtained residual stress through the thickness of a circumferentially butt-welded pipe (Ritchie, 1987) 59

Figure 1.6 – Specimens used to quantify FCGR properties of various regions of a welded joint (Mutoh, 1984) 59

Figure 1.7 – FCGR as a function of ΔK^{eff} for different weld regions (Mutoh, 1984) 60

Figure 1.8 – FCGR as a function of ΔK^{eff} for WM and heat treated PM (Mutoh, 1984) 60

Figure 1.9 – FCGR Paris law for various weld regions (Shi, et al., 1990) 61

Figure 1.10 – Strain in the welding direction measured at one inch from the weld bead (Weck, 1948) 62

Figure 1.11 – Center cracked plate with fixed ends 63

Figure 1.12 – Center cracked strip with twin opening loads 63

Figures 1.13 - 1.15 – Normalized SIF as a function of normalized crack length for several plate lengths and boundary conditions (Isida, 1971) 64

Figure 1.16 – Effect of boundary condition on normalized SIF as a function of crack length for a self-equilibrating residual stress field (Wu, 1983) 65

Figure 1.17 – Comparison of finite element and weight function K^{res} computations for an overloaded plate containing a hole (Graham, 1988) 65

Figure 1.18 – Three specimens used to study the effect of residual stress on FCP (Glinka, 1979) 66

Figure 1.19 – Measured residual stress distributions in the plane of fatigue crack growth (——) and approximations (– – –) used in FCP analysis (Glinka, 1979) 66

Figure 1.20 – Fatigue crack growth of specimens U, P, and L (Glinka, 1979) 67

Figure 1.21 – Fatigue crack growth rates measured in specimens U, P, and L and analytical predictions (Glinka, 1979) 67

Figure 1.22 – Comparison of FCGR predicted by Glinka (1979) and by a simplified closure model (Nelson, 1982) with data from (Glinka, 1979) 68

Figure 1.23 – Comparison of residual stress measured Glinka (1979) and the approximation used by Terada (1987) 69

Figure 1.24 – Comparison of prediction of Terada (1987) with data taken by Glinka (1979) 69

Figure 1.25 – Summary of Adams' FCP experiments (Adams, 1973) 70

Figure 1.26 – Residual stress measured by Adams for specimen N (Adams, 1973) 71

Figure 1.27 – Residual stress measured by Adams for specimen W (Adams, 1973) 71

Figure 1.28 – Crack opening behavior measured by Itoh for various applied stress ratios (Itoh, 1989) 72

Figure 1.29 – FCGR measured by Itoh for base metal and welded joints (Itoh, 1989) 73

Figure 1.30 – Residual stress distributions measured by Itoh (1989) 74

Figure 1.31 – K^{res} resulting from weld residual stress (Itoh, 1989) 74

Figure 1.32 – Crack opening ratio as a function of effective stress ratio (Itoh, 1989), with data adapted fromNewman (1981) 75

Figure 1.33 – Comparison of measured FCGR with predictions made by Itoh (1989) 75

Figure 1.34 – Specimens used by Torii, et al. (1989) 76

Figure 1.35 – Residual stress introduced by heat treatment and remaining residual stress at the cycle of crack initiation for several stress amplitudes (Torii, 1989) 76

Figure 1.36 – Surface FCGR for specimens with and without residual stress (Torii, 1989) 77

Figure 1.37 – Result of including residual stress measured at crack initiation in evaluation of K_{max} (Torii, 1989) 77

Figure 1.38 – Result of including initial residual stress in evaluation of K_{max} (Torii, 1989)........78

Figure 1.39 – FCGR in the depth direction for surface cracks in specimens without residual stress (Torii, 1989)........78

Figure 1.40 – Specimen used by Underwood, et al. showing indentations used to introduce residual stress and gages used to measure elastic strain (Underwood, 1977)........79

Figure 1.41 – Residual stress measured in several specimens of the type shown in Figure 1.40 (Underwood, 1977)........79

Figure 1.42 – FCGR results of Underwood, et al. (1977)........80

Figure 1.43 – Fatigue test specimen used by Lam and Lian (1989)........80

Figure 1.44 – Central portion of test specimen showing indentation location, “predefined lines”, and strain gages (Lam, 1989)........80

Figure 1.45 – Residual stress along crack plane for specimen SP 6 (Lam, 1989)........81

Figure 1.46 – K^{res} for specimen SP 6 determined by the weight function (WF) and by an FEM crack opening displacement method (Lam, 1989)........81

Figure 1.47 – FCGR measured and predicted with K^{res} from Figure 1.46 for specimen SP 6, and for a specimen without residual stress (Lam, 1989)........82

Figure 1.48 – Crack growth history measured and predicted with K^{res} from Figure 1.46 for specimen SP 6, and for a specimen without residual stress (Lam, 1989)........82

Figure 1.49 – Summary of S-N fatigue results presented in a fracture mechanics framework (Harrison, 1969)........83

Figure 1.50 – Idealization of deformation in the weld region (Brand, 1993)........84

Figure 2.1 – Front, top, and right side views of desired defective weld......... 86

Figure 2.2 – Sketch of samples used to experiment on fusion inhibiting methods for thin plate welds......... 89

Figure 2.3 – Detail of the modified double bevel weld preparation used to simulate a lack of fusion weld defect......... 91

Figure 2.4 – Fit-up of weld preparation used to simulate a lack of fusion weld defect.... 91

Figure 2.5 – Weld passes for welds with simulated LOF defect......... 92

Figure 2.6 – Welded specimens containing a simulated lack of fusion......... 93

Figure 3.1 – Directions relative to a weld......... 98

Figure 3.2 – Section through a measurement point where Gunnert's technique was applied. 99

Figure 3.3 – Residual stresses reported by Gunnert (1961). 100

Figure 3.4 – Schematic of the technique presented by Procter and Beaney (1987). 101

Figure 3.5 – Two slices removed in the Rosenthal-Norton technique (1945). 102

Figure 3.6 – Slotting set-up and numbering system used by Ritchie and Leggatt (1987). 104

Figure 3.7 – Illustration of the effective inherent strain principle. 106

Figure 3.8 – Two planes which have the same eigenstrain distribution. 110

Figure 3.9 – Schematic of the slice-and-dice method proposed by Ueda (1985). 110

Figure 3.10 – Sample in which residual stress is to be determined (dimensions in inches). 112

Figure 3.11 – Residual stresses at the center of the sample, through the thickness of the plate, generated by finite element analysis. 112

Figure 3.12 – Residual stress at the center of the weld length, across the top surface. 113

Figure 3.13 – Stress released at the middle of the length of the transverse slice. 115

Figure 3.14 – Stress released at the middle of the length of the longitudinal slice. 115

Figure 3.15 – Results of the Rosenthal-Norton technique at the middle of the welded block. 116

Figure 3.16 – Results of Ueda's method at the middle of the block compared with true values. 116

Figure 3.17 – Gage layout and cutting lines for experiment on eigenstrain distribution. 117

Figure 3.18 – Strain change at various points along the length of a longitudinal slice removed from a weld. 118

Figure 3.19 – Results of Ueda's method at the center of the weld length, across the top surface. 118

Figure 3.20 – Specimen proposed for benchmark testing of residual stress determination techniques. 120

Figure 4.1 – Schematic of the slice-and-dice method proposed by Ueda (1985). 130

Figure 4.2 – (a) Block and (b) slice removed from the end of the block. 131

Figure 4.3 – Functions used to define a distribution of eigenstrain. 133

Figure 4.4 – Stress in the block resulting from eigenstrain on the line x = 4.0 on the free surface, z = zmax, and the mid-plane of z symmetry, z = 0. 134

Figure 4.5 – Stress in the block resulting from eigenstrain on the mid-plane, z=0, on the lines y = 0 and y=-0.75. 135

Figure 4.6 – Background mesh and finite element mesh used in solving the model problem for the cross-sectional eigenstrain. 137

Figure 4.7 – Finite element mesh used to determine the longitudinal eigenstrain. 138

Figure 4.8 – Exact (FEA) and approximate (IE) stress in the slice on line x=3.8 on the free surface, z = zmax, and the mid-plane, z = 0. 140

Figure 4.9 – Exact (FEA) and approximate (IE) stress in the slice on the line y = -0.75 on the free surface, z = 0. 140

Figure 4.10 – Error in approximation of stress shown in Figure 4.8. Points with symbols (□ and ◇) represent points on the background mesh. 141

Figure 4.11 – Exact (FEA) and approximate (IE) stress in the block on the mid-plane, z=0, on the lines y = 0 and y=-0.75. 142

Figure 4.12 – Exact (FEA) and approximate (IE) stress in the block on the line x = 3.8 on the free surface, z = 0, and mid-plane, z = zmax. 143

Figure 4.13 – Exact (FEA) and approximate (IE) shear stress in the block on the line x = 3.4.on the free surface, z = 0, and mid-plane, z = zmax. 143

Figure 4.14 – Stress on the free surface of the slice due only to longitudinal eigenstrain on the line x=3.8. 144

Figure 5.1 – Layout of points where residual stress was determined for input into the eigenstrain method for residual stress determination. 147

Figure 5.2 – Stress released at various values of y when a slice is removed from the block, xx component. (a) experimental data, and (b) modeling results. 149

Figure 5.3 – Stress released at various values of y when a slice is removed from the block, yy component. (a) experimental data, and (b) modeling results. 149

Figure 5.4 – Stress released at various values of y when a slice is removed from the block, xy component. (a) experimental data, and (b) modeling results. 150

Figure 5.5 – Hole-drilling residual stress results for Rosette #6, at x=3.213, y=-0.239. 152

Figure 5.6 – Hole-drilling residual stress results for Rosette #32, at x=3.213, y=-0.478. 152
Figure 5.7 – Residual stress at a depth of 0.013 inch, xx component. 153
Figure 5.8 – Residual stress at a depth of 0.013 inch, yy component. 153
Figure 5.9 – Residual stress at a depth of 0.013 inch, xy component. 154
Figure 6.1 – Tube specimen to be used for verification of the eigenstrain approach. 158
Figure 6.2 – Finite element mesh used in preliminary analysis of the swage process. The mesh extends in the axial (z) direction to 8 inches. 159
Figure 6.3 – Residual stress at the tube's midlength predicted by preliminary analysis. 161
Figure 6.4 – Flow curve for A516 Gr70 (Panontin, 1994). 162
Figure 6.5 – Fabrication plan for the tube to be used for verification of the eigenstrain technique. 163
Figure 6.6 – Data gathered during the swage operation compared with results of the model. 164
Figure 6.7 – Layout of instrumentation for the axisymmetric eigenstrain method. 166
Figure 6.8 – Sectioning procedure for the axisymmetric eigenstrain method. 167
Figure 6.9 – Twelve shape functions used to interpolate eigenstrain in the radial direction. Interpolation nodes correspond to stress measurement locations. 167
Figure 6.10 – Finite element mesh of the tube used to form the eigenstrain system. 168
Figure 6.11 – Experimental estimate of residual stress provided by measured stress changes and the eigenstrain method. 173
Figure 6.12 – Finite element mesh used in further analysis of the swage process. The mesh extends in the axial (z) direction to 8 inches. 174
Figure 6.13 – Data gathered during the swage operation compared with results of the model for a friction coefficient of 0.075. 175
Figure 6.14 – Residual stress predicted to exist near the midlength of the tube by finite element analysis. 177
Figure 6.15 – Residual stress prediction for various variations of analytical parameters. 177
Figure 6.16 – Results of the eigenstrain method when stress is obtained from a finite element model. 180

Figure 6.17 – Estimate of residual stress provided by measured stress and the eigenstrain method compared to finite element prediction of residual stress. 182
Figure 6.18 – Eigenstrain in the tube estimated from experimental measurements. 182
Figure 6.19 – Mesh used to model the final section. This model is three dimensional and has five layers of elements in the z-direction (out of the paper). 183
Figure 6.20 – Stress in the final section which exists when eigenstrain found from the elastic-plastic simulation is present. 183
Figure 6.21 – Residual stress predicted when model data which account for stress in the final section are used in the eigenstrain method. 184
Figure 6.22 – Measured and predicted stress change accompanying geometry change from (a) slice to final section, and (b) tube to final section. 186
Figure 6.23 – Arc specimen removed from the tube to investigate residual stress near the inner diameter. 187
Figure 6.24 – Finite element mesh constructed to investigate mesh refinement. Mesh shown at the midlength of the tube. 188
Figure 6.25 – Influence of mesh refinement on residual stresses predicted at the midlength of the tube. (a) Axial component, and (b) hoop component of residual stress. 188
Figure 7.1 – Region of interest within a block of material where residual stress is to be determined by the localized eigenstrain method. 191
Figure 7.2 – Strip in which eigenstrain is distributed. 192
Figure 7.3 – Region of interest within a strip, a possible eigenstrain distribution, and different eigenstrain distributions which would cause the same stress in the chunk. 193
Figure 7.4 – Sectioning procedure for a strip containing a longitudinal variation of eigenstrain, showing the slice, chunk, and dice. 194
Figure 7.5 – Shape functions used to discretize the eigenstrain. 195
Figure 7.6 – Results of the localized eigenstrain method for a strip subject to a sinusoidal temperature variation of varying frequency. 198
Figure 7.7 – Finite element meshes used to a) obtain stress estimates for input to the localized eigenstrain method, and b) form the linear system for eigenstrain estimation. 199
Figure 7.8 – Exact and FEA estimate of stress for the case 199

Figure 7.9 – Results of the localized eigenstrain method for a strip subject to a sinusoidal temperature variation 200

Figure 7.10 – Relation between b/W and stress at the center of the strip and the square. 203

Figure 7.11 – Stress release versus d/ρ, where d is the dice size and ρ is the local radius of curvature of the temperature field. 205

Figure 7.12 – Sectioning procedure used in the localized eigenstrain technique for continuous welds. 206

Figure 7.13 – (a) Block of material in removed from a welded joint, (b) slice removed from the block, and (c) chunk removed from the slice. 207

Figure 7.14 – Measurement locations within the region of interest. 207

Figure 7.15 – Interpolation functions used to distribute in the chunk. 210

Figure 7.16 – Stresses in the chunk computed by FEA and the localized eigenstrain method. Each plot represents a separate stress component, as shown in each legend. 213

Figure 7.17 – Interpolation functions used to distribute eigenstrain determined from stress in the slice. 214

Figure 7.18 – Stresses in the slice computed by FEA and the localized eigenstrain method. Each plot represents a separate stress component, as shown in each legend. (Results for and on x=3.8 and x=4.2 are virtually identical, so they cannot be distinguished in the plots.) 215

Figure 7.19 – Stresses on the block midplane computed by FEA and the localized eigenstrain method. Each plot is for a different x-location, as indicated at the bottom-right. 216

Figure 7.20 – Stresses in the block computed by FEA and the localized eigenstrain |method, on the block midplane. 217

Figure 7.21 – Stresses due to in the block computed by FEA and the localized eigenstrain method. Each plot is for a different x-location, as indicated at the bottom-right. 218

Figure 7.22 – Longitudinal stress at the midplane due to in the abbreviated block computed by FEA and the localized eigenstrain method. 219

Figure 7.23 – Longitudinal stress due to in the scaled abbreviated block computed by FEA and the localized eigenstrain method. 220

Figure 7.24 – Stress at the midplane of the block induced by the model eigenstrain function as computed by FEA, compared to those estimated by the localized eigenstrain method. Each plot is for a different x-location, as indicated at the bottom-right. 221

Figure 7.25 – (a) Error in stress estimated by the regular and localized eigenstrain methods, and (b) nominal values of stress, both on the midplane of the block and the line x=3.8. 222

List of Tables

Table 1.1 – Summary: Effect of defect severity on reduction in fatigue strength (see text for details) 48

Table 2.1 – Summary of defect production methods attempted with 0.25 inch A36 steel. 88

Table 2.2 – Weld pass order and data for sound weld. 94

Table 2.3 – Weld pass order and data for defective weld AN1. 95

Table 2.4 – Weld pass order and data for defective weld BN1. 96

Table 6.1 – Physical properties and composition (wt%) of A516 Gr70 as reported by Panontin (1994) 162

Table 6.2 – Strain change accompanying the slice to final section geometry change (με). 172

Table 6.3 – Strain change accompanying the tube to final section geometry change (με). 172

Table 7.1 – Stress release from strip to dice for various frequencies, h=d=0.4 and W=1.5. 204

Chapter 1

Introduction

This chapter represents a comprehensive literature survey which reviews topics related to fatigue crack propagation initiating at lack of fusion and lack of penetration weld defects under cyclic loading. The review focuses on these two types of flaws because they are especially detrimental to cyclically loaded structures. This is the case because they can occur as hidden defects and, since they can be crack-like following fabrication, life spent in crack initiation at such defects may be negligible. The prediction of crack propagation starting at these types of defects is complicated by a number of factors, including material variations and residual stress brought about by the welding process. Methods used to account for these factors are reviewed. Several methods are summarized which can be used to determine residual stress. Methods for superposition of residual and applied stress are outlined. Possible problems with superposition methods are enumerated and the use of numerical analysis to address the issue is explored. Several papers are summarized which contain experimental work on the influence of residual stress on fatigue crack growth. Early work on the influence of weld defects on fatigue strength is reviewed. Finally, the use of sound-weld residual stress distributions to characterize the residual stress in defective joints is discussed and the possible influence of weld internal defects on residual stress is postulated. To conclude the chapter, a description of the remainder of the thesis is laid out.

Nomenclature relevant to this chapter is provided for convenience on the next page.

Nomenclature for Chapter 1

LOF	lack of fusion weld defect
LOP	lack of penetration weld defect
WM	weld metal
PM	parent metal
HAZ	heat affected zone
FCP	fatigue crack propagation
a	crack size
N	number of loading cycles or fatigue life
N_p	portion of fatigue life spent in crack propagation
LEFM	linear elastic fracture mechanics
K, SIF	stress intensity factor
K_c	critical stress intensity
K^{app}	SIF due to applied loading
K^{res}	SIF due to residual stress
ΔK	range of SIF under cyclic loading
FCGR	fatigue crack growth rate
$\frac{da}{dN}$	fatigue crack growth rate
C, n	Coefficient and exponent in Paris or Forman equation
S_{op}	crack opening stress
K_{op}	SIF at S_{op}
ΔK^{eff}	effective SIF range $= K_{max} - K_{op}$
U	crack opening ratio $=\Delta K^{eff} / \Delta K$
R	applied stress ratio $= K^{app}_{min} \big/ K^{app}_{max}$
R^{eff}	stress ratio including residual stress $= (K^{app}_{min} + K^{res}) \big/ (K^{app}_{max} + K^{res})$
$\boldsymbol{m}(x,y,a)$	weight function for applied tractions (vector quantity)
$\boldsymbol{m}^*(x,y,a)$	weight function for applied displacements (vector quantity)
$m(x,y,a)$	weight function for applied tractions (scalar quantity)
$m^*(x,y,a)$	weight function for applied displacements (scalar quantity)
E	Young's modulus
ν	Poisson's ratio
H	Generalized elastic modulus $= \begin{cases} E \text{ in plane stress} \\ \frac{E}{1-\nu^2} \text{ in plane strain} \end{cases}$
G	crack driving force
CCT	center cracked tension specimen
LPD	localized plastic deformation
XRD	X-ray diffraction
TEPA	thermal elasto-plastic analysis
$\Delta\sigma$	range of cyclic stress
t	specimen thickness
σ_u	ultimate tensile strength
ε^*	eigenstrain or effective inherent strain
$\mathbf{H}^*$	Linear system relating elastic strain release to eigenstrain

1.1 Background

1.1.1 Welds as the site for failure initiation

Defects can arise in the fabrication of welded structure. Weld defects often act as sites from which cracks form and grow by fatigue and/or stress corrosion to critical sizes that can jeopardize structural integrity. Owing to the complex nature of the welding process, the size, location and type of defects cannot be predicted. Only post-fabrication inspections can provide information about the defect population present in such structures. Over the years, these inspections have provided a base of knowledge about the types, and in some cases the size range, of defects likely to be found in typical weld configurations.

Flaws in and around the weld bead can generally be split into two groups: internal (or buried) and external (or surface) defects. Several different types of defects are shown in Figure 1.1. Internal defects include porosity, slag inclusions, lack of fusion, and lack of penetration. These flaws can also be classified as surface defects if they break through the surface of the joint. Surface defects may also represent geometrical discontinuities, for example undercuts, start-stop marks, ripples, and overly steep reinforcement angles. As discontinuities in geometry, defects cause stress concentration and are therefore prone to fatigue crack initiation. Lack of penetration (LOP) and lack of fusion (LOF) are of particular concern in a fatigue assessment since their shape can be “crack-like” at the outset, and the stress concentration can be particularly high at the tip of such flaws. Since these defects usually occur deep within the welded joint, their presence can go undetected, again making them very troublesome.

1.1.2 Fatigue in the weld region

Considering planar (two-dimensional, crack-like) defects to be the most deleterious type of weld flaw, analysts have attempted to use fracture mechanics to assess the severity of such defects in relation to design loading. The weld region presents a number of complicating features which make the application of fracture mechanics difficult. Crack analysis in the weld region is affected by: 1) the effect of residual stress caused by incompatible (plastic and thermal) strain which arises during welding, 2) the interaction of the crack with other defects or with the complex stress distribution presented by the weld geometry, and 3) material variations due to dissimilar weld and base metals and microstructural variations in the weld region resulting from the welding thermal cycle.

There are many examples in the literature of cases where weld joints have caused unexpected failure of engineering structures. In light of such failures, considerable work has already been devoted to the study of the fatigue of welded structures. A number of texts, in fact, have been devoted to the subject (e.g., Gurney(1968), Masubuchi(1980), Radaj(1990)). The following review of the literature is intended to provide background to this specific thesis but is also thought to be of general interest to engineers concerned with the integrity of welded structure.

1.1.3 Scope of the current research

The context for this thesis is the influence of LOP or LOF defects on welded steel butt joints. In the analysis of such joints, modeling the influence of residual stress and property variations are primary difficulties in life assessment. Current methods used to account for residual stress superpose the effects of residual stress fields in sound welds onto applied loadings to compute the fatigue life for an initial weld defect. Residual stress in the vicinity of a lack of fusion defect, however, may be quite different than that produced in a defect-free region. The major goal of this research is to investigate methods capable of revealing the interaction of LOP or LOF defects with the attending residual stress field. Accordingly, the literature survey concentrates on topics related to the measurement and effects of weld residual stress.

1.2 Factors influencing crack growth in the weld region

1.2.1 Elements of prediction of fatigue crack propagation

Since much of the following deals with fatigue crack propagation some of the critical aspects of this subject will be briefly reviewed here. The essential assumption of a linear elastic fracture mechanics (LEFM) fatigue crack propagation analysis is that the fatigue crack growth rate (FCGR, or da/dN), expressed as increment of crack advance per loading cycle, is a function of (at least) the variation of the stress intensity factor (SIF, or K) which occurs with cyclic loading, denoted ΔK. This basic assumption is represented by the equation

$$\frac{da}{dN} = f(\Delta K). \tag{1.1}$$

Assuming that a form can be determined for $f(\Delta K)$, separation of variables may be used to find the required number of loading cycles to extend a crack from some initial crack size, as long as ΔK is not a function of the loading cycle, N. The number if cycles required for a crack to grow from a specified initial size, a_i, to a critical crack size for failure, a_{cr}, is called the fatigue crack propagation life, N_p. If the above conditions are met, this may be determined from

$$N_p = \int_{a_i}^{a_{cr}} \frac{1}{f(\Delta K)} da \tag{1.2}$$

The LEFM analysis represented by Equation 1.1 and Equation 1.2 is quite powerful as it allows one in principle to estimate the effect of an assumed initial crack-like defect (e.g., a LOP or LOF weld defect) on structural integrity, with the assumption that LEFM can be applied. This generally requires that the plastic zone at the crack tip or front be much smaller than the crack size (“small-scale yielding”), as typically occurs for lower stress levels and higher strength metals. Also, crack size must be large enough relative to microstructural features (e.g., grain size) for LEFM to apply.

A great deal of work has been done on determining expressions for $f(\Delta K)$ in Equation 1.1. The pioneering work of Paris (1961), for example, showed that over a wide range of ΔK Equation 1.1 could be represented by

$$\frac{da}{dN} = C(\Delta K)^n, \tag{1.3}$$

which is referred to as the “Paris law”. In general, for a given material, the parameters C and n depend on the stress ratio, R, defined as

$$R = \frac{K_{min}}{K_{max}} = \frac{S_{min}}{S_{max}}, \tag{1.4}$$

as well as on specimen thickness, the ambient environment, among other things. Forman, et al. (1967) realized the need to for FCGR to become infinite as K_{max} approaches the fracture toughness of the material, K_c. To model this effect, they used the equation

$$\frac{da}{dN} = \frac{C(\Delta K)^n}{(1-R)K_c - \Delta K} \tag{1.5}$$

Equation 1.5 will be referred to as the “Forman equation”. This formulation has the added advantage of reflecting the general influence of R on FCGR: the same ΔK will usually cause increased FCGR if applied at a higher R. Even so, the assumed functional form does not always represent this effect faithfully for all materials, so that the FCGR remains dependent on R. It should be noted that the parameters C and n in the Forman equation and the Paris Law are numerically different. This does not usually lead to confusion as the two equations are not generally used in the same analysis. Many more equations have been developed to relate ΔK to FCGR, but the above two serve to illustrate the LEFM approach. It is generally accepted that no one functional form assumed for $f(\Delta K)$ will be applicable under all conditions. Once a parameter based form of $f(\Delta K)$ is assumed, such as Equation 1.3 or Equation 1.5, the usual course of action is to use ΔK and FCGR test data generated with the specific material to determine the parameters in $f(\Delta K)$ (e.g., C and n).

As mentioned above, the stress ratio, R, is also a primary cause of variability of FCGR for given ΔK. As will be seen, residual stress present in the weld region will cause a variation of the stress ratio near the weld. Accordingly, a closer look at the effect of stress ratio on FCGR is called for. Generally, an increase in positive R increases FCGR while a decrease in R has the opposite effect. Elber (1970; 1971) considers that the variation of FCGR with R stems from “crack closure” which results from plastically deformed material left in the path taken by the crack, referred to as the “plastic wake”. Upon unloading the body from maximum stress, the material in this wake on one crack face contacts the other crack face before minimum load is reached (since material in the wake has been permanently stretched). When the crack is loaded again, Elber reasoned that there is no increase in K at the tip of the crack until the crack is fully open. Elber was able to show experimental evidence of closure by monitoring test specimen compliance. He found, for a crack which had grown some distance into the specimen, that the compliance of the specimen for small loads was nearly the same as the compliance of the uncracked body, then changed gradually with increasing load and reached a final value which corresponded to the elastic compliance of the cracked body. When the compliance reaches a value corresponding to the elastic compliance of the cracked body, the crack is said to be fully open. That is, load is no longer being transferred across the crack faces. The value of K in the fully open condition is referred to as K_{op}. If K_{op} is greater the K_{min}, the variation of K experienced at the tip of the crack is reduced compared to that which would occur in the absence of the plastic wake. Elber asserted that accounting for closure explained the dependence of FCGR on R.

The reduced range of K due to closure effects is most often referred to as ΔK^{eff}, read as effective range of K and defined by

$$\Delta K^{eff} = K_{max} - K_{op}. \tag{1.6}$$

Elber also defined the quantity *U*, which is the ratio between ΔK^{eff} and ΔK. To account for closure in an FCP analysis, then, ΔK can be replaced by $U\Delta K$. Furthermore, Elber and other investigators have confirmed experimentally that K_{op} increases with K_{max}, but that *U* increases with R.

Many investigators have attempted to relate *U* to applied loading. Elber found that the equation $U = 0.5+0.4R$ was a reasonable approximation for $-0.1 \leq R \leq 0.7$ in the aluminum specimens he tested. But further research by Unangst, et al. (1977) among others showed that this equation was not generally applicable, as *U* is not independent of K_{max}. Certainly, a dependence of closure level on K_{max} is not surprising, since that is an indication of the extent of plasticity under small-scale yielding conditions. However, research by many people has shown that *U* is a function of S_{max} rather than of K_{max} (McClung, 1991). In either case, closure is not independent of some measure of maximum load. Also, since closure stems from plasticity, it seems reasonable to add to the factors upon which *U* depends some measure of the constraint at the crack-tip, which depends on the state of stress, the stress-strain characteristics of a given material, as well as specimen thickness and geometry. As a result, general relations between *U* and the applied loading have not been forthcoming; however, Newman (1981) has developed an analytical model that can be used to predict closure effects, at least for certain crack geometries.

Fatigue crack closure allows insight into the effect of load variation during FCP. As an example, consider a large tensile overload applied to a structure during fatigue cycling. If the overload is large enough it can cause a dramatic decrease in the FCGR, as illustrated by Figure 1.2. In a crack-closure framework, this drop-off in FCGR results from the plastic deformation which is initially ahead of the crack, but with each cycle following the overload, gradually moves into its wake. In the wake of the crack, the plastically deformed material acts to increase K_{op}. If a component contains an initial residual stress field, then it may be possible to take into account the interaction of a variable amplitude stress history with the pre-existing residual stress and the resulting effect on crack growth using a crack closure approach.

1.2.2 Residual stress and crack growth

The metal in and surrounding a weld bead generally contains significant levels of residual stress created by the welding process. Peak tensile stress levels can be yield strength or higher and may thus play an important role in determining the structural integrity of weldments. One of the most pronounced effects of residual stress is to accelerate, or in some cases retard, crack growth in structures subject to cyclic loading. Residual stress can alter the shape of surface cracks in thick welds, causing them to grow long and shallow and jeopardizing the leak-before-break criteria on which some design codes are based (Mills, 1987). They can cause crack growth to occur in regions subject to purely compressive cycling where fatigue would normally not be a problem (Ohta, 1987 and 1988). They have also been shown to accelerate environmentally assisted cracking in structures subject to static loading (Glinka, 1987).

In an elastic analysis, residual stress is taken into account by superposing residual stress on applied stress. In the framework of LEFM, the stress intensity factor due to residual stress, assuming it can be calculated, is added to that due to applied cyclic loading:

$$K_{max} = K_{max}^{app} + K^{res} \tag{1.7}$$

$$K_{min} = K_{min}^{app} + K^{res}. \tag{1.8}$$

The effective stress intensity range and stress-ratio, accounting for residual stress, are then found from:

$$\Delta K = \Delta K^{\mathrm{app}} \tag{1.9}$$

$$\mathrm{R}^{\mathrm{eff}} = \frac{K_{min}^{app} + K^{res}}{K_{max}^{app} + K^{res}} . \tag{1.10}$$

Then, any of several models for predicting the FCGR from ΔK and R can be used to evaluate the expected fatigue lifetime, replacing R with $\mathrm{R}^{\mathrm{eff}}$. If a closure analysis is to be performed, the effect of residual stress would be included in that also.

In order to predict the effect of residual stress in a fatigue lifetime assessment, the analyst must know its magnitude and three-dimensional distribution for a given weld, but that is difficult to predict from theoretical considerations. Progress is being made in development of analytical models for predicting residual stress (Goldak, 1985), but the models are not yet developed to the point where they are used routinely in structural integrity evaluations. Instead, residual stress distributions for a given weld are generally still determined by experimental means (destructive, in most cases). For commonly encountered types of weldments, representative nominal residual stress distributions have been determined. Examples include butt-welded plate and pipe. However, there is no generally accepted method for the experimental determination of residual stress in thick plates, each method having it's own particular assumptions.

An example of such distributions is shown in Figure 1.3. This figure represents the state of residual stress found in a torch-welded butt joint in a thin plate as put forth by Baldwin (1949). The general characteristic of this distribution which can have a deleterious impact on structural integrity is the tensile stress which exists in both the longitudinal and transverse directions of the plate at its center. It is generally found for low strength steels that the maximum longitudinal stress is roughly equal to the yield strength of the base material. The maximum transverse stress is much smaller than the maximum longitudinal component, roughly 20% of the yield strength in low strength steel welds (Masubuchi, 1980, p. 223). Even though the transverse component is smaller, it can be quite important when considering a defective weld since hidden crack-like defects may occur more often in the longitudinal direction (e.g., longitudinal cracking, lack of fusion and lack of penetration). As pointed out by Baldwin (1949), the width of the zone of tensile transverse stress varies with the weld process, being wider for torch welding, as shown in the figure, and much narrower for arc welding. The distribution shown in the figure together with its approximate magnitude provide the general character of residual stress due to butt welding of thin plates.

For thin butt-welded plates, it is often assumed that the residual stresses are constant through the thickness of the plate. However, data from Hampton and Nelson (1989a) show that variations in residual stress do exist through the thickness in thin plates. For thick, multi-pass welds, however, the residual stress state usually varies with position through the thickness, and stresses can be generated in the through-thickness direction. Measurements of the variation of stress with depth have been reported by several researchers (e.g., Rosenthal and Norton, 1945; Ritchie and Leggatt, 1987; Ueda, 1989), and show that wide variation with depth can exist in the longitudinal and transverse stress. Such variations make creation of a picture similar to Figure 1.3 for a thick plate nearly impossible. However, distributions of stress through the thickness at the center of the weld bead in a thick butt welded plate and a thick circumferentially welded cylinder are shown in Figure 1.4 and Figure 1.5.

It is prudent to note at this point that a residual stress is actually brought about by an incompatible strain field. Incompatible strain is referred to by many different names, and the authors adopt the terminology of T. Mura (1982) who refers to it as “eigenstrain”, adapting to English the title of an earlier German paper (Reissner, 1931). Eigenstrain is that strain brought about by any non-elastic means (e.g., plastic deformation), and this will result in residual stress if it is incompatible in the body of interest. In an elasticity problem, the eigenstrain will remain constant, and may be treated as an equivalent body force in the equilibrium equations. Mura’s book is devoted almost solely to the problem of determining the residual stress corresponding to a given distribution of eigenstrain. In theory, such analytical work could be applied to the problem of weld residual stress. Of course, one must first know the distribution of eigenstrain present in the weld. As will be shown later, the experimental work of Ueda (1975) has as its goal the determination of eigenstrain in the weld region (what he calls “inherent strain”). Also, Mura’s book is devoted almost entirely to the case of an infinite three-dimensional body. In the case of many engineering structures, the influence of finite dimensions is expected to be of importance, and many LEFM schemes deal with two-dimensional geometries, so that solutions presented by Mura cannot be applied without considerable alteration.

Nevertheless, the general approach taken by Mura provides excellent insight into the problem of eigenstrain and residual stress.

1.2.3 Material and microstructure variation

Since welding involves a thermal cycle with maximum temperatures reaching beyond melt, the microstructural characteristics of the base plate and weld metal are altered by welding. If cooling rates are high in steel welds, extensive martensitic transformation will occur, resulting in a large gradient in hardness across the weld and a localized volumetric expansion. Mutoh (1984) lists microstructural factors influencing FCGR in steels as: grain size, inclusions, presence of delta ferrite, and martensitic transformation. The region of changed microstructure in a base metal is referred to as the heat affected zone (HAZ). The HAZ has been shown to have inferior fracture properties compared with either the base or weld metals in both aluminum and steel welds (Masubuchi, 1980; p. 28). Microstructural variations occur in a weldment even if the base and weld metals have the same chemical composition and strength prior to welding.

There can also be a variation in properties of the weld and base materials due to their differing composition. Since the weld thermal cycle generally changes the toughness of the weld and base material, it has been common practice to use a more or less ductile weld metal. In this way, the fracture properties of the weldment can be made to more closely match those of the base material. However, the result can be a gradient in the yield strength and hardening properties across the weld. When the weld metal has a higher yield than the base material, the weld is said to be overmatched, and the converse is called undermatch. The match quality affects the strength and fracture properties of the weld.

Such property gradients call into question the applicability of existing methods used to predict crack growth or fracture. For most welds, the elastic properties of the weld and base metals are very nearly the same. That being the case, if the crack tip stresses satisfy small-scale yielding conditions, prediction of the applied stress intensity factor (SIF) is not sensitive to variations in inelastic properties. In the ductile regime, calculation of the applied J-integral which assumes a homogeneous material is called into question by the variation of inelastic material behavior across the weld. In either the small- or large-scale yielding regime, material properties to be used in crack growth and failure predictions will depend on the location of the crack-tip in relation to the weld bead.

1.3 Analysis methods for crack growth in the weld region

1.3.1 Determination of crack growth parameters

The usual way to determine crack growth parameters for welded structures is to perform fatigue crack growth rate (FCGR) testing, just as would be done for any other type of metal. In this way, a functional form is found for FCGR in terms of ΔK for the welded joint. In this relation effects of stress ratio and opening behavior may or may not be included. Testing is performed on specimens produced under welding conditions and with materials which as closely as possible match the structure to be analyzed. To simplify testing and subsequent FCP analyses, the weld region is generalized as consisting of three areas: weld metal (WM), heat affected zone (HAZ), and parent metal (PM). Specimens suitable for FCGR testing are then produced to determine the crack growth behavior of each region. Such specimens can be made either with the line of crack growth oriented across the weld, or with the initial crack front lying in the region of interest and the line of crack growth oriented along the weld. With the latter specimens, more data can be taken from fewer specimens since there is more material of each type available for crack propagation. In the first type, the weld metal crack propagation distance is somewhat less than the bead width (which is usually comparable with the plate thickness), so the number of FCGR data points is limited. A few examples of typical specimens used in FCGR testing are shown in Figure 1.6. Problems exist with attempting to measure FCP parameters in the HAZ region since the crack frequently diverges into the neighboring weld or parent material. In order to keep the crack front in the proper material region side-grooves are often added to the basic specimen. At any rate, experimental measurement of as-welded plates is presently the only method available to account for the effects of material variation in the weld region.

A study by Mutoh (1984) on type 304 stainless steel welds showed that the FCGR in the weld metal is significantly higher than that in the parent metal for the same ΔK_{eff}

(where ΔK_{eff} = K_{max} - K_{op} and K_{op} is the stress intensity at crack opening, measured experimentally), as shown in Figure 1.7. By using ΔK_{eff}, mechanical factors, such as residual stress, are assumed to be separated from microstructural influences. Quoting results from Bathias (1973), which showed that the crack growth rate for martensitic steel is higher than that for austenitic steel, he surmises that martensite in the WM is the reason for the increase in FCGR. With fractographic analysis, Mutoh found that the austenitic PM had a grain size of 80µm while the WM consisted of dendritic delta ferrite in an austenitic matrix, where the dendrite was approximately 950µm. Mutoh concludes that the dendritic structure in the weld metal is so coarse that martensitic transformation occurs easily during the weld thermal cycle. Mutoh also performed fatigue crack propagation (FCP) tests on PM specimens heat treated to achieve a grain size of 950µm. The results of these tests were nearly identical to results for the WM specimens, as shown in Figure 1.8. By investigating the martensite content of all these specimens, he found martensitic transformation had occurred in the 950µm grain diameter PM, in the WM, but not in the 80µm grain diameter PM specimens. To further show that the increase in FCGR was not due to residual stress, Mutoh presented results for solution treated WM specimens which agreed with those of the non-solution treated WM (again, in terms of ΔK_{eff}).

Shi (1990) studied the effects of residual stress and microstructural variation on FCGR in API X52 (0.13% C) steel welds. He utilized three types of specimens: parent metal, weld metal, and “cross-bond” (CB). The CB specimen has the crack oriented such that one portion of the crack front was in the HAZ and the other in the weld metal, as shown in Figure 1.6. Shi found that under the same ΔK^{app} the PM had the fastest growth rate followed by the WM, with the CB region showing the smallest growth rate. Opening behavior was measured on the WM and CB specimens and the results of testing are presented in terms of ΔK^{eff} in Figure 1.9 represented by a Paris Law fit. Here it is seen that the CB specimen has a higher FCGR than the WM in terms of ΔK^{eff}. Although opening behavior was not measured for the PM specimens, such measurements would shift the PM FCGR results to lower ΔK values. Accordingly, we can conclude that Shi’s data show a tendency for the PM to have a higher FCGR than the WM at the same value of ΔK^{eff}, in contrast to the results of Mutoh for a different metal.

Ohta (1986) found no variation in crack growth properties, in terms of ΔK^{app}, of the HAZ or weld metal of non-stress-relieved welded joints of several steels (JIS SM50B, HT80, and JIS SB42, and JIS SPV50). There was a difference in the FCGR between the welded specimens and the as received parent material, however, which was greatest near ΔK_{th}. No measurement was made of opening behavior in these studies, and so it is difficult to determine whether these results merely demonstrate the influence of residual stress overwhelming the influence of microstructural variation.

It is apparent from the results cited thus far that the fatigue crack growth of a welded joint depends on the microstructure of region in which the crack-tip lies. Unfortunately, it is nearly impossible to predict such effects based on theory. Since the limited amount of data available show differing effects of welding on FCGR, it is difficult to even make generalizations regarding this topic. In short, it appears that FCP tests must be conducted to quantify these properties for the welded joint of interest. Furthermore, each combination of WM, PM, and welding conditions must be treated as a distinct case and characterized separately.

1.3.2 Superposition of residual stress on applied loading

1.3.2.1 Weight functions

Assuming that residual stress in the weld region is known, it must be included in an LEFM crack growth assessment. It has been argued that the weight function of Beuckner may be employed to compute the stress intensity factor associated with the residual stress (Parker, 1982). It is well known that weight functions can be used to calculate the SIF for a body under arbitrary applied loading conditions. These loading conditions, applied on the boundary of the body, are of two types: applied tractions, $\mathbf{t}(x,y)$, and applied displacements $\mathbf{u}(x,y)$. Accordingly, there are two weight functions, one for each boundary condition type. Further, the weight functions for the body of interest are derived for a *particular* boundary subdivision into two parts, that where a traction is applied, Γ_t, and that where a displacement is applied, Γ_u. These two subsets must satisfy the relations

$$\Gamma_t + \Gamma_u = \Gamma \qquad (1.11)$$

$$\Gamma_t \cap \Gamma_u = \emptyset \qquad (1.12)$$

i.e., the two subsets must make up the whole boundary and may not overlap. Once the weight functions are determined, the contribution to the crack tip stress intensity factor for each boundary condition, the displacement **u**(x,y) and the traction **t**(x,y), can be calculated separately from

$$K^u = \int_{\Gamma_u} \boldsymbol{u}(\mathrm{x}, y) \bullet \boldsymbol{m}^*(x, y, a)\, d\Gamma \tag{1.13}$$

$$K^t = \int_{\Gamma_t} \boldsymbol{t}(\mathrm{x}, y) \bullet \boldsymbol{m}(x, y, a)\, d\Gamma\,. \tag{1.14}$$

Here we have adopted the notation of Parker, who uses ***m***(x,y,a) and ***m****(x,y,a) to denote the weight function for applied stress and for applied displacement, respectively (Parker, 1982). Also, the "•" in the two equations is the dot- or scalar-product operator, and **u**(x,y), ***m****(x,y,a) and **t**(x,y) are vector quantities in general. One important thing to note is that a particular boundary subdivision gives a pair of ***m*** and ***m****. The interpretation of Equation 1.13 or Equation 1.14 is elucidated by substituting a Dirac delta function for one component of **u**(x,y) or **t**(x,y). Performing that substitution, it becomes apparent that the value of the weight function is the SIF corresponding to a unit displacement or a unit load in that direction, respectively, at one point on the boundary. Accordingly, the weight function is equivalent to a Green's function for the SIF.

A weight function can be determined for geometries of interest from previous elastic stress analysis. As reported by Parker (1983), Bowie and Freese (1981) modified earlier work by Rice (1972) to show that the SIF can be determined from a previous elasticity solution. When two loading systems, 1 and 2, act on the same cracked body and have the same division of Γ into Γ_t and Γ_u, the following relation must hold for a particular but arbitrary crack length:

$$K^{(1)}K^{(2)} = \frac{H}{2}\int_{\Gamma}\left[\boldsymbol{t}^{(2)} \bullet \frac{\partial \boldsymbol{u}^{(1)}}{\partial a} - \boldsymbol{u}^{(2)} \bullet \frac{\partial \boldsymbol{t}^{(1)}}{\partial a}\right] d\Gamma \tag{1.15}$$

where

$$H = \begin{cases} E & \text{in plane stress} \\ \dfrac{E}{1-\nu^2} & \text{in plane strain} \end{cases} \tag{1.16}$$

E = Young’s modulus
ν = Poisson’s ratio.

The superscripts in the above relation denote the loading system (1 or 2) associated with the corresponding quantity. To obtain the weight functions ***m***(x,y,a) and ***m****(x,y,a), novel choices are made for the loading systems 1 and 2. First, assume that tractions $\mathbf{t}^{(1)}$ do not change with crack length and that $\mathbf{u}^{(2)} = 0$. Combining these systems with Equation 1.15, we have

$$K^{(2)} = \frac{H}{2K^{(1)}} \int_{\Gamma_t} \boldsymbol{t}^{(2)} \bullet \frac{\partial \boldsymbol{u}^{(1)}}{\partial a} d\Gamma . \tag{1.17}$$

Comparing Equation 1.17 and Equation 1.14, we find

$$\boldsymbol{m}(x,y,a) = \frac{H}{2K^{(1)}} \frac{\partial \boldsymbol{u}^{(1)}}{\partial a} . \tag{1.18}$$

Now assuming that displacements $\mathbf{u}^{(1)}$ do not change with crack length and the boundaries are traction free so that $\mathbf{t}^{(2)} = 0$, it can be shown that

$$\boldsymbol{m}^{*}(x,y,a) = -\frac{H}{2K^{(1)}} \frac{\partial \boldsymbol{t}^{(1)}}{\partial a} . \tag{1.19}$$

In Equation 1.18, the right hand side depends on position (i.e., x and y) through $\mathbf{u}^{(1)}$ and depends on crack length (i.e., a) through both $K^{(1)}$ and $\mathbf{u}^{(1)}$ (a similar statement can be made regarding $\mathbf{t}^{(1)}$ and $K^{(1)}$ Equation 1.19).

It should be noted that although the weight function is in general a vector quantity, many times it is presented as a scalar. This frequently is the case for weight functions derived to be used with crack-line loading, where the loading is applied to each side of the crack face in the opening direction (i.e. normal to the crack). In this case, the orientation of the loading relative to the crack is fixed, and a vector representation is no longer necessary. As an example of such a weight function, consider an infinite body in plane stress with a through crack of length 2a located at the origin oriented along the x-axis. Suppose that the problem posed is to determine the SIF corresponding to an arbitrary distribution of pressure, p(x), applied to the crack faces in the y-direction (acting to open the crack). To solve this problem, the weight function can be used where *m* is determined from a “reference” solution.

The reference we will use is a well-known SIF solution for an infinite body under the action of remote uniform stress σ, applied the y-direction. To compute the weight function according to Equation 1.18, we will need to know the value of K as a function of a and the crack-face displacement as a function of a and x along $\Gamma_t = \{\ |x| < a,\ y = 0\}$ for the reference solution. Since the pressure distribution p(x) acts normal to the faces, we only need the displacement component in that direction, $u_y(x,a)$. All other terms in the scalar-product of Equation 1.14 will be zero. These functions are known to be

$$K = \sigma\sqrt{\pi a} \tag{1.20}$$

$$u_y(x,a) = \frac{2}{E}\sigma\sqrt{a^2 - x^2}\,. \tag{1.21}$$

We now use Equation 1.20 and Equation 1.21 in Equation 1.18, with H=E since we have assumed plane stress, and obtain the weight function component in the y-direction

$$m_y(x,a) = \left(\frac{a}{\pi}\right)^{\frac{1}{2}} \frac{1}{\sqrt{a^2 - x^2}}\,. \tag{1.22}$$

The unknown SIF for loaded crack faces may now be determined by using Equation 1.22 in Equation 1.14 with $t_y(x,y) = p(x)$ on Γ_t :

$$K(a) = \left(\frac{a}{\pi}\right)^{\frac{1}{2}} \int_{-a}^{a} \frac{p(x)}{\sqrt{a^2 - x^2}}dx\,. \tag{1.23}$$

Frequently in the literature, a scalar representation of the weight function is assumed and the corresponding direction of applied boundary conditions is determined to be consistent with that representation. In that case, the subscript “$_y$” on *m* in Equation 1.22 is dropped. Regarding the computation of Equation 1.23, often residual stress is known from experimental points rather than any mathematical function and the integration will be carried out numerically. Optimal methods for numerical integration of weight functions have been demonstrated by Moftakhar and Glinka (1992).

According to Parker (1983), it is possible to determine the stress intensity factor due to an applied displacement from either an ***m***- or an ***m****-type weight function, i.e., from either Equation 1.13 or Equation 1.14. As an example, consider the case of a finite plate with a centrally located crack and fixed ends as shown in Figure 1.11. Here, Γ_t is defined as the crack faces and the edges of the plate perpendicular to the crack while Γ_u encompasses the ends of the plate which are parallel to the crack. Suppose now that a displacement,

$$\mathbf{u}(x,|y|=c) = \{0\ ,\ v_o,\ 0\}^T \tag{1.24}$$

is applied to the ends of the plate. The SIF for this case may be determined in two ways. One way is to use Equation 1.13, integrating over the top and bottom edges of the plate. However, it is also possible to use Equation 1.14 with the proper definition of $\mathbf{t}(x,y)$ and $\boldsymbol{m}(x,y,a)$. First, $\mathbf{t}(x,y)$ is determined as the stress that would exist on the crack line in the uncracked body (Parker, 1983), so that $\Gamma_t = \{\ y = 0 \cap |x| \leq a\ \}$. This may now be used in Equation 1.14 provided that $\boldsymbol{m}(x,y,a)$ was derived with $\mathbf{u}(x,y) = 0$ on the plate ends. This calculation is common, and most weight functions are derived for the crack line, rather than the remainder of the boundary (e.g., the plate edges and ends in this example).

When the evaluation of SIF is performed by using the crack line stresses, the weight function must be carefully chosen to match the boundary conditions imposed. In the above example, the particular $\boldsymbol{m}(x,y,a)$ used must be derived for a plate with fixed ends. A common mistake made in applying the weight function is to overlook this distinction and use the weight function derived for traction loaded plate ends. In fact, weight functions derived with displacement boundary conditions are not common. Use of the incorrect weight function can cause significant error in determination of the SIF, as will be illustrated, especially when the displacement is applied in a region “close” to the crack.

We can examine this discrepancy by first considering the case of an infinite strip, and then the case of a plate which is finite in both directions. Tada (1973) considered the case of an infinite strip with a center crack subjected to twin point loads acting to open the crack, as shown in Figure 1.12. Since this is the solution for a point load, it is the Green’s function needed for a weight function definition. The point load here, P, is given as load per unit thickness. Tada’s solution for the SIF at the right crack-tip is:

$$K = \frac{P}{\sqrt{2W}} f(d, a) \tag{1.25}$$

where

$$f(d, a) = [1 + 0.297\sqrt{1 - \alpha^2}(1 - \cos(v))]\sqrt{g(u, v)} \tag{1.26}$$

$$u = \frac{\pi d}{2W} \qquad v = \frac{\pi a}{2W} \qquad \alpha = \frac{d}{a}$$

and,

$$g(u,v) = \frac{\tan v}{1 - (\cos v / \cos u)^2}\left[1 + \frac{\sin u}{\sin v}\right]^2 .$$

This solution may be transformed into the weight function, defined on the crack faces (i.e., $y = 0$ and $|x| \le a$), by substituting $P = \sigma(x)\, dx$, where $\sigma(x)$ is the stress acting normal to the crack and dx is the infinitesimal distance over which the stress is distributed. The SIF at the right crack-tip may then be calculated from

$$K = \frac{1}{\sqrt{2W}} \int_{-a}^{a} \sigma(x) f(x, a) dx . \tag{1.27}$$

By comparing Equation 1.27 with Equation 1.14, we see that

$$m(x,y,a)|_{y=0} = \frac{1}{\sqrt{2W}} f(x, a) \tag{1.28}$$

$$\Gamma_t = \{ y = 0 \cap |x| \le a \}.$$

Therefore, Equation 1.28 defines the weight function for a strip of finite width and infinite length to be used with crack line loading. Notice that we are now using the scalar notation for the weight function since the loading direction is fixed in this problem. It should be noted that the boundary conditions implied in Tada’s derivation are traction free strip edges. The conditions at the ends of the infinite length strip do not need to be specified, as they are infinitely far from the crack location. The effect of differing boundary conditions at the ends of *finite* length plates will have an effect on the SIF, and Equation 1.27 becomes an approximation.

Now, we examine the effect of differing boundary conditions for finite length plates. Consider a plate of length 2c and width 2b with a center crack of length 2a, as shown in Figure 1.11. Isida (1971) solved for the SIF for this geometry under both applied displacements and applied tractions, showing that the two will result in different stress intensity factors for the same initial crack-line stress. By initial crack line stress, we refer to the stress present on the crack-line prior to mathematically opening the crack faces. Suppose that such a plate is gripped at the ends and given a uniform end displacement. Further consider that the grip is totally rigid such that the displacement imposed on the plate is given by Equation 1.24. The stress resulting from this displacement is uniform along the crack-line; however, since lateral contraction is being restrained, the stress will depend on the plate length. For plates which are long compared to their width (c/b is large), stress at the center is not affected by the lateral restraint, so the crack line stress will be

$$\sigma(x) = \frac{Ev_o}{2h} \quad \text{for c/b large.} \tag{1.29}$$

As the ratio c/b becomes small, the stress will be effected by the restraint and in the limit

$$\sigma(x) = \frac{Ev_o}{2h(1-\nu^2)} \quad \text{for c/b small.} \tag{1.30}$$

The SIF corresponding to the applied displacement can be compared to the SIF computed for a plate subject to a uniform stress field of a magnitude bounded by Equation 1.29 and Equation 1.30. The SIF for the applied displacement condition is shown in Figure 1.13 while the SIF for uniform traction is shown in Figure 1.14. In both plots, the SIF has been normalized by the infinite plate SIF given by Equation 1.20. The difference for shorter plates is quite striking. Furthermore, performing a weight function calculation with the initial crack line stress would give results equivalent to those in Figure 1.14 if the weight function used was not derived with displacement boundary conditions. The initial crack line stress can be determined for each separate c/b in Figure 1.13 from the value of the normalized K at a/b = 0. The stress corresponding to Equation 1.29 would be represented by 1.0 on this axis, while the stress corresponding to Equation 1.30 would be 1.10 ($\nu = 0.3$ is assumed by Isida). By making such a comparison, we can conclude that neglecting any imposed displacement boundary conditions can drastically affect calculation of the SIF.

The difference between the two solutions above results from the differing nature of traction and displacement boundary conditions. As the crack is opened in the plate, the compliance of the plate changes, so that crack line stresses are not independent of crack length. Accordingly, the reaction load at the location of the fixed displacement diminishes as the crack is opened. For long cracks in short plates, the average stress resulting from the fixed displacement is much smaller than the initial stress in the plate. Accounting for the change in average stress at the plate ends greatly improves the estimate of the SIF, as shown in Figure 1.15. In this figure the average stress computed at the ends of the plate with the crack open is used to scale the SIF instead of the initial stress.

Wu and Carlsson (1983) used the work of Isida to show the difference in SIF between free and fixed end conditions for a finite plate subjected to an arbitrary but self-equilibrating stress field. Their approach was to use Isida's K(a) results to determine the weight function for the free and fixed ended plates. They assumed that the boundary condition would not affect the shape of a crack under load, but merely change the amount of opening at the center of a crack. By assuming that the crack opening profile is elliptical, as it is for an infinite plate under uniform stress, the amount of crack opening, $u_o(a)$ can determined by using Equation 1.14. If the same K(a) solution is used to define the SIF on both sides of the equation and Leibnitz rule is used on the resulting equation, it can be shown that

$$\int_0^a [K(x)]^2 dx = H\int_0^a \sigma(x) u(x,a) dx \tag{1.31}$$

which, for the assumptions of Wu and Carlsson, leads to

$$u_o(a) = \left\{\int_0^a [K(x)]^2 dx\right\} \Big/ \left(H\int_0^a \sigma(x) u^*(x/a) dx\right) \tag{1.32}$$

Here, the function u*(x/a) represents the assumed elliptical opening shape of the crack,

$$u^*(x/a) = \sqrt{1-(x/a)^2} \tag{1.33}$$

and $\sigma(x)$ is the original crack line stress. Once the crack opening is calculated from Equation 1.32, the crack shape is given by

$$u(x,a) = u_o(a)\, u^*(x/a) \tag{1.34}$$

This crack shape is then used in Equation 1.18 to define the weight function under fixed or free end conditions defined on the crack faces. Wu and Carlsson found the weight function in this manner and used it to obtain the SIF results shown in Figure 1.16. Clearly, the difference between fixed and free end conditions is large even for a self-equilibrating stress field.

Petroski and Achenbach (1978) introduced a method similar to that of Wu and Carlsson to determine the weight function from a known SIF solution. Instead of dealing with a center crack, their attention was focused on an edge crack; however, their method could theoretically be applied to center cracks. The difference between the two methods lies in the definition of the assumed crack opening profile (e.g., Equation 1.34). Instead of assuming a scaling, as Wu and Carlsson did, Petroski and Achenbach assumed the form

$$u(x,a) = u^{\infty}(x,a) + \frac{\sigma}{H\sqrt{2}} G(a/W)a^{-1/2}(a-x)^{3/2} \tag{1.35}$$

where, $u^{\infty}(x,a)$ is the crack face displacement in the infinite domain under uniform stress. The function G(a/W) can be determined from Equation 1.31, then the derivative of Equation 1.35 used to determine the weight function from Equation 1.18. In a more recent paper, Ojdrovic and Petroski (1991) extended this method to include more terms in Equation 1.35 which are determined from additional reference K(a) solutions having the same domain and boundary division into Γ_t and Γ_u. The accuracy of the method relative to handbook solutions was also demonstrated in this later paper for several different loading profiles applied to an edge crack in a semi-infinite space. Glinka, et al. (1991) presented a similar methodology to that contained in (Ojdrovic and Petroski, 1991) but applied it to different crack geometries. Methods such as these for determination of weight functions are extremely powerful since they allow previous K(a) solutions to be used to define the weight function and therefore the SIF for an arbitrary crack line loading, even when the crack opening profile is unknown (as is often the case).

As mentioned previously, residual stress results from an eigenstrain in the body of interest. Accordingly it would be of interest to find a method that might be used to determine the SIF resulting from an arbitrary distribution of eigenstrain, rather than a known stress distribution. Parker (1983) reported generalizations of the weight function to deal with either distributed strain or body force. The form of the stress intensity solution for a body force **F** distributed over a region A_t was first given by Rice (1972) and is

$$\mathrm{K} = \int_{A_t} \boldsymbol{F} \bullet \boldsymbol{m}(x, y, a)\,dA\,. \tag{1.36}$$

Parker assumed the same form would apply to a strain field distributed over a region A_u, such that

$$\mathrm{K} = \int_{A_u} \boldsymbol{D} \bullet \boldsymbol{m}^*(x, y, a)\,dA\,. \tag{1.37}$$

In this equation **D** "represents a distributed strain field," in the words of Parker (1983). Clearly **D** can not *be* the distributed strain, as strain is a second order tensor, and a vector quantity is needed in the equation. Unfortunately, the proper method for determination of **D** was not given by Parker, leaving the method of handling a distributed strain unknown. However, in an elastic body it is possible to treat a distributed eigenstrain by defining an equivalent body force. Mura (1982; Chapter 1, Section 2) states that a distributed eigenstrain can be replaced by an equivalent body force in the elasticity equilibrium equations. Knowing how to compute that body force, it would be possible to use Equation 1.36 to compute the SIF for a distributed strain. Mura gives the body force components as

$$\mathrm{F_i} = -\,\mathrm{C_{ijkl}}\frac{\partial \varepsilon^*_{kl}}{\partial x_j} \tag{1.38}$$

where

$\mathrm{C_{ijkl}}$ = elastic moduli

$\varepsilon^*_{\mathrm{kl}}$ = components of distributed eigenstrain which are functions of position

$\frac{\partial(\bullet)}{\partial x_j}$ denotes the derivative of (•) by $\mathrm{x_j}$.

Summation convention is implied. In the case of a homogeneous body, we may rewrite Equation 1.38 as

$$\mathrm{F_i} = \frac{\partial}{\partial x_j}\,[-\,\mathrm{C_{ijkl}}\varepsilon^*_{\mathrm{kl}}]\,. \tag{1.39}$$

The bracketed quantity in this equation is the stress which would develop in the body if no deformation was allowed. The use of Equation 1.38 in Equation 1.36 to compute the SIF for cases of distributed strain has not, to the author's knowledge, been performed. Instead, normal stress is determined along the crack-line in the uncracked body, and calculations similar to those leading to Equation 1.23 are performed. It has yet to be shown that these two methods are equivalent.

A number of authors have argued that use of initial crack line stress to compute the SIF may give inaccurate results. In a finite body, residual stress must be self-equilibrating. The residual stress then can be divided into two portions, the "active" portion, which is within the region of non-zero eigenstrain, and the "compensating" portion made up by the remainder of the body (Shi, 1990). If the active stress changes the reactive stress must also change so that the body remains in equilibrium. In the context of a crack problem, opening a crack in the active region will alter the stress there and so the stress in the compensatory region must also change. Along this line of reasoning, several authors have argued that the weight function and other superposition methods which treat residual stress by utilizing crack line stress in the uncracked body are inherently flawed. Just as in the case of an imposed displacement, stress due to eigenstrain is a function of the compliance of the body in which it is imposed. Since introduction of a crack changes that compliance, it will also change the stress. It has been argued that the crack line stress is therefore not independent of crack length and that the SIF computed from it is in error (Nelson, 1982; Lam, 1989; Underwood, 1977; Glinka, 1987). This question seemingly remains unresolved.

Another difficulty with the weight function occurs when there is crack closure during a portion of loading. When crack faces are completely closed, the appropriate boundary condition on those faces is applied displacement (equal to zero). However, when the crack begins to open, the portion of the crack face not closed has an applied traction boundary condition (equal to zero). In this way, the boundaries Γ_t and Γ_u are constantly changing during the loading cycle. The problem of crack face contact has been addressed by Beghini (1990) by using FEM, and by Bakioglu (1977) using an iterative mathematical scheme. However, no general approach has been developed to deal with crack face contact problems.

1.3.2.2 Computational techniques

One of the best methods which can be used to obtain solutions to finite geometry eigenstrain problems is the finite element method (FEM). In fact many commercial FEM packages can be utilized by either distributing anisotropic thermal expansion coefficients in proportion to the eigenstrain distribution of interest and then applying a unit temperature variation, or more simply by distributing an equivalent body force computed from Equation 1.38. After imposing the eigenstrain in this manner, a crack can be opened in the model and the stress intensity factor can be determined from the resulting stresses or displacements by using any of several methods (e.g., Itoh, 1986; Lam, 1989; Cook, 1989, Sec. 8.9).

A few authors have performed stress intensity computations in this manner, and have shown good agreement with the crack line stress weight function method. However, some have shown that there can be considerable differences between the two methods. The apparent discrepancy here can likely be explained by specimen (finite) geometry considerations. For example, studies which have used center cracked tension (CCT) specimens which are “long” and in which the residual stress is similar on planes near the plane of crack growth (e.g., a central weld parallel to the loading axis) generally show fairly good agreement between the FCP analysis and experiment (Itoh, 1989), or between weight function and eigenstrain FEM stress intensity calculations (Legatt, 1984).

When the eigenstrain is distributed over a smaller region, the weight function method used with crack line stresses has been shown to give less than satisfactory results (Lam, 1989; Graham, 1988). Lam (1989) used an applied displacement method and FEM to obtain an improved result in predicting FCP compared with the weight function. However, the weight function he used was one for an infinite strip under applied stress, but in his FEM computations he used a finite strip under applied displacement conditions. When Lam made FCP predictions, he found that use of K^{res} computed from FEM applied displacement analysis better matched his experimental results. More on Lam’s work can be found in Section 1.5.3. Graham (1988) performed a weight function calculation for a crack emanating from a hole in a strip of finite width. Residual stress was introduced by applying a large tensile load to the strip. The stress concentration at the hole caused localized plastic deformation and when the strip was unloaded, a compressive residual stress was left behind. This overload process was modeled with FEM, and the residual stress on the crack plane obtained. The crack line residual stress computed was then used with a weight function solution to calculate the SIF. The results of the weight function solution were compared to calculations obtained by extending a crack within the overloaded FEM model. There is a notable difference in the two results, as seen in Figure 1.17. Both of these studies show that FEM is capable of predicting the SIF for a given eigenstrain distribution. A systematic study of the effect of residual stress redistribution on SIF computation has not yet been performed; however, FEM provides a valuable framework for such research.

Another potential use of FEM in crack problems is in defining the weight function. If one were to use the weight function method to compute the stress intensity factor from a body force distribution corresponding to an eigenstrain field of interest, the weight function at points remote from the crack would be needed. As noted by Rice (1972), the weight function can be partitioned into two parts, one which is singular at the crack tip, and one which is non-singular everywhere. Further, he suggested that the functional form of the singular portion is known from the SIF solution in an infinite body. Since FEM can represent non-singular displacements (some distance from the crack-tip) with good accuracy even for a coarse mesh, he noted that FEM could be used to determine the non-singular part of $\boldsymbol{m}(x,y,a)$ for x and y away from the crack-tip. If the weight function is not needed at points close to the crack tip, the usual problems of mesh refinement at the crack tip and mesh alteration with crack extension can be bypassed, as long as the SIF solution is previously available.

Access to the proper weight function appears to be a common difficulty when using that method, and the ability to “package” the weight function from FEM results appears promising (Beghini, 1989). In this approach, a piecewise weight function is generated by performing repetitive FEM calculations. The weight function at a point is equal to the value of the SIF caused by a unit traction (for $\boldsymbol{m}$) or a unit displacement (for $\boldsymbol{m}^*$) applied at that point. The procedure is to apply point loads or displacements at a series of locations, find the resulting SIF for a series of crack lengths in a geometry of interest, and then curve fit the results to obtain $\boldsymbol{m}(x,y,a)$ or $\boldsymbol{m}^*(x,y,a)$. Beghini utilized this method to obtain the applied traction weight function over the crack face boundary for a compact tension specimen.

In closing, it should be noted that the generality of FEM is its strongest suit. Any geometry can be modeled, and any type of loading can be imposed. Also, constraints on displacement can be imposed so that crack face contact can be included in SIF computations. FEM offers the ability to include plastic deformation and therefore investigate crack closure and load interaction effects (Zhang, 1992). It also might be used to investigate the effect of loading on initial residual stress. Although use of FEM can be a demanding discipline, its many advantages merit its pursuit for analyses of the type reviewed here.

1.4 Determination of residual stress

The techniques just described, which attempt to account for residual stress when making fatigue life predictions, assume knowledge of the residual stress which exists at least along the expected plane of crack growth, if not within the entire body of interest. The determination of residual stress has been studied for some time and a wealth of information can be found in the literature.

An early study of weld residual stress was performed by Weck (1948) on well restrained butt welds of mild steel plate. His approach was to measure the deformation in the vicinity of a weld. In this manner, he not only obtained the residual stress, but also the plastic deformation which occurred during welding. Several grid points were marked on the surface of the unwelded plates along the weld-line. These points were located along the direction of welding at 1 inch intervals near the edges of the plate and at one-half inch intervals toward the center. One set of points was laid at 1 inch from the weld line and another at 2 inches. By measuring the distance between the points before and after welding, average strain over a one inch gage length was measured. Accordingly, the location of transverse strain measurement was at 1.5 inches from the bead while the location of the longitudinal strain measurements was at 1 inch from the bead.

Three measurements of deformation were taken at several locations along the weld. These three consisted of deformation from unwelded to welded state, from unwelded to welded but unrestrained, and from welded state to a state where the weld bead was removed (Weck referred to this as “elastic recovery”, and assumed it to be proportional to residual stress). Weck’s measurements of deformation along the direction of welding for two different weldments are shown in Figure 1.10. Four numbered curves are presented in the figure for each weld, and each curve is defined in the figure. Plastic deformation can be obtained by adding curve (4) and curve (2) and elastic deformation in the unrestrained state is approximately proportional to curve (4) and of the opposite sign. The 3/4 inch plate was welded under a moderate restraint condition, while the 3/8 inch plate was welded with extreme restraint. The results show that there was almost twice as much plastic deformation 1 inch from the bead in the 3/8 inch plate compared with the 3/4 inch plate, but that the elastic deformation is greater for the less restrained 3/4 inch plate and of opposite sign. By examining only curves (1) and (2) for each of these two welds, the reversal of sign of residual stress (proportional to curve (4)) is unexpected. This shows that point values of plastic deformation are of relatively little use in determining residual stress without knowledge of the remainder of the plastic deformation field. Further study of the total residual stress field requires measurement of the deformation in the entire weld region instead of just along one line one inch from the weld bead. Even with this consideration, Weck’s results are unique in illustrating measurement of weld region deformation.

By far the most popular and widely used class of methods for residual stress determination is called “relaxation”. Relaxation methods include sectioning, slitting, and hole-drilling techniques. One way to use relaxation is simply to cut the specimen into small pieces and measure the deformation each piece undergoes as it is cut from the body. If the removed piece is small enough, it will contain no residual stress, and the residual stress in the piece is said to be “relaxed”. By measuring the corresponding relieved strain or deformation, it is possible to relate that strain to the original state of residual stress that existed prior to cutting. When obtaining stress from measured strain, it is usually assumed that the material at the measurement point was in a state of plane stress before cutting making the calculation rather simple; however, existence of out of plane stress near the surface may also have an influence on the relaxed strain, but this is usually ignored. Partial relaxation methods also exist in which only a portion of the residual stress is released. When using these methods, calibration specimens or analytical correlations are used to relate an amount of cutting and resulting strain release to the preexisting residual stress.

Other residual stress measurement techniques include methods that measure material properties which vary with stress. For instance, the speed of sound is a property dependent on the stress in a material. In some cases, ultrasonic methods can be used to measure the variation of this property within a body and therefore estimate the residual stress distribution. Atomic lattice spacing is a material characteristic which depends on stress, and X-ray diffraction is used to measure the variation in lattice spacing which is then related to the local residual stress. Several techniques for the determination of residual stress are discussed in the following section.

1.4.1 Techniques for surface stress

1.4.1.1 Hole drilling

Hole drilling is one of the relaxation methods which can be used to determine stress near the surface of a part and is classified as semi-destructive. The result of a hole drilling measurement is a point surface stress averaged over the region where the hole is drilled, typically less than a few mm in diameter, but stress gradients near the surface can also be measured. The procedure is to attach a special foil type resistance strain-gage rosette to the specimen, and then to use a high-speed end mill to drill a hole to a depth of about one hole diameter. Analytical results have shown that for this depth, nearly all of the residual stresses in the region around the hole periphery are relaxed. The measured strain is then related to stress in either of two ways: in formulae which depend on the size of hole, type of gage, specimen geometry, and material properties; or in empirical relations derived from calibration specimens tested under known stress. The real time consuming aspect for this type of method comes in the installation of the strain-rosette and the milling guide needed to center a hole with respect to it. Since the measured residual stress is fairly sensitive to alignment, extreme care is taken at that step. An excellent overview of this method can be found in SAE Handbook Supplement J936 (1965), and an example of its use on welded joints found in Hampton and Nelson (1989b).

1.4.1.2 Ultrasonic testing

Ultrasonic residual stress determination takes advantage of the weak dependence of the speed of sound in metal on stress. Waves travel through solids with different waveforms, longitudinal and shear, and travel along the surface as Rayleigh waves. The speed of a longitudinal wave is dependent on the sum of principal stresses in metal, while the velocity difference between two orthogonally polarized shear waves is dependent on the difference in principal stresses. By "stresses" here we are referring to stress averaged over the direction and distance of wave travel used for velocity measurement, so that ultrasonic methods are used to give the average residual stress through the thickness or along the length of the plate or part. Unfortunately, the dependence of the speed of sound can be more affected by microstructure and hardness variations than by stress. Ultrasonic stress determination is generally not well suited to application to welded materials, then, since residual stress is most significant in the region of the weld, which is subject to variations in both hardness and microstructure. A review of the determination of residual stress through ultrasonic methods can be found in (Allen, 1982).

1.4.1.3 X-ray diffraction (XRD)

The principal which is exploited by XRD is that the crystal lattice spacing of metals is proportional to elastic strain. Since lattice spacing also determines the angle of diffraction for an incident X-ray wave, an altered stress state will also alter the diffraction angle for the material. Accordingly, if an X-ray beam is directed at the surface of a specimen, it will diffract at an angle related to the residual stress in the body. The change in diffraction angle from a stress-free to a known stress condition is used to calibrate the equation (SAE, 1965)

$$\sigma = k\,(2\theta_{\perp} - 2\theta_{\Psi}) \tag{1.40}$$

where,

k = Stress factor for a given angle, material, and radiation wavelength
$2\theta_{\perp}$ = Angle of diffraction for normal incidence
$2\theta_{\Psi}$ = Angle of diffraction for oblique incidence.

The stress calculated from Equation 1.40 has direction defined by the intersection of the planes of the normal and oblique X-ray beams. Determination of principal stresses and directions can be performed by taking multiple measurements corresponding to a different stress direction. This method has the advantage of providing surface stress in a completely non-destructive manner. However, the technique does require special surface preparation (electropolishing) and skilled personnel and can encounter problems with texture, large grain size, etc. There are several private companies which perform XRD residual stress determination on a fee-per-measurement basis. Further information on this method of residual stress determination can be found in (Noyan, 1986).

1.4.2 Techniques for subsurface stress

There have been relatively few methods presented in the literature to perform triaxial residual stress determination deep within welded plates. One promising new method is neutron diffraction, but that requires access to a nuclear reactor. In this thesis, we will focus on destructive methods for triaxial residual stress determination. Such methods use tools readily available in most industrial laboratories, so they are often the most practical, although not the most simple. Since the major portion of this thesis is devoted to the study of subsurface triaxial residual stress measurement, a number of techniques for performing such measurements are described in detail and contrasted in Chapter 3.

1.4.3 Computational simulation

Despite the complexities of the weld process, current research has shown that characterization of weld residual stress can be performed with varying degrees of success using numerical methods. The general field of weld-process modeling has been called “computational weld mechanics” by Goldak (1985). This method encompasses modeling the heat transfer during welding and use of the resulting transient temperature solution to predict deformation (thermal strain). Temperatures near or above melt are involved in such an analysis, and accordingly plastic deformation will occur and also needs to be predicted. In welding, heat sources are much larger than heat produced by the plastic deformation which occurs (Goldak, 1985), so that the analysis can be simplified by uncoupling the heat transfer and mechanical problems. The analysis of a temperature-driven mechanical problem which includes plasticity is referred to as “thermal elasto-plastic analysis” (TEPA) by Ueda (1991). In general, both the heat transfer analysis and TEPA of the weld process can be carried out in the framework of a general non-linear finite element program.

Of course, in order to model the weld process a great deal of information about the materials used and the process itself are needed. In the case of arc welding, the transfer of energy from the electrode to the work piece must be described, including the shape of the energy transfer interface and the distribution of power within it. Also, the process efficiency, power consumption, and welding speed must be known. The material being used must be characterized for its elastic, plastic, and thermal properties, all as a function of temperature ranging from ambient to melt. In addition, effects of phase-transformation should be defined, including latent heats, recovery from strain hardening, and volume change. Furthermore, although computer codes are available which can handle many of these effects, the accuracy of the resulting analysis is only as good as the data provided.

The usefulness of weld analysis can hardly be argued, especially with regard to process optimization. However, its use as a general design tool is still some time away, as the complexities and resulting uncertainties of the problem are restrictive and computational costs are high. The method has nevertheless seen considerable development in recent years, and its routine use in the future would not be surprising. An excellent review of the various aspects and nuances of weld process modeling is contained in (Goldak, 1985), and some examples of its application to structural welds in Ueda (1991). Masubuchi (1980, Ch. 5 and 6) also gives a number of examples of this technique.

1.5 Experiments on crack propagation in residual stress fields

1.5.1 Residual stress due to welding

One researcher who made an attempt to account for residual stress in an LEFM crack growth assessment was Glinka (1979). He utilized two types of welded steel specimens. One type had the line of crack propagation along the weld-line (denoted specimen type P) while the other had the line of crack propagation perpendicular to it (denoted type L). He measured residual stresses in each type of specimen after fabrication by a relaxation method and assumed that there was no residual stress relaxation during crack growth. Glinka recognized that to be an imperfect assumption, but noted its practicality. With the measured distributions of residual stress, Glinka calculated K^{res} from the weight function where crack line stress was assumed constant with crack extension.

To make crack growth predictions Glinka used the Forman equation, Equation 1.5, with R^{eff} from Equation 1.10 in place of R. The parameters in the Forman equation were determined with data from FCP tests on residual-stress-free base metal for stress ratios of R = 0.2, 0.64, and 0.75. By testing specimens at different stress ratios, Glinka sought to account for the effect of R on FCGR. This is important for specimens subject to residual and applied stress since K^{res}, and therefore R^{eff}, are functions of crack length. Fatigue cracks were started at notches produced by cutting a slot in the plate following welding. To avoid the problem of dealing with material variations near the crack-tip, the slot was cut in the base plate in specimen type P and specimens of type L had a slot long enough to extend beyond the weld bead and HAZ. The details of the specimens are shown in Figure 1.18, the measured residual stresses in Figure 1.19, and the results of crack growth predictions in Figure 1.20.

As can be seen from Figure 1.20, the method used by Glinka to account for residual stress appears promising, although not perfect. In the case of R=0.35 loading, the crack growth prediction is quite good. For the R=0.5 loading, the predictions for the specimens containing residual stress are not as good, but are not much worse than that for the unwelded specimen. As pointed out by Nelson and Parker in written discussion following a paper by Nelson (Nelson, 1982), the Forman equation used by Glinka tends to over-predict the effect of stress ratio on FCGR. Accordingly, one would expect the predictions to become increasingly worse at higher R, as shown in Figure 1.20.

When the results from Glinka’s study are plotted in FCGR - ΔK format, as shown in Figure 1.21, another difference between the data and the prediction can be seen. While the predictions for specimens L3 and L4 show a drop in FCGR when K^{res} is decreasing, there is no corresponding drop in the data (the drop is indicated on the plot by an arrow). Nelson (1982) explained this in a crack closure framework, reasoning that while the FCGR would be increased when the crack tip was within the tensile residual stress zone, there should be no effect on FCGR when the crack tip is in the zone of initial compressive residual stress. Nelson pointed out that since a residual stress must be self balancing, a re-equilibration must occur with crack growth. Specifically, that the compressive residual stress, being reactive in nature, must relax when its tensile (active) counterpart does. To predict the crack growth for Glinka’s experiment, Nelson assumed that crack closure did not occur in the region of tensile residual stress, i.e., that $\Delta K^{eff} = \Delta K^{app}$, while it did occur outside that region. The result of this assumption is shown in Figure 1.22. The cross-hatched region in the figure represents an uncertainty in the width of the tensile residual stress zone.

Although not a rigorous analysis, Nelson’s approach does suggest the value of the crack closure concept.

There may be several mechanisms that cause problems in Glinka’s predictions. An interesting aspect of FCP under varying load which is related to crack closure is that of “capacitance”. That is to say, under certain conditions an abrupt variation in loading (either ΔK or R) will not bring about an immediate variation in FCGR. There is a certain tendency for the FCGR to remain at its current level and then change gradually to another level, as illustrated in Figure 1.2 for the case of a single tensile overload. It is apparent in this figure that the fatigue crack growth rate was not immediately affected by the overload. There was approximately 0.6mm of crack growth before the crack growth rate reached a minimum. This seems reasonable in light of the discussion of crack closure in Section 1.2.1, where it was reasoned that plastically deformed material in the *wake* of the crack increases the opening stress. Accordingly, there is some increment of crack growth necessary before changes are realized. This concept suggests the *transition* which occurred in the FCGR of Glinka’s specimens when the effective stress ratio was diminishing, rather than the sharp drop which is the result of Glinka’s prediction (Figure 1.21).

Another problem in the analysis of Glinka’s type L specimen is that the plastic-zone size under the R=0.5 loading, at a crack half-length of 20mm as calculated from

$$a_p = \frac{1}{2\pi}\left(\frac{K_{max}^{app} + K_r}{\sigma_y}\right)^2 \tag{1.41}$$

is very nearly the thickness of the specimens used (4 mm). Hence, the small-scale yield criteria is violated, significant plasticity is generated by the crack itself, and residual stress near the crack-tip may have been altered (relaxed) by the fatigue loading. A further difficulty in Glinka’s predictions is the rectangular approximation used to represent the residual stress distribution, which complicates interpretation of the methodology used for predicting crack growth, as mentioned following (Nelson, 1982).

Glinka’s work was also examined by Terada (1987). Instead of using Glinka’s measured residual stress distribution, he used a distribution determined mathematically from the two parameters σ_o and c which represent the maximum residual stress at the centerline of the weld and the width of the tensile residual stress zone, respectively. This distribution is shown with that measured by Glinka in Figure 1.23, and does not agree well outside the region of tensile residual stress, nor does it satisfy equilibrium. Terada also used a somewhat unconventional method to account for the residual stress. He assumed a correlation of FCGR with ΔK^{eff} defined as

$$\Delta K^{eff} = \Delta K\left(1+ \frac{\sigma_o}{\Delta\sigma} F_{res}\right) \tag{1.42}$$

with

$$F_{res} = \frac{K^{res}}{\sigma_o\sqrt{\pi a}}. \tag{1.43}$$

K^{res} in Equation 1.43 was determined by the weight function approach with Terada's assumed crack line stress distribution. The motivation for this parameter is not apparent, but the result as shown in Figure 1.24 appears encouraging. Essentially, Terada's analysis suggests that a simple model can be used to estimate K^{res} in the absence of an in depth knowledge of the residual stress distribution (i.e., only the values of σ_o and c need be determined). His crack growth prediction, however, shows possibly fortuitous agreement with the data, since the ΔK^{eff} definition used is unproven.

Earlier work by Adams (1973) exhibited roughly the same level of success in correlating experiment and prediction as shown by Glinka. Adams' welded specimens, as shown with a summary of his results in Figure 1.25, consisted of a crack growing between and perpendicular to two butt welds. He used specimens with two different weld bead separation distances, 100mm and 150mm, which we will refer to as specimen N(arrow) and W(ide) here.

Adams measured the residual stress distribution across the specimens at a distance midway between the loading fixture and the line of fracture using a relaxation technique following fatigue testing to fracture. Accordingly, the residual stress measured reflected any cyclic relaxation during fatigue. The distribution for specimen N is shown in Figure 1.26, and for specimen W in Figure 1.27. With these distributions, Adams used the weight function approach to calculate K^{res}. To make crack growth predictions, he used the Forman equation like Glinka, where the parameters C and n were determined by FCP tests on base metal conducted with R=0.1. The crack growth data used to find C and n are also shown in Figure 1.25, labeled “plain specimen”. Crack growth predictions made using the Forman equation are shown in that figure for the welded specimens.

Comparison with test data shows that the prediction method worked better for specimen N than for specimen W (Figure 1.25), but that both predictions are hardly adequate. The lack of correlation for either specimen is possibly due to a number of factors. As pointed out by Adams, the residual stress which existed originally in the specimens on the plane of crack growth was possibly altered by the fatigue loading; therefore, the residual stress measured post-mortem is possibly a misrepresentation of residual stress which acted on shorter crack lengths. Also, his residual stress distributions, as shown in Figure 1.26, all assume zero initial stress in the region of the starter notch, but show no data points in that region. When using the weight function, the stress existing before the introduction of the notch should be used in the calculation, and a zero value should not, as a matter of course, be assumed. Such an assumption can greatly affect the value of the stress intensity factor computed with the weight function. For example, if the measured value closest to the notch for specimen W is assumed to exist across it prior to machining, the *magnitude* of K^{res} is increased by 18% at $a = 25$mm, and by 11% at $a = 37.5$mm, compared with the result for zero stress in the notch region.

It might also be pointed out that the residual stress magnitude measured by Adams at the center of the fractured half-specimen may be quite different than that which existed in the whole specimen prior to fracture. This can result from elastic redistribution of a self-equilibrating residual stress field which will occur at the center of a plate if the length of the half-specimen is not twice its width (Rosenthal and Norton, 1945). Since the original specimens were 890mm long and 305mm wide ($l/w \approx 3.0$) before they were severed by fatigue crack growth, such redistribution likely did occur. The amount of redistribution found by Rosenthal and Norton for a plate cut from $l/w=3.0$ to $l/w=1.5$ was between 10 and 25 percent of the preexisting residual stress. It is then possible that the residual stress measured is smaller in magnitude than that which acted during fatigue. However greater compressive residual stress would serve to further reduce the predicted crack growth rate within the compressive residual stress zone (by decreasing R^{eff}). Accordingly, the error for specimen W would be increased.

Another possible problem with the predictions is that the data used to find the Forman equation parameters, C and n, were taken using only one stress ratio (R=0.1), so that the variation of FCGR with R^{eff} may not be well represented. From the data given by Adams, it is possible to make an approximate estimation of the R^{eff} variation which occurred during his testing. It should be noted that since interpolation from graphs is required in this estimate, accuracy may not be maintained. Using the weight function for a center cracked strip, Equation 1.15, and the stress distribution shown in Figure 1.26, we find K^{res} to be -7 $\mathrm{MPa}\sqrt{\mathrm{m}}$ at a crack length of 10mm and -23 $\mathrm{MPa}\sqrt{\mathrm{m}}$ at 30mm for specimen N. With the applied loading for specimen N reported by Adams (R^{app} = 0.1, σ_{max} = 138MPa), it can be found that R^{eff} varies from -0.3 at a=10mm to -1.3 at a=30mm. It has been suggested in discussion of Glinka's study that the Forman equation does not always represent the effect of stress ratio well, even when C and n were determined from data representing various applied stress ratios. This problem may be compounded in Adams' case, since data from only one stress ratio was used to fit the Forman equation. When examining Adams' work, it is also not clear whether R was calculated including residual stress or not, or how ΔK was defined, so that it is difficult to make conclusions about the fatigue crack growth predictive technique used.

A study which used specimens similar to that of Glinka's L type (see Figure 1.18) was performed by Itoh (1989). Itoh performed FCP studies on the SUS304 and SS41 parent materials at R=0.14 and R=0.5. During the tests he gathered data on S_{op}, so that he was able to monitor the variation in crack opening ratio, *U*, with crack length. These results are shown in Figure 1.28. It is interesting to note that *U* is constant for each R after a small increment of crack growth in the base metal, even though K_{max} is increasing with crack length, suggesting that closure is more a function of the applied stress than K_{max}. This has been demonstrated both experimentally and computationally (McClung, 1991). Using the measured values of *U*, Itoh found that FCGR for both stress ratios correlated well with $\Delta K^{eff} = U\Delta K$, using the relation

$$\frac{da}{dN} = C(\Delta K^{eff})^n. \tag{1.44}$$

This relation is shown together with Itoh's data in Figure 1.29.

For the welded specimens, Itoh performed testing at several stress ratios, R=0.14, 0.5, and 7.0 for SUS304 and R=0.14, 0.5, 4.0, and 10.0 for SS41.(A stress ratio greater than 1.0 has both $K_{max}^{app} < 0$ and $K_{min}^{app} < 0$.) Itoh measured weld residual stresses using a sectioning technique and strain gages. Distributions found are shown in Figure 1.30. He used FEM to predict K^{res} by applying the measured residual stress on the crack faces, as might be done with the weight function. K^{res} is plotted as a function of half-crack length in Figure 1.31. In order to assure material homogeneity at the crack tip, Vickers hardness was measured across the welded joint to assess the extent of the HAZ, and FCGR data were only taken outside of that region (half-length > 10mm). Again, crack-opening data were collected as a function of crack length, allowing a calculation of U, and it was shown that welded joint data could be collapsed onto the base metal correlation in terms of ΔK^{eff} as shown in Figure 1.29.

In order to make crack growth predictions in the presence of residual stress, Itoh used the ΔK^{eff} - FCGR relation, where ΔK^{eff} was found from the stress ratio. Using the data generated in his tests, Itoh found a correlation between R^{eff} and U, as shown in Figure 1.32. Also plotted in the figure is a scatterband representing tests performed on an aluminum alloy, adapted from (Newman, 1981). Some differences are noted between Itoh's result and that of Newman but should be expected due to the dissimilarity in material. Nevertheless, the trend is the same for both materials. It should also be noted that all R^{eff}-U data for negative stress ratios were taken from welded joints, and no base metal testing was performed for $R^{app}<0$. It would be interesting to verify that data with unwelded specimens and $R^{app} < 0$. Assuming the relation between R^{eff} and U is valid in the absence of such data, Itoh's procedure to predict FCGR from the applied loading was:

1. Determine residual stress.

2. From a stress analysis, find K_{min}^{app}, K_{max}^{app}, and K^{res}.

3. Calculate $R^{eff} = \frac{K_{min}^{app} + K^{res}}{K_{max}^{app} + K^{res}}$.

4. Use Figure 1.32 to find $U(R^{eff})$.

5. Calculate $\Delta K^{eff} = U\Delta K$.

6. Find FCGR from the $\frac{da}{dN}$ - ΔK^{eff} relation.

Itoh reports the result of this analysis for two of the specimens, as shown in Figure 1.33. The resulting prediction is quite good, at least as displayed in the FCGR-ΔK format of the figure. There may be several reasons for the success of Itoh's analysis compared to those of Glinka and Adams. One reason is that the combination of applied and residual stresses were not high enough to have caused small-scale yielding conditions to be violated. Since plastic deformation was limited, similitude of the crack-tip stress state and FCP are well characterized by using an LEFM, K-based approach. Furthermore, the applied loading appeared to be small enough that residual stress was not altered by the loading, and that K^{res} at any crack length could be calculated from the initial residual stress distribution.

No assumption was made by Itoh for the functional form of the effect of stress ratio on crack propagation. Assuming such a form (e.g., the Forman equation) appears to have caused some problems for Glinka and Adams. Instead Itoh used the data he obtained to map ΔK to ΔK^{eff}, accounting for the variation of U with R^{eff}. It should be noted that stress ratio effects were *interpolated* from the data rather than *extrapolated*, as in Adams' case. Finally, Itoh ensured that there would be no influence of microstructure on the FCP in his specimens by not using data taken within the HAZ or weld metal.

1.5.2 Residual stress due to heat treatment

A study by Torii, et al. (1989) involved the propagation of surface cracks in a residual stress field created by water-cooling. Specimens of the type shown in Figure 1.34 were annealed to relieve machining residual stress and then some of the specimens were water-cooled between metal plates from a uniform temperature of 873K. Hardness measurements indicated that there was not a great variation in hardness between these "cooled specimens" and other, more slowly cooled, annealed specimens. Fatigue testing was conducted on the cooled specimens at a stress ratio of R=-1 with a constant stress amplitude for each specimen, and on the annealed specimens at various stress ratios. Crack length was measured on the surface of the specimen by using a photomicroscope with 100x magnification. Crack depth was measured postmortem by examining markings left on the fracture surface (by load variation at specified intervals during the test) with a 20x projector.

Residual stress measured in the cooled specimens by X-ray diffraction is shown by the dashed line in Figure 1.35, and was assumed to be constant through the thickness of the specimen. For each of the four specimens tested, residual stress was re-measured at crack initiation (surface crack length of 0.1mm). These distributions are shown in Figure 1.35 and demonstrate that the residual stress is relaxed by the loading, and that the degree of relaxation increases with increased loading, as might be expected. Similar effects could also be important for residual stress fields generated by welding. Torii, et al., note that the sum of the maximum applied stress (which is equivalent to the stress amplitude, since R=-1) and the maximum residual stress at the center of the specimen is very nearly 220MPa for all four cooled specimens. This is far below the static yield strength of the material (specified as S 45 C, a mild steel), reported as 319MPa. It is also likely below for the cyclic yield strength, as low strength steels usually exhibit cyclic hardening resulting in a cyclic yield which is higher than the static yield. In any event, this study shows the importance of accounting for residual stress relaxation, as will be shown.

Crack propagation results obtained in this study are shown in Figure 1.36. In the figure results are given as surface FCGR versus $\{\Delta K^{0.5}(K_{max})^{0.5}\}$. Torii, et al. argue that this parameter correlates data for various stress ratios and, as can be seen by the narrow scatter-band for the annealed specimens, use of the parameter appears encouraging (testing for the annealed specimens was performed at R= -1, -0.83, -0.67, -0.48, -0.22, 0, and 0.2). Also shown in the figure are the results for the water cooled specimens, without accounting for residual stress. It is apparent that residual stress accelerates crack growth, as is expected since the residual stress is tensile over nearly the whole range of crack length used to gather data (a < 6.2mm). To account for residual stress, the authors substitute

$$K_{max} = K^{res} + K_{max}^{app} \tag{1.45}$$

into the parameter given above. For calculation of K^{res}, the authors use the residual stress measured at crack initiation and a weight function method for elliptical flaws proposed by Shah and Kobayashi (1971) with a correction for finite thickness proposed by Raju and Newman (1979). Results of this analysis are shown in Figure 1.37. It is clear from the figure that the method used to account for residual stress effects gives excellent results. As shown in Figure 1.38, use of the original residual stress distribution (the dashed line in Figure 1.35), in place of the relaxed one, causes the residual stress effects to be over-emphasized which is expected as relaxation lowers the residual stress magnitude.

An interesting aspect of the study by Torii, et al., is that the FCGR was measured in both the surface and depth. The results presented from Torii so far have all been related to surface growth rate. However, the results of measurements in the depth direction are shown in Figure 1.39. Also shown in the figure are two lines, a dashed line indicating the median of the depth measurements, and a dot-dash line representing the median of the surface results. It was pointed out by the authors that for the same FCGR in depth and surface, the value of $\{\Delta K^{0.5}(K_{max})^{0.5}\}$ for the depth measurements is 91% of that on the surface. As was argued in Section 1.2.1, the state of stress of a test specimen will alter the FCGR of a material. In the case of a surface cracked specimen, the state of stress varies along the crack front, being nearly plane stress at the surface and nearly plane strain at the deepest point. This experimental work shows that the FCGR is higher in plane strain than in plane stress.

1.5.3 Residual stress due to localized plastic deformation

Several researchers have used localized plastic deformation (LPD) to create residual stress in specimens. Compared to other ways in which residual stress is formed, induced LPD is relatively simple to create and has fewer side effects. For instance, welding causes not only residual stress, but also wide variations in microstructure. Heat treatment can also change the microstructure while introducing residual stress. By inducing LPD in a specimen by mechanical means, there should be no change in the microstructure of the specimen, and its effect on mechanical properties of the material is limited to the region of the deformation. Using LPD enables a researcher to isolate the effect of residual stress on FCP.

Underwood, et al., used LPD in a study of fatigue crack propagation in a high strength steel. The specimen used was a single edge cracked strip with dimensions: L=200, W=30, and B=5.1mm. LPD was produced on the edge of the specimen opposite that where crack growth initiated by making several indentions with a 25mm diameter pin. The nominal indentation was 1mm deep and 5mm long. Each specimen was strain-gaged prior to indentation so that the residual stress could be measured. A representative specimen is shown in Figure 1.40. As indicated in the figure, and verified by close inspection of Underwood, et al., the strain gages were far enough from the indentations that only elastic strains were measured. The measured residual stress resulting from the indentations is shown in Figure 1.41, measured at positions across the specimen. In this figure, position “y” refers to location across the specimen, y=0 at the edge opposite LPD, and y=30mm at the other edge. Since the measured residual stress was very nearly linear for each specimen, the state of stress on the crack plane can be broken into bending and uniform tension components and K^{res} can be computed from the sum of these two known solutions.

As stated several times by now, the effect of residual stress is to change the effective stress ratio. Underwood, et al., were apparently not aware of this, or chose not to consider it. Therefore, their interpretation of the results is not particularly informative, but we will present some of the data and try to provide some interpretation. FCGR data are presented in Figure 1.42 for deeply notched specimens tested at various load amplitudes. For completeness we note that R=0.06 for specimen T-1 and R=0.09 for the other two specimens, and that testing was carried out in three-point bending with a span of 120mm. Note that the ΔK axis in the figure has been modified to be $\Delta K(1 - [a/W]^2)$ for reasons described by Underwood, et al. The solid line represents data from tests on specimens containing no residual stress, conducted at R=0.09. The open symbols show results for the specimens containing residual stress. It is clear that the residual stress decreases the FCGR at the same ΔK^{app}, compared to the undented specimens. It is possible to compute the R^{eff} for these specimens from results provided in the paper. For specimen T-1, we find that $R^{eff} = -4.3$ at $a/W = 0.3$ and $R^{eff} = -2.17$ at $a/W = 0.5$. These stress ratios are quite different from those at which the residual stress free specimens were tested, and it could be that the difference in crack growth rate is due to the differing stress ratio. Unfortunately, no investigation was made by Underwood, et al., into the effect of stress ratio on FCGR. As a result, this study merely serves to illustrate the ease of use of LPD for introduction of residual stress.

Lam and Lian also used LPD to produce residual stress, but accounted for the R variation in crack growth predictions. They computed K^{res} with both FEM and the weight function, found R^{eff}, and used it to predict the crack growth of their 2024-T3 aluminum specimens. The specimen type used is shown in Figure 1.43 and the thickness of the gage section is 2.7mm, which was reduced to its final thickness by gentle machining to minimize surface residual stress caused by fabrication. Residual stress specimens were produced by applying approximately 225kN to a 20mm diameter punch in two locations on the specimen, resulting in a pair of indentations on the surface, as shown in Figure 1.44. Strain gages on the specimen monitored the residual stress introduced into the specimen. Following the punch process, deformation between the two “predefined lines” shown in the figure was measured at 1mm increments across the specimen. Assuming the specimen was in plane stress, the deformation of these two lines was used to determine the residual stress in the “region of interest” shown in the figure by using the deformation as input to an elastic finite element code. Residual stress determined from this method for one of the specimens is shown in Figure 1.45.

The residual stress determined by the above method was used to determine K^{res} using both the weight function and FEM. The weight function Lam used is for an infinite strip with a single edge crack under applied loading, while the FEM solution employed imposed displacements of the two “predefined lines” mentioned above. Recalling the discussion in Section 1.3.2, we realize that the weight function used should not produce results comparable with the FEM solution, because it does not employ the displacement boundary conditions used in the FEM analysis. However, examining the resulting crack growth predictions may provide a way to compare the two methods used to evaluate K^{res}.

The method used by Lam for FEM computation of the SIF involved monitoring of near crack-tip crack-face displacements. The stress intensity in plane stress is related to these displacements by

$$K = \frac{E\sqrt{\pi}}{2\sqrt{2}} \lim_{r \to 0} [u / \sqrt{r}], \tag{1.46}$$

where u is the crack opening displacement at a distance r from the crack-tip. K is determined by plotting the right-hand side of Equation 1.46 versus r and extrapolating the linear portion of this plot to r=0. This method was verified by Lam and Lian on their mesh for a classical load case at several crack lengths and the maximum error obtained relative to the known solution was 5%. The result of both FEM and weight function calculations is shown in terms of K^{res} in Figure 1.46. The large difference in K^{res} is striking, but not surprising, in view of the discussion above.

Once K^{res} was determined, Lam and Lian use it to determine R^{eff} from Equation 1.10. This was then used to find U from the equation

$$U = 0.2362R^2 + 0.4194R + 0.5101 \tag{1.47}$$

given in their paper. Finally $\Delta K^{eff} = U\Delta K$ was used in a correlation for FCGR determined from specimens containing no residual stress. The resulting prediction of crack growth is compared with the data in Figure 1.47. The data points (x's) show that compressive residual stress reduces the FCGR when the crack is short but that its effect gradually decreases with crack length. At a crack length of about 15mm, the FCGR is the same as that predicted in the absence of residual stress, as shown by the dashed line. This implies that K^{res} should be nearly zero at a crack length of 15mm, as predicted by FEM (Figure 1.46). It follows that FEM gives a much better assessment of K^{res} than the weight function, since it gives a better prediction of FCGR. This suggests that, for this geometry and eigenstrain distribution, imposed displacements are more appropriate than applied tractions in deriving the SIF. Even so, residual stress effects are small enough in this study that the improvement in FCGR prediction does not improve the life prediction greatly, as demonstrated by Figure 1.48. This study shows the importance of using the proper method for prediction of K^{res}, and that in some cases the weight function can give erroneous results when applied without taking into account the proper boundary conditions, as discussed in Section 1.3.2.

From this survey, it is apparent that residual stress can exert a considerable influence on crack growth emanating from weld defects. But, methods for predicting that influence need further development to resolve uncertainties such as those described in this report.

1.6 Influences of internal weld defects

1.6.1 Early experimental data

Although linear elastic fracture mechanics as an engineering discipline can probably be traced to 1948 (Kanninen, 1985, p. 4), the use of LEFM to quantify fatigue crack propagation was first demonstrated in 1961 (Paris, 1961). Earlier experimental data on weldment fatigue was typically discussed on an empirical basis in an S-N framework. The basic procedure to assess the effect of a particular flaw was to produce defective weldments by altering the weld process, inspect them with radiography or ultrasonics to divide them into classes of defect severity, and then to present the results of each class in an S-N format. This approach is not the same as might be taken today. Instead, local strain amplitude at points of stress concentration might be used to predict crack initiation, and LEFM used to compute life spent in crack propagation. Also, using this approach, residual stress can be taken into account. Nevertheless, the findings of earlier research can provide insights into the effects of defects on weld fatigue life.

1.6.1.1 Results in an S-N format

In the late 1950's, the British Welding Research Association began a program to study the effect of internal defects on fatigue life. From this study came several papers by R. P. Newman, W. O. Dinsdale, and others. In one of the earliest literature reviews on the subject, R. P. Newman (1959) discusses the effects of internal weld defects on fatigue strength. He discusses in separate sections the effects of cracking, lack of fusion, lack of penetration, porosity, and slag inclusions. Attention here will be limited to crack-like defects. The reader is referred to the original paper for the substantial discussion of the effect of porosity and to a lesser degree the effect of slag inclusions.

Newman discusses the effect of weld cracking, citing a paper by W. G. Warren (1952). Much of his discussion of Warren's paper makes it clear that the defect size is not well documented. Nevertheless, surmising from an illustration of the fracture surface that the defect severity (area reduction) was about 5%, Newman estimates a 60% reduction in fatigue strength compared to a sound weld at 10 million cycles due to this type of defect. The extreme reduction in the joint performance due to such a relatively minor defect is surprising. In fact, this contrasts markedly with the results for lack of fusion and penetration as discussed below, where a severity of 30 to 40% was required to cause the same reduction. The reason for this difference may possibly be linked to the time of defect formation. Since weld cracking occurs toward the end of the thermal cycle (in a tensile residual stress field) its shape could be more "crack-like" than other defects. Flaws which are present from start to end of the thermal cycle may become blunted due to the combination of high thermal stress and high temperature and such deformation may relieve residual stress in the defect region, but that is strictly hypothesis. Additionally, there may be a difference in the number of cycles needed to initiate a fatigue crack at a weld crack compared with LOF and LOP defects.

One series of tests (R. P. Newman, 1956) was performed on pipe butt joints containing intentional lack of fusion defects. The defect was produced along the entire circumference of the pipe, with the defect laying along the original 40° edge preparation of the pipe and extending from the outside surface to about mid-thickness. Loaded under alternating bending, fatigue cracks in this study consistently initiated at the weld root / backing ring interface, and only initiated at the tip of the intentionally introduced defect once. At least in this case then, the notch effect was greater at the weld root than at the tip of the defect. Different results may have been obtained for tests performed under fluctuating uniform tension. Newman (1959) states that production of the defects for this study necessitated oxyacetylene welding, as metal-arc welding could not produce the above mentioned defects without great difficulty. He concludes then, that “the frequency of occurrence of lack of fusion in metal-arc welded construction is something which might, therefore, be considered carefully before making any proposals for investigating this fault.”

In the same series of tests (Newman, 1956), it was found that a continuous 0.125 inch deep lack of penetration at the root of butt welds in 0.375 inch thick pipe (33% severity) caused a 60% reduction of fatigue strength at 2 million cycles. Newman reviews two studies of lack of penetration defects resulting from double sided welds, where the defect is centrally located in the thickness of the joint. Warren (1952) did not give any sound-weld control data, leaving Newman to hazard a guess that the approximately 20% severity caused a reduction in the fatigue strength at 2 million cycles of about 50%. The other study on these defects reviewed by Newman (Wilson, Munse, and Snyder; 1950), was performed on 7/8 inch thick A7 steel plates containing more extensive lack of penetration. Specimens with a 40% severity showed a 64% reduction in the fatigue strength at 2 million cycles while specimens with a 60% severity defect had a 69% reduction. The effect of reinforcement removal was also studied by Wilson, et al., who found that it caused only a slight change in the fatigue strength for the 40% severity specimens while the reduction in strength increased to 76% for the 60% severity specimens.

In a two part BWRA report (Dinsdale, 1962 and 1964), W. O. Dinsdale discusses the effect of defects in aluminium alloy welds. The first part of the report discusses the effects of lack of "fusion", which is actually lack of root penetration, in 0.25 and 0.5 inch thick NP5/6 Al-Mg-Mn alloy (U.T.S. = 40 ksi; 29% elongation). Our attention here is on the results for the fatigue properties, but the effect of defects on static strength is also discussed. The lack of penetration defects for this study were produced by welding on both sides of the plate and varying the degree of edge preparation to give the appropriate defect severity. Defects were measured with radiography and ultrasonics, as well as with macro-sectioning. There is an excellent accounting of the defect size, specimen loading, cycles to failure, and the details of failure which included the failure initiation location, and any accompanying defects present. It is worth noting that the lack of penetration defects produced were accompanied by lack of side fusion quite frequently, in contrast to the finding of R. P. Newman mentioned above. This may be due to the difference in weldability of the material, steel in Newman's study and aluminum in Dinsdale's.

The effect of the shape of the weld reinforcement causes some problems in Dinsdale's work. The fatigue tests for sound welds show two distinct populations, and this is attributed to differences in the reinforcement angle of the two plates from which the specimens were taken. For the two plates, the angle was 125° and 160°, respectively, while the fatigue strength at 5 million cycles was 3.0 and 5.0 tons/sq.in. For the 0.25 in. thick specimens with lack of penetration defects less than 25% of the plate thickness, the shape of the reinforcement controls the fatigue strength. Dinsdale observed that a defect severity of 7% (based on plate area) is needed to shift the point of fatigue initiation from the root of the reinforcement to the tip of the defect. For severity larger than 25%, the failure consistently initiated at the defect, and strength should be related to the defect size.

The defect size was measured for all specimens, but Dinsdale did not use it to account for specimen variability. Instead the specimens were merely categorized into three groups: slight, moderate, and deep corresponding to <25%, between 25% and 50% and >50% severity, based on plate area. It is clear that production of a consistent defect size was nearly impossible in this study. A summary of the fatigue results is given in the Table 1.1. Clearly, the effect of these defects is much greater if the reinforcement has been removed, mostly due to the higher sound weld fatigue strength with reinforcement removed.

Reinforcement	Steel: t = 0.375”	A7 Steel: t = 0.875”		Al: t = 0.25”		Al: t = 0.5”		Reference
	—	On	Off	On	Off	On	Off	
Weld Crack 5% Sev.	60%							(Newman, 1959)
LOP 20% Severity	50%							(Newman, 1959)
Surface breaking LOP 33% Severity	60%							(Newman, 1956)
LOP 40% Severity		64%	≈ 64%					(Wilson, 1950)
LOP 60% Severity		69%	76%					(Wilson, 1950)
LOP < 25% Severity				≈ 0	27%	33%	64%	(Dinsdale, 1962)
LOP 25% to 50% Sev.				14%	64%	66%	73%	(Dinsdale, 1962)
LOP > 50% Severity				42%	—	83%	—	(Dinsdale, 1962)

Table 1.1 ***–*** *Summary: Effect of defect severity on reduction in fatigue strength (see text for details).*

1.6.1.2 Reassessment of early data using fracture mechanics

The advent of fracture mechanics based fatigue evaluation has enabled the analyst to more easily assess the significance of crack-like weld defects. As an example of this methodology, J. D. Harrison (1969) reassessed previously gathered S-N data for butt welds containing LOP defects. Several sources or data were reviewed but attention here will be restricted to the data reported by Dinsdale and Young (1962; 1964) mentioned in the previous section. Essentially, Harrison used the applied loading, the reported initial defect size and type, and an estimate of the critical crack size to present all the data on the same plot. The methodology he pursued is described in the following.

Several assumptions were required to make the analysis tractable, most of which reflect that information presented in the earlier studies was not always complete. First a way was needed to calculate ΔK resulting from the given applied loading. Since the defects reported by Dinsdale and Young were centrally located and continuous along the length of the specimen, the equation used for the SIF was

$$\Delta K = \Delta\sigma\sqrt{\pi a}\left[\frac{2t}{\pi a}\tan\frac{\pi a}{2t}\right]^{1/2} \tag{1.48}$$

where $\Delta\sigma$ = range of cyclic stress

t = specimen thickness.

The bracketed term in Equation 1.48 is meant to account for the finite thickness of the plate in relation to the crack size. The Paris Law was used in this study to determine the FCGR, where the Paris exponent, n, was assumed to be 4. Using the Paris Law with n=4 and Equation 1.48, the FCGR was given by

$$\frac{da}{dN} = C(\Delta\sigma)^4\left[2t\ \tan\frac{\pi a}{2t}\right]^2 . \tag{1.49}$$

The advantage of assuming n=4 in the Paris Law is that it allows exact integration of Equation 1.49. Separating variables and integrating from the initial crack length, a_i, to the a critical crack length, a_{cr}, the life spent in crack propagation, N, is found from

$$\left[\frac{\Delta\sigma}{EX^{1/4}}\right]^4 N = \frac{1}{\pi C'} \tag{1.50}$$

where C' = CE^4, E is Young’s modulus, and

$$X = \frac{1}{2t}\left[\cot\frac{\pi a_i}{2t} - \cot\frac{\pi a_{cr}}{2t} - \frac{\pi}{2t}(a_{cr} - a_i)\right]. \tag{1.51}$$

An estimate of initial defect size was reported by the original researchers but an assumption had to be made to define a_{cr}. Harrison reasoned that since the crack is growing fast near the end of its life, N found from Equation 1.50 is not very sensitive to the method of determining a_{cr}. Accordingly, he assumed that fracture occurred when the stress on the net section was equal to the ultimate strength of the material, σ_u, so that the critical crack size could be determined from

$$a_{cr} = t\left[\frac{\sigma_u - \sigma}{\sigma_u}\right]. \tag{1.52}$$

To assess the validity of this simplified LEFM fatigue assessment procedure, the S-N data of Dinsdale and Young was used with Equation 1.50. By plotting $\frac{\Delta\sigma}{EX^{1/4}}$ versus N in log-log coordinates, as shown in Figure 1.49, it is possible to judge the appropriateness of the method. Not only are the data of Dinsdale and Young shown in the figure, but also the results of an anonymous study published by the International Institute of Welding on the effect of discontinuities in aluminum welds (IIW Doc. XIII-262-61). The scatter is quite large, representing approximately a factor of 100 on life. However, the trend of the data is predicted by Equation 1.50, as demonstrated by the two lines on the plot, each of which represents Equation 1.50 for a different value of C'. Considering that there was no accounting for variation in cycles to initiation in each specimen, nor the effect of residual stress, the result of this simplified analysis bodes well for the LEFM fatigue crack propagation method in predicting crack growth emanating from internal weld defects.

1.6.2 Effect of defects on the formation of residual stress

A potentially important aspect of internal weld defects is the impact of such defects on the accompanying residual stress field. The distribution of residual stress around a naturally occurring defect may be quite different than that produced in a defect-free region. Once a defect has been created in a weld, local stress must change to accommodate the new boundary conditions presented by the defect. The final distribution of residual stress is likely to depend on when the defect formed during the welding process. If the defect formed near the end of the process when the metal has cooled, the new residual stress state may consist of only a local redistribution of the residual stress that would have developed under flaw-free conditions, and may then be handled by an elastic analysis (unless small-scale yielding criteria are violated). On the other hand, if a defect forms near the beginning of the welding process, the generation of local thermal stress and resulting plastic deformation may be more complicated, depending on the subsequent thermal history of the region.

The history of the welded region in a steel GTA bead-on-plate weld was examined by Brand, et al. (1993). Explaining the formation of residual stress, they reasoned that while tensile residual stress is formed in the longitudinal direction of the weld at complete cooling, during the initial heating of the weld, large compressive stress forms and is greatly relieved by plastic deformation, which is aided by the elevated temperatures (which lower the yield strength). Upon cooling, tensile residual stress forms in the weld region, and plastic deformation will again relieve this to some degree. Finally, a state is reached where no additional plastic deformation takes place and further cooling produces the usual thermal stress. Thus, the formation of residual strain in the weld region can be broken into three phases: primary plastic deformation (compressive in this example), secondary plastic deformation (tensile), and the final thermal deformation. The longitudinal stress at the center of the weld which exists after each of these three phases in shown qualitatively in Figure 1.50 as a function of the distance from the weld line, x. (In the figure, $T^*(x)$ refers to the temperature profile at the end of secondary plastic deformation.)

For a lack of fusion defect present during the entire weld thermal cycle, the implication of this line of reasoning is that residual stress of one sign due to cooling is preceded by stress of the opposite sign during heating. If this type of defect is in a tensile zone after cooling, it will be subjected to compressive stress during primary plastic deformation, and the defect should not affect the stress formation at this stage. However, during secondary (tensile) plastic deformation, the high temperature/low yield strength of the material is likely to cause extensive yielding in the defect-tip region. Such action will redistribute the stress away from the defect, thus reducing its significance after complete cooling. For a defect which is in a compressive zone following cooling, the material near the tip of the defect undergoes concentrated tensile plastic deformation during the primary cycle. If the concentrated strains at the defect tip are not completely removed by secondary plastic deformation, the crack tip condition will be similar to that following a high-low overload sequence, the result of which will likely depend on the ratio of the stress acting in the defect-region to the yield strength at the time of the overload for each portion of the residual stress formation.

The significance of defect/residual stress interaction is complicated by a lack of knowledge of the local temperature and stress history. It may be that yield-level residual stress does not develop until the material has regained its strength. Clearly, yield strength and tensile thermal stress (caused by shrinkage) both increase with decreasing temperature. On the other hand, compressive thermal stress (caused by expansion) increases with increasing temperature while yield stress is decreasing. Therefore, deformation occurring during heating will have a larger plastic component than tensile deformation which occurs during cooling. The plastic deformation resulting from a defect present during the weld cycle is the essential factor in defect-residual stress interaction.

Therefore the interaction of defects with weld residual stress fields is expected to be greater for defects which end up in compressive residual stress fields.

The type of coupling of weld defects and local residual stresses just described has apparently been little investigated, either experimentally or computationally, in spite of its potential impact. The usual approach has been to experimentally determine residual stress fields in regions presumably free of flaws, and then assume that a defect can be mathematically introduced into that field for the purpose of analyzing structural integrity. The validity of that approach needs to be confirmed or denied.

1.6.2.1 Simulation of the thermal elasto-plastic problem

One way to study the interaction of an internal defect with the residual stress field is to simulate the entire welding thermal and mechanical cycle with the defect present in the analysis. As discussed in Section 1.4.3, methods are currently being pursued to study the formation of weld residual stress which simulate the thermal elasto-plastic problem. In theory, all that would need to be done to address defect interaction is to add the boundary conditions in the defect region so that the defect could open if under tensile stress. This could be done through the use of interface or gap elements in the context of FEM, since such elements allow opening to occur, but provide contact forces under compression. Due to the stochastic nature of the welding process, a match of computational and experimental results would be difficult to achieve, but such an analytical approach would certainly provide great insight into the problem.

The difficulties presented by thermal elasto-plastic analysis are compounded if one tries to introduce a sharp defect into the problem. Since the mechanical portion of the simulation is hampered by large strains and large strain gradients, introduction of a crack-like defect only makes the situation more difficult because the crack would introduce a large strain and stress concentration on its own. It is expected that the mesh refinement required to obtain useful results from this type of analysis would drive the computation cost quite high. As the degree to which coupling exists between the defect and the resulting residual stresses is not known, an experimental program seems justified as a first step.

1.6.2.2 Experimentation

To investigate the interaction of a naturally occurring weld defect with the resulting residual stress field, a series of experiments could be conducted. Initially, demonstrating the alteration of the residual stress field would be of primary concern while the method of demonstration would be secondary. This way, if no great interaction is demonstrated, the problem need not be pursued. Measuring the residual stress in the defect vicinity is the most straight forward way to show any variation from the sound weld case, however this is not a simple task. Since the alteration in residual stress may be restricted to a region very near the defect, the method used to measure it must be quite sensitive spatially.

1.7 Summary

This review has considered a number of factors which influence the fatigue crack propagation behavior of cracks initiating in the weld region. Among the primary influences of this process are variations in material properties which occur in the weld region and the effects of residual stress. Commonly used procedures for dealing with these issues have been described, and several illustrative examples have been taken from the literature. The major conclusions that can be drawn from this survey are:

1. To deal with microstructural and property variations in the weld region, material characterization must be carried out on as-welded plates. In such testing, a particular combination of weld metal, base metal, and welding parameters must be characterized separately. Even generalizations about material behavior for particular welds are difficult to make.

2. Residual stress can be accounted for in a fatigue crack propagation analysis by superimposing it on applied loading as long as LEFM is applicable. The method of superposition most widely used is the weight function method, utilizing crack line stress determined from the uncracked body. This method has been questioned in the case of residual stress, as the crack line stress depends on the compliance of the structure. This issue has never been fully addressed and could be investigated systematically with the finite element method.

3. When using the finite element method to treat problems of residual stress, either the measured eigenstrain or an equivalent body force should be used in the model. The inherent strain method of Ueda can be used to determine the eigenstrain distribution in the entire body of interest. Imposing the actual eigenstrain would allow the problem of residual stress redistribution due to plasticity to be addressed through the use of an elastic-plastic FEM code.

4. Residual stress near the surface of welded joints can be determined by experimental means. For fracture mechanics analysis, it is useful to know the residual stress in the entire weld region, although its determination along the expected plane of crack growth may be satisfactory.

5. Experimental evidence shows that predicting the influence of residual stress on fatigue crack propagation is possible. Stress ratio changes caused by the residual stress field alter the opening behavior of a fatigue crack even under constant amplitude loading. Assuming a dependence of crack opening on the stress ratio, including the contribution of residual stress, appears to have given good results. Use of empirical relations to account for stress ratio effects does not give consistent results, especially if the relation was not derived for the particular material and specimen geometry being studied. Relaxation of residual stress accompanying crack extension should be accounted for in FCP analyses, but the stress relaxation may be difficult to predict.

6. Internal defects have been shown experimentally to cause a marked decrease in fatigue strength of welded joints. Further, this decrease in strength is larger than would be predicted based on the loss of net-section area, as would be predicted by the use of LEFM. Systematic investigation of the influence of internal weld defects has been hampered by the inability to create welded defects of a predetermined location and orientation.

7. The possibility exists for coupling between weld residual stress formation and the existence of subsurface weld defects. However, the significance of such coupling is unknown. This problem can be addressed through weld simulation, experimentation, or a combination of both.

1.8 Contributions of this thesis, a road map

The prediction of fatigue crack growth originating at subsurface weld defects is needed to assure structural integrity and safety for a large number of structures critical to infrastructure. Several factors particular to welds influence this phenomenon and must be accounted for in lifetime assessment, including the presence of discontinuous geometry, material variation, and residual stresses. The preceding literature review indicates several strengths and weaknesses of current predictive capabilities. One of the primary issues hindering current methods is the lack of ability to accurately determine weld residual stresses surrounding naturally occurring subsurface weld defects.

This thesis investigates and develops technology capable of finding residual stress surrounding lack of fusion or lack of penetration weld defects. To this end, a hybrid numerical and experimental approach has been pursued. In Chapter 2 we recount the development of a welding process capable of producing a sizable defect in a thick multipass weld which has a predetermined location, shape, and size. Three welds were manufactured with this process, two containing defects and a third which is defect-free. Residual stresses within these welds can be used to compare residual stress which develops in defective and defect-free welds. However, measurement of these residual stresses was found to be extremely difficult.

Several competing sectioning techniques are discussed in Chapter 3. This chapter demonstrates that a basic assumption underlying some techniques is not well suited to the problem of determining weld residual stress. Further, this chapter shows experimentally that the principal assumption of the eigenstrain method is solidly based.

Chapter 4 describes a numerical examination of the eigenstrain method devised by Ueda (1975). This study shows the technique to be viable, but that it requires extensive experimental effort. Initial application of the eigenstrain method, reported in Chapter 5 but executed prior to the numerical evaluation detailed in Chapter 4, was entirely unsuccessful, and the failure of the experiments is discussed.

Chapter 6 of this thesis describes an experimental verification of the eigenstrain method. This experiment attempts to validate the eigenstrain approach by investigating residual stress in a swage-autofrettaged tube.

Finally, in Chapter 7, we develop and numerically verify a new technique based on the eigenstrain method. This method amounts to a localization of Ueda’s technique and provides residual stress estimates in the vicinity of the weld bead, where defects commonly lie. The localized eigenstrain method allows the estimation of residual stress with far less experimental and computational effort. Further, numerical verification shows that this new method produces stress estimates which are just as accurate as those provided by Ueda’s technique.

Major conclusions which can be drawn from this thesis are described in Chapter 8.

1.9 Figures

The following pages contain figures for Chapter 1.

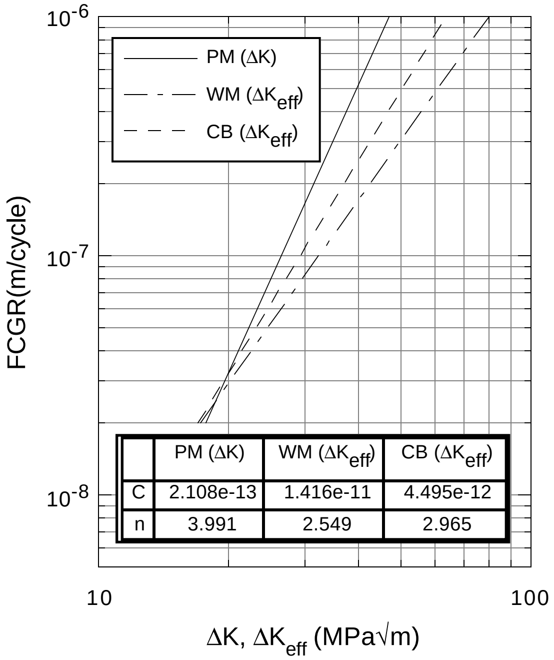

	PM (ΔK)	WM (ΔK$_{eff}$)	CB (ΔK$_{eff}$)
C	2.108e-13	1.416e-11	4.495e-12
n	3.991	2.549	2.965

Figure 1.9 – FCGR Paris law for various weld regions (Shi, et al., 1990)

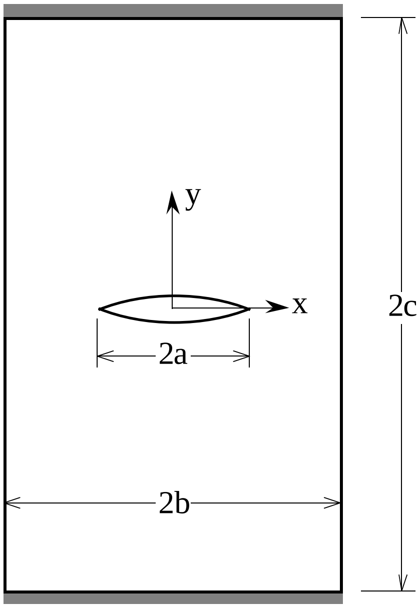

Figure 1.11 – Center cracked plate with fixed ends

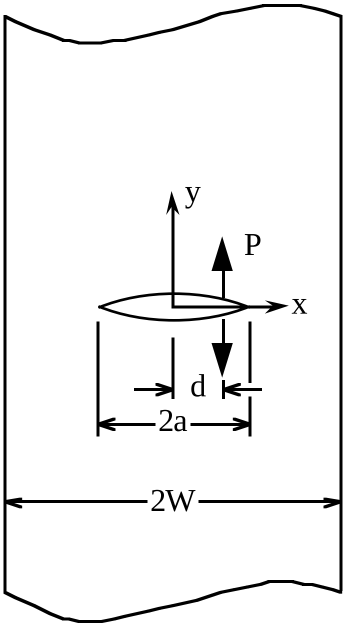

Figure 1.12 – Center cracked strip with twin opening loads

CHAPTER 1: INTRODUCTION

CHAPTER 1: INTRODUCTION

Chapter 2

Fabrication of Defective Welds

One of the key aspects of this research is to investigate the residual stress state surrounding a lack of fusion (LOF) type weld defect. This problem might be attacked in several ways, but the chosen approach has been experimental. Modeling of the weld process, so-called computational weld mechanics, is not currently developed to the point where it can be routinely applied. Placing a geometric singularity, like a LOF defect, within the computational problem would be a valuable yet intensive task due to the relatively undeveloped nature of weld modeling. Even if the problem were solved computationally, one would still need to verify modeling assumptions and results and would most likely be left with unresolved questions. Therefore, we set out to manufacture welds containing LOF defects and compare them to non-defective welds made under the same conditions. The process by which the final defective welds were made was arrived at by intensive experimentation performed in the welding shop. In the following section, we review these experiments and describe the defective welds produced.

2.1 Description of the desired defect

As this research has potential application for recertification of pressure systems, a pressure vessel steel, A516 Gr 70, was selected for use in the experimental aspects of the research. Early on in this effort, experiments were performed with the goal of finding a welding process and procedure by which a “controlled” lack of fusion defect could be created.

Several qualities were desired of the defective welded joints to be produced. One of the most basic parameters chosen was joint thickness. Large pressure system walls are often on the order of one to two inches thick, and since residual stress measurements were to be made on these welds, it was desirable to have our weld specimens fairly thick. For convenience, we also wanted the samples to be small enough to facilitate hand carrying when necessary. A thickness of 1.5 inches was considered as a nominal size. Further, the welding process needed to simulate current construction techniques, so submerged arc welding was selected.

As for the defect produced, we wanted a shape and location that would be amenable to fracture mechanics analysis with a profile which was constant along the weld length. Also, we wanted a defect large enough to possibly influence the residual stress field but small enough to allow measurable crack growth to occur prior to fracture in potential fatigue experiments. The simplest form of subsurface defect which met these criteria is shown in Figure 2.1. This resembles a buried lack of fusion defect located at mid-thickness and oriented perpendicular to the surface. In fracture mechanics terminology, the right side view in Figure 2.1 is a center-cracked geometry, commonly used in fatigue and fracture assessment.

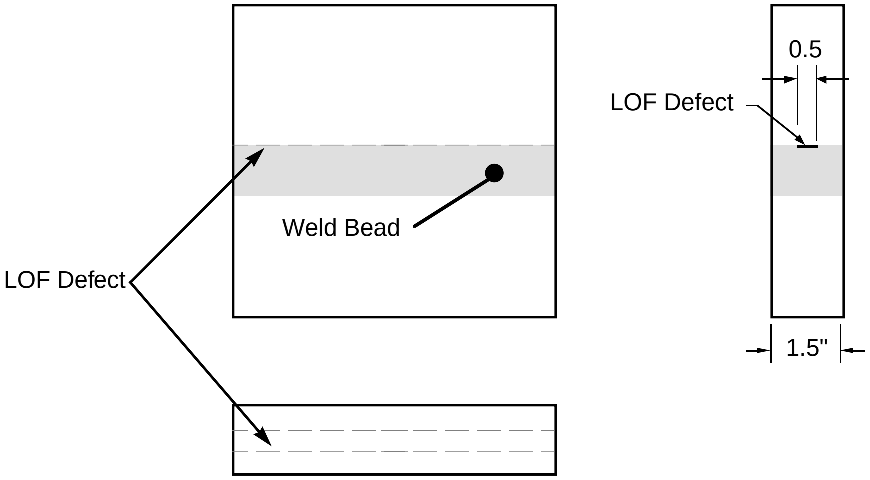

Figure 2.1 – Front, top, and right side views of desired defective weld.

Several features of the method used to produce defective welds were desired. Essentially, the method of introducing the defect should not disturb the welding process.

The proper procedure would produce a defect-containing weld which was otherwise the same as a non-defective weld. There should be no attending defects present, and the heat flow from the electrode into the base metal should not be too different from the defect-free case. Anything placed in the weld preparation to act as a fusion inhibitor was also to be pliable, or have similar thermal behavior as steel, so that plastic deformation around the weld bead was not dependent on the insert used. We wanted a defect which as closely as possible imitated a real buried lack of fusion, yet was produced under controlled conditions.

2.2 Trials on thin plates

All together, there were many parameters to be considered, and the only way to discover the best method was to experiment. Since welding of thick plates is a time consuming process, and assessing defects in such welds is difficult, initial experiments were carried out on thin plates. Samples could then be sectioned and inspected with relative ease. Jim Govorko, a welder in the NASA-Ames Metal Fabrication Branch, was employed to help find a process by which LOF defects could be produced on thin plates. Several small coupons were made from 0.25 inch thick A36 steel, and each welded sample produced was roughly four inches square. The samples were prepared with a 45° single bevel and butt-welded in a single pass. After welding, each sample was chilled in liquid nitrogen and fractured so that the weld quality could be observed. In several cases, the microstructure was visually examined with standard metalographic techniques. The desired defect for these tests was a through thickness LOF along 2 inches of the weldline. Results of these experiments are summarized in Table 2.1.

As indicated in the table, the variables in the experiments were the welding process, the form of the fusion inhibitor, and the substance from which it was made. The welding process consists of the equipment used and its voltage and current settings. Two different welding processes were used, gas-metal-arc welding (GMAW or "stick welding") and metal-inert-gas welding (MIG). The operator was requested to use each process as would be done when normally welding 0.25 inch thick A36 steel. These two processes, as implemented, were quite different physically and so produced different results. The GMAW process had a much greater energy transfer than the MIG process. The GMAW

Process	***Inhibitor Form***	***Inhibitor Substance***	***LOF***	***Comments***
GMAW	Wrap	0.030" Al sheet	No	Extreme porosity
GMAW	Wrap	0.060" Al sheet	Yes	Extreme porosity
GMAW	Wrap	0.060" Cu sheet	No	Cu fused into weld metal
GMAW	Wrap	0.015" Zirconia cloth	No	LOF present, but intermittent
GMAW	Wrap	0.030" Zirconia cloth	Yes	Operator electrode manipulation observed
MIG	Wrap	Zirconia cloth	Yes	Worked for both thicknesses of cloth
GMAW	Shielded	0.030” Al sheet	Yes	Al mixed into weld metal
GMAW	Shielded	0.030” Zirconia cloth	Yes	Desired result obtained
MIG (two sided)	Groove	Zirconia cement	Yes	Pockets of melted zirconia within the weld metal
GMAW	Rusted	Rust	No	Good quality weld produced

Table 2.1 – *Summary of defect production methods attempted with 0.25 inch A36 steel.*

weld pool was accordingly much more turbulent, and more heat was put into the weld. MIG was much easier for the operator to control, but demanded more skill in its execution. There was, therefore, a tendency for him to use his skill with MIG to obtain the desired result (an LOF defect). This tendency was difficult to suppress.

The fusion inhibitor took four forms. The first attempts merely wrapped the inhibitor material around the edge of the plate for 2 inches of the 4 inch weld length, as shown in Figure 2.2. Next, the inhibitor material was over-wrapped, or “shielded”, by a piece of 0.030 inch thick mild-steel sheet. The steel sheet was used to protect the inhibitor material from the energy of the weld arc and turbulence of the weld pool. Next, a groove was cut at mid-thickness of the square edge of the preparation all along the 4 inch weld length. This groove was then filled with the inhibitor material and the plate welded. In addition to the above, a rusted plate was also welded so that the effectiveness of an oxide layer in producing LOF could be ascertained.

Three different materials were tested as a fusion inhibiting substance: an alloy insoluble in steel, aluminum, a soluble alloy, copper, and a high temperature ceramic, zirconia. All metals were used in sheet form. The zirconia was available in several forms, a felt which was too fragile to be used, a cloth in 0.015 and 0.030 inch thicknesses, and a liquid cement which dried into a rigid form.

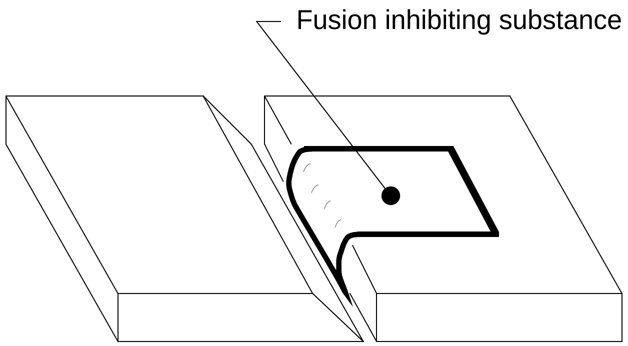

Figure 2.2 – Sketch of samples used to experiment on fusion inhibiting methods for thin plate welds.

Results for each combination of the above used are reported in Table 2.1. The first series of tests employed GMAW. The MIG results will be discussed later. The aluminum alloy wrap caused intense weld splatter during the welding process, and the resulting weld was filled with porosity. The dissimilarity of aluminum and steel succeeded in producing a defective weld; however, the defect was not consistent along the weldline and the attending weld porosity was undesirable. The copper alloy, on the other hand, was so readily drawn into solution with the ferrous weld metal that no defect was obtained at all. Zirconia cloth was able to produce LOF in our testing. However, it was obvious from weld heat tinting on the sample that the electrode had been drawn away from the zirconia wrap and operator electrode manipulation was suspected. Use of rust as a fusion inhibitor was unsuccessful.

One of the major difficulties revealed by the initial testing with GMAW was that a tremendous amount of mechanical energy is transferred by the arc, and the inhibitor substance used to produce LOF needed to be robust enough to withstand the severe environment. Yet the insert material also needed to be pliable so that it would not disturb the plastic deformation within the vicinity of the weld. Two strategies were employed to address these problems. The weld process (GMAW) was changed to a lower energy welding process (MIG), and the insert material was covered with a piece of steel sheet to shield it from some of the arc force. Each of these strategies produced good results. MIG welding with a zirconia cloth wrap produced LOF for two thicknesses of cloth used. As previously stated, MIG welding requires precise and skillful control of the electrode by the operator. Probably such control assisted in the production of the resulting LOF defects.

Use of the shield showed that it successfully absorbed much of the mechanical energy of the arc. However, thermal energy was still transferred. Two samples were made in which the inhibitor substance was placed under a piece of 0.030” thick steel sheet, one with aluminum and one with 0.030” zirconia cloth. The shield remained intermittently intact along the weldline. In some places it was completely eroded by the arc, and in others it was not. Since thermal energy was transferred into the insert, in places where the shield was breached molten aluminum mixed with the weld pool, causing a peculiar metallurgy. The zirconia, on the other hand, did not melt, and the metallurgy of the weld appeared to be undisturbed by the zirconia insert.

2.3 Trials on thick plates

Single-sided welds on thin plates suggested that a zirconia cloth insert shielded from the weld arc by sheet steel could be used to approximate a naturally occurring lack of fusion weld defect. The resulting defect was consistent along the weldline, did not appear to change the metallurgy of the weld based on observation of the microstrucutre, and could be repeatedly produced. Next, the knowledge obtained from single pass welds on thin plates needed to be applied to multi-pass welds on thick plates. Apart from geometry, there would be differences in the welding process and the form of the defect desired. Whereas we employed GMAW and MIG on the thin plates, submerged-arc welding (SAW) would be used on the thick plates. The defect would be buried and located at mid-thickness of the joint, as shown in Figure 2.1. Of course, such a defect might be thought of as several passes similar to the one laid on the thin plate and subsequently covered over by several passes with complete fusion. From that perspective, the biggest differences between the thin and thick welds were expected to result from changes in the welding process.

On the basis of the thin plate trials, a procedure was developed to produce two 1.5 inch thick butt welds, each of which would contain a 0.5 inch simulated LOF defect at mid-thickness. A double bevel weld preparation was employed, and a shielded zirconia cloth insert was placed on the square edge, as shown in Figure 2.3. This preparation was fitted up as shown in Figure 2.4 and welded with SAW. The first attempt at this procedure used a 0.09 inch thick steel shield, which was incapable of withstanding weld forces produced during submerged-arc welding. The SAW process, in fact, imparted an enormous amount of mechanical and thermal energy. Only a few weld passes were needed before it was clear that this method was not going to give the desired result.

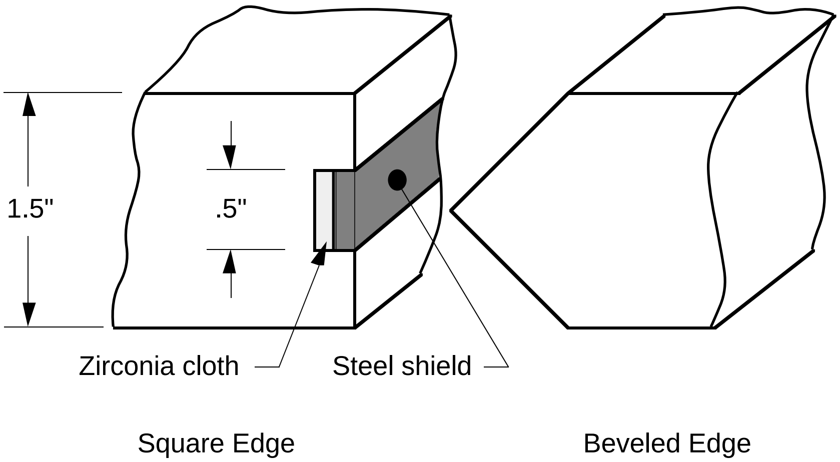
1.5"
.5"
Zirconia cloth
Steel shield
Square Edge
Beveled Edge

Figure 2.3 – Detail of the modified double bevel weld preparation used to simulate a lack of fusion weld defect.

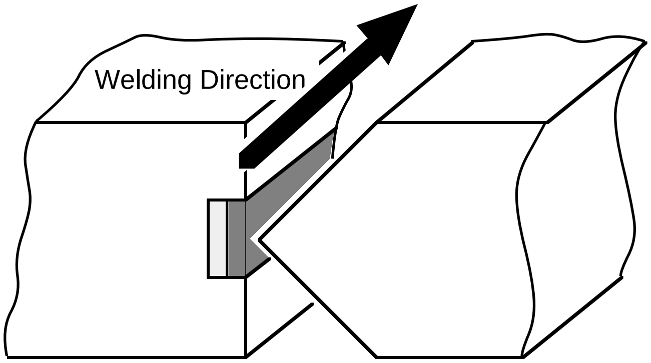
Welding Direction

Figure 2.4 – Fit-up of weld preparation used to simulate a lack of fusion weld defect.

2.4 Defective welds produced

In consultation with Gary Ferea of March Metalfab, Inc., an alternative procedure was attempted. The weld was fitted-up and an initial root pass done using tungsten-inert-gas welding (TIG) which allowed him to fill the root without breaching the shield. Then three passes were made using MIG. The weld was then rolled over, and the same sequence followed: one TIG pass followed by three MIG passes. The remainder of the weld was filled by SAW: three passes, roll over, nine passes, roll, then a final five passes. The shield withstood the TIG and MIG arc forces, and the MIG passes withstood the SAW arc forces so that a final defect containing weld was produced. The final weld cross-section is shown in Figure 2.5. This process was completed for three welded joints, two defective and one non-defective, or "sound". The defective welds are illustrated in Figure 2.6. (The non-defective weld has the same overall dimensions as the defective ones.) The parameters for each weld pass are given in Tables 2.2, 2.3, and 2.4.

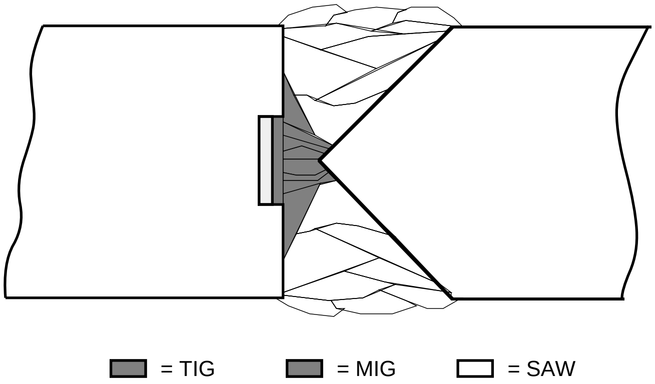

Figure 2.5 – Weld passes for welds with simulated LOF defect.

2.5 Summary

In this chapter, a procedure was developed for producing intentionally defective welds. The culmination of these efforts provided defective and sound welded joints made under similar conditions. In total, three welded joints were fabricated, two of which contained a sizeable buried defect and one which was defect-free. To investigate possible coupling between residual stresses and defects, residual stresses in the sound weld can be directly

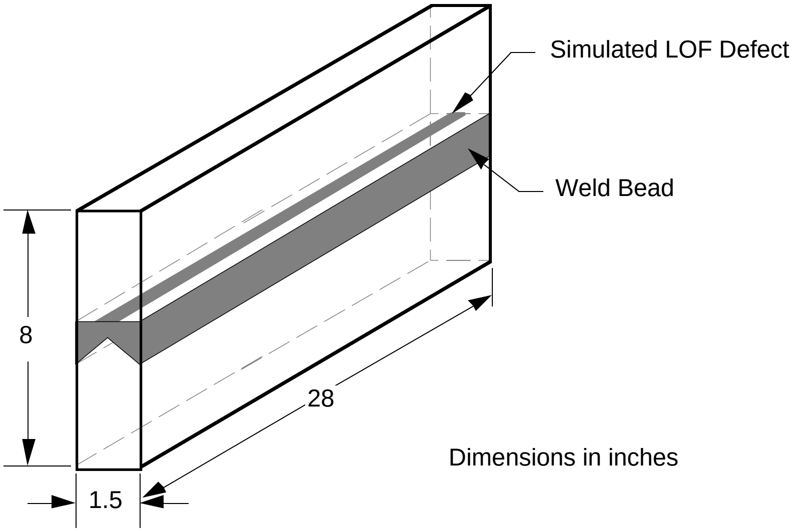
Simulated LOF Defect
Weld Bead
8
28
1.5
Dimensions in inches

Figure 2.6 – Welded specimens containing a simulated lack of fusion.

compared to those in the defective welds, *assuming they can be measured*. As it turns out, the measurement of these stresses is quite challenging. In fact, the remaining chapters in this thesis are devoted to the study of residual stress determination for thick welded plates. Specimens used in various experimental aspects of this thesis were obtained from the welded plates described in this chapter.

Pass	Side	Process	Time Before Pass (min)	Voltage (V)	Current (A)	Time (min)	Tr. Spd. (in/min)	Wire Feed (in/min)	El. Diam. (in)	Matl. Add. (in^3/min)	Pass Area (in^2)
1	A	TIG	Heat to ≈ 130°F	29	100	12	2.50	14.17	0.0625	0.043	0.0174
2	A	MIG	8	20	140	3.17	9.46	264.00	0.0350	0.254	0.0268
3	A	MIG	30	20	140	4.75	6.32	264.00	0.0350	0.254	0.0402
4	A	MIG	10	20	140	4	7.50	264.00	0.0350	0.254	0.0339
5	B	TIG	25	20	150	16.25	1.85	15.58	0.0625	0.048	0.0259
6	B	MIG	15	20	140	4.4	6.82	264.00	0.0350	0.254	0.0373
7	B	MIG	15	20	150	4.25	7.06	264.00	0.0350	0.254	0.0360
8	B	MIG	15	20	150	4.25	7.06	264.00	0.0350	0.254	0.0360
9	B	SAW	50	30	400	3.3	9.09	133.33	0.0781	0.639	0.0703
10	B	SAW	2	30	400	1.88	15.96	133.33	0.0781	0.639	0.0401
11	B	SAW	2	30	400	1.8	16.67	133.33	0.0781	0.639	0.0383
12	A	SAW	15	30	400	2.5	12.00	133.33	0.0781	0.639	0.0533
13	A	SAW	2	30	400	1.5	20.00	133.33	0.0781	0.639	0.0320
14	A	SAW	3	30	400	1.5	20.00	133.33	0.0781	0.639	0.0320
15	A	SAW	10	30	400	1.75	17.14	133.33	0.0781	0.639	0.0373
16	A	SAW	≈ 310°F	30	400	1.5	20.00	133.33	0.0781	0.639	0.0320
17	A	SAW	3	30	400	1.75	17.14	133.33	0.0781	0.639	0.0373
18	A	SAW	10	30	400	1	30.00	133.33	0.0781	0.639	0.0213
19	A	SAW	2	30	400	1.66	18.07	133.33	0.0781	0.639	0.0354
20	A	SAW	5	30	400	1.75	17.14	133.33	0.0781	0.639	0.0373
21	B	SAW	40	30	400	1.33	22.56	133.33	0.0781	0.639	0.0283
22	B	SAW	2	30	400	1.08	27.78	133.33	0.0781	0.639	0.0230
23	B	SAW	5	30	400	1.9	15.79	133.33	0.0781	0.639	0.0405
24	B	SAW	5	30	400	1	30.00	133.33	0.0781	0.639	0.0213
25	B	SAW	20	30	400	1.67	17.96	133.33	0.0781	0.639	0.0356
										Total Area	0.8685
										Prep. Area *(Less reinforcement)*	0.84375

***Table 2.2** – Weld pass order and data for sound weld.*

Pass	Side	Process	Time Before Pass (min)	Voltage (V)	Current (A)	Time (min)	Tr. Spd. (in/min)	Wire Feed (in/min)	El. Diam. (in)	Matl. Add. (in^3/min)	Pass Area (in^2)
1	A	TIG	n/a	30	100	24	1.25	8.97	0.0625	0.028	0.0220
2	A	MIG	20	19	140	4.5	6.67	264.00	0.0350	0.254	0.0381
3	A	MIG	1	19	140	4.5	6.67	264.00	0.0350	0.254	0.0381
4	A	MIG	2	19	140	4.5	6.67	264.00	0.0350	0.254	0.0381
5	B	TIG	40	20	150	13	2.31	6.97	0.0625	0.021	0.0093
6	B	MIG	960 (Heat 120 °F)	20	140	6	5.00	264.00	0.0350	0.254	0.0508
7	B	MIG	2	20	150	5	6.00	264.00	0.0350	0.254	0.0423
8	B	MIG	2	20	150	3.2	9.38	264.00	0.0350	0.254	0.0271
9	B	SAW	50	30	400	2.75	10.91	120.00	0.0781	0.575	0.0527
10	B	SAW	2	30	400	2.33	12.88	150.00	0.0781	0.719	0.0558
11	B	SAW	2	30	400	2.33	12.88	120.00	0.0781	0.575	0.0447
12	A	SAW	120 (≈ 100°F)	30	400	2	15.00	150.00	0.0781	0.719	0.0479
13	A	SAW	2	30	400	1.67	17.96	150.00	0.0781	0.719	0.0400
14	A	SAW	2	30	400	1.67	17.96	150.00	0.0781	0.719	0.0400
15	A	SAW	2	30	400	2.67	11.24	150.00	0.0781	0.719	0.0640
16	A	SAW	2	30	400	2	15.00	150.00	0.0781	0.719	0.0479
17	A	SAW	2	30	400	4.25	7.06	150.00	0.0781	0.719	0.1019
18	A	SAW	2	30	400	1.8	16.67	150.00	0.0781	0.719	0.0431
19	B	SAW	90	30	400	2.25	13.33	150.00	0.0781	0.719	0.0539
20	B	SAW	2	30	400	2.833	10.59	150.00	0.0781	0.719	0.0679
21	B	SAW	2	30	400	2.25	13.33	150.00	0.0781	0.719	0.0539
22	B	SAW	2	30	400	1.67	17.96	150.00	0.0781	0.719	0.0400
23	B	SAW	2	30	400	1.67	17.96	150.00	0.0781	0.719	0.0400
										Total Area	1.0598
										Prep. Area	0.84375
										(Less reinforcement)	

Table 2.3 – *Weld pass order and data for defective weld AN1.*

Pass	Side	Process	Time Before Pass (min)	Voltage (V)	Current (A)	Time (min)	Tr. Spd. (in/min)	Wire Feed (in/min)	El. Diam. (in)	Matl. Add. (in^3/min)	Pass Area (in^2)
1	A	TIG	n/a	30	100	12.5	2.40	16.32	0.0625	0.050	0.0209
2	A	MIG	30	19	150	5.5	5.45	264.00	0.0350	0.254	0.0466
3	A	MIG	5	19	150	6	5.00	264.00	0.0350	0.254	0.0508
4	A	MIG	3	19	150	6	5.00	264.00	0.0350	0.254	0.0508
5	B	TIG	960 (Heat 150 °F)	20	190	11	2.73	12.36	0.0625	0.038	0.0139
6	B	MIG	≈ 130 °F	20	140	3.5	8.57	264.00	0.0350	0.254	0.0296
7	B	MIG	15	19	140	6.5	4.62	264.00	0.0350	0.254	0.0550
8	B	MIG	1	19	140	5.5	5.45	264.00	0.0350	0.254	0.0466
9	B	SAW	30	30	400	1.66	18.07	150.00	0.0781	0.719	0.0398
10	B	SAW	3	30	400	2.25	13.33	171.43	0.0781	0.822	0.0616
11	B	SAW	2	30	400	2	15.00	150.00	0.0781	0.719	0.0479
12	A	SAW	45	30	400	2	15.00	150.00	0.0781	0.719	0.0479
13	A	SAW	2	30	400	2.25	13.33	150.00	0.0781	0.719	0.0539
14	A	SAW	6	30	400	2	15.00	150.00	0.0781	0.719	0.0479
15	A	SAW	2	30	400	2.25	13.33	150.00	0.0781	0.719	0.0539
16	A	SAW	2	30	400	1.5	20.00	150.00	0.0781	0.719	0.0360
17	A	SAW	30	30	400	1.75	17.14	150.00	0.0781	0.719	0.0419
18	A	SAW	7	30	400	1.5	20.00	150.00	0.0781	0.719	0.0360
19	A	SAW	2	30	400	1.5	20.00	150.00	0.0781	0.719	0.0360
20	B	SAW	60	30	400	1.765	17.00	150.00	0.0781	0.719	0.0423
21	B	SAW	2	30	400	2.1	14.29	150.00	0.0781	0.719	0.0503
22	B	SAW	15	30	400	2.67	11.24	150.00	0.0781	0.719	0.0640
23	B	SAW	5	30	400	2	15.00	150.00	0.0781	0.719	0.0479
24	B	SAW	2	30	400	2	15.00	150.00	0.0781	0.719	0.0479
										Total Area	1.0696
										Prep. Area	0.84375
										(Less reinforcement)	

Table 2.4 *– Weld pass order and data for defective weld BN1.*

Chapter 3

Methods for Triaxial Residual Stress Estimation

In this chapter, we compare sectioning methods which reportedly can be used to find triaxial residual stress in thick welded plates. A simulation of two representative techniques, based on the finite element method, is discussed. Each technique is contrasted against the others in terms of accuracy and the amount of work required to obtain the estimated residual stress. Finally, a test specimen is proposed, into which a known residual stress field can be introduced, for physical experiments to verify the computations on which this chapter is based.

The little data available in the literature for thick welds suggest that several characteristics of the residual stresses make their determination difficult. Perhaps the foremost challenge with such welds is the presence of high stress gradients with respect to geometry. Also, the residual stress field is always triaxial, with possibly all six components of residual stress being nonzero. Thick welded plates, therefore, present one of the most difficult residual stress distributions to measure.

One of the most frustrating aspects of residual stress for the engineer is that residual stress is altered when a weld is sectioned to allow access for instrumentation. Samples must be removed from a structure in the process of residual stress determination, and these samples must be sectioned into smaller pieces. Assumptions about how residual stresses change when samples and sections are separated must always be made. The validity of these assumptions often determines the accuracy of the method. The change in strain which occurs on the surface of a removed section is usually measured and used to find the preexisting residual stress. The calculation of residual stress from measured strains is sometimes referred to as “back-calculation” in the literature.

3.1 Methods to be compared

We will compare the techniques proposed by Gunnert (1961), Rosenthal and Norton (1945), Ritchie and Leggatt (1987), and Ueda (1975). Each of these methods were reported to be capable of revealing triaxial residual stress deep within welded joints. Throughout this discussion we will refer to the directions in a butt welded plate shown in Figure 3.1.

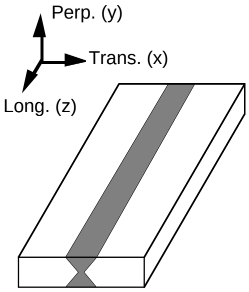

Figure 3.1 – Directions relative to a weld.

3.1.1 Method proposed by Gunnert (1961)

Perhaps the earliest and most complete treatise on measurement of weld residual stress was provided by Gunnert, originally written in Swedish (about 1936) and then translated into English (1955). He presented results of a novel technique to measure triaxial residual stress somewhat later (Gunnert, 1961). This method makes use of pairs of measuring holes and incremental overcoring to release residual stress. In Figure 3.2 we show a section cut through a measurement site. Two pairs of small holes are drilled completely through the thickness of the welded plate, one pair lying in the x-y plane, and the other in the y-z plane. For each pair of holes, the center-to-center distance is measured as a function of depth in the perpendicular direction following drilling. A core including these holes is then removed from the plate by “overcoring”, and the distances are measured again. The strain released in each direction is then computed as a function of depth. Residual stress originally in the plate is determined from the measured strain, assuming that the core is stress-free.

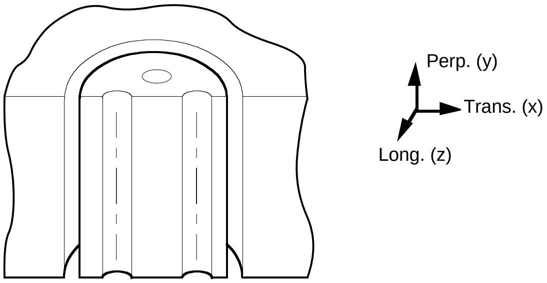

Figure 3.2 – Section through a measurement point where Gunnert’s technique was applied.

To include the measurement of perpendicular residual stress, the core is removed in an incremental fashion. Overcoring is done to a specified depth, then the length of the core in the perpendicular direction is measured using a special gage. By measuring this length as a function of overcore depth, strain released can be computed as a function of distance in the perpendicular direction and used to find residual stress.

Two important assumptions are made in Gunnert’s method. First it is assumed that the creation of the measuring holes does not alter the initial residual stress field, and second, that the removed core is stress free. Creation of the measuring holes will surely disturb the residual stress field within the region near the holes. If the removed core is large compared with the size and layout of the holes, the stress released by overcoring will not be significantly influenced by the measuring holes. However, if the core removed is to be stress free, then it must be small relative to the spatial variation of the initial residual stress field in the transverse and longitudinal directions. It is widely accepted that the variation of residual stress is small in the longitudinal direction some distance from the ends of a welded plate. However, measurements of residual stress on the top surfaces of welded plates show that the variation in the transverse direction is large, except near the middle of the bead. In selecting measuring hole and overcore dimensions, these competing factors must be carefully balanced.

Despite these difficulties, Gunnert's work represents the most complete results provided by a direct strain relaxation based experimental method. More involved sectioning techniques, such as that suggested by Rybicki and Shadley (1986), make use of more complex and less obvious assumptions than those called for in Gunnert's technique. For this reason, it may be reasonable to assume that the Gunnert technique provides at least a good approximation to the residual stress field present in welded plates. In that spirit, we present Gunnert's results for residual stress at the center of the bead and middle of the weld-length as a function of distance through the thickness for a double-sided butt welded plate. These are shown in Figure 3.3. We take these results to be representative of the basic character of weld residual stress at this location in such a joint.

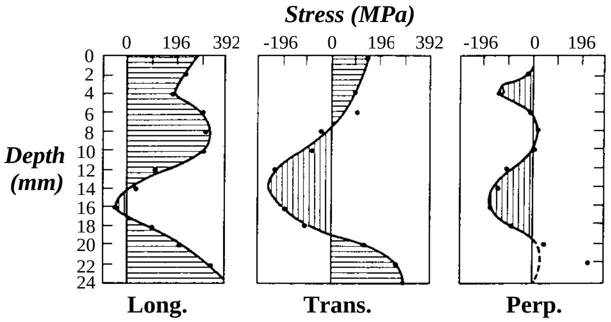

Figure 3.3 – Residual stresses reported by Gunnert (1961).

Gunnert's technique has been updated by Procter and Beaney (1987). Their procedure uses only one measuring hole, the diameter of which is measured in three directions, before and after overcoring, with a special transducer. This method is depicted in their paper as shown in Figure 3.4. The use of a single hole allows the removed core to be smaller, improving accuracy in regions of residual stress gradients. The length of the core in the perpendicular direction is measured during overcoring with an LVDT and is used to find the perpendicular residual stress. Their method uses a back-calculation routine derived from finite element simulations to find residual stress from the measured displacements. When compared with Gunnert's technique, the method requires a greater displacement measurement accuracy for the same accuracy in released strain and residual stress since the effective gage length for measured strain is reduced. To execute these high-accuracy measurements, Procter and Beaney developed a special, high-sensitivity

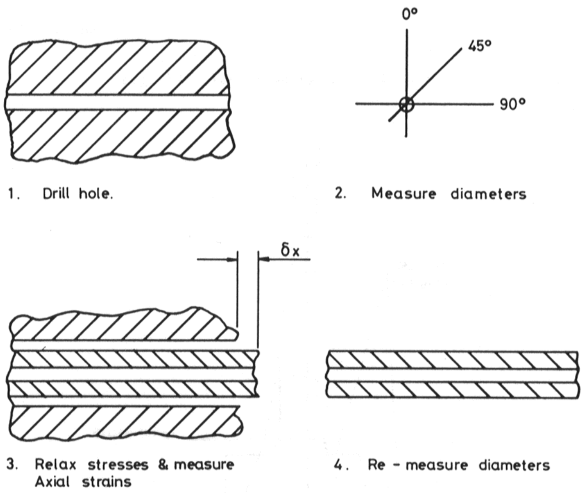
0°
45°
90°
δx
1. Drill hole.
2. Measure diameters
3. Relax stresses & measure Axial strains
4. Re - measure diameters

Figure 3.4 – Schematic of the technique presented by Procter and Beaney (1987).

transducer. The active portion of the transducer consisted of two beams which contact the hole in diametrically opposed locations. The device is drawn through the length of the hole, and the beams deflect with changing the hole diameter. Deformation of each beam is measured by electric-resistance strain gages cast into its outer fiber. According to verification experiments they conducted, this gage allows diameter measurement to six micro-inch accuracy. When used to measure the nominally one-eighth inch hole specified in their technique, 50 μin/in resolution in strain measurement was obtained.

3.1.2 Method proposed by Rosenthal and Norton (1945)

Rosenthal and Norton suggested a method based on removal of two thin slices of material from a thick weld. The location and orientation of these two samples is shown in Figure 3.5. One sample lies in the longitudinal-perpendicular plane, and one in the transverse-perpendicular plane. These are referred to as the longitudinal and the transverse samples, respectively.

Residual stress in the welded plate is known to be the residual stress in each slice added to the residual stress released when the slices are removed from the plate, as follows from superposition. Rosenthal and Norton estimate the residual stress in each slice

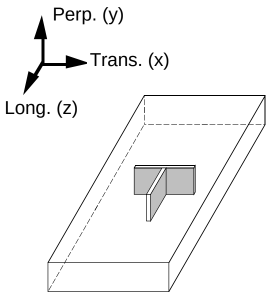

Figure 3.5 – Two slices removed in the Rosenthal-Norton technique (1945).

assuming that residual stress exists only along the long axis of the slice. They make use of a combined splitting and layer-removal technique to reveal this assumed-uniaxial residual stress field in each slice. But, virtually any surface stress measurement technique could be applied to find these stresses. The stress released when the samples are removed from the plate is found based on one simple assumption: the stress released in the long axis of the slice is a linear function of the perpendicular coordinate. Therefore, stress release is measured on the top and bottom surfaces of the plate by installing electrical-resistance strain gages prior to cutting. The stress released at any point through the thickness is then found by linear interpolation. Finally, the initial residual stress in the plate is found by adding the residual stress in the removed samples to the linearly distributed stress released when the samples were removed from the plate. This method relies on the linear stress release assumption. However, that assumption has never been shown to be valid and the task of doing so would be difficult as it requires use of a specimen with known residual stress or the ability to measure stress deep within the material by some other means. Both types of verification of this primary assumption require a great deal of effort.

3.1.3 Slotting methods

Cheng and Finnie (Cheng, 1990) have presented an experimentally simple way to obtain residual stress as a function of depth called the crack compliance method. The crack compliance method (and other similar slotting methods) determines stress on one plane in the body. The method involves incrementally extending a slit through the residual stress field, and measuring the change in strain at specified locations along or near the slit.

Following the experiments, back computation yields the distribution of residual stress normal to the slot. The back computation is based on the theory of elasticity, so that only analytical computation is required. As with most of the relaxation methods, a few simplifying assumptions are made. The residual stress is assumed to have the same distribution along the length of the slot and to be symmetric with respect to the cutting plane. Thus, the method lends itself to axisymmetric or planar symmetric problems. When the residual stress field is not symmetric with respect to the cutting plane, normal slot-face tractions are accompanied by shear tractions and the back computation procedure is prone to error. Cheng and Finnie have applied this method to the measurement of residual stress in bent beams (Cheng, 1991), hoop stress in quenched cylinders (Cheng, 1986), and stress near the toe of an attachment weld (1993). Also, the axial stress in a butt-welded cylinder (Cheng, 1990) has been measured using this technique. However, adherence to the symmetry assumption of the residual stress field was not carefully investigated for the weld experiment.

Ritchie and Leggatt (1987) used a method similar to that of Cheng and Finnie to determine the residual stress in a circumferential butt weld in steel pipe. Their analysis used FEM to develop a set of influence coefficients which relate the strain at a point near the slot to a unit slot face traction, at a specified distance along the slot measured from the surface, for a particular slot depth. The slot is extended in an incremental fashion, as shown in the slotting set up illustrated in Figure 3.6. In Ritchie's words, "the strain change at gage k due to unit stress at slot depth increment m in the model with the slot extended to n increments is F_{kmn}." The strain at gage k for a slot extended to n increments is then

$$\varepsilon_{kn} = \sum_{m=1}^{n} \sigma_m F_{kmn} \tag{3.1}$$

where σ_m is the residual stress at depth increment m prior to cutting the slot. The coefficients F_{kmn} are found by running several FEM analyses of the geometry of interest. Slotting is performed, and the resulting strain data are then used in a least squares scheme to obtain the values of σ_m.

In their paper, Ritchie and Leggatt applied this method to determine residual stress in a plastically bent beam and axial stress in a circumferentially butt-welded cylinder. In one respect, this method is preferable to that of Finnie and Cheng because the specimen

Figure 3.6 – Slotting set-up and numbering system used by Ritchie and Leggatt (1987).

geometry can be complex; however, there is a large amount of numerical computation required, especially when contrasted with the crack compliance method which is dependent only on analytical computations. Futhermore, both the applications reported by Ritchie and Leggatt represent two-dimensional rather than three-dimensional stress determination problems. The stresses reported to exist in the welded cylinder examined result from combining slotting results on a small coupon with the stresses released when that coupon was removed from the cylinder. These released stresses are found by measuring strain changes on the top and bottom surfaces of the sample which result when the specimen is removed. It is then surmised that stress released through the thickness can be fully determined by these measured surface strain changes. Their method of determining these “parting out stresses” is quite similar to that used by Rosenthal and Norton. Therefore, we restate that the ability to use surface strain changes to determine through-thickness stress release has never been fully investigated.

3.1.4 Method proposed by Ueda (1975)

Conventional methods of residual stress determination by dissection, such as those of Rosenthal and Norton (1945) or Ritchie and Leggatt (1987), have been widely used over the years. Ueda (1975) has recently developed a method which may be used to measure three-dimensional residual stress. The method relies on determination of the “inherent strain" distribution in the body of interest. Inherent strain is defined by Ueda as being the source of residual stress, and is equivalent to the eigenstrain of Mura (1982) which was introduced in Section 1.2.2. In reviewing Ueda's work, we will use the term inherent strain and eigenstrain interchangeably, as they are equivalent. If the distribution of inherent strain is known in the body, the residual stress distribution can be obtained with the aid of the finite element method. This method assumes that when a specimen is parted from the original body no new inherent strains are produced. Thus, deformation accompanying sectioning is assumed to be elastic, a reasonable assumption in many situations. Sectioning produces different geometries which contain the same inherent strain field, but different residual stresses. Ueda has shown that the difference in residual stress between sectioned geometries can be used to determine the inherent strain and therefore the residual stress in the original body prior to sectioning.

Another important aspect of this method is that only the "effective" part of the inherent strain needs to be determined. This portion of inherent strain is defined as that part of the total inherent strain which causes residual stress, the remaining portion causing only stress-free deformation. An example will serve to illustrate the distinction between effective and ineffective eigenstrain and to introduce the method.

Consider the case of two elastic rods which are joined at a condition of zero stress to a rigid wall at one end and to a slider at the other end, as shown in Figure 3.7. Further imagine that they both have unit modulus, length, and area, and only differ in thermal expansion coefficient, α. If the joined rods are then subjected to a unit temperature rise, the whole assembly will change length, and stress will develop in each of the rods. Adopting the notation of Ueda (1989), we write $\varepsilon = \boldsymbol{\varepsilon}^{\mathbf{e}} + \mathbf{g}$, where

$$\varepsilon = \begin{bmatrix} \varepsilon_1 \\ \varepsilon_2 \end{bmatrix} \text{ is the total strain} \tag{3.2}$$

$$\boldsymbol{\varepsilon}^{\mathbf{e}} = \begin{bmatrix} \varepsilon^e{}_1 \\ \varepsilon^e{}_2 \end{bmatrix} \text{ is the elastic strain} \tag{3.3}$$

$$\mathbf{g} = \begin{bmatrix} g_1 \\ g_2 \end{bmatrix} \text{ is the inherent strain.} \tag{3.4}$$

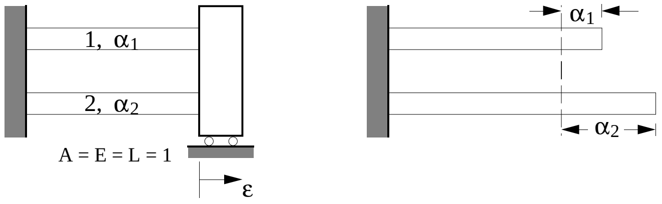

Stress-free
initial condition

Stress-free condition
following unit
temperature increase

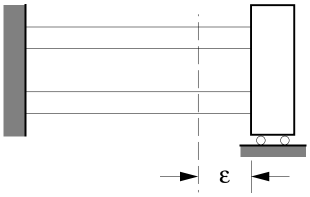

Compatibility boundary condition
enforced following unit temperature increase

Figure 3.7 – Illustration of the effective inherent strain principle.

Here, the numerical subscript, 1 or 2, refers to one of the two elastic rods. Since **g** is known (from thermal expansion), it is possible to derive from equilibrium ($\sigma_1 + \sigma_2 = 0$), the constitutive equation with unit modulus ($\sigma = \varepsilon^{\mathbf{e}}$), and the uniform end condition ($\varepsilon_1 = \varepsilon_2$), the total strain ε, and therefore the elastic strain $\varepsilon^{\mathbf{e}}$, and the stress σ:

$$\mathbf{g} = \begin{bmatrix} \alpha_1 \\ \alpha_2 \end{bmatrix} \tag{3.5}$$

$$\varepsilon = \begin{bmatrix} \dfrac{\alpha_1 + \alpha_2}{2} \\ \dfrac{\alpha_1 + \alpha_2}{2} \end{bmatrix} \tag{3.6}$$

$$\sigma = E\varepsilon^{\mathbf{e}} = 1(\varepsilon - \mathbf{g}) = \begin{bmatrix} \dfrac{\alpha_2 - \alpha_1}{2} \\ \dfrac{\alpha_1 - \alpha_2}{2} \end{bmatrix} \tag{3.7}$$

Notice that stress depends on the difference in the inherent strain of the two rods, while deformation of the body, ε, depends on their sum (i.e., $\sigma \propto (g_1 - g_2)$, and $\varepsilon \propto (g_1 + g_2)$). The inherent strain may then be broken into these two parts, the effective inherent strain, ε*, which causes stress, and the ineffective part which causes change of length. Any total inherent strain, then, which has the same effective part will result in the same stress distribution in the body. There are infinitely many such strain distributions, but since we are only concerned with the stress, only one solution needs to be found. Therefore, it is necessary to specify the effective inherent strain at one point in the body in order to determine a unique ε*. A logical choice is to fix the effective inherent strain in one of the bars to be zero.

Now, consider the problem of determining the stress when the inherent strain is not known but the elastic strain is. This is the case which frequently happens when sectioning techniques are used, since when the restraint is removed from the rods, the elastic strain is determined from measured strain (ε^m) as

$$\varepsilon^{\mathbf{e}} = -\varepsilon^m. \tag{3.8}$$

Alternatively, the measured strains may be used to determine ε* which then can be used to determine the stress. If the effective inherent strain is assumed to be zero in rod 2 for reasons mentioned above, then we can write

$$\varepsilon^* = \begin{bmatrix} \varepsilon^*_1 \\ 0 \end{bmatrix}. \tag{3.9}$$

Applying equilibrium $(\sigma_1 + \sigma_2 = 0)$ and uniform end displacement conditions to the system, we arrive at the relation

$$\varepsilon^{\mathbf{e}} = \frac{1}{2}\begin{bmatrix} -\varepsilon^*_1 \\ \varepsilon^*_1 \end{bmatrix}. \tag{3.10}$$

Combining Equations 3.8 and 3.10, we have

$$\begin{bmatrix} -\varepsilon_1^m \\ -\varepsilon_2^m \end{bmatrix} = \frac{1}{2}\begin{bmatrix} -\varepsilon^*{}_1 \\ \varepsilon^*{}_1 \end{bmatrix}, \tag{3.11}$$

which reduces to

$$\varepsilon^*{}_1 = 2\varepsilon_1^m = -2\varepsilon_2^m\,. \tag{3.12}$$

The second equality will only hold if there is no error in measurement. Notice that since the residual stress in dependent on one parameter, and we have made two measurements, it is possible to minimize random error by employing statistical methods. In general, a least squares method can be utilized to minimize the error in estimating the non-zero inherent strain, $\varepsilon^*{}_1$.

In this simple example, relations were determined between the assumed inherent strain distribution and the resulting elastic strains by enforcing equilibrium and boundary conditions. In more complicated bodies, the finite element method (FEM) may be employed, where the values of inherent strain at several locations are treated as parameters to be determined. In terms of FEM, an inherent strain imposed onto an element is transformed into an equivalent nodal force via the local constitutive relation and the local strain-displacement relation. Imposing equilibrium, a set of equations is obtained relating each imposed inherent strain to the elastic strain at strain measurement locations.

In Ueda's notation, we express this algebraic relation in terms of the linear system

$$\varepsilon^m = \mathbf{H}^* \bullet \varepsilon^* \tag{3.13}$$

where ε^m and ε^* are the measured elastic and effective inherent strains as above, except that now there is a row in both vectors for each component of strain at each point. The matrix $\mathbf{H}^*$ is defined to relate the two, and can be derived from principles of FEM (Ueda, 1975) or, more generally, from repetitive application of the finite element method as described in Chapter 4 of this thesis. If the number of measured strains and the number of imposed inherent strains are equal, then $\mathbf{H}^*$ is square and if it is non-singular, the system can be solved. Non-singularity of $\mathbf{H}^*$ is assured if ε^* is effective (i.e. there are no values of ε^* which produce zero ε^m). If the number of measured strains is smaller than the number of imposed inherent strains, additional relations must be added. For example, one may be able to assume that the inherent strain may be spatially interpolated (Ueda, 1989). If the number of measured strains exceeds the number of imposed inherent strains, least squares may be employed in order to minimize the residual error (Ueda, 1975).

The most powerful element of this method is the assumption that when a body is sectioned into smaller and hopefully simpler specimens, the inherent strain distribution in the removed specimen does not change. Therefore, no measurement of strain while parting-out the specimen from a larger structure is necessary. Accordingly, assumptions about stress release, like those made by Rosenthal and Norton and by Ritchie and Leggatt, are not needed in Ueda's method.

When measuring the residual stress in a three dimensional body, the inherent strain will in general contain six components, each of which is a function of position within the body. However, it may be possible to section the part into specimens which contain a limited number of *effective* inherent strain components. In that case, each component might be measured on separate specimens. Residual stress can then be determined by imposing the estimated inherent strain distribution on the original body in the framework of a finite element analysis. This procedure has been laid out by Ueda in a series of papers (1975, 1985, 1986b, 1986d, 1989).

In the case of a long continuously welded plate, the determination of the inherent strains is simplified by such "intelligent" sectioning of the body (Ueda, 1985). The assumption of continuous welding allows Ueda to consider an eigenstrain field that is dependent on the transverse and perpendicular coordinates, while independent of the longitudinal coordinate. The basis for this assumption is that each plane in the weld cross-section is thought to experience nearly the same thermal and mechanical processes during welding. Two such planes are shown in Figure 3.8. Clearly this assumption does not hold in either the thermal or mechanical sense near the ends of the joint, as noted by Ueda.

An illustration of Ueda's technique for a welded joint is shown in Figure 3.9 (Ueda, 1985). A sample of a welded plate is obtained from the structure of interest and an array of strain gages is attached to one of the sample's longitudinal faces (shown shaded in the figure). Two strain-relaxation measurements are then performed, one from block to thin

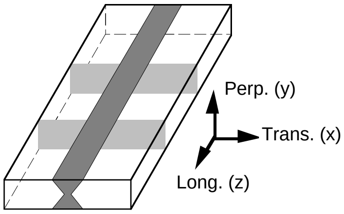

Figure 3.8 – Two planes which have the same eigenstrain distribution.

slice and the other from slice to small pieces (dice), each containing a strain gage. The slice-to-dice data allow determination of the eigenstrain (or, inherent strain) components in the transverse-perpendicular plane. Using these results with the block-to-slice strain relaxation data allows determination of the eigenstrain component associated with the longitudinal direction. The determination of eigenstrain components from measured strain changes involves solution of the linear system represented by Equation 3.13.

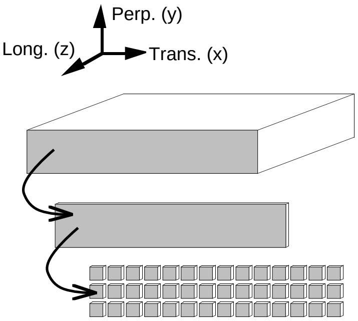

Figure 3.9 – Schematic of the slice-and-dice method proposed by Ueda (1985).

The application of the eigenstrain method for welded joints uses an assumption about the eigenstrain field. This is the key aspect of the method which differentiates it from the others we have presented. The method proceeds from an observation regarding the process which imposes the residual stress: continuous welding leaves behind an eigenstrain field which is independent of longitudinal position. This observation allows stress and strain on the transverse-perpendicular free-plane of the welded plate and the slice removed from its end to be used to *peer* into the joint and find stress at any location along the length of the weld. However, the entire method revolves around this assumption and its validity should be ascertained. Again, the eigenstrain method is fundamentally different than other sectioning methods because it uses an assumption about the eigenstrain distribution rather than one regarding the stress release which accompanies sectioning.

3.2 Numerical application of the methods

Numerical simulation has been performed to investigate the methods proposed by Rosenthal and Norton and by Ueda. Results of these simulations are summarized here. Details of the simulation of Ueda's eigenstrain method will be presented in Chapter 4. The method proposed by Gunnert will not be simulated here as Procter and Beaney have already executed a similar study of their Gunnert-like technique (Procter, 1987). Their results show that the method is able to capture the residual stress distribution with good accuracy. However, their simulations address neither the sensitivity of the method to variations of residual stress in the transverse and longitudinal directions nor the influence of the measuring hole on the stress relaxed by overcoring. Results obtained for the Rosenthal-Norton method will also speak to the accuracy of the method proposed by Ritchie and Leggatt. Both of these methods make the assumption that through-thickness stress release caused by sample removal can be completely determined by measurements made on the joint surface.

3.2.1 Baseline residual stress state

We assume that residual stress is to be determined within a sample of welded plate shown in Figure 3.10. The residual stress field present in this sample is one which resembles both the results of Gunnert, shown in Figure 3.3, and the well known characteristics of residual stress on the surface of thick welded plates. Residual stress is shown in Figure 3.11 and Figure 3.12 along contours within the x–y (transverse-perpendicular) plane at the middle of the sample with respect to the weld direction. These plots serve to demonstrate the character of this sample residual stress field. These stresses are the result of a finite element computation and are identified as "exact", meaning that a perfect measuring technique would obtain the same results.

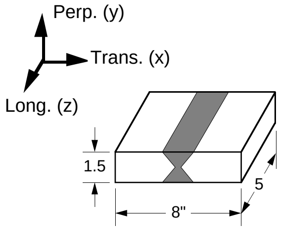

Figure 3.10 – Sample in which residual stress is to be determined (dimensions in inches).

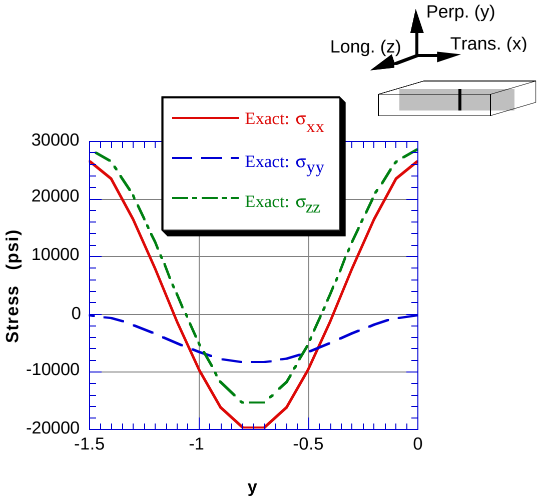

Figure 3.11 – Residual stresses at the center of the sample, through the thickness of the plate, generated by finite element analysis.

Residual stress is produced in a finite element model of the specimen shown in Figure 3.10 by introduction of an eigenstrain field. The resulting residual stress state is fully three-dimensional, and exists everywhere within the body. The specific eigenstrain field used is given in detail in Section 4.2.1. This field was developed to produce a complicated residual stress field that *resembles* the character of thick-weld residual stress; however, this field should not be construed to *be* the residual stress state present in any real weld. Its sole purpose is to provide a basis by which to compare techniques for residual stress determination.

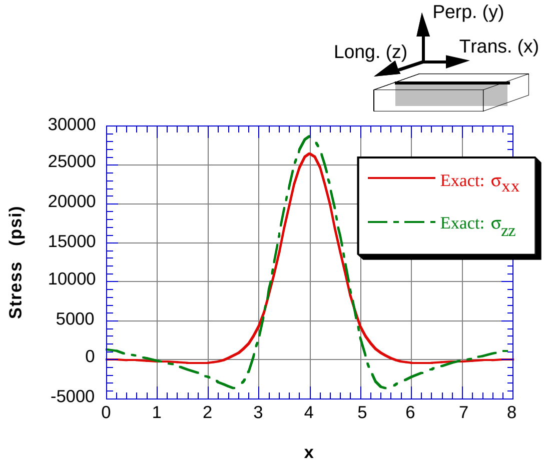

Figure 3.12 – Residual stress at the center of the weld length, across the top surface.

3.2.2 Technique used to compare the methods

To simulate a measurement technique using the finite element method, we analyze each sample and section removed using three-dimensional finite element models. Stress in each piece is due to the eigenstrain field, which is known since we assume that the cutting process causes no new eigenstrain (i.e., inelastic deformation) in the removed pieces. The stress change due to removal of a sample is determined by subtraction of the stress in the sectioned configuration from the stress in the original configuration. We “measure” the stress and strain changes by taking nodal results from the computation. In this way, no effort is made to account for the finite size of the strain gages which would be used in the corresponding physical experiments.

3.2.3 Simulation of the Rosenthal and Norton method

Simulation of the Rosenthal-Norton method requires three finite element models. The first model represents the sample shown in Figure 3.10, the second and third models correspond to the two specimens shaded in Figure 3.5. These two slices both measure 3 inches long, 1.5 inches wide, and 0.25 inch thick. Stress released when these two slices are removed from the plate is found at the mid-length of each slice at points corresponding to the top and bottom surfaces of the original welded sample.

It is not our goal here to review the determination of the supposedly uniaxial residual stress which is present in these thin slices. This subject has been summarized in several places, including the SAE handbook supplement on residual stress determination (SAE, 1965). It is noteworthy, however, that the uniform uniaxial assumption made by Rosenthal and Norton can lead to large errors when applying the layer-removal technique to the transverse slice (Cheng, 1986).

We will assume that the stress along the axis of the slice is measured with perfect accuracy and address the aspects of the method related to the triaxial nature of the technique. This amounts to checking the linear-stress-release assumption.

3.2.4 Simulation of Ueda’s method

Simulation of Ueda’s method will be described in detail in Chapter 4 and requires two finite element models, one of the block shown in Figure 3.10 and one of a 0.25 inch thick slice removed from the x–y free surface of the block shown in Figure 3.9. A measuring grid is set up on the block face such that most dice cut from the slice measure 0.4 inch by 0.25 inch, x by y. Dice cut from the top and bottom of the slice, with respect to the perpendicular direction, are smaller, 0.4 inch by 0.125 inch.

We do not model the dicing of the block, since we wish to focus on the three-dimensional aspects of the method. As was done in simulating the Rosenthal-Norton technique, we assume that residual stress in the slice is measured exactly. In this method, however, the measured stress field is not assumed to be uniaxial, as it was by Rosenthal and Norton, so all three components of the planar stress field are measured.

3.3 Results

Residual stress present in the two Rosenthal-Norton slices is shown in Figure 3.13 and Figure 3.14, together with that in the welded block. The stress released in the sectioning process is the difference between the stress in the two geometries, and is also shown in the figures. It is clear from these plots that the released stress is far from a linear function of the perpendicular coordinate. Accordingly, the estimated residual stress in the block is inaccurate as shown in Figure 3.15. The accuracy is so poor in fact as to preclude the use of the method altogether. It is true that the method gives good results near the surface, but many other options exist to obtain near-surface results. Ueda's method, on the other hand, gives much less error in stress, as shown in Figure 3.16. This method has little error, except in the longitudinal component of residual stress near the mid-thickness of the block. The success of the method is due to the suitability of its basic assumption: residual stress in the block is caused by an eigenstrain field which *is* independent of the longitudinal coordinate.

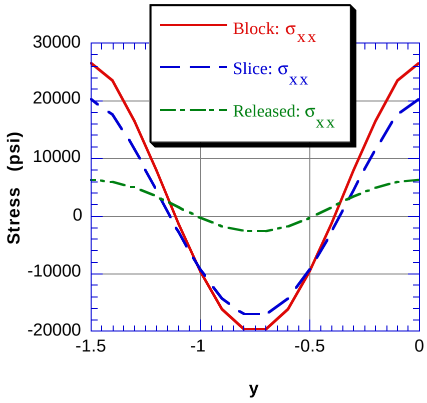

Figure 3.13 – Stress released at the middle of the length of the transverse slice.

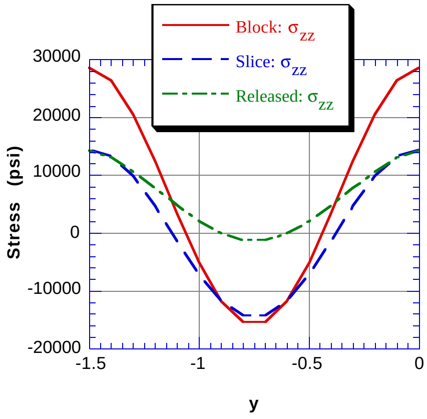

Figure 3.14 – Stress released at the middle of the length of the longitudinal slice.

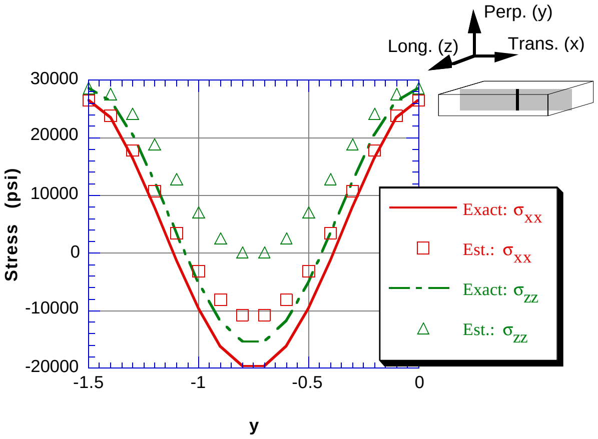

Figure 3.15 – Results of the Rosenthal-Norton technique at the middle of the welded block.

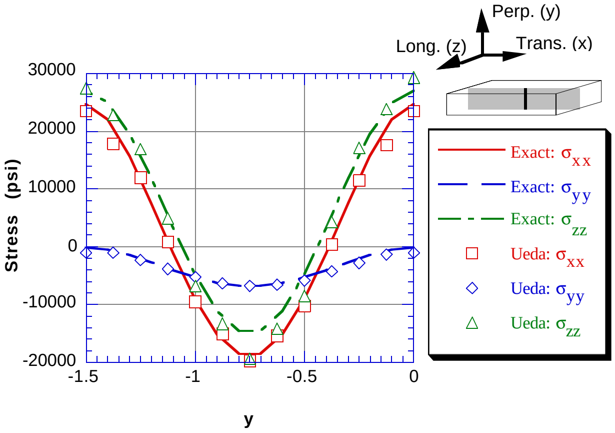

Figure 3.16 – Results of Ueda's method at the middle of the block compared with true values.

3.4 Investigation of Ueda's assumption

The following physical experiment was conducted to investigate the independence of eigenstrain in the longitudinal coordinate in a long continuous weld. The weld used to perform this experiment was one of the defective welds fabricated as described in Chapter 2. A longitudinal slice was removed from the center of this weld in exactly the way as would be done in executing the Rosenthal-Norton method (Figure 3.5). This slice was 8 inches in length, 0.25 inches thick, and 1.66 inches wide (the additional width is due to overfill of the welded joint). Strain gages were attached to the specimen and the slice sectioned as shown in Figure 3.17.

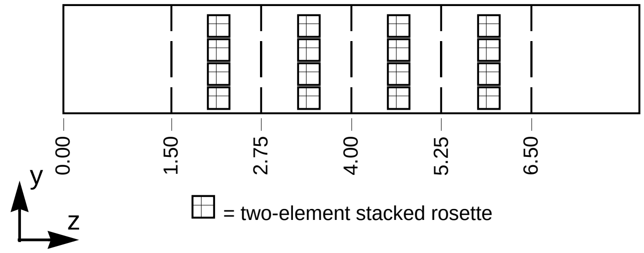

Figure 3.17 – Gage layout and cutting lines for experiment on eigenstrain distribution.

Results show that the strain released during sectioning was independent of the location along the sample as shown in Figure 3.18. In this plot, strain release is plotted versus position across the slice, *y*. The distribution of strain release in *y* is not of particular interest, rather the variation which occurs at each *y*-location from one *z*-location to another. The lack of variation with *z* indicates that the residual stress in the sample and, therefore, the eigenstrain field causing it are independent of position *z* along the sample. It can then be surmised that in this weld, the eigenstrain distribution is independent of the longitudinal coordinate. Whether this is true in most cases, or how the eigenstrain method will perform when the assumption is not valid, is a subject for further study. These experiments indicate that this assumption is valid for the one continuously welded joint examined.

3.5 Comparison of the methods

Aside from the level of accuracy of residual stress estimates, the two methods which were simulated have other differences. As described in the original paper, the Rosenthal-Norton technique gives results only where slices of material are removed from the plate. The complete state of stress is determined, albeit inaccurately, by interpolation of the results from one slice removal location to another. In this example, having removed two slices, stress is fully determined at the center of the block as a function of perpendicular distance from the top surface to the bottom. The method proposed by Ueda, on the other hand,

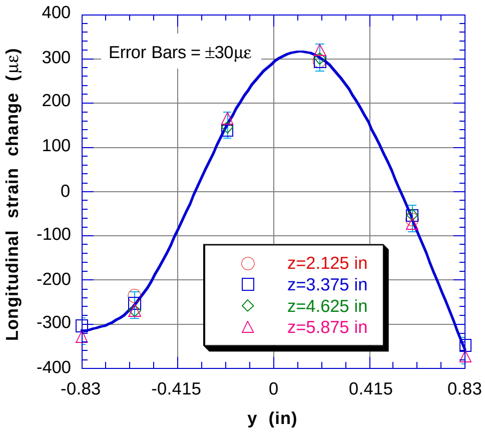

Figure 3.18 – Strain change at various points along the length of a longitudinal slice removed from a weld.

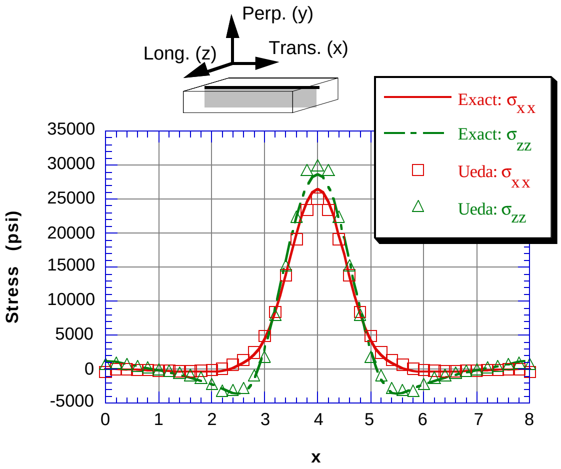

Figure 3.19 – Results of Ueda's method at the center of the weld length, across the top surface.

estimates the residual stress state in the entire body. We have shown results at the center of the joint, through the thickness, but similar plots may be made with respect to any line through the body. For example, stress is plotted in Figure 3.19 along the same line as in Figure 3.12.

The additional information provided by Ueda's method does not come for free. As will be shown in Chapter 4, the physical experiment corresponding to the numerical one summarized here would require use of 140 three-element strain gage rosettes, each being measured a minimum of three times. Execution of this method requires a large amount of work, especially when compared to the simpler method advanced by Gunnert. We have made progress toward a localized eigenstrain approach, which offers the completeness and accuracy of Ueda's method but provides results only within a specific region of the welded joint. In this technique, significantly fewer strain gage rosettes are employed. Our work on this localized eigenstrain method is discussed in Chapter 7.

The Gunnert technique appears to produce fairly accurate results, according to Procter and Beaney (1987). The method seems fairly easy to execute given the proper tools and measuring devices. One drawback, however, is that results are obtained only in the region of the overcore. As such, the whole residual stress field cannot be measured as it can be with Ueda's method. Nevertheless, the method is quite valuable if subsurface stresses are needed in only one spot.

3.6 Testing to verify numerical results

Several conclusions have been drawn above based solely on numerical modeling and investigation of one particular residual stress field. Most engineers would agree that while such evidence is valuable, some sort of physical evidence is needed to judge one method superior to another. One possible way to perform such a comparison is to find a combination of specimen geometry and mechanical process by which a known residual stress field can be introduced.

This has been done in the past to evaluate other residual stress measurement methods. Two-dimensional residual stress measurement techniques have been evaluated using elasto-plastically deformed rectangular cross section beams, for example. Similarly, hydraulically-autofrettaged tubes have been employed to evaluate axisymmetric methods. These two types of specimens contain a residual stress state which is either easily measured or can be obtained with good accuracy by direct calculation. Experimental results are then compared with the available theoretical or known solution. For a general triaxial residual stress field, it is difficult to develop such a specimen.

Since welding is the most common source of triaxial residual stress, it is tempting to use it as a verification tool. However, despite the advances made in weld-mechanics, the residual stress state imposed by a given welding process remains unknown. Something more simple and more predictable is needed to verify these methods.

Our thought is to make use of the autofrettage process, since it is deformation-based, applied in a rectangular rather than axisymmetric geometry. The ability to model this process requires a nonlinear finite element code and a knowledge of the room temperature constitutive behavior of the material of interest. This is clearly much simpler than attempting to model the weld process, with temperature dependent material properties, weld-pool turbulence, and transformation strain, among other complications.

A sketch of a proposed benchmark specimen is shown in Figure 3.20. The holes drilled through the length of the specimen would be autofrettaged, setting up a triaxial residual stress state in the region between the holes. These holes only make the task of finding residual stress marginally more difficult. The boundary of the hole can be handled mathematically in a similar manner to an eigenstrain field. Accordingly, the ability to include the influence of the holes should not be a great leap.

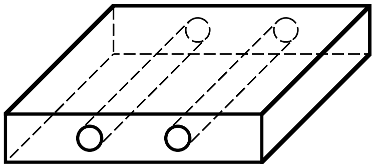

Figure 3.20 – Specimen proposed for benchmark testing of residual stress determination techniques.

3.7 Conclusions

In the above we have discussed three triaxial residual stress measurement techniques. Based on computational simulation of these techniques the following conclusions can be drawn.

1) The methods proposed by Gunnert and Ueda appear to be accurate enough for application to weld residual stress, and these two have very different benefits.

2) The overcoring method proposed by Gunnert and further refined by Procter and Beaney is useful for the determination of residual stress at one location, through the thickness of the joint. The method appears to be free of overly-simplistic assumptions about the underlying residual stress state, and was shown to produce good results by Procter and Beaney. However, execution of the method requires access to specialized machining and measurement equipment.

3) A basic assumption underlying the Rosenthal-Norton technique (i.e., a linear distribution of released stresses with thickness) can be quite erroneous. A similar assumption is made in the “parting-out” step of the method proposed by Ritchie and Leggatt (1987). Therefore, their proposed technique is also inaccurate.

4) The method proposed by Ueda allows determination of residual stress throughout the entire welded joint when the eigenstrain field is independent of the longitudinal coordinate. The method produced good results when this assumption was valid. As will be shown in Chapter 4 and Chapter 5, this method requires a large experimental effort.

5) Experimental evidence indicates that the eigenstrain distribution in long continuously welded joints is independent of the longitudinal coordinate.

6) There is need for a triaxial residual stress specimen which would allow comparison of these techniques on the basis of physical experiments.

Chapter 4

Exposition of the Eigenstrain Method

In this chapter, we further investigate and describe the method proposed by Ueda (1975) for determining three-dimensional subsurface residual stress. As we discussed in introducing this technique in Section 3.1.4, the method relies on assumptions about eigenstrain distribution rather than stress release. This is a hybrid experimental/analytical method which determines the source of residual stress by sectioning and strain measurement, and then uses it to deduce residual stress in the original body. When certain assumptions about the spatial distribution of the source of residual stress can be made, estimates of residual stress can be generated for locations which are remote from strain measurement points. We outline the method and then illustrate its application to measurement of residual stress in a long welded joint. First, background regarding the nature of residual stress and a formulation of the eigenstrain approach to residual stress determination is discussed. Then, application of this method to a long continuously welded joint is described. A model problem is developed and solved by application of finite element analysis. Taking the finite element stress results as if they were experimental measurements, the eigenstrain method is used to find residual stress. The accuracy of the method is then investigated by comparing the eigenstrain and finite element solutions. Finally, the advantages and drawbacks of this relatively new method are discussed.

4.1 Description of the eigenstrain method

The source of residual stress in a body is an incompatible strain field. By incompatible, we mean that the strain field cannot exist within the body without stress. Stress must be present so that the strain field will fit within the body. Thinking of this as a mechanical operation, the body must be deformed to fit the strain field in. If the loads required to deform the body are then removed and equilibrium enforced, the residual stress state can be found. The ill-fitting strain field could be produced by plastic deformation, thermal strain, phase-transformation, or other means. Ueda (1975) refers to the sum total of all such possible causes of incompatible strain as the "inherent strain" present in the body. We adopt Mura's (1982) terminology in calling it "eigenstrain". Any stress present in the unloaded body is then a result of the incompatible eigenstrain.

When a body contains residual stress, cutting the body along an arbitrary plane will alter the stress. This fact is problematic for many stress measurement techniques, but is exploited by the present method. If we have an ideal cutting process, the eigenstrain in each piece of the original body will not be altered by the process. Sectioning of the body changes the distribution of residual stress, but not that of eigenstrain. By measuring the stress change when the body is sectioned, the eigenstrain can be determined. Further, it need not be assumed that residual stress is entirely relieved by the cutting process in applying this method.

4.1.1 Stress as a function of eigenstrain

Assuming that the material behavior of a body is linear elastic, we seek a relation between the stress present in an unloaded body, $\underset{\sim}{\sigma}$, and the eigenstrain field distributed within the body, $\underset{\sim}{\varepsilon}^*$. Representing this relation in tensor notation, we have:

$$\underset{\sim}{\sigma} = \underset{\sim}{f}(\underset{\sim}{\varepsilon}^*) . \tag{4.1}$$

Note that $\underset{\sim}{\sigma}$ and $\underset{\sim}{\varepsilon}^*$ are second order tensor functions of the spatial coordinates, so that $\underset{\sim}{f}(\bullet)$ is a second order tensor-valued function, also dependent on spatial coordinates. $\underset{\sim}{f}(\bullet)$ represents the set of operations required to solve for stress given a specific distribution of eigenstrain.

Eigenstrain enters the elasticity problem through the constitutive relation for an elastic material

$$\underline{\sigma} = \underline{C} \bullet (\underline{\varepsilon} - \underline{\varepsilon}^*) \ . \tag{4.2}$$

where

$\underline{\sigma}$ = stress
$\underline{\varepsilon}$ = total strain
$\underline{\varepsilon}^*$ = eigenstrain
$(\underline{\varepsilon} - \underline{\varepsilon}^*)$ = elastic strain
$\underline{C}$ = elastic constitutive tensor

To determine stress, the total strain field, $\underline{\varepsilon}$, must be found so that equilibrium is satisfied (i.e., $\nabla \bullet \underline{\sigma} = 0$) in the geometry of interest. In view of Equation 4.2, the function $\underline{f}(\bullet)$ is called the elastic response function of the body due to eigenstrain. The solution of Equation 4.1 can be readily pursued for some specific definition of $\underline{\varepsilon}^*$ by applying the finite element method. Finding $\underline{f}(\bullet)$ in the case of an unknown $\underline{\varepsilon}^*$ is called for here, since we wish to find the eigenstrain which causes $\underline{\sigma}$, requiring inversion of Equation 4.1.

4.1.2 Reduction to a linear system

Several approaches to the inversion of Equation 4.1 might be employed; however, we will proceed as follows. First, a common set of basis functions for $\underline{\sigma}$ and $\underline{\varepsilon}^*$ is adopted. We choose the familiar node points, elements, and linear interpolation functions of finite element analysis (FEA). This is tantamount to assuming that eigenstrain and stress are interpolated linearly within several subspaces (elements) within the space of the problem. Stress will be determined experimentally at the nodes, then eigenstrain components will be defined at these same nodes. Within the elements, each component of eigenstrain is interpolated linearly from the nodal values. As with FEA, the basis functions chosen are not complete, but provide an approximation to $\underline{\varepsilon}^*$ within the space of the problem.

Some cumbersome notation can be avoided if we adopt a vectorization of $\underline{\sigma}$, $\underline{\varepsilon}^*$ and $\underline{f}(\bullet)$. We will therefore assume that at each interpolation node point we have a definition for each component of $\underline{\sigma}$, $\underline{\varepsilon}^*$, and $\underline{f}(\bullet)$. If all these components are assembled in a *specified but arbitrary* order, each may be referred to by only a single index. The assembled vectors of stress, eigenstrain, and elastic response are denoted σ and ε^*, and $\boldsymbol{f}(\bullet)$. In the following then, ε^*_i refers to a specified component of $\underline{\varepsilon}^*$ at a specified node and similarly for σ_i, and $f_i(\bullet)$. Further, N_i refers to a specific interpolation function for each specific component (even though all components are interpolated with the same functions at a given node).

Having chosen a set of basis functions, the spatial variation of each component of eigenstrain, $\varepsilon^*_{ij}(x, y, z)$, can be written as a summation of the product of each nodal value and its corresponding basis function. The basis functions provide the spatial distribution, while the nodal values scale each basis function. The summation is performed over indexes within the vectorized system which correspond to a particular component of eigenstrain. These indexes reflect the arbitrary but specified order in which the components were arranged to arrive at the vectorized representation. The set of indexes within the vector ε^* which correspond to a particular component of eigenstrain, ε^*_{ij}, is denoted E_{ij}. We can then represent the spatial variation of ε^*_{ij} as

$$\varepsilon^*_{ij}(x, y, z) = \sum_{k \in E_{ij}} \varepsilon^*_k N_k(x, y, z) . \tag{4.3}$$

Similarly, we represent the spatial variation of stress and elastic response components as

$$\sigma_{ij}(x, y, z) = \sum_{k \in S_{ij}} \sigma_k N_k(x, y, z)$$

$$f_{ij}(x, y, z) = \sum_{k \in F_{ij}} f_k N_k(x, y, z) .$$

In these equations, S_{ij} and F_{ij} represent the set of indices within the vectors σ and $\boldsymbol{f}(\bullet)$ which correspond to the "*ij*" component of the tensors $\underline{\sigma}$ and $\underline{f}(\bullet)$, respectively.

Since $\boldsymbol{f}(\varepsilon^*)$ can be defined for any arbitrary ε^* with the finite element method, we find it for each $\varepsilon^*_i N_i$ with $\varepsilon^*_i = 1$, and define

$$M_{ij} = f_i\left(\varepsilon^* = \varepsilon^*_j N_j\big|_{\varepsilon^*_j = 1}\right) \tag{4.4}$$

Note that M_{ij} needs to be derived from the equilibrium equations for the geometry of interest. Finally, we can represent Equation 4.1 as

$$\sigma_i = \sum_j M_{ij} \varepsilon^*_j$$

or, using matrix notation

$$\sigma = \boldsymbol{M} \bullet \varepsilon^* . \tag{4.5}$$

Here, we have used the fact that each solution $\boldsymbol{f}(\bullet)$ is itself in equilibrium. Therefore, any linear combination of such solutions will also be in equilibrium according to the principle of superposition.

Now, the complex problem presented by the inversion of Equation 4.1 is reduced to inversion of the linear system represented by Equation 4.5. The matrix **M** can be interpreted as having columns which represent the stress caused when a single eigenstrain degree of freedom (DOF) is equal to unity. Each DOF represents a particular component of $\underset{\sim}{\varepsilon}^*$ at a particular nodal position. Filling the columns of **M** for all degrees of freedom, ε^*_j, is clearly a job for the computer, and can be accomplished by a general purpose finite element code.

Since we will use the finite element method, which will have its own associated mesh, we will refer to the mesh used to interpolate eigenstrain as the background mesh (BGM). We use the term background mesh to avoid confusion with the actual FEA mesh used in the computations. Linear displacement elements are employed in the FEA calculation so that only a constant strain field can be represented exactly within each element. Since the BGM imposes a linear strain field, at least two linear displacement elements need to be used within each background element. For our purposes, the FEA mesh and the BGM will never be the same.

Formation of the matrix **M**, is relatively straight forward using the finite element method. Since all eigenstrain DOFs are imposed on the same mesh, assembly and factorization of the global stiffness matrix is done only once. Each DOF is then handled as a separate load case in the linear analysis. Post-processing is done to represent **M** in a way that can be imported into a matrix analysis package (e.g., MATLAB) to solve Equation 4.5.

If the values of σ_i can be determined experimentally, and if **M** is formed from repetitive calculation and assembly, it is possible to solve Equation 4.5 for the values of ε^*_j. This can be accomplished if the number of stress components is equal to or greater than the number of unknown eigenstrain components, and if **M** is non-singular. If there are more experimentally determined stresses than unknown eigenstrains, a least-squares approach can be used to solve the system with minimized error. Singularities in **M** arise if there is some eigenstrain field which produces no stress; such an eigenstrain field will satisfy the compatibility relations of elasticity.

The eigenstrain method is married to the finite element method in that only certain stress and strain fields can be represented exactly, and therefore singular modes in Equation 4.5 can be identified and removed. As illustrated by H. Reissner (1931), there are infinitely many possible strain fields which satisfy the compatibility relations. Each of these fields will result in zero stress, and therefore cause a singularity in Equation 4.1. However, only certain of these will cause zero stress in the finite-element-approximated system described by Equation 4.5. By considering the type of finite elements used and the type of interpolation used for eigenstrain, such singular modes can be identified and removed.

Modes which should cause zero stress, but which do not do so because of the inexact nature of the FEA approximation, will make the linear system (Equation 4.5) ill-conditioned, but not singular. Ill-conditioning occurs when the ratio of smallest to largest eigenvalue of the matrix **M** is much smaller than unity. When **M** is ill-conditioned, the solution for eigenstrain will include some eigenstrain field which causes only small stress at points of the BGM. Since our interest is mainly in reproducing residual stress, and not in the absolute form of eigenstrain, such low order modes present in Equation 4.5 are not of concern. If the eigenstrain field is important, it is possible to use the *pseudo-inverse* to solve Equation 4.5 and specifically eliminate lower-order eigenmodes (Albert, 1972). It is interesting to note that refinement of the FEA mesh used in the solution for eigenstrain improves the quality of any stress solution, and so serves to further ill-condition the system.

Restricting ourselves for the time being to plane-stress elasticity, we can investigate the form of zero-stress modes for the implementation of the eigenstrain method described above. We have assumed linear strain interpolation and linear displacement finite elements. The compatibility condition for plane stress is:

$$\frac{\partial^2 \varepsilon_{xx}}{\partial y^2} + \frac{\partial^2 \varepsilon_{yy}}{\partial x^2} = \frac{\partial^2 \varepsilon_{xy}}{\partial x \partial y} \tag{4.6}$$

(Note: Engineering shear strain is assumed throughout this chapter.) Any eigenstrain field which satisfies this relation will create stress-free deformation. Constant and linear functions of any of the strain components will satisfy Equation 4.6. For example, the following strain fields will satisfy Equation 4.6 and therefore give rise to stress free deformation in an unrestrained body in plane stress:

$$\varepsilon_{11} = yf_1(x) + g_1(x) + c_1 \tag{4.7}$$

$$\varepsilon_{22} = xf_2(y) + g_2(y) + c_2 \tag{4.8}$$

$$\varepsilon_{12} = f_3(x) + g_3(y) + c_3 \tag{4.9}$$

where, $f_i(\bullet)$ and $g_i(\bullet)$ are arbitrary functions, and c_i are arbitrary constants. These three fields are the only ones which can exactly produce zero stress in our implementation of the eigenstrain method. They can be suppressed by setting certain eigenstrain degrees of freedom to be zero in the system. Suppression of modes contained in Equation 4.7 can be accomplished by setting nodal values of ε^*_{11} to be zero along two lines of y = constant within the background mesh. Similarly, modes contained in Equation 4.8 can be suppressed by setting nodal values of ε^*_{22} to be zero along two lines of x = constant within the BGM. Finally, modes contained in Equation 4.9 can be suppressed by setting ε^*_{12} to be zero along one line of y = constant and along one line of x = constant.

Eigenstrain can be found by measuring residual stress in a body, as just described, or by measuring stress *changes* that occur as a result of sectioning. When a body is sectioned into another geometry, a change in stress occurs which is due both to the change in geometry and the change in eigenstrain within the sectioned body. If we assume that the sectioning process causes no inelastic deformation, the change in eigenstrain is zero. Under the condition of elastic stress release, the change in stress is dictated by the change in geometry which is completely determined by the change in elastic response function. Since an eigenstrain system, **M**, can be formed for any geometry, it can be formed for the configuration before and after sectioning. If we denote these configurations (1) and (2), eigenstrain can be found by solving the system

$$[\sigma^{(1)} - \sigma^{(2)}] = [\boldsymbol{M}^{(1)} - \boldsymbol{M}^{(2)}] \bullet \varepsilon^* . \tag{4.10}$$

The left side of Equation 4.10 is the difference in stress between configurations (1) and (2): the stress change resulting from the elastic sectioning process. The eigenstrain within the body can be found by inverting Equation 4.10 if the system is non-singular. Finally, this eigenstrain field is used to find residual stress which existed prior to sectioning by imposing it in a finite element model of the original configuration.

4.1.3 Application of the eigenstrain method to a long welded joint

Of particular interest here is the determination of through-thickness residual stress in a large multi-pass steel weld. If the joint is long and is welded continuously, several assumptions can be made about the distribution of eigenstrain in the welded joint (Ueda, 1989). As mentioned before, eigenstrain will only exist in a region close to the weldline. If welding is performed in a continuous fashion, each plane of material transverse to the weldline undergoes nearly the same thermal history. In other words, the thermal history experienced by an element of material during this type of welding is independent of the position along the weld. Eigenstrain resulting from welding is a combination of thermal and plastic strain. Thermal strains result from heating and cooling, and plastic strains result when the material surrounding the weld bead restrains thermal straining. If the plate is restrained equally along its length, then the process of welding gives rise to eigenstrain which is independent of position along the weld line. It also can be assumed that residual stress in continuous welds is symmetric about the transverse weld direction at the middle of the weld length. This allows elimination of shear components of eigenstrain involving the welding direction (e.g., if the weldline corresponds to the z–direction, $\varepsilon^*_{13} = \varepsilon^*_{23} = 0$), as they would cause asymmetrical stresses to arise.

An illustration of Ueda’s technique for a welded joint is shown in Figure 4.1 (Ueda, 1985). A sample of a welded plate is obtained from the structure of interest and an array of strain gages is attached to one of the sample’s longitudinal faces (shown shaded in the figure). Two strain-relaxation measurements are then performed, one from block to thin slice and the other from slice to small pieces (dice), each containing a strain gage. If the dice are small enough they will contain no stress, and the strain change from slice to dice is sufficient to determine residual stress in the slice. Residual stress which existed on the surface of the block prior to sectioning can then be found from stress in the slice and measured strain change from block to slice. Residual stress in the slice allows determination of the eigenstrain components in the transverse-perpendicular plane. Using these results with the block residual stress measurements allows determination of the eigenstrain component associated with the longitudinal direction. The cross-sectional and longitudinal eigenstrain can then be used to find residual stress in the entire welded block. The details of this procedure are described in the following sections.

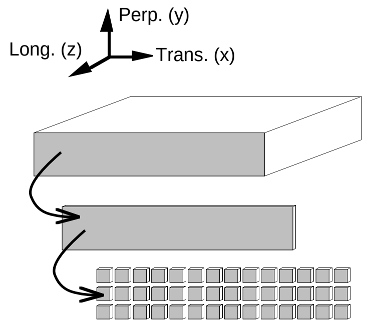

Figure 4.1 – Schematic of the slice-and-dice method proposed by Ueda (1985).

4.2 Model problem to examine the method

The method proposed by Ueda for finding residual stress in a welded plate appears promising. However, there have been no experiments discussed in the literature which validate the technique relative to a known residual stress state. The following discussion describes a *simulation* of the eigenstrain method which provides both a detailed example of the method and examines its accuracy. To simulate the method, functional forms of each eigenstrain component are assumed. The finite element method is then used to determine (to a high degree of accuracy) the residual stress distribution caused by this eigenstrain distribution at all points in both the block and slice geometries. The eigenstrain method is then applied to find an approximate eigenstrain field given the residual stress on the free-surface of the block and slice (determined by FEA). Stress in the block caused by this approximate eigenstrain field is then compared to the results of the finite element analysis deep within the plate where no measurements were made. Comparison of these two sets of stress results allows conclusions to be drawn regarding the accuracy of the technique.

4.2.1 Definition of geometry and assumed eigenstrain distribution

The body in which eigenstrain is distributed is shown in Figure 4.2. This represents a block of material removed from a long welded joint, where the weld runs in the *z*-direction (the coordinate system referred to throughout this chapter is shown in Figure 4.2). It is assumed that the elastic properties of the material are uniform and given by E = 30×10^6 psi and ν = 0.292. Eigenstrain is imposed within the shaded area of the block only. The eigenstrain is dependent on the *x* and *y* coordinates and is independent of *z*, following assumptions about continuous welding.

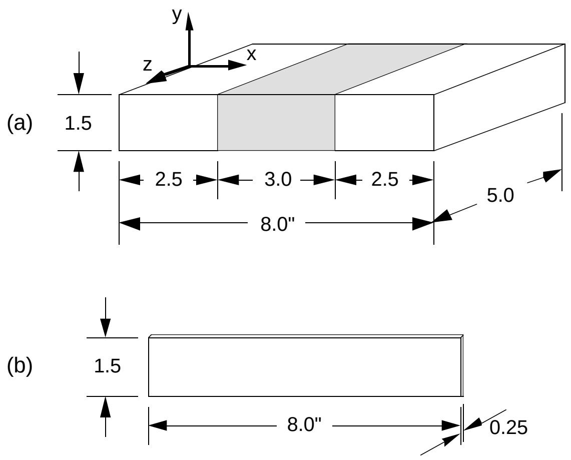

Figure 4.2 – (a) Block and (b) slice removed from the end of the block. (Dimensions in inches).

Several qualities of the mathematical form assumed for the eigenstrain were desirable. First, the functions were to be spatially continuous and smooth. Since plastic strains due to welding of thick plates have been shown to exist only within two thicknesses of the weldline in the *x*-direction (Ueda, 1989), functions should be zero outside that region. Also, we wanted these functions to represent a case of deformational symmetry about the *x* and *y* center-planes of the body. (Accordingly, the shear strains are asymmetric while the normal strain components are symmetric.) This means that

$$\begin{aligned} \varepsilon^*_{ij}(x',y') &= \varepsilon^*_{ij}(-x',y') && (i=j) \\ \varepsilon^*_{ij}(x',y') &= \varepsilon^*_{ij}(x',-y') && (i=j) \\ \varepsilon^*_{ij}(x',y') &= -\varepsilon^*_{ij}(-x',y') && (i\neq j) \\ \varepsilon^*_{ij}(x',y') &= -\varepsilon^*_{ij}(x',-y') && (i\neq j) \qquad (4.11) \end{aligned}$$

where i, j = 1, 2, or 3

and where x' and y' are “central” coordinates: $\begin{cases} x' = x - 4 \\ y' = y + 0.75 \end{cases}$.

Other than these considerations, the choice of functions used to represent the eigenstrain was arbitrary. Mathematical forms chosen for the eigenstrain components in this illustrative example are:

$$\begin{aligned} &\varepsilon^*_{11} = \varepsilon^*_{22} = \varepsilon^*_{33} = 0.001 * f(x) * g(y) \\ &\varepsilon^*_{12} = 0.001 * u(x) * v(y) \\ &\varepsilon^*_{13} = \varepsilon^*_{23} = 0 \qquad (4.12) \end{aligned}$$

where, for $x \in [2.5, 5.5]$

$$f(x) = 0.5\left[\cos\left(2\pi\frac{x-2.5}{3.0}\right) - 1\right]$$

$$u(x) = 1.73\left(1 - \left|\frac{x-4}{1.5}\right|\right)\sin\left(\pi\frac{x-4}{1.5}\right)$$

$$g(y) = 0.5\left[1 + \cos\left(2\pi\frac{y}{1.5}\right)\right]$$

$$v(y) = \cos\left(\pi\frac{y}{1.5}\right)$$

and, for $x \notin [2.5,5.5]$

$$f = g = u = v = 0.$$

These functions are shown graphically in Figure 4.3. (In these plots, and those in the remainder of the chapter, linear dimensions are given in inches but are not specifically labeled as such.)

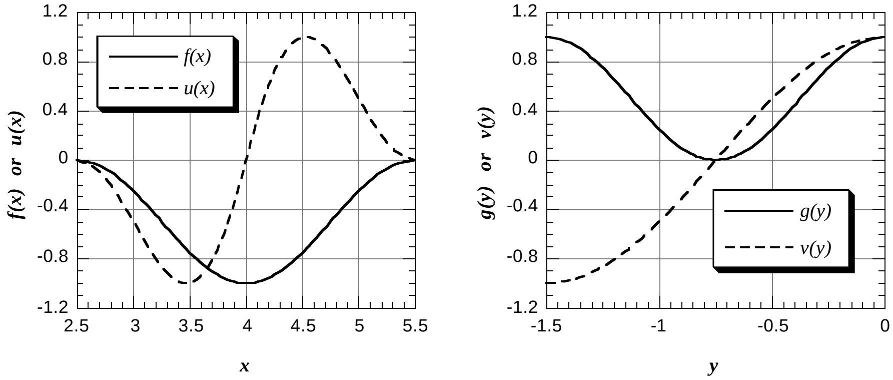

Figure 4.3 – Functions used to define a distribution of eigenstrain.

4.2.2 FEA solution to the model problem

The finite element method is employed to find the residual stress caused by the eigenstrain field represented by Equation 4.12 within the body shown in Figure 4.2. A general purpose elastic finite element code was used, and eigenstrain was imposed by thermal analysis. Recalling that thermal strain is a subset of eigenstrain, the thermal strain capabilities in most finite element codes can be exploited to impose eigenstrain on a finite element model. For a general eigenstrain field, anisotropic thermal expansion coefficients must be defined in the model as a function of position. At a given point in the model, each component of the thermal expansion tensor is set equal to its corresponding eigenstrain component (e.g., $\alpha_{11} = \varepsilon^*_{11}$). Mathematically, the eigenstrain field is then given as

$$\underline{\varepsilon}^* = \underline{\alpha}\Delta T \tag{4.13}$$

where $\underline{\alpha}$ is the second order anisotropic thermal expansion tensor and ΔT is a temperature change. Residual stresses are obtained by specifying a unit temperature change and allowing the finite element solver to find the equilibrium solution for total strain.

Sample distributions of the residual stress field resulting when the eigenstrain is imposed in the block geometry of Figure 4.2 are shown in Figure 4.4 and Figure 4.5.

Stresses found by FEA on the free-surface of the block will be used in lieu of experimental measurements when demonstrating the eigenstrain method in Section 4.3, and so will be referred to as the “experimental stress”.

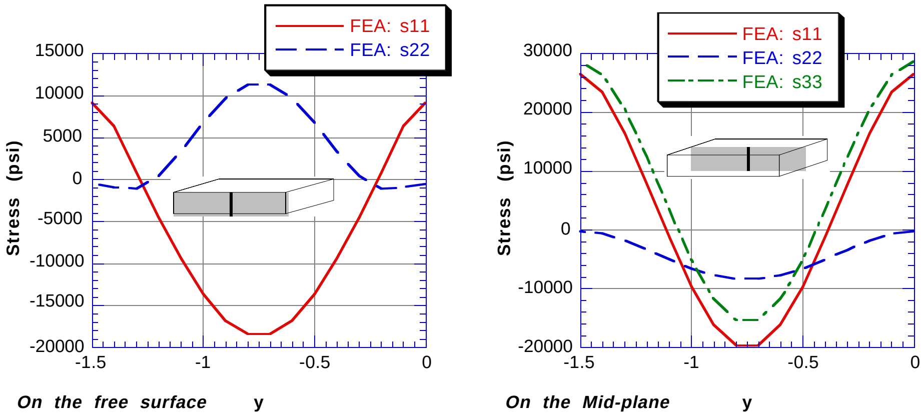

Figure 4.4 – Stress in the block resulting from eigenstrain on the line x = 4.0 on the free surface, $z = z_{max}$, and the mid-plane of z symmetry, z = 0.

The 3D finite element mesh used in the “experimental” solution was more refined than the one used in execution of the eigenstrain method, described in Section 4.3. This is important in that any numerical advantage given to the eigenstrain method is minimized, so the eigenstrain method will truly approximate the more exact experimental solution. The eigenstrain method, as described in this chapter, is subject to discretization error from two sources. First, the true eigenstrain function is approximated by linear interpolation between points of the background mesh. Secondly, the stresses found are an FEA approximation of the “true” stress solution to the approximated eigenstrain field. By having both an eigenstrain field and an experimental stress field which cannot be represented exactly on the mesh used in execution of the method, we are more likely to examine all the potential errors in the eigenstrain method. We therefore designed more refinement into the FEA mesh used to find the experimental solution so that the method could be fully tested.

Eigenstrain was imposed in both the block and slice geometry shown in Figure 4.2 using the same mesh layout. The depth of the block is 5.0" and the depth of the slice is 0.25". One mesh was generated for the block geometry, and then the mesh was scaled in

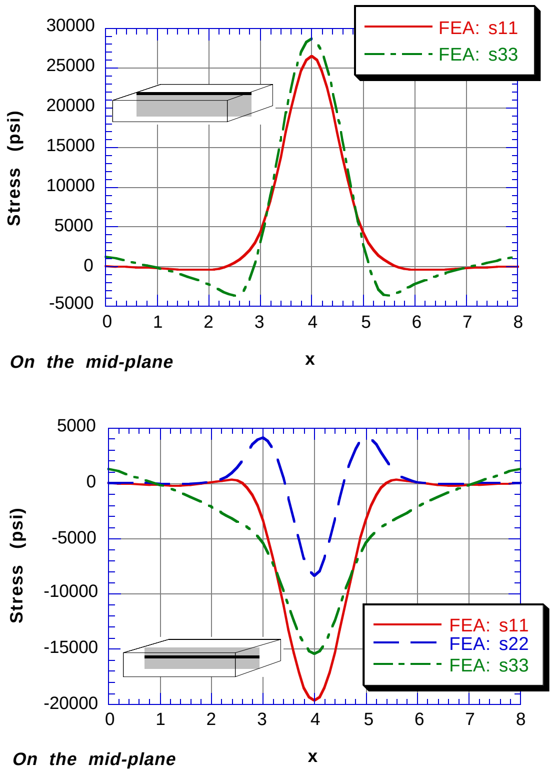

Figure 4.5 – Stress in the block resulting from eigenstrain on the mid-plane, z=0, on the lines y = 0 and y=-0.75.

the *z*-direction to obtain a mesh for the slice. Accordingly, the nodal layout in the *x*-*y* plane for both meshes is identical. Some of the nodes on this mesh were coincident in the *x*-*y* plane with nodes of the BGM so that experimental stress vectors could be assembled. Experimental stress vectors were assembled from free-surface stress to give results on both the block, σ_b, and on the slice, σ_s.

4.3 Solution for eigenstrain

The following method for finding eigenstrain in a continuously welded plate was presented by Ueda (1985), and introduced in Section 3.1.4 of this thesis. Two measurements of stress will be performed on this object, corresponding to what would be done in actual experiments. At each point where stress is determined, it is assumed that all three components of surface stress are estimated, σ_{11}, σ_{22}, and σ_{12}. First, the difference in stress on the surface $z = z_{max}$ will be measured when a slice of material is cut from the block, as shown in Figure 4.1. To physically perform this measurement, three element strain gage rosettes would be attached to the free surface $z = z_{max}$ of the block at nodal points in the eigenstrain interpolation mesh. Strain released by removing the slice would be measured. The stress change due to cutting, $\Delta\sigma_s$, would then be calculated from the strain changes and plane stress elastic constitutive relations,

$$\begin{bmatrix} \Delta\sigma_{11} \\ \Delta\sigma_{22} \\ \Delta\sigma_{12} \end{bmatrix} = \frac{E}{(1-\nu^2)} \begin{bmatrix} 1 & \nu & 0 \\ \nu & 1 & 0 \\ 0 & 0 & \frac{1-\nu}{2} \end{bmatrix} \begin{bmatrix} \Delta\varepsilon_{11} \\ \Delta\varepsilon_{22} \\ \Delta\varepsilon_{12} \end{bmatrix} . \tag{4.14}$$

Secondly, the stress change will be recorded when the slice is cut into small pieces. The pieces, if small enough, will have no stress in them at all. Thus, the stress change between the slice and the small pieces will be the negative of the total stress in the slice, σ_s. Now that the stress which existed in the slice is known, the stress which existed on the block free surface may be estimated from

$$\sigma_b = \sigma_s - \Delta\sigma_s \tag{4.15}$$

Two quantities have now been estimated: the stress on the free surface of the block, σ_b, and the stress in the slice σ_s. The above procedure is called slice-and-dice.

Since this is a numerical experiment, we will use the stress solutions for σ_b and σ_s obtained using FEA and described in Section 4.2.2 to *simulate* the application of the eigenstrain method.

Ueda (1985) assumes that if the slice is cut thinly enough, stress caused by the eigenstrain component normal to the slice will be zero. If this is indeed the case, the problem is reduced to one of plane stress, greatly reducing the complexity of the problem, and the computational burden in formulating **M**. This also de-couples the components within the plane (ε^*_{11}, ε^*_{22} and ε^*_{12}) from that out of the plane (ε^*_{33}). These two sets of eigenstrain components are respectively referred to as the cross-sectional eigenstrain and the longitudinal eigenstrain by Ueda. The next two sections describe how the eigenstrain method is used to determine the longitudinal and cross-sectional eigenstrain.

4.3.1 Finding cross-sectional eigenstrain

Making the assumption that a thin slice can be modeled in plane stress, a 2D finite element mesh is constructed based on the slice geometry shown in Figure 4.2. With the background mesh defined by a strain gage layout, degrees of freedom for **M** are also defined. At each point in the BGM on the slice, we have a degree of freedom for ε^*_{11}, ε^*_{22} and ε^*_{12}. Some degrees of freedom, however, need to be eliminated to suppress singularities in **M**. Once the system **M** is formed, as outlined in Section 4.1.2, the stress on the surface of the slice σ_s is used to solve Equation 4.5 for the cross sectional eigenstrain, ε^*_c, at the nodes of the BGM.

To solve the model problem, the BGM assumed is rectangular, with nodal spacing $\Delta x = 0.4"$ and $\Delta y = 0.25"$, as shown schematically in Figure 4.6. The mesh points fall within $x \in [0.2,7.8]$ and $y \in [0,-1.5]$, yielding 140 background nodes (7 in the y-direction by 20 in the x-direction). Note that all elements of the BGM are the same size, except for elements at the ends, where $\Delta x = 0.2"$ instead of 0.4". The finite element mesh used to construct **M**, also shown in Figure 4.6, had four elements for each element of the BGM, except on the ends. All finite elements were the same size, $\Delta x = 0.2"$ and $\Delta y = 0.125"$.

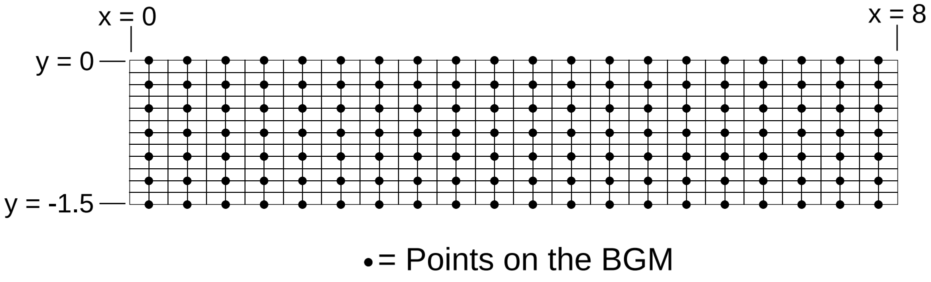

Figure 4.6 – Background mesh and finite element mesh used in solving the model problem for the cross-sectional eigenstrain.

To remove singular modes represented by Equation 4.7, ε^*_{11} is taken to be zero at all nodes on $y = 0.0$ and $y = -1.5"$. There are no nodes on $x = 0$ and $x = 8.0$ so modes represented by Equation 4.8 are already suppressed. Modes represented by Equation 4.9 are suppressed by setting $\varepsilon^*_{12} = 0$ for all nodes on y=0. The background mesh contains 140 nodes, but instead of 420 DOFs, we have only 360 non-zero components (i.e., we have suppressed 60 DOFs). Therefore, the dimension of **M** is 420 by 360, and least squares is used to solve for the eigenstrain.

4.3.2 Finding longitudinal eigenstrain

Now that ε^*_c has been estimated on the BGM, these eigenstrain components are defined within the block geometry on a 3D FEA mesh, and the equilibrium solution obtained from a thermal analysis. The stress on the free surface $z = z_{max}$ is collected at the points of the BGM. This is the stress in the block resulting only from the estimate of cross-sectional components of eigenstrain, denoted $\sigma_b{}^c$. Now, we construct the difference between σ_b, defined in Equation 4.15, and $\sigma_b{}^c$ at each point in the BGM

$$\Delta\sigma_b = \sigma_b - \sigma_b{}^c. \qquad (4.16)$$

The stress defined in Equation 4.16, $\Delta\sigma_b$, is the stress due to the absent longitudinal eigenstrain component, ε^*_{33}. So, a new system **M** is assembled relating ε^*_{33} to stress on the free surface of the block, and the system solved for ε^*_{33} given $\Delta\sigma_b$.

The 3D FEA mesh used to find $\sigma_b{}^c$ and to form **M** has the same layout in the x-y plane as the planar mesh used to find ε^*_c, as shown in Figure 4.7. The layout in the thickness direction consists of five elements. The nodes are spaced in the z-direction in geometric progression such that the ratio of the thickness of the last element to the first is 10:1.

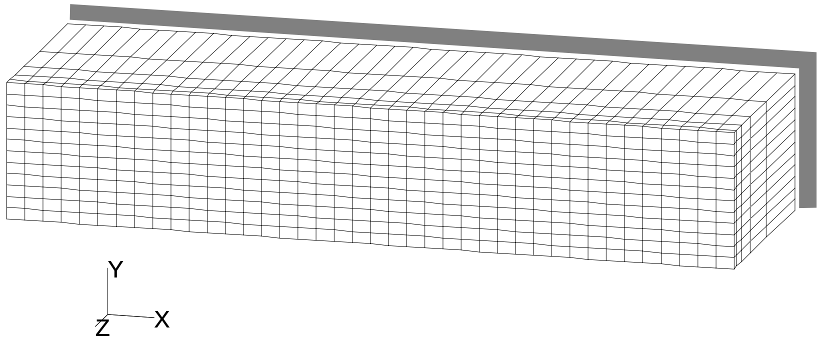

Figure 4.7 – Finite element mesh used to determine the longitudinal eigenstrain. (The shaded plane represents a plane of deformational symmetry.)

4.3.3 Results of the eigenstrain method

Executing the eigenstrain method, as described in Section 4.3.1 and Section 4.3.2, and imposing the resulting approximated eigenstrain distribution onto the 3D FEA mesh for the block shown in Figure 4.7 gives the approximate distribution of residual stress at all points in the block. Scaling this same mesh in the z-direction and imposing the approximate eigenstrain gives results for the slice. Note that all components of eigenstrain were imposed in the slice geometry, even though we assumed that ε^*_{33} would cause no stress in the slice in our application of the eigenstrain method. We can now compare the results of the eigenstrain method with the FEA predicted stress described in Section 4.2.2 which will be referred to as the “exact” solution.

Results for the residual stress in the slice are shown in Figure 4.8 and Figure 4.9. In the figures, the eigenstrain solution is denoted “IE” and the exact solution “FEA”. Agreement between the estimated and exact values of stress is apparent. The error in the approximation on the line x=3.8 is shown in Figure 4.10. In this section, “error” refers to the difference between finite element results and estimates provided by the eigenstrain method. As might be expected, errors are largest at nodes not coincident with the background mesh. (Nodes coincident with the background mesh are shown with symbols in the figure.) Among values at points on the background mesh, errors are less than 1.5 ksi, or 8% of the maximum measured stress. It should be noted that errors on the line x=4.0 are somewhat larger that those on x=3.8, since background mesh points do not fall on x=4.0.

Results for residual stress in the block are shown in Figure 4.11, Figure 4.12 and Figure 4.13. Stress results on the free surface, where stress measurements were taken, show agreement which is not quite as good as for the slice. Maximum error in the stresses found by the eigenstrain method is 17% of the maximum measured stress on the free surface, and occurs at x = 3.8, y = -0.75. Mid-plane results show more absolute error, especially in the longitudinal stress, σ_{33}. However, maximum percent error is still about 17% of the maximum stress for this component. Since the longitudinal stress was never measured and no stress measurements were done in the vicinity of the block mid-plane, that there is any sort of agreement at all may still be somewhat surprising.

The errors present in the block stress are higher than one would like, especially in the longitudinal stress at the block mid-plane. A likely explanation for larger errors in the

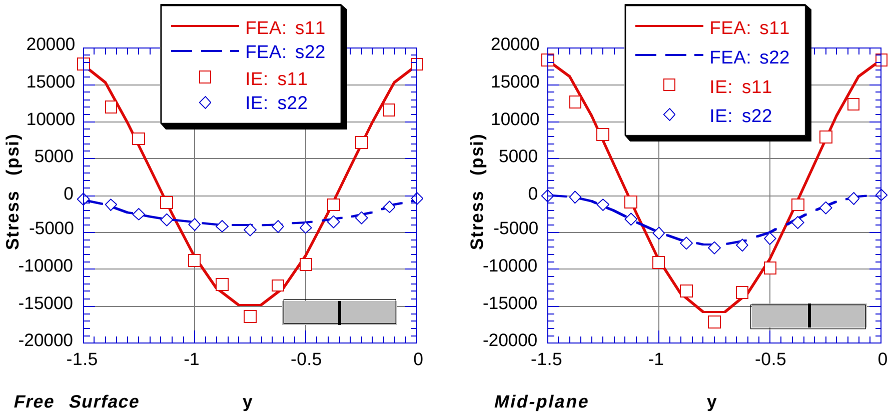

Figure 4.8 – Exact (FEA) and approximate (IE) stress in the slice on line x=3.8 on the free surface, $z = z_{max}$, and the mid-plane, z = 0.

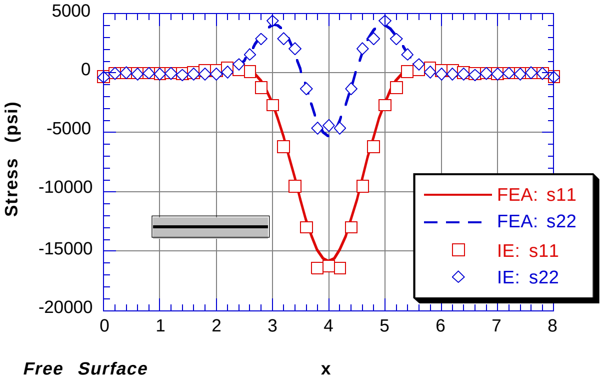

Figure 4.9 – Exact (FEA) and approximate (IE) stress in the slice on the line y = -0.75 on the free surface, z = 0.

longitudinal stress might be that the approximation of the cross-sectional eigenstrain is used to predict the longitudinal eigenstrain. So, errors in the cross-sectional eigenstrain propagate into the prediction of longitudinal eigenstrain, causing larger errors in estimated longitudinal stress. Perhaps use of the eigenstrain prediction of slice stress to find σ_b in Equation 4.15 would lessen this error, but that has not been investigated. Another explanation might be that the longitudinal eigenstrain actually causes stress in the slice, and the cross-sectional and longitudinal components cannot be uncoupled without errors.

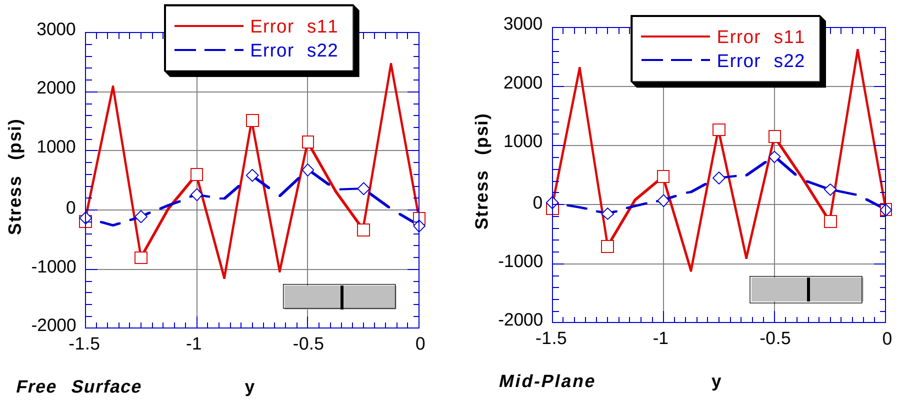

Figure 4.10 – Error in approximation of stress shown in Figure 4.8. Points with symbols (▫ and ◇) represent points on the background mesh.

Figure 4.14 shows the stress produced on the free surface of the slice when only the approximate longitudinal eigenstrain is imposed. Values here are as much as 10% of the stresses present in the slice shown in Figure 4.8.

4.4 Discussion

The method proposed by Ueda (1985) to measure three-dimensional residual stress using a hybrid experimental-analytical approach has been shown to provide reasonable predictions of residual stress for the model problem considered here. However, noticeable errors are present in results of the method, the source of which could be more thoroughly investigated. Coupling of longitudinal and cross-sectional eigenstrains could be investigated by modeling the slice as three-dimensional. The use of other basis functions could also be studied, perhaps finding a set which excludes singular modes of eigenstrain. Also, the type and number of finite elements used to solve the eigenstrain problem could be optimized. Despite these shortcomings, this approach holds promise and provides reasonably accurate results when its use is simulated numerically.

More importantly, this is one of the few methods available for finding subsurface three-dimensional residual stresses. The method proposed previously by Norton and Rosenthal (1945) could have also been used to find residual stress deep within the welded

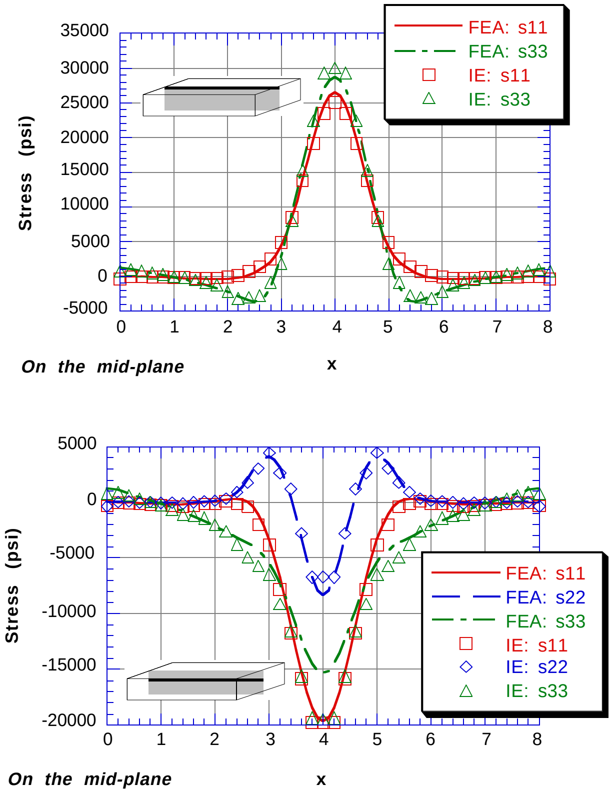

Figure 4.11 – Exact (FEA) and approximate (IE) stress in the block on the mid-plane, z=0, on the lines y = 0 and y=-0.75.

plate. This method unfortunately makes use of an erroneous assumption, as shown in detail in Chapter 3. Ueda's method provides a way to bypass the overly simplified assumptions of Norton and Rosenthal in solving for residual stress.

The eigenstrain method is attractive in that it provides a whole field approach to the prediction of residual stress. Most methods of residual stress estimation described in Section 1.4.2 provide results on a single plane or at a single point within a component. Such information is useful for fatigue and linearly elastic fracture mechanics analyses. However, if elastic-plastic fracture analysis is to be pursued, having stress on a single plane does not allow for generalized redistribution of residual stress caused by plasticity. Such redistribution could only be studied if the entire residual stress field were known.

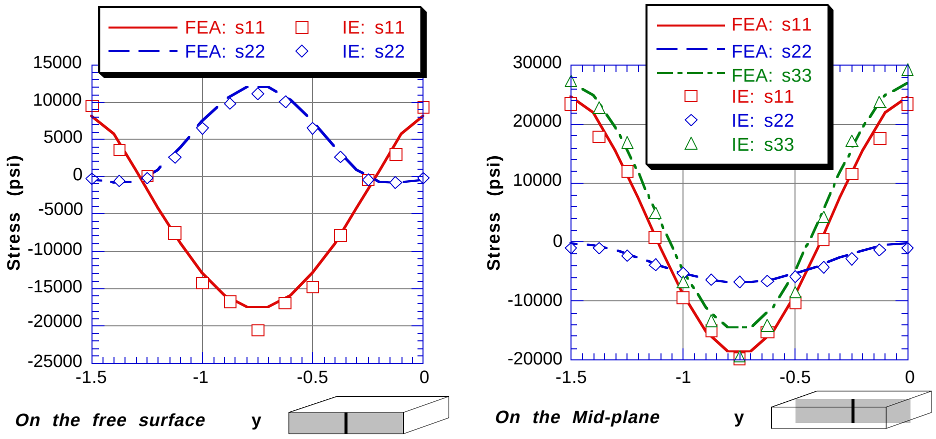

Figure 4.12 – Exact (FEA) and approximate (IE) stress in the block on the line x = 3.8 on the free surface, z = 0, and mid-plane, z = z_{max}.

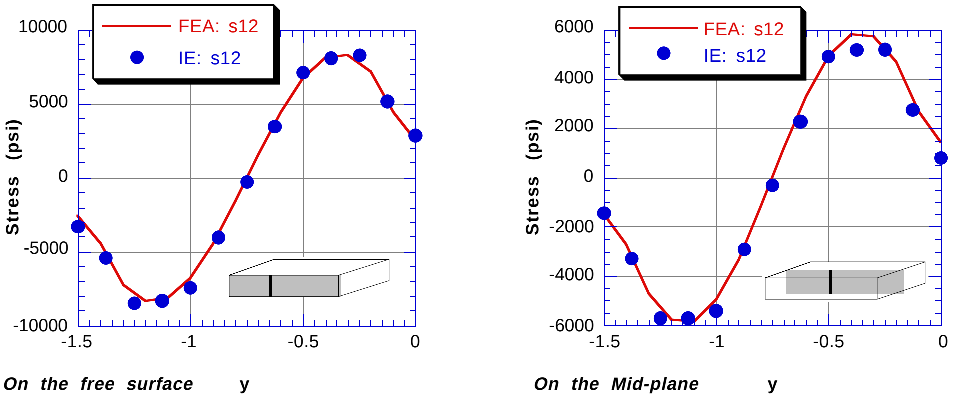

Figure 4.13 – Exact (FEA) and approximate (IE) shear stress in the block on the line x = 3.4.on the free surface, z = 0, and mid-plane, z = z_{max}.

Use of the eigenstrain method would provide information necessary to perform an elastic-plastic fracture assessment including residual stress relaxation due to plastic flow.

Considering that an eigenstrain field is the outcome of many mechanical operations, finding eigenstrain provides a way to characterize manufacturing processes. Manufacturing processes such as grinding, shot-peening, welding, and induction hardening have been characterized to a large degree by the residual stresses they produce.

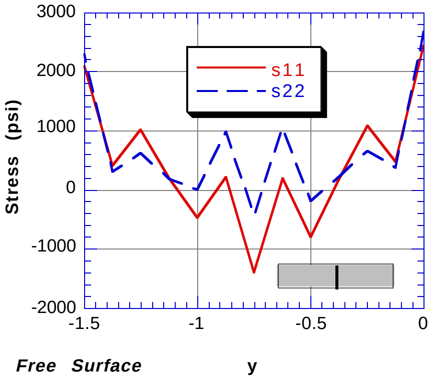

Figure 4.14 – Stress on the free surface of the slice due only to longitudinal eigenstrain on the line x=3.8.

But, since residual stress depends on the geometry of the part, eigenstrain may provide a better basis for comparison of similar processes.

Although solution for the distribution of residual stress at all points within a body is an attractive feature of the eigenstrain method, it also mandates the need for a large amount of experimental measurements. (In the solution to the model problem, 140 three-element strain rosettes would have been employed, each being measured three times.) If residual stress is needed only within a small region of interest within the body, it would be interesting to investigate if this method could be localized, thereby reducing the number of experimental measurements required for stress prediction. Such an approach could provide the benefits of the method which were just described, while not requiring as much experimental effort. The localization of the eigenstrain method is discussed in Chapter 7.

Further, the eigenstrain method is attractive because it implicitly includes the ability to find residual stress in the defective welds. In this method, the link between measured stress change due to sectioning and the eigenstrain field is made through elastic finite element modeling. Since no assumptions are made regarding the actual shape of the welded plate, any prismatic geometry could be modeled without alteration of the overall approach. The simulated lack of fusion weld defects described in Chapter 2 lie along the entire length of the weld. Accordingly, the influence of the defect should be independent of longitudinal position. In principle, then, one merely needs to include the defect in the finite element model and proceed as normal. No other method of residual stress determination lends itself so readily to finding residual stress in defective welds like those discussed in Chapter 2.

Chapter 5

Implementation of the Eigenstrain Method

In this chapter we describe experiments conducted to implement the eigenstrain method discussed at length in the preceding chapter. These experiments were actually performed before the numerical investigation described in the previous chapter. Further, the failure of this set of experiments mandated the need for further study of both the experimental and analytical aspects of the eigenstrain method. In some respects, then, this chapter properly belongs ahead of the previous one. However, the familiarity with the method gained by perusal of the foregoing chapter will allow us a better vantage point from which to describe the shortcomings of these experiments.

5.1 Description of the experiments

Several details of the implementation pursued here are different from those described in Chapter 4, although the basic procedure is the same. A block was removed from the non-defective welded joint described in Chapter 2 and similar to the defective joint shown in Figure 2.6. Since this was our first implementation of the eigenstrain method, we sought to simplify the experimental work. Significantly fewer measurement points were used than were in the numerical experiment described in the last chapter. Whereas the numerical investigation assumed 140 rosettes would be used, we employed 23 rosettes for measuring stress released by slicing and 35 for determination of stress in the slice. The procedure used to estimate stress in the slice also differed from that described in the previous chapter. Instead of the dicing procedure, hole-drilling residual stress determination was employed after the slice had been removed from the block. An additional 10 rosettes were used to measure surface residual stress on the mid-plane of the block, after the slice was removed. The layout of points where residual stress was determined is shown in Figure 5.1.

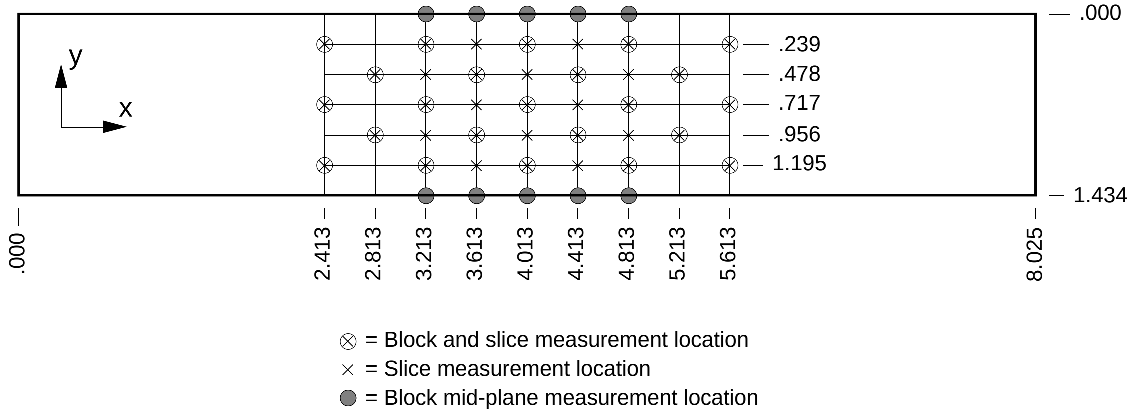
.000
.239
.478
.717
.956
1.195
1.434
y
x
.000
2.413
2.813
3.213
3.613
4.013
4.413
4.813
5.213
5.613
8.025
⊗ = Block and slice measurement location
× = Slice measurement location
● = Block mid-plane measurement location

Figure 5.1 – Layout of points where residual stress was determined for input into the eigenstrain method for residual stress determination.

5.2 Choice of surface stress measurement method

Residual stress in the slice, σ_s, was determined using the hole-drilling strain gage method. A primary reason for selecting this method was the significant experience NASA collaborators have with it. This method for residual stress determination has been established for some time, and was briefly described in Section 1.4.1.1. Determination of residual stress which is uniform with hole depth is an accepted standard, detailed in ASTM Standard E 837. For determination of residual stresses which have a variation with depth measured from the surface, an extension of the hole-drilling method can be used, the Integral Method proposed by Schajer (1988a and 1988b). This method was applied by Hampton (1989) to determine residual stresses in thin welded plates. Hampton, in fact, prepared a computer program to analyze hole-drilling data which implements the Integral Method (Hampton, 1991). This program was used to find the variation of residual stress with depth in the slice removed from the block, which was in turn removed from the welded joint of interest.

5.3 Measurement of block to slice stress release

To measure block to slice stress release, $\Delta\sigma_s$, twenty-three hole-drilling strain gage rosettes were laid out on the free surface of the block. The layout of measurement locations on the transverse-perpendicular free surface of the block is shown in Figure 5.1. Strain gage rosettes laid on the block are indicated by the symbol “ ⊗ ” in the figure. These gages were then covered with a moisture proof enclosure to protect them from cutting fluids and a slice removed from the end of the block. The block measured 8.025x1.434x5.0", and the slice measured 8.025x1.434x0.25". The strain gage rosettes were measured before and after slicing relative to a stable strain gage so that the strain released by cutting was known at each of the 23 rosette locations. The “stress released” by slicing is obtained by subtracting the strain gage readings on the block from the readings on the slice and using plane stress isotropic stress-strain relations (Equation 4.14). Stress released when the slice was cut from the block at each of the 23 rosettes is shown in the left half of Figures 5.2 through 5.4. For comparison, stress released in the numerical experiment of Chapter 4 is also plotted in Figures 5.2 through 5.4.

The similarity in shape between the measured data and that resulting from the numerical experiment in encouraging. In developing the test eigenstrain field used in the numerical experiment, we sought to produce a stress field representative of weld residual stress. Therefore, the plots shown in the right side of Figures 5.2 through 5.4 indicate *qualitatively* what we would expect to find in the block to slice stress release experiment. The measured data are, in fact, reasonably similar in form, although their magnitude is quite different. More importantly, the spatial variation of released stress is approximately the same as expected from the numerical modeling.

5.4 Measurement of stress in the slice

Following the cutting operation, hole-drilling was performed to determine the residual stress remaining in the slice. This was done at the twenty-three locations where gages

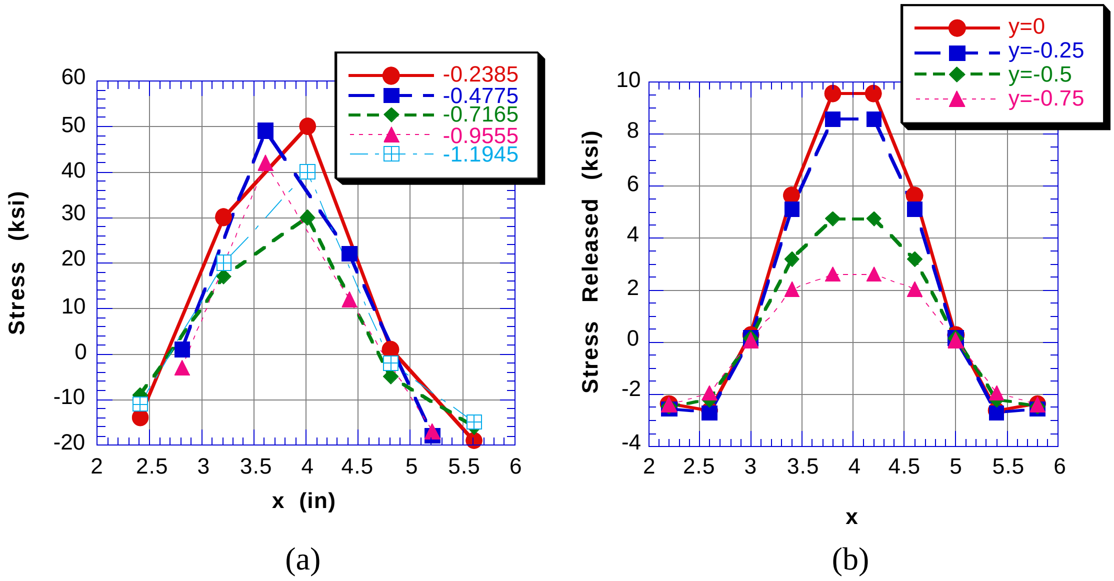

Figure 5.2 – Stress released at various values of y when a slice is removed from the block, xx component. (a) experimental data, and (b) modeling results.

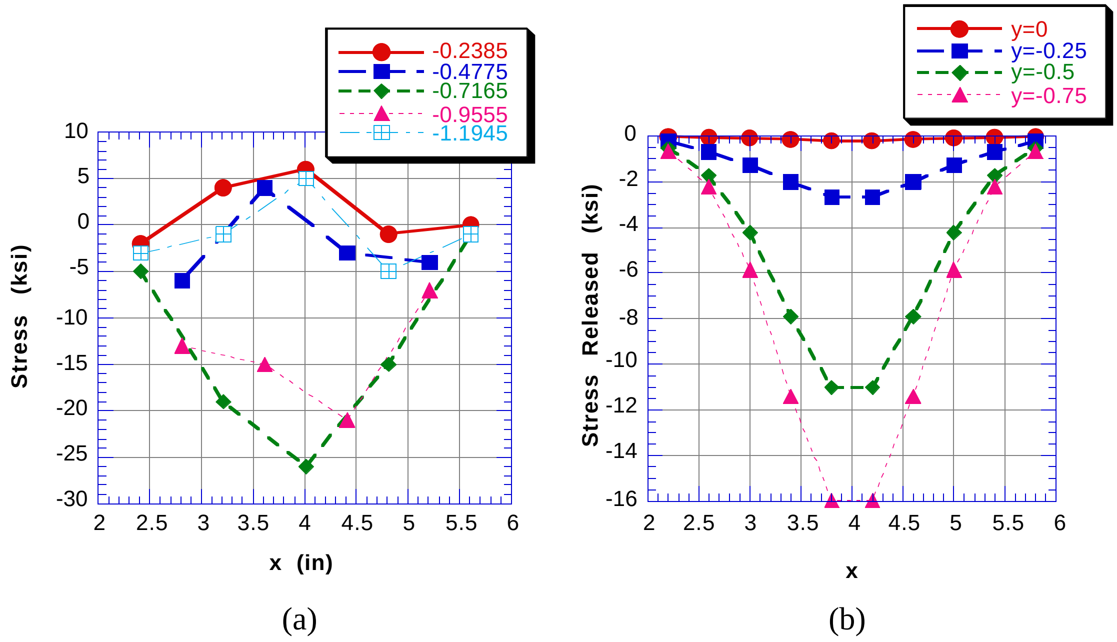

Figure 5.3 – Stress released at various values of y when a slice is removed from the block, yy component. (a) experimental data, and (b) modeling results.

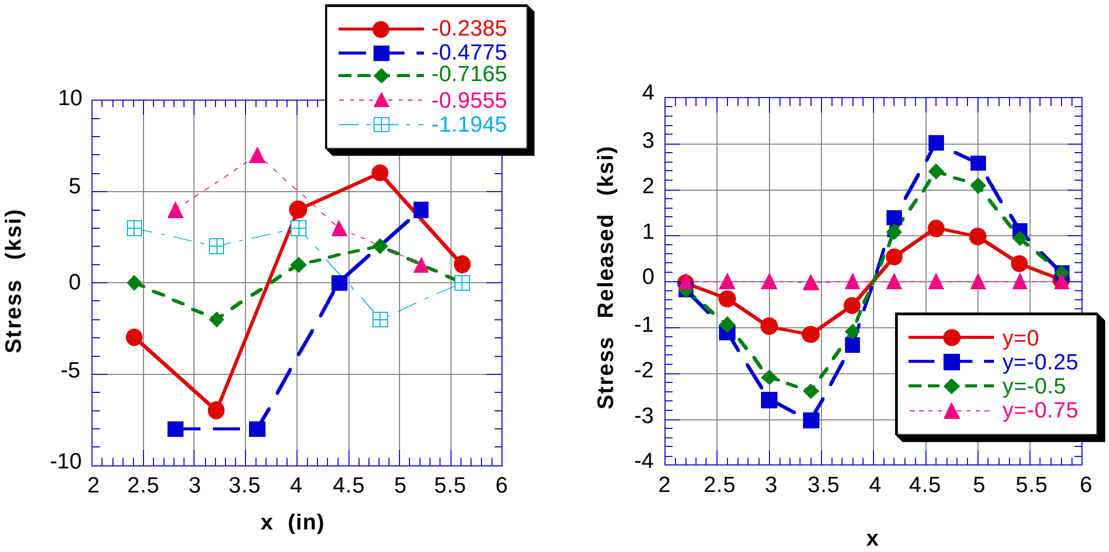

(a) (b)

Figure 5.4 – Stress released at various values of y when a slice is removed from the block, xy component. (a) experimental data, and (b) modeling results.

were attached prior to removal of the slice, and at twelve other locations shown by the symbol “×” in Figure 5.1. Further hole-drilling residual stress measurements were also conducted at the block mid-plane following removal of the slice. These measurements were performed at the x-y locations indicated in Figure 5.1 by the symbol “●”. Hole drilling was performed incrementally at each stress measurement location. By using the computer program developed by Hampton (1991) to process the collected data, we obtained in-plane stress components as a function of hole depth.

On the surface of the slice there exists residual stress from two sources. First, there is residual stress in the metal due to the welding process. If assumptions made about continuous welding are correct, these stresses should not vary significantly with hole depth. (Hole depth is coincident with the slice thickness and, therefore, the welding direction.) Superimposed on the stress due to welding are residual stresses from cutting and grinding operations performed during removal of the block from the welded joint. These residual stresses exist in only a shallow surface layer, perhaps only 0.010 inch thick or less. Accordingly, we expected that the hole-drilling method would indicate a varying residual stress field near the surface and then essentially constant residual stresses due to the welding process.

Unfortunately, results of the hole-drilling method indicate that residual stresses in the slice varied significantly with depth at many locations up to the maximum depth investigated, 0.02 inch. How to interpret these results and use them in the eigenstrain approach is not clear. Results of the hole-drilling experiments are therefore problematic. Representative examples of the hole-drilling results are shown in Figures 5.5 and 5.6. Results for rosette six, shown in Figure 5.5, indicate that residual stresses are fairly constant with depth. On the other hand, data for rosette thirty-two, shown in Figure 5.6, indicate a significant variation of stress with depth. Results at the remainder of the measurement sites indicate a mix of results of stress versus depth. At approximately half the measurement locations, steep gradients of residual stress with depth are indicated, like that shown in Figure 5.6.

One way to look at the residual stress results is to examine a particular depth for all locations. The data are presented this way in Figures 5.7 through 5.9 for a depth of 0.013 inch. These results are spatially unsmooth. If the data truly represent the state of residual stress in the slice, then the spatial density of residual stress measurement is not fine enough to capture its variation and more measurements need to be taken. However, stresses released by slicing indicated that the residual stress state is smoother, and that the gage layout used might have been refined enough, as shown in Figures 5.2 through 5.4. It may be that uncertainties in the hole-drilling results are too large given the magnitude of the stress being estimated.

Schajer has published a recent paper in which he investigates uncertainties in the Integral Method for hole drilling (Schajer, 1996), which was used in this work. In this study, he addressed four error sources which can be expected in using the method. These error sources represented uncertainties in strain measurement, hole depth at each increment of drilling, hole diameter, and material constants used to relate stress to strain release around the hole. He assumed typical values for these uncertainties and proceeded to find the resulting uncertainty in calculated stress. According to his analysis, errors in stress estimates grow larger with the number of increments of depth from the surface. At a depth of 0.013 inch, the depth for which stress results are reported in Figures 5.7

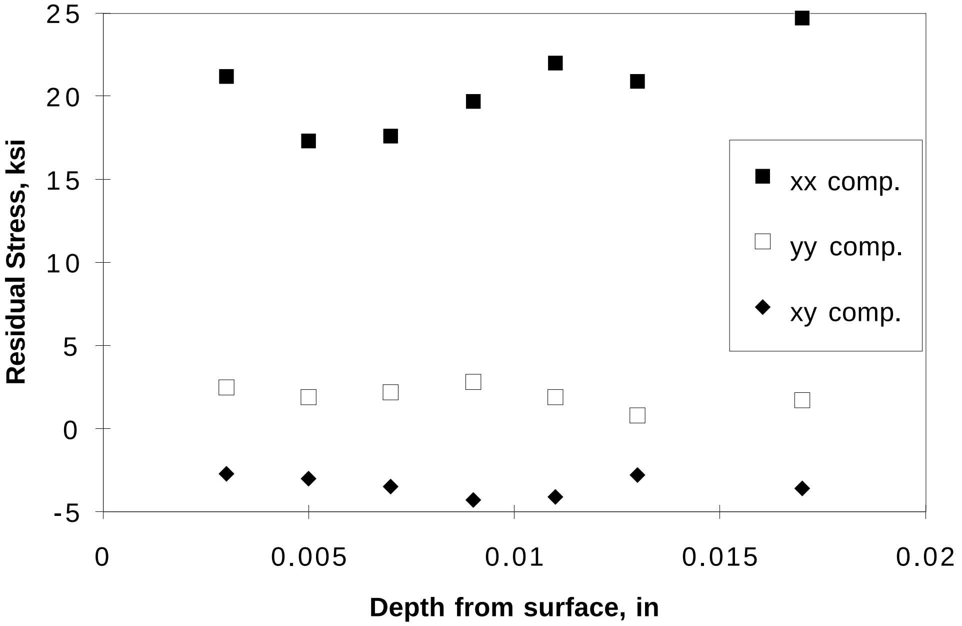

Figure 5.5 – Hole-drilling residual stress results for Rosette #6, at x=3.213, y=-0.239.

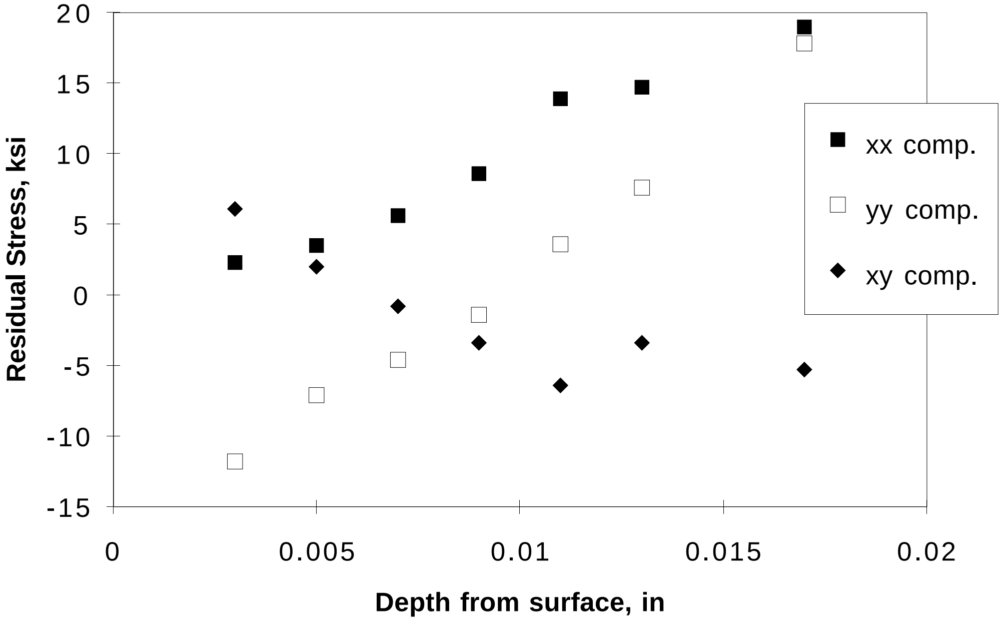

Figure 5.6 – Hole-drilling residual stress results for Rosette #32, at x=3.213, y=-0.478.

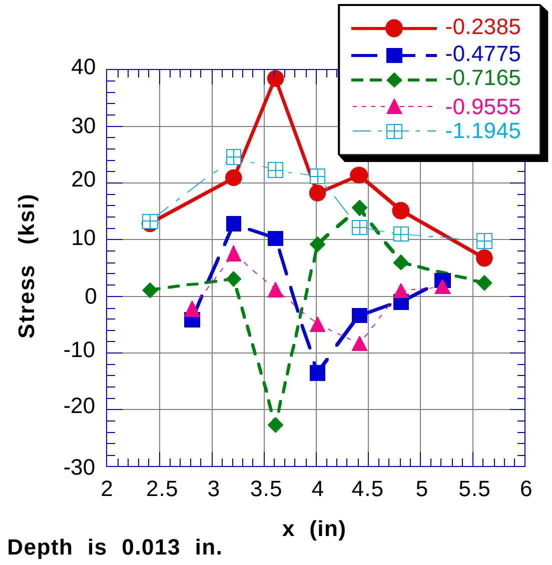

Figure 5.7 – Residual stress at a depth of 0.013 inch, xx component.

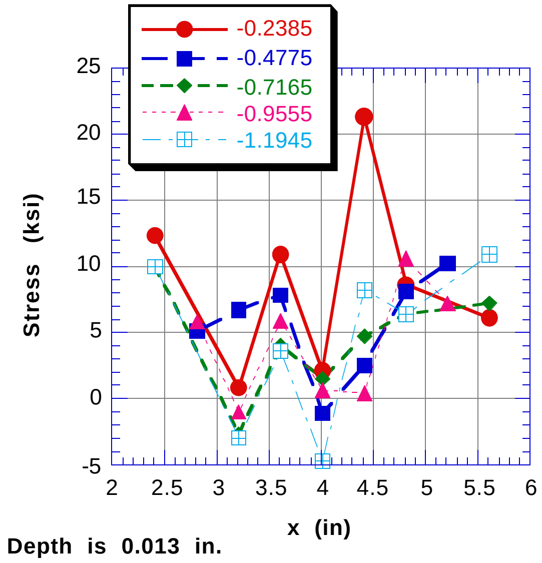

Figure 5.8 – Residual stress at a depth of 0.013 inch, yy component.

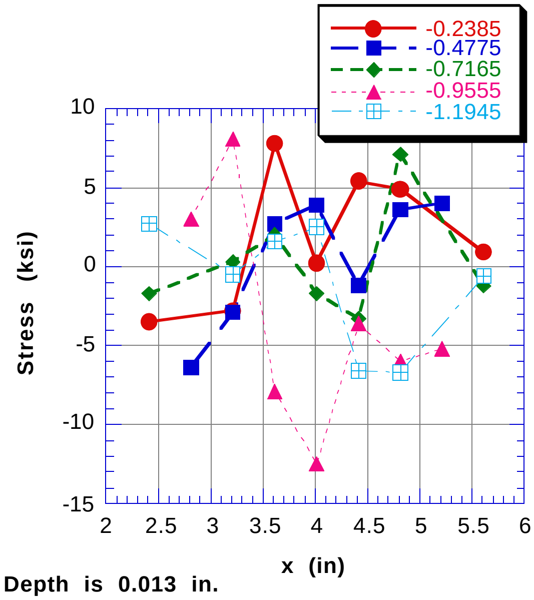

Figure 5.9 – Residual stress at a depth of 0.013 inch, xy component.

through 5.9, he reports a two-sided 90% confidence interval of 12.8 ksi. Of course, this error band is dependent on the magnitude and distribution of stress being estimated. But, according to Schajer, part of this uncertainty is *independent* of the stress present prior to drilling. Using the data he reports, we find that 8.4 ksi of the reported 12.8 ksi error band is independent of the residual stress being measured. Schajer's recent results indicate that there is sizeable uncertainty in residual stress computed using the Integral Method. Returning to the results presented in Figures 5.7 through 5.9, we see that the likely error in measured stress found by Schajer, at least ±4.2 ksi, is comparable to the magnitude of stress reported, especially for σ_{yy} and σ_{xy}.

The spatially unsmooth estimates of residual stress in the slice may be due to several factors which together possibly make hole-drilling residual stress measurement inadequate for use with the eigenstrain technique. One of these is the systematic error just described. The other possible problem with hole-drilling is that the residual stress field due to welding may not be constant along the weldline or smoothly varying in the planar directions *relative to a small length scale*. It might be that although the weld induced eigenstrain field induces residual stresses which are smooth when averaged over some scale, they are not smooth over the small length scale examined with hole-drilling which is on the order of 0.040 inch. In the slice and dice method proposed by Ueda, these small-scale variations in eigenstrain would cause stresses which are not released in the dice, even though the larger scale variations are released.

For the sake of illustration, assume that the eigenstrain field has a mean value at every point which is independent of the longitudinal coordinate. Further assume that there is some perturbation field added onto the mean which varies in length along the weldline and in the planar directions. If the period of variation is small and the amplitude of the perturbation not large in comparison with the mean, then the residual stress field might indeed reflect the mean value of eigenstrain. However, one must consider the scale on which residual stress is desired. For micromechanical type models, the perturbation of eigenstrain and residual stress may be important. For macromechanical analyses (like most fatigue and fracture methods in use today), some sort of average is probably more desirable. It is left then to determine a procedure by which the proper average can be obtained. However, the disassembly of eigenstrain into a portion which is constant along the weldline and a perturbation with spatial coordinates is pure conjecture, and more research needs to be performed to determine the actual state of affairs in real welds.

Execution of the eigenstrain method using the hole-drilling data just reported produced unrealistic estimates of residual stress in the welded block. At the conclusion of these experiments, it was not clear as to whether the data or the eigenstrain method was the culprit. Accordingly, the study laid out in Chapter 4 was performed to more fully evaluate the eigenstrain method. The significance of that study cannot be overemphasized, for it revealed several strengths and weaknesses of Ueda’s proposed method and in our execution of the approach. The extensive, and frustrating, experimental effort just described gave little confidence in the eigenstrain method, and yet the numerical study which followed offered encouragement. We therefore set out to formulate an experiment which would provide a *physical* verification of the eigenstrain method.

Chapter 6

Evaluation of the Eigenstrain Method

In this chapter, we pursue an experimental evaluation of the eigenstrain technique. The object is to lend credence to the conclusions drawn in Chapter 3 and Chapter 4 based on numerical experiments. In order to physically verify any residual stress measurement technique, one must first obtain a specimen which contains some known residual stress field. The usual problems with obtaining a specimen of this type are further complicated in our case because we need to characterize a method for triaxial residual stress measurement. A specimen which contains a known triaxial residual stress state is not easily obtained. Our approach is to manufacture a specimen and perform a mechanical operation which imposes localized plastic deformation, which in turn gives rise to stress. We have adopted the swage autofrettage process to induce the localized plastic deformation. In this process, an oversized mandrel is forced down the length of a thick walled tube. After the swage is complete, this process leaves behind large compressive hoop residual stress near the inner-diameter, and also imposes radial, and axial residual stresses. The autofrettage process is similar to continuous welding in that the eigenstrain caused by the swage is, in principle, independent of position along the tube, neglecting regions near the ends. On that basis, the eigenstrain method is adapted for application to the axisymmetric case and verified by numerical experiment. Actual measurements of strain release due to sectioning are then made on the tube, and residual stress estimated at its midlength based on the resulting data. The stress estimates provided by the eigenstrain method are then compared to the result of an elastic-plastic finite element calculation of residual stress.

6.1 Development of a test specimen

The original intention was for this effort to verify the eigenstrain technique using the specimen discussed in Chapter 3 and shown in Figure 3.20 on page 120. This specimen is the size of the welded block which was used to demonstrate the eigenstrain technique in Chapter 4. There are two holes drilled down the length of the plate which would be expanded by autofrettage. The autofrettage process would leave behind compressive residual stress in the thickness direction near each hole at the mid-thickness of the plate, which would give way to tensile stress at the midpoint between the holes.

The autofrettage process is favored for introducing a residual stress state because it causes residual stress by imposing localized plastic deformation. As discussed in Chapter 1, the introduction of localized plastic deformation is the technique for producing residual stress that is most amenable to analysis. Although our goal is to produce a specimen with a *known* residual stress state, our approach is to use elastic-plastic finite element analysis to *estimate* these stresses with reasonable accuracy. We can then compare the prediction to the experimentally determined stress. The swage process has relatively few parameters which must be determined to obtain residual stress estimates. In fact, we only need to know the stress-strain properties of the material from which the tube is made, the elastic properties of the mandrel, assuming that it is sufficiently hard, the coefficient of friction on the swage interface, and the geometry of the specimen and mandrel. This is a relatively small amount of information to obtain, especially when compared to other processes generating residual stress, like welding. Furthermore, reasonable estimates of these properties might be made based on experience, allowing trial modeling to commence prior to knowledge of the actual values of the properties.

In Section 3.6 we discussed the task of physical verification. The specimen proposed there, shown in Figure 3.20 on page 120, represents a three-dimensional problem. In order to model the swage process, it was assumed that each hole could be modeled separately, as they sit rather far apart. Accordingly, two symmetry planes are drawn, one across the thickness, and one across the width of the plate, both running down the axis of the hole.

An initial mesh was constructed exploiting this symmetry, for both the block and the mandrel. The geometry of the mandrel was taken to be a sphere, which would be pushed through the hole from behind. Initial computation on this mesh indicated that this was a more complex problem than anticipated, especially in relation to the computing power at our disposal. (The computer used for the analysis is an IBM RS6000/340 with 32MB of RAM, and its performance is about half that of the fastest engineering workstations currently available.) The analysis is time consuming because the problem is three-dimensional, includes non-linear material behavior, finite strain formulations, and non-linear contact between the mandrel and hole periphery. Since dozens of finite element runs would be needed to assure a refined mesh and adapt the mesh to the actual as-fabricated geometry, it was decided to abandon this geometry and move instead to the geometry shown in Figure 6.1.

The specimen shown in Figure 6.1 presents a simpler problem because the tube is an axisymmetric geometry. As an axisymmetric problem, it is much more appropriate for the computing facilities available, and for the level of personal experience with the particular problem. This is not to say the problem is simple, solution times on the IBM RS6000/340 are still on the order of ninety-thousand seconds, but relative to the three-dimensional problem the calculation is reasonable. The axisymmetric nature of this problem allows simplification of the experimental determination of residual stress as well. This will be exploited, as described in Section 6.3.1, to produce residual stress estimates with fairly high spatial resolution. This experiment serves to examine the accuracy of the eigenstrain

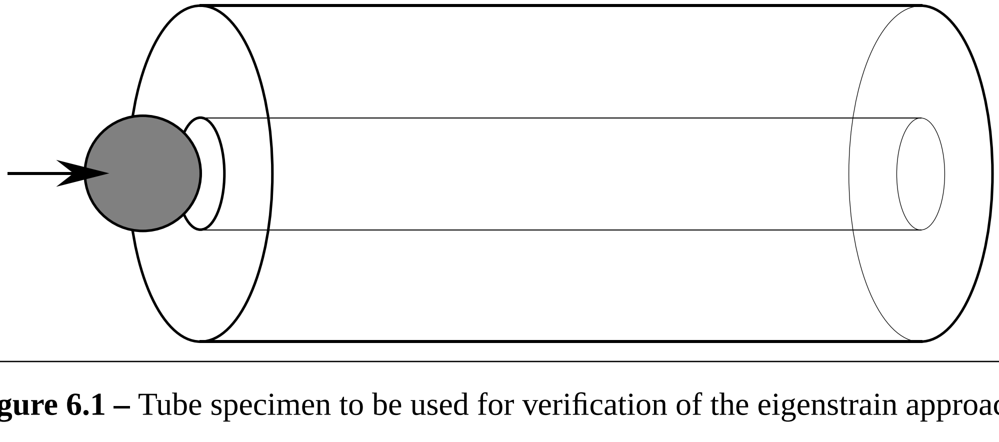

Figure 6.1 – Tube specimen to be used for verification of the eigenstrain approach.

method in general, and to verify the procedures used to numerically validate the method in the earlier chapters of this thesis.

In the process of developing this experiment, the guidance of G. Peter O'Hara, of the U.S. Army's Benét Labs at Watervliet Arsenal, was extremely helpful. The Arsenal uses the swage autofrettage process to introduce compressive hoop residual stresses at the inner diameter of large gun-tubes. These residual stresses serve to suppress fatigue crack propagation which would normally occur in these armaments in service. O'Hara was a valuable resource not only because he had practical experience in the area, but also because he has performed a great deal of finite-element-based modeling of the process (O'Hara, 1991). Based on these consultations, an ordinary ball bearing was selected as the mandrel to be used in our swage process. Also, we used a special swage grease which he provided to lubricate the tube bore. Based on his experience with the swage process and this particular grease, we assumed a coefficient of friction in our initial analysis of 0.015.

We should take a moment here to provide some details on the finite element procedures used in the preliminary analysis, as successive modeling inherits the same basic scheme. We have used the general finite element package ABAQUS, version 5.3, published by Hibbitt, Karlsson, and Sorensen, Inc. This package provides sufficient generality to solve nearly any non-linear stress analysis problem. The mesh we have used is shown in Figure 6.2, and uses axisymmetric elements. Initially, linear displacement elements were used with a selective-reduced integration rule, but these elements produced

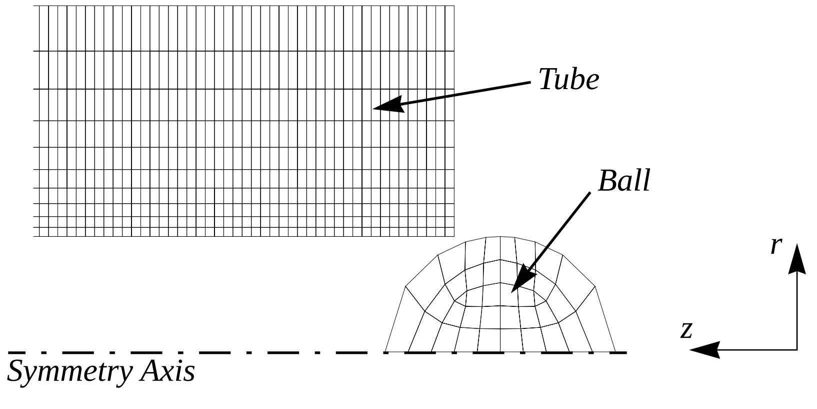

Figure 6.2 – Finite element mesh used in preliminary analysis of the swage process. The mesh extends in the axial (z) direction to 8 inches.

spurious radial and shear residual stresses at the inner diameter of the tube that cannot physically exist (since the inner diameter is traction-free following the swage). The spurious stresses were eliminated by using elements with linear displacement interpolation but a fully reduced integration rule. In total, the model depicted in Figure 6.2 had 2038 axisymmetric elements. The nodal spacing in the tube portion of the model was 0.04 inch in the *z*-direction. There were ten elements in the radial direction which had a geometric progression in size such that the elements at the outer diameter were five times larger than those at the inner diameter.

In the swage problem, the surfaces of the mandrel and tube slide against each other. In an axisymmetric problem, this contact occurs on a surface that is axisymmetric. Therefore, the contact surface reduces to a curve in the axisymmetric plane of the model. In the analysis, contact is handled by placing slide-line contact elements along the tube surface and assigning these a “master surface” which runs along the mandrel. As the mandrel is forced down the tube, the contact elements on the inner diameter are made to displace so that they do not pass through the surface of the mandrel. Through the tube-mandrel interface, the mandrel pushes on the tube, and the tube pushes back on the mandrel. The amount of force passed through the interface is dictated by the compliance of the tube and the distance the contact element must move to lie just outside of the master surface. In this way, forces are transferred normal to the interface. There is also some frictional force that accompanies the swage. In the analysis, frictional contact is handled by assuming that the shear force transferred across the interface is equal to the normal force multiplied by the friction coefficient, μ. Further detail on the simulation of contact problems can be found in the ABAQUS documentation (Hibbitt, 1995, Chapter 5).

Simulation of the swage must be carried out in an incremental fashion. In each increment, a small displacement is applied to move the mandrel further down the tube. After imposing the displacement, the position of contact elements is noted and forces are imposed to move the contact elements outside of the mandrel surface, and the cycle repeated. This process proceeds in small steps until the mandrel has exited the tube. In the preliminary analysis, the mandrel was moved no more than 0.005 inch per increment down the 8.0 inch tube. Within each increment, contact forces were computed which satisfied the interface conditions, equilibrium, and the elastic-plastic flow rule. Usually, three to six iterations within each increment were required to converge to a solution. In some increments, however, iterations could not converge and the 0.005 inch incremental mandrel displacement had to be reduced until similar iterations obtain convergence. The preliminary analysis required 1797 increments and approximately 5992 iterations to move the mandrel down the tube length.

Both practical considerations and early simulations of the swage autofrettage process helped to specify the geometry to be used in the problem. The tube used in the initial analysis was chosen have a three-inch outer diameter and a nominally one-inch inner diameter. This size left a one-inch wall, which allowed room for strain gage instrumentation to be used in the experiments. A one-inch ball bearing was chosen for the mandrel. In the finite element analysis, the ball was made to thermally expand by a specified amount prior to the swage. That approach allowed investigation of the influence of the amount of interference (percent difference between ball and bore diameters) without time consuming re-modeling of the geometry. To change the interference, the ball was made to swell uniformly by a differing amount. Based on these early runs, a one-percent interference between ball and tube was found to impose significant residual stress. The residual stress at the midlength of the tube resulting from this initial calculation is shown in Figure 6.3. Here we see the expected compressive hoop residual stress in the region of the inner diameter. There are also compressive axial and radial residual stresses present, giving a triaxial residual stress state. (The coordinate system is polar: *r*, θ, and *z* represent the radial, hoop, and axial directions respectively.)

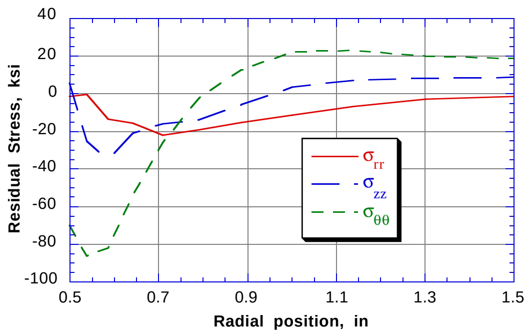

Figure 6.3 – Residual stress at the tube's midlength predicted by preliminary analysis.

The stress-strain properties used in this analysis were those of A516 Gr70 steel, the material to be used in the experiment. This is a high-hardening pressure vessel steel, with composition and properties shown in Table 6.1. This material was chosen because it is used extensively by NASA-Ames Research Center, the sponsor of a large portion of the research on which this thesis is based. Also, Panontin (1994) used this material in a large number of experimentally verified finite element computations at Ames. In her work, she took great care to obtain accurate elastic-plastic characterization of the material to high levels of plastic strain. The flow curve she obtained is shown in Figure 6.4, and is used in our analysis. The material model assumed is strain-rate independent with a von Mises yield criterion, associative flow rule, and isotropic hardening. The elastic modulus of both the steel ball and tube were assumed to be 30x10^6 psi and Poison's ratio to be 0.3, adopting typical values for steel. Further, the ball bearing was assumed to behave elastically throughout the swage since bearings have a high surface hardness.

S_y	S_u	*Elongation in 2 in*	*C*	*Mn*	*P*	*S*	*Si*	*Al*
44.5 ksi	81 ksi	25%	.20	1.11	.009	.014	.24	.053

***Table 6.1** – Physical properties and composition (wt%) of A516 Gr70 as reported by Panontin (1994).*

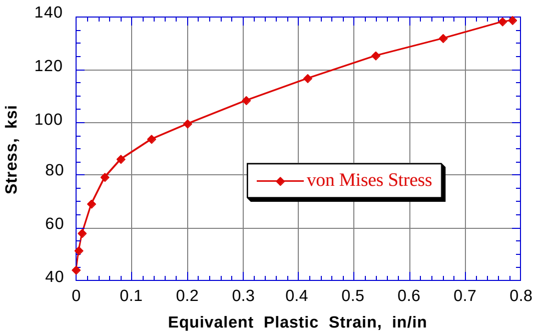

Figure 6.4 – Flow curve for A516 Gr70 (Panontin, 1994).

6.2 Fabrication of the test specimen

Following these initial computations, a specimen was fabricated for use in the experiment. The fabrication plan is shown in Figure 6.5. A taper on the inner diameter was added to one end of the tube to allow clearance for the exit of the ball bearing. As shown in the figure, nominal dimensions of the tube were specified to be OD = 3.0" and ID = 0.9900". A one-inch ball bearing was purchased from a local supplier. It had a diametral tolerance of twenty-five-millionths of an inch, an accuracy normal for ball bearings. On the other hand, assuring dimensional accuracy of the inner diameter along the ten inch length of the

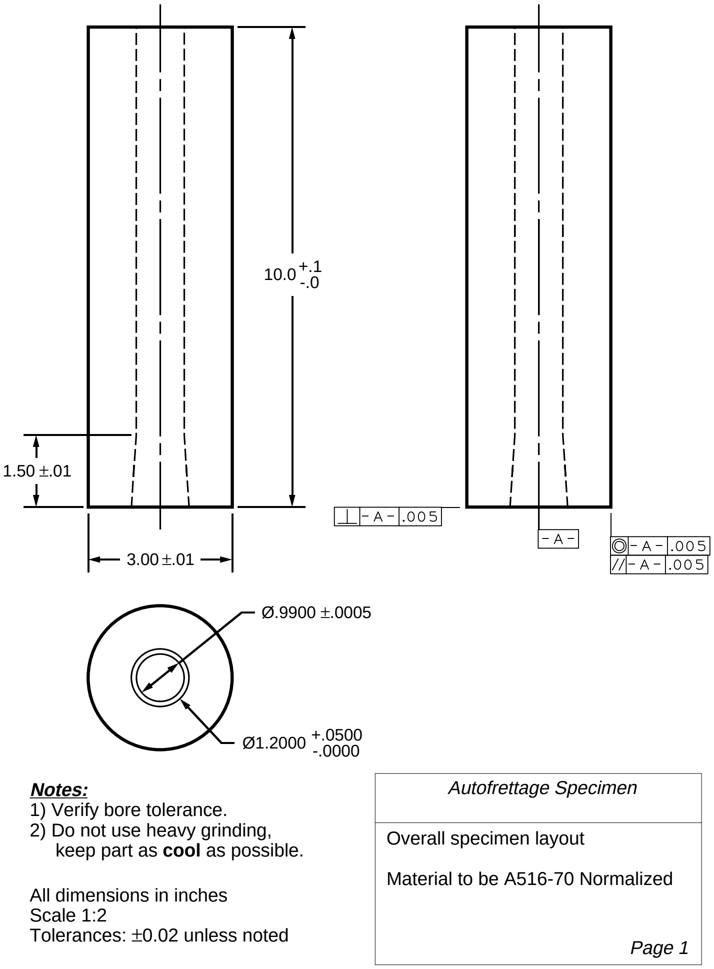

Notes:
1) Verify bore tolerance.
2) Do not use heavy grinding, keep part as **cool** as possible.

All dimensions in inches
Scale 1:2
Tolerances: ±0.02 unless noted

Autofrettage Specimen

Overall specimen layout

Material to be A516-70 Normalized

Page 1

Figure 6.5 – Fabrication plan for the tube to be used for verification of the eigenstrain technique.

tube was not as simple. By using gun-drilling and repetitive honing, the inner diameter was machined to a reported mean diameter of 0.9897 inch, with a minimum of 0.9896 inch and maximum of 0.9900 inch. These numbers are based on only a few measurements taken within two inches of each end of the bore, and the actual variation of inner diameter may be larger than the reported 0.0004 inch. Also, the outer diameter of the tube, as fabricated, was 2.95 inches.

Following fabrication, the tube was swaged. The inner bore of the tube was coated with special swage grease, the ball placed on the entrance to the tube, and the ball pressed through. Initial analysis indicated that the swage operation would require approximately 8 kips of force to drive the ball through the hole. To perform this operation, a 40 kip hydraulic press under displacement control was used to which was bolted a 10 inch long 0.98 inch (25 mm) nominal diameter threaded rod. The rod was small enough to fit in the bore, yet large enough to withstand up to 16 kips of compressive load, according to Euler-Johnson buckling criteria. The tube was swaged slowly so that the deformation could be assumed to be quasistatic. The entire swage operation took 28 minutes to complete. During the press, data were collected on ram displacement, load required, and hoop strain at the outer diameter. The hoop strain data were taken from a single strain gage located 4.88 inches from the entrance to the tube. The data gathered during the experiment are shown in Figure 6.6. These results enable some verification of the parameters used in the elastic-plastic computation of residual stress.

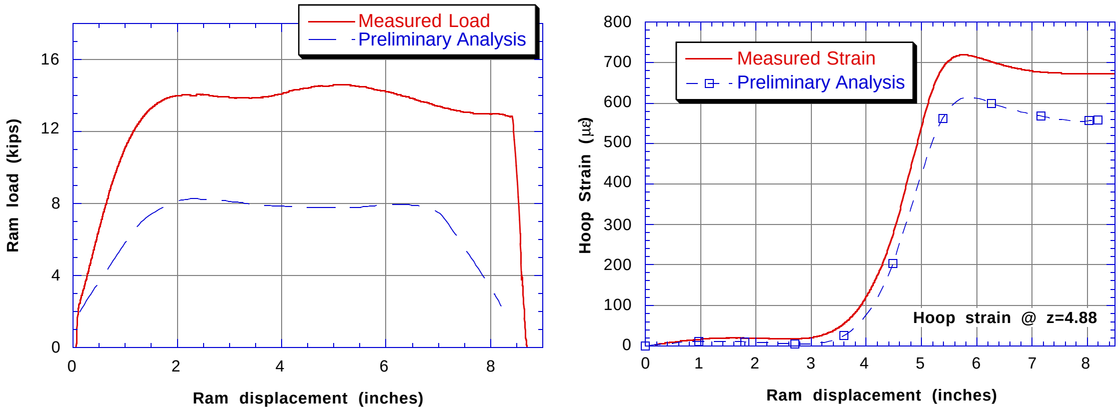

Figure 6.6 – Data gathered during the swage operation compared with results of the model.

6.3 Measurement of residual stress

We now turn to the experimental determination of residual stress in the tube. In this section we will first describe the development of an axisymmetric eigenstrain method for the autofrettaged tube. This method is then applied using experimental measurements to estimate residual stress at the midlength of the tube. The accuracy of the axisymmetric eigenstrain method is discussed in Section 6.4.3, where the method is simulated numerically.

6.3.1 Development of an axisymmetric eigenstrain method

Residual stress in the swaged tube is the result of an eigenstrain field which is independent of position along the tube, excluding regions within one inch of the tube end. By removing two inches from the swage-entrance end of the tube, a free-surface is created on which residual stress is caused by the same eigenstrain field assumed to give rise to residual stress at the tube's midlength. The independence of eigenstrain on length is similar to that of continuous welding, described in Chapter 4. Accordingly, we can use a slice-and-dice technique to reveal the eigenstrain field and then estimate residual stress at the midlength of the tube. The axisymmetric nature of the problem allows a relatively small number of measurements to be used to reveal the eigenstrain field. It should be noted that Ueda (1986d) reported an axisymmetric method that was used with solid cylinders but which proceeded in a very different way from the following. The sectioning process presented in that paper does not resemble the slice-and dice technique used for a welded joint, and therefore cannot be used to verify it.

The instrumentation layout for this procedure is shown in Figure 6.7. Two sets of thirteen strain gages are attached on or near the tube's free-surface, on diametrically opposite radial lines. One set of gages will measure changes in hoop strain which occur with sectioning, and one set will measure radial or axial changes. Gages located on the inner and outer diameters are positioned 0.05 inch from the free surface down the tube. At these two radial positions, one set of gages measures hoop strain, as described, while the other measures axial strain. Measuring two orthogonal components of strain at each radial location allows the use of plane stress relations to compute stress changes in those two directions. Implicit in this measurement scheme is the assumption of axisymmetry of the residual stresses. That is, stresses on the two radial lines are assumed to be the same. We also assume that gages are placed at the same radial locations on these two lines.

The sectioning procedure used to reveal the eigenstrain is shown in Figure 6.8. First, a slice is removed from the end of the instrumented tube. Then a small region including the instrumented area is removed from this slice. Ideally, this small region would then be diced, however the close spacing of the gages (0.08 inch) makes this operation difficult, and so it was not attempted. The small piece is therefore referred to as the “final section”. As will be described later, stresses which remain in the final section will have an impact on the accuracy of residual stress estimates provided by the eigenstrain method.

Interpolation of eigenstrain is performed in the radial direction by the functions shown in Figure 6.9. As can be seen, these shape functions have a spacing which is the same as that for the strain gages. Residual stress in the tube is caused by some combination of radial, hoop, and axial eigenstrain components. However, hoop and radial eigenstrain are capable of causing the *same* residual stress in an axisymmetric geometry. If the interpolation of both of these components is included in the eigenstrain system, the linear

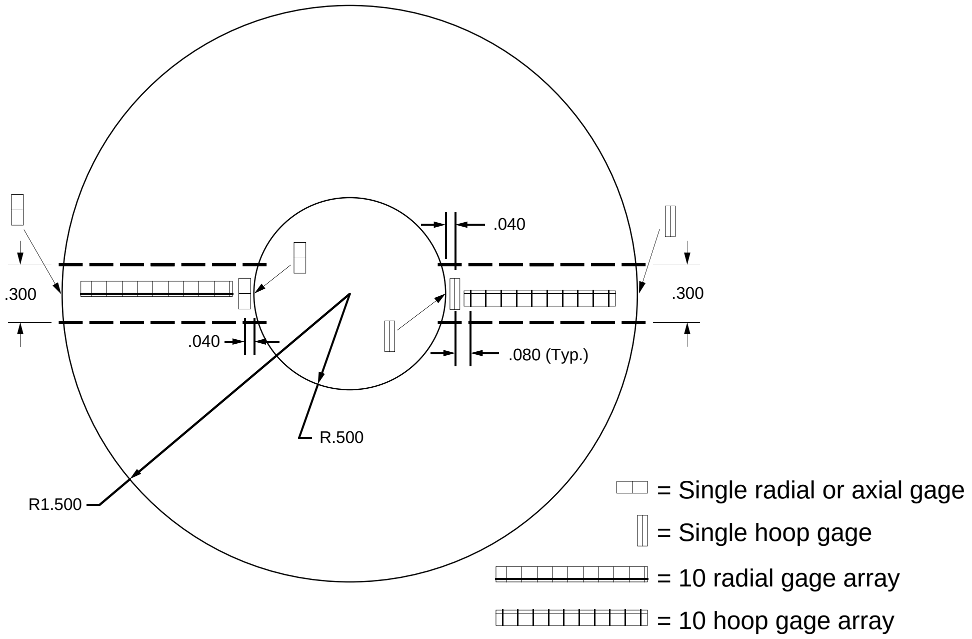

Figure 6.7 – Layout of instrumentation for the axisymmetric eigenstrain method.

system will be singular. The singularity is removed by choosing either to interpolate hoop *or* radial eigenstrain and setting the other component to zero. Again, the cause of the singularity is the fact that the hoop and axial components of eigenstrain can cause the same stress in the tube. To illustrate this point, we turn to the case of elastic deformation.

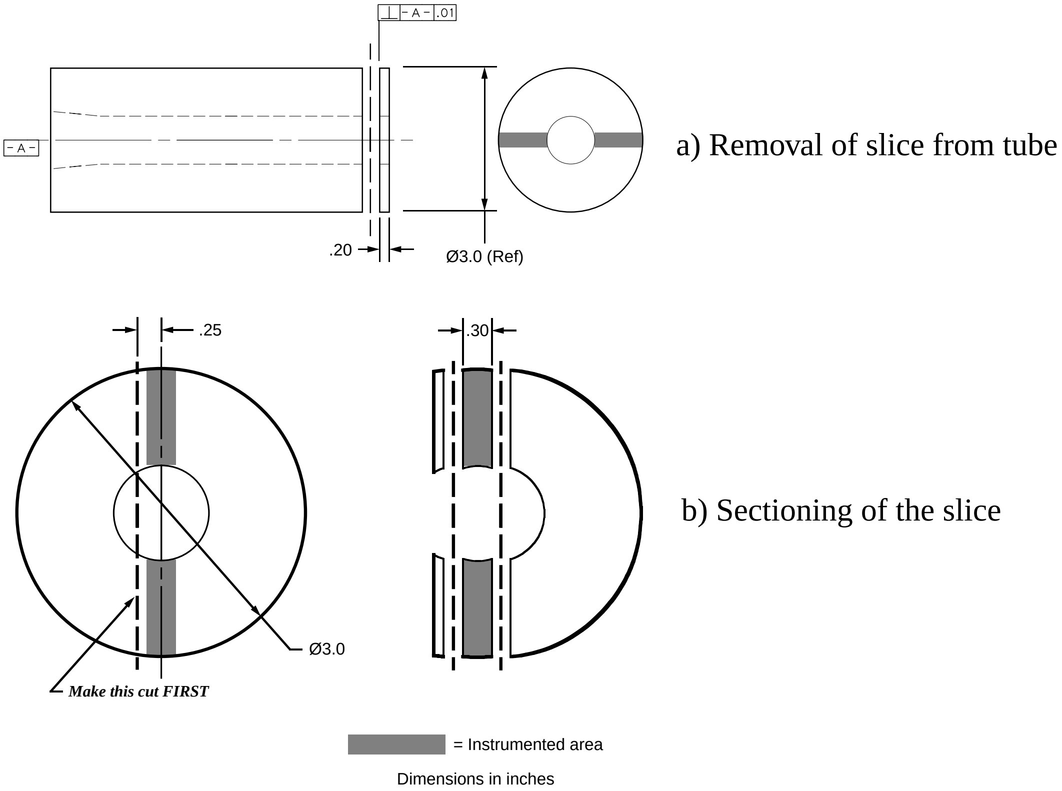
⊥ - A - .01
- A -
.20
Ø3.0 (Ref)
a) Removal of slice from tube
.25
.30
b) Sectioning of the slice
Ø3.0
Make this cut FIRST
= Instrumented area
Dimensions in inches

Figure 6.8 – Sectioning procedure for the axisymmetric eigenstrain method.

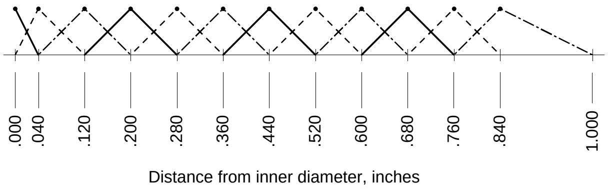
.000
.040
.120
.200
.280
.360
.440
.520
.600
.680
.760
.840
1.000
Distance from inner diameter, inches

Figure 6.9 – Twelve shape functions used to interpolate eigenstrain in the radial direction. Interpolation nodes correspond to stress measurement locations.

In the elasticity problem, the two components of elastic strain are *both* related to radial displacement, u, in an axisymmetric problem. These two relations are given by

$$\varepsilon^{e}_{rr} = \frac{\partial u}{\partial r} \tag{6.1}$$

$$\varepsilon^{e}_{\theta\theta} = \frac{u}{r}. \tag{6.2}$$

Turning from elastic strain to eigenstrain, these same equations dictate the deformation caused by the eigenstrain field which must be overcome by residual stress. The residual stress, in turn, is completely determined by that displacement field. Since either a radial or hoop eigenstrain can be used to define the same displacement field through Equation 6.1 or Equation 6.2, they can induce the same residual stress. For this reason, radial eigenstrain is assumed to be zero and residual stress assumed to be due to only the axial and hoop components, ε^*_{zz} and $\varepsilon^*_{\theta\theta}$. (Alternatively, one could choose radial and axial components. The choice between radial and hoop eigenstrain is arbitrary.) Each of these two components is distributed in the radial direction by the shape functions shown in Figure 6.9, yielding twenty-four eigenstrain parameters.

The linear system to be used to determine eigenstrain from measured stress changes is formed by repetitive finite element calculations on a well-refined mesh. Two axisymmetric meshes are constructed, one to model the tube, shown in Figure 6.10, and one to model the

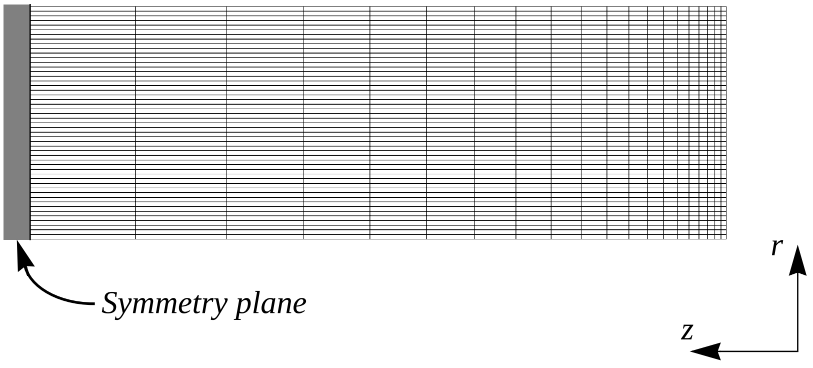

Figure 6.10 – Finite element mesh of the tube used to form the eigenstrain system.

slice. For these models, symmetry about the axial length is used to reduce the size of the computation. The length of the models are 2.0 inches for the tube and 0.1 inch for the slice, giving physical dimensions of 4.0 inches and 0.2 inch after considering symmetry. The inner diameter was assumed to be 1.0 inch and the outer diameter 2.96 inches. This geometry represents a slight departure from the as-fabricated tube dimensions but was convenient with regard to mesh creation. The difference between tube and model represents only 0.3% difference in outer diameter and 0.4% in inner diameter, not enough to have a significant impact on the calculations. The mesh within these geometries consists of 49 elements along the radial direction, evenly spaced at a 0.02 inch pitch, and 20 elements in the axial direction with a geometric progression of element size such that the elements at the free surface are twenty times smaller than the elements at the symmetry plane. The mesh for the slice is obtained by scaling the tube mesh axially by 0.05.

Formation of the linear system which relates eigenstrain to measured stress changes is performed following the general procedure outlined in Chapter 4. One finite element calculation is performed on each of the two meshes for each eigenstrain parameter in the analysis. By eigenstrain parameter, we refer to a single component of eigenstrain, ε^*_{zz} or $\varepsilon^*_{\theta\theta}$, distributed by a single shape function. For each run, nodal stress results are collected at points corresponding to strain gage locations on the surface of the tube or slice. Completing this procedure for each eigenstrain parameter on both the tube and the slice models results in two linear systems, $\boldsymbol{M}_s$ for the slice and $\boldsymbol{M}_t$ for the tube. Each of these systems has dimension (26x24), since each relates 26 stress components to 24 eigenstrain parameters. We combine these two linear systems into one, so that the eigenstrain is determined from measured stress on the free surface of both the slice and tube simultaneously, in a least-squares sense. The system to be solved is then a partitioned system which combines both linear systems and is given by

$$\left\{\frac{\sigma_s}{\sigma_t}\right\} = \left\{\frac{\boldsymbol{M}_s}{\boldsymbol{M}_t}\right\}\{\varepsilon^*\} \tag{6.3}$$

where,

σ_s = stress measured on the slice
σ_t = stress measured on the tube
$\boldsymbol{M}_s$ = linear system for the slice

$\boldsymbol{M}_t$ = linear system for the tube
ε^* = eigenstrain parameters,

and where the horizontal line indicates a partition of the system, rather than division.

The least-squares solution for ε^* given the measured stresses is obtained by using a linear equation solver (e.g., MATLAB). After the eigenstrain has been found, stresses are found at the midlength of the tube geometry by using another linear system which relates stress on the midlength of the tube to the eigenstrain parameters. This approach was adopted over putting the eigenstrain into a finite element computation because the necessary calculations have already been performed in forming the linear system $\boldsymbol{M}_t$. To get the linear system for midlength stress, one needs only to gather stress results at points on the midlength instead of the surface. Furthermore, this approach was found to produce the same results as are found by imposing the determined eigenstrain on a finite element model of the tube, as should be expected.

6.3.2 Experimental execution of the axisymmetric eigenstrain method

Given the previous description of the development of the eigenstrain method for an axisymmetric problem, the description of the experimental application of the technique is relatively straightforward. However, certain experimental aspects call for detailed description and demanded careful execution. The foremost issue related to the execution of the measurements is the required assurance that changes in strain which are recorded by the instrumentation employed are due only to the release of stress from the sectioning process.

Measurement of the strain change caused by sectioning is made difficult by two main factors. First, the sectioning is carried out using electric-discharge machining (EDM) which requires that a high pressure water jet be used during the cut. Secondly, individual strain gages must be disconnected from the electrical device used to measure their strain during sectioning. Introduction of high pressure water to a strain gage installation invites failure of the gages as water attacks the adhesive used to bond the strain gage to the surface. Even if the bond does not fail, water molecules can migrate into the adhesive causing swelling of the glue and deformation of the gage. This will result in “apparent” strain, a strain which is read by the measurement system but is not due to deformation of the body being investigated. To circumvent this problem, an acrylic coating was applied to the area where the gages were applied, overlapping the installation adhesive by at least 0.05 inch on all sides. This coating blocked the migration of water to the glue line, thus minimizing errors caused by swelling of the adhesive.

Disconnection and reconnection of the strain gages from the instrumentation can produce errors in measured strain from several sources. First, strain in each of the strain gages must be read relative to a stable gage. For this purpose, a strain gage of the type used in the experiment was installed on a piece of material cut from the tube. Before any of the active gages were read, the instrumentation was zeroed relative to this stable gage. Since *changes* in strain are to be determined from these measurements, the actual state of this stable gage is irrelevant, as it will cancel out when the difference between strain readings is taken. The indicated strain will also be affected by the process of connecting the strain gage lead wires due to changes in electrical contact resistance. To reduce these errors as much as possible, connection of the leads was done by soldering, and disconnection by de-soldering. This method of connection provides highly repeatable electrical properties of the connection and so will introduce the least error in measurement. Finally, to minimize random errors in measurement, all strain gages were measured four times for each geometry: tube, slice, and final section. Between measurements, each gage was disconnected from the instrumentation and then re-connected for the next reading. These four readings were then averaged to obtain the actual strain in each geometry relative to the stable gage. (The reader may be interested to know that the maximum sample standard deviation computed from any group of four measured strains was 12 $\mu\varepsilon$, or 0.5% of the maximum measured strain change, indicating that the measurement process was highly repeatable.)

Indicated strain changes are shown in Table 6.2 and Table 6.3 for the slice to final section and tube to final section strain changes, respectively. At each radial coordinate in the tube, we have measured radial and hoop strain changes, except for points on the inner and outer diameter where axial and hoop changes were recorded. By assuming a plane stress condition, the strain change perpendicular to the surface can be found from

r (inches)	*ΔRadial*	*ΔHoop*	*ΔAxial*
0.5	-803	2489	-615
0.54	-242	1807	-671
0.62	-60	1224	-499
0.7	186	681	-371
0.78	403	195	-256
0.86	541	-201	-146
0.94	613	-476	-59
1.02	560	-578	8
1.1	481	-540	25
1.18	411	-426	6
1.26	348	-441	40
1.34	250	-473	95
1.475	-37	-370	457

Table 6.2 – *Strain change accompanying the slice to final section geometry change (με).*

r (inches)	*ΔRadial*	*ΔHoop*	*ΔAxial*
0.5	-661	2001	-459
0.54	-164	1472	-561
0.62	-254	823	-244
0.7	-16	306	-124
0.78	308	-130	-76
0.86	573	-454	-51
0.94	717	-684	-14
1.02	685	-731	20
1.1	572	-633	26
1.18	467	-473	2
1.26	398	-429	13
1.34	297	-519	95
1.475	-181	-291	714

Table 6.3 – *Strain change accompanying the tube to final section geometry change (με).*

$$\varepsilon_3 = -\frac{\nu}{1-\nu}(\varepsilon_1 + \varepsilon_2) \tag{6.4}$$

where ε_1 and ε_2 are the measured orthogonal surface strains and ε_3 is the component normal to the surface. From these strains, stress changes are computed by using the elastic constitutive relation for a plane stress condition. Putting the results into Equation 6.3, solving for eigenstrain, and computing stress at the midlength of the tube results in the residual stress estimates shown in Figure 6.11.

6.4 Computation of residual stress

Initial computations for residual stress were performed to aid in the design of this experiment, as discussed in Section 6.1. Data gathered during the swage of the tube are compared to results from this initial computation in Figure 6.6. As shown in the figure, there is reasonable agreement in hoop strain on the outside of the tube, while the data for load indicate a large discrepancy. Accordingly, further computation was undertaken to determine the source of this discrepancy.

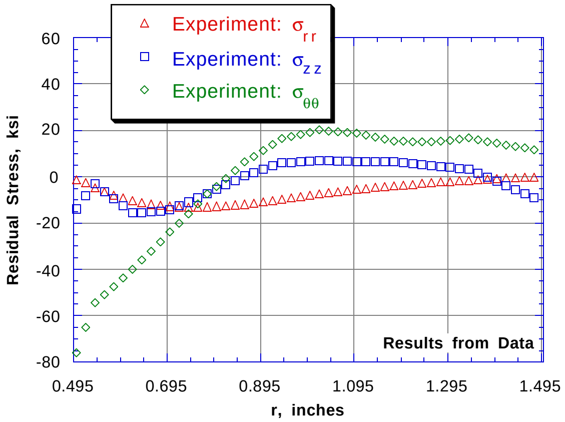

Figure 6.11 – Experimental estimate of residual stress provided by measured stress changes and the eigenstrain method.

6.4.1 Matching the analysis to measured data

The results of the computation are influenced by several factors, including the coefficient of friction between ball and tube, the amount of interference between bore and ball, and stress-strain properties assumed for the ball and tube. A model of the tube was constructed that represents the as-fabricated tube dimensions, and several runs were conducted which varied each of the these factors. The amount of variation assumed in each parameter depended on its expected uncertainty. Accordingly, the variation of ball diameter is assumed to be effectively zero while that for bore diameter is assumed to be 0.0003 inch, which is the maximum reported deviation from the mean diameter. For the material flow properties, we assumed a variation of 10% based on stress would be reasonable (i.e., the flow curve shown in Figure 6.4 was translated upwards or downwards by 10% at each point). The friction coefficient was the most uncertain of the parameters in our model. The initial computation assumed that the coefficient would be 0.015 and was based on a laboratory condition with careful application of the lubricating grease. Our conditions were less than ideal, and so a large variation in coefficient of friction might be expected.

The mesh used to investigate the influence of these variables and to make a final estimate of residual stress is more refined than that used in the preliminary analysis. This mesh is shown in Figure 6.12. Relative to the previous mesh, this mesh has more refinement in the ball and in the radial direction of the tube. In the radial direction, there are fifteen elements, and element size increases with radial position in geometric

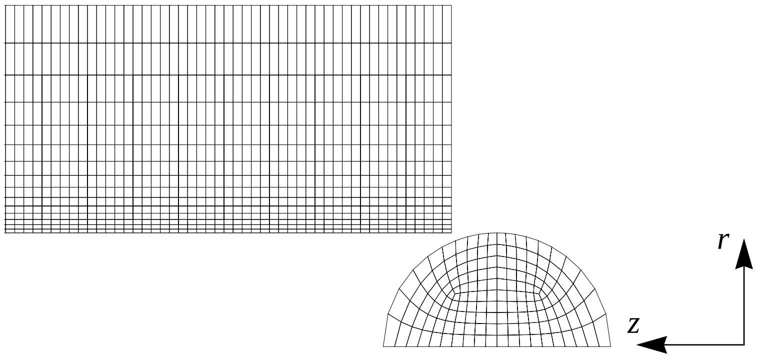

Figure 6.12 – Finite element mesh used in further analysis of the swage process. The mesh extends in the axial (z) direction to 8 inches.

progression such that the outer elements are ten times larger than those on the inner diameter.

These analyses indicate that the maximum load reached during the swage is strongly dependent on the coefficient of friction assumed. By altering the friction coefficient, we find that a value of 0.075 creates a good match between the predicted and the measured load, as shown in Figure 6.13. The mean tube diameter was reported to be 0.9897 inch, which results in a 1.03% interference between the ball and tube. Taking a variation of 0.03% (0.0003 inch) about this interference alters the maximum load by only 0.74 kip in either direction, as shown in the plot. Furthermore, by assuming that the flow curve of the tube material is reduced by 10%, only a 0.15 kip difference in measured load is obtained. It was also found that increasing the flow curve by 10% results in a decrease in measured load of similar magnitude to that produced by decreasing the curve. Since the coefficient of friction is primarily responsible for determining the maximum load achieved during the swage, the variation of this parameter was not thoroughly investigated and a value of 0.075 was assumed in all further analyses.

Data gathered on hoop strain measured during the swage are presented with data from three FEA runs in Figure 6.13. These results show that both increasing the interference and decreasing the flow curve of the material increase the hoop strain at the outside of the tube and decrease the difference between model and experiment. The difference between

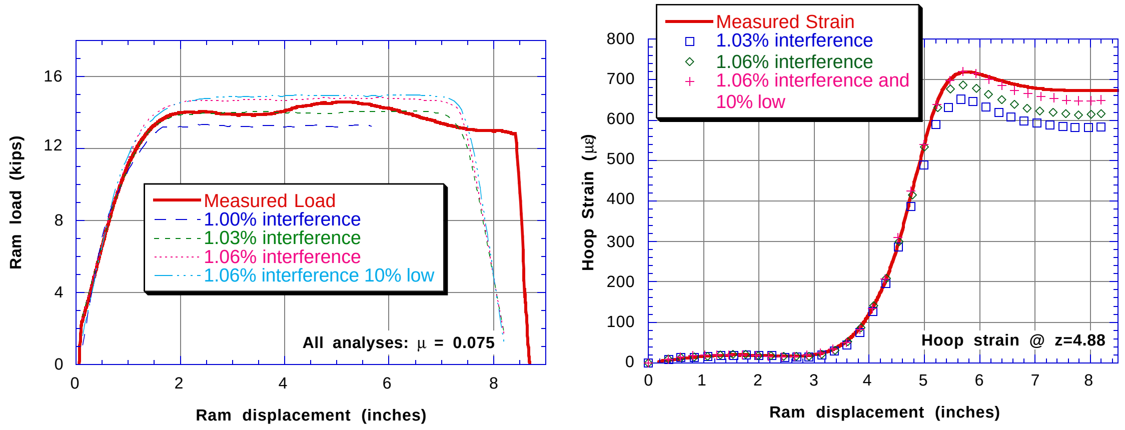

Figure 6.13 – Data gathered during the swage operation compared with results of the model for a friction coefficient of 0.075.

model and experiment of maximum hoop strain attained during the swage is less than 10% for each model.

The measured load data shown in Figure 6.13 invite another interesting observation. If conditions down the tube bore are similar from one location to the next, the measured load should not fluctuate as the swage is conducted. However, at approximately 3.8 inches of swage displacement the load increases until it reaches a maximum at 5.1 inches, and then falls back to its original level. This leads to the supposition that either the friction at the bore interface increased or the tube bore was smaller at the center of the tube length or other factors were at work. Assuming, for example, that the bore was smaller at that location, resulting in an interference of 1.06%, would increase the hoop strain as indicated in Figure 6.13, providing a better match with gathered data. Since hoop strain was measured at only one location, this supposition merely speaks to the uncertainty of the analytical prediction of residual stress in the tube.

6.4.2 Residual stress prediction

Residual stresses estimated by the finite element model using the reported mean bore interference of 1.03%, the flow curve for A516 Gr70 obtained from (Panontin, 1994), and a friction coefficient of 0.075 are shown in Figure 6.14. These stresses differ significantly from those obtained in the preliminary analysis in only one respect. Axial stress (σ_{zz}) at the tube inner diameter is large and tensile in a shallow layer in this analysis but was only slightly tensile in the preliminary analysis. These large tensile stresses result from the significantly higher friction coefficient used in the analysis for the reasons described previously.

Variations in residual stresses resulting from interference and flow properties are shown in Figure 6.15. As can be seen, the variation present in residual stress is fairly small with respect to the assumed variations in flow properties and interference. However, the increase in residual stress which accompanies the increase in friction coefficient is quite large, especially in the axial component, but this difference falls off with distance from the inner diameter. We might expect that actual residual stresses in the tube should fall within this range of variation if the range assumed for the parameters is reasonable.

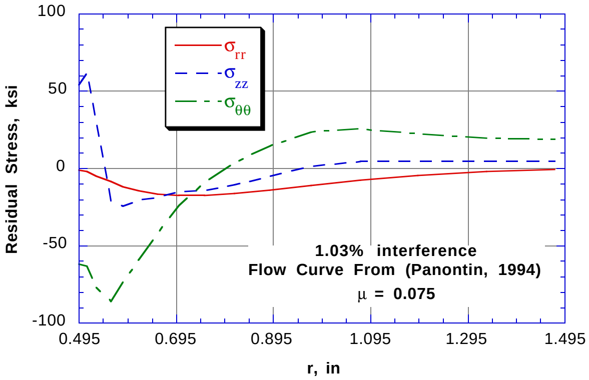

Figure 6.14 – Residual stress predicted to exist near the midlength of the tube by finite element analysis.

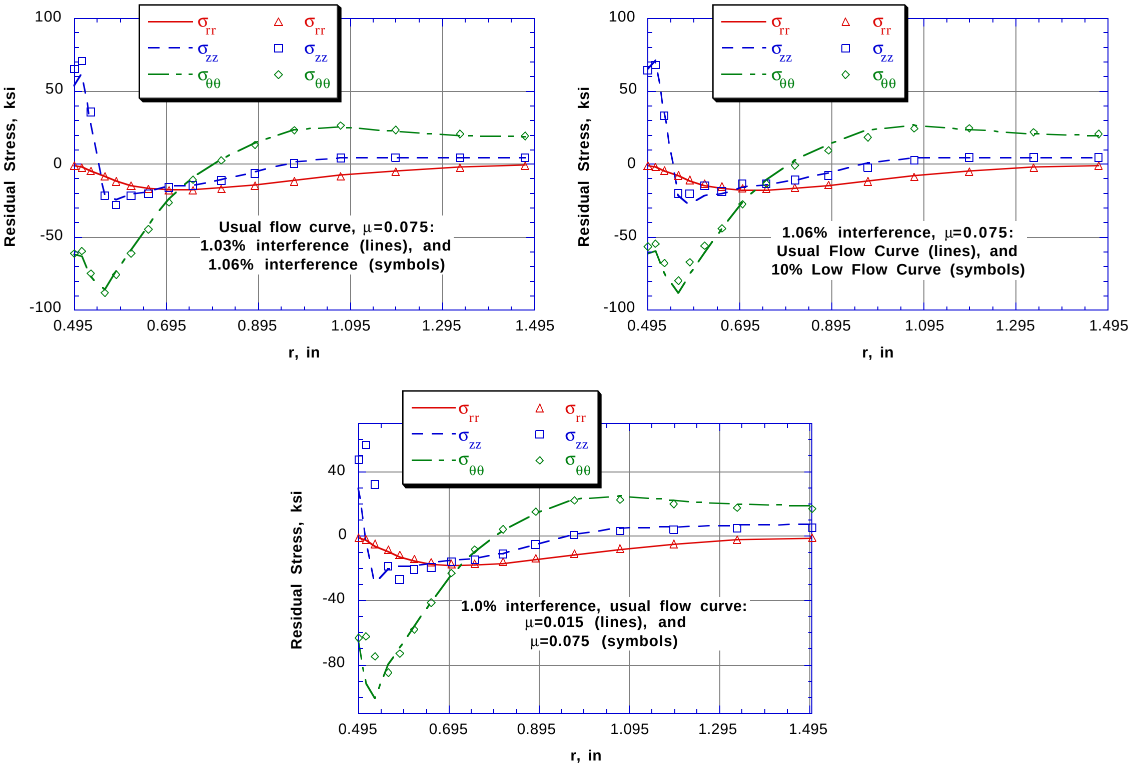

Figure 6.15 – Residual stress prediction for various variations of analytical parameters.

While we have investigated the variability of the residual stress with parameters in the analysis, there are other effects that we have not. Among these influences are modeling assumptions, including a von Mises plasticity model and a simple frictional contact model. These models represent conventional wisdom with regard to elastic-plastic analysis with contact; however, the models should not be expected to exactly match the physical processes occurring during swaging. Assumptions behind each of these models will have the greatest impact on stresses at the inner diameter where plastic straining is large and contact forces are imposed. Consequently, computational estimates of residual stress for the swage autofrettage process may be especially prone to error close to the inner diameter. Another assumption implicit in our analysis is that effects of machining of the tube are minimal. Clearly this is a simplification since it ignores both residual stress and material work-hardening caused by machining. Both initial stress and hardening will have an impact on plastic deformation near the inner diameter and so will alter the residual stress there. However, such stresses are usually shallow (i.e., a few thousandths of an inch deep).

6.4.3 Numerical verification of the axisymmetric eigenstrain method

To assess the performance of the measurement scheme developed in Section 6.3.1, we can simulate its application numerically. To do this, we make use of the eigenstrain determined from the simulation of the swage process which was described in Section 6.4.2. Imposing that eigenstrain in elastic models of the tube and the slice, free surface stress results on these two bodies are determined. Inserting these stresses in Equation 6.3, the eigenstrain is determined by inverting the system. Finally, residual stresses are computed from this eigenstrain on the midlength of the tube and compared to the results reported in Section 6.4.2.

Since the eigenstrain imposed by the swage process is not independent of axial position within the tube until the ball has passed some distance into the bore, free surface stress on the elastic-plastic tube model cannot be used directly in this verification. Instead, the stabilized eigenstrain field must be obtained from the analysis and imposed in an elastic finite element model. It is tempting to use the plastic strain from the swage analysis as the eigenstrain field. Unfortunately, this cannot be done for two reasons. First, the stress and strain in that model, following the swage, lie in a non-linearly deformed geometry. Accordingly, element sizes in the deformed and undeformed geometries are different. Even if the computation was executed on the *deformed* geometry, residual stresses which would result from using plastic strain as eigenstrain would still be grossly in error. This is due to the second problem with using plastic strain directly; the residual stresses and plastic strain in the swage analysis result from using incremental plasticity rather than deformation plasticity.

In deformation plasticity, the state of stress is completely determined by the total strain at a point. This model is frequently used to model monotonic processes. If deformation plasticity had been used to model the swage, the plastic strain could be used directly as eigenstrain. Incremental plasticity, on the other hand, defines plastic strain by tracking the change in stress which accompanies a change in loading. If the stress state at the end of an increment of loading would violate the assumed flow rule, plastic deformation is imposed to satisfy the flow rule. The incremental model must be used in cases where unloading occurs. For the swage process, material at the inner diameter yields in tension as the mandrel passes by, and then yields in compression as the outer part of the tube attempts to return to its initial state. This loading and unloading of the material mandates the use of incremental plasticity, and plastic strain cannot be used directly as eigenstrain to determine residual stress.

Instead of plastic strain, the negative of the elastic strain at the midlength of the swaged tube is used as the eigenstrain. Recall that residual stress in an elastic body is due only to eigenstrain. Now, consider the state of stress at the midlength of the swaged tube. Since the tube is free from applied loads, equilibrium is satisfied. Therefore,

$$\nabla \bullet \sigma = \nabla \bullet [\underline{C}(\varepsilon - \varepsilon^*)] = 0 . \tag{6.5}$$

For our purposes, any two eigenstrain fields which impose the same residual stress are equivalent. Assume that the negative of the elastic strain at the midlength of the tube is taken from the elastic-plastic swage analysis and is denoted $-\varepsilon_A^e$. If this field is now imposed as eigenstrain in an *elastic* model of the tube, the equilibrium equations become

$$\nabla \bullet [\underline{C} \bullet (\varepsilon + \varepsilon_A^e)] = 0 . \qquad (6.6)$$

Since equilibrium is satisfied at the midlength of the tube and the elastic constants do not depend on position, Equation 6.6 is satisfied for $\varepsilon = 0$, and the stress is given as

$$\sigma = \underline{C} \bullet \varepsilon_A^e . \qquad (6.7)$$

Stress computed directly from the elastic strain satisfies the equilibrium conditions at the midlength and therefore no further deformation is needed there. Near the free surface of the tube, however, and at all points in the slice, deformation will occur and stresses different than those at the midlength of the tube will result, as must be the case.

To numerically verify the axisymmetric eigenstrain technique, stresses at the measurement points are obtained by performing an elastic analysis which assumes that $\varepsilon^* = -\varepsilon_A^e$. These stresses are then used to solve for the eigenstrain parameters, and the estimated eigenstrain used to provide midtube stress estimates. The resulting estimates of residual stress at the midlength of the tube are shown with the exact stresses in Figure 6.16. As can be seen excellent results are obtained. However, errors are present in the axial component of residual stress near the inner diameter. These errors result from the assumed eigenstrain shape functions. These functions are not capable of resolving the scale of variation of the actual residual stress state at the inner diameter, and an error in stress

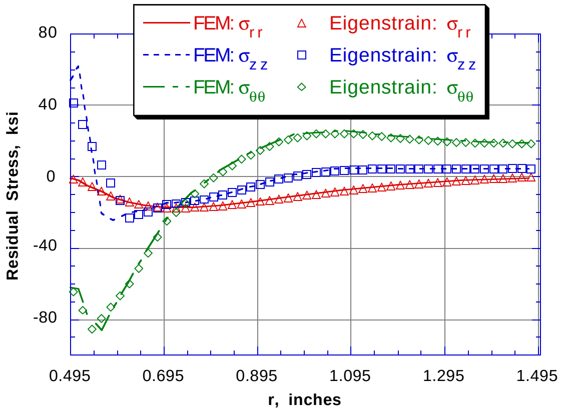

Figure 6.16 – Results of the eigenstrain method when stress is obtained from a finite element model.

results. Such errors must be expected when using a technique like the eigenstrain method that uses discrete measurement locations. (This matter is discussed in some detail in Chapter 7.) Despite the error present in the axial residual stress near the inner diameter, there is good agreement between FEM and eigenstrain results for the other residual stress components everywhere, and axial stresses are well predicted a small distance from the inner diameter. Therefore, we conclude that the eigenstrain method, as developed for application to an axisymmetric geometry, works with a reasonably high degree of accuracy. However, the variation of eigenstrain in the computational model is captured fairly well by the interpolation scheme developed, and residual stress in the tube and slice are known exactly (from the computation). If the eigenstrain field in the actual tube varies more sharply than indicated by the analysis, or if residual stresses are not fully relaxed with the sectioning process adopted, errors in stress estimates provided by the eigenstrain method will result which are not indicated by this numerical verification.

6.5 Comparison of measured and computed stress

Residual stresses predicted by the finite element method and measured by the eigenstrain technique are generally in agreement, as shown in Figure 6.17, except in the region near the inner diameter. Here, there is a significant discrepancy between the predicted and measured stresses, especially for the axial stress component. Away from the inner diameter, the results indicate generally lower levels of stress than are predicted by the model. That observation follows from the radial, axial, and hoop components of stress uniformly, regardless of the specific component.

One factor which influences the prediction of midtube residual stress by the eigenstrain method is the amount of residual stress which remains in the final section cut from the slice. When verifying the axisymmetric eigenstrain method in Section 6.4.3, stress was taken directly from the tube and slice models, ignoring residual stress existing in the final section. In Section 7.1.2 we will discuss the relation between stress release and dice size, and suggest that full stress release is assured if the local radius of curvature of the eigenstrain field, ρ, is larger than one-third the dice size, *d*. Assuming that this same guideline is applicable to the rectangular final section and taking *d* to be the length of the short side (0.3 inch), it follows that if ρ is smaller than 0.1 inch, incomplete stress relief should be suspected. As shown in Figure 6.18, axial eigenstrain determined from released stress indicates that $\rho < 0.1$ inch at the inner diameter and we conclude that stress likely exists in the final section.

Stress in the final section, denoted σ_{fs}, can be computed given the results of the elastic-plastic analysis of the swage. Just as was done for the tube and slice geometries, we use the negative of the elastic strain at the midtube of the elastic-plastic model as eigenstrain. The mesh used to model the final section is shown in Figure 6.19. Imposing the eigenstrain field in this finite element model of the final section gives stress results

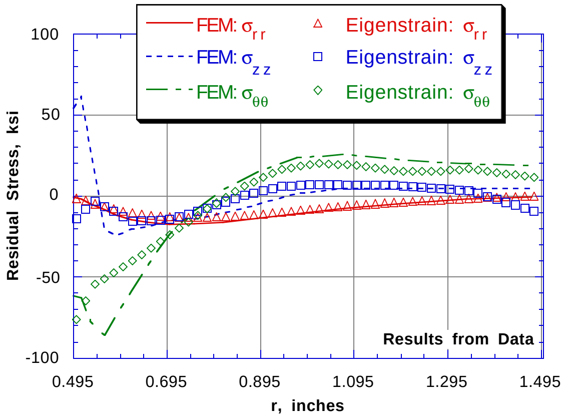

Figure 6.17 – Estimate of residual stress provided by measured stress and the eigenstrain method compared to finite element prediction of residual stress.

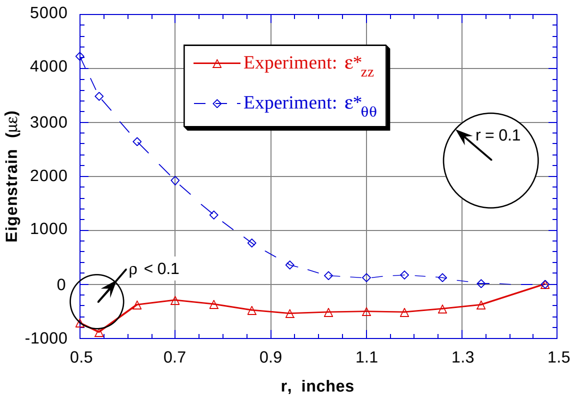

Figure 6.18 – Eigenstrain in the tube estimated from experimental measurements.

shown in Figure 6.20. According to this calculation, sizable stresses still exist in the final section. The amount of residual stress remaining in the final section will influence the results of the eigenstrain technique and should be accounted for in some way by the method.

Residual stress in the final section might be accounted for in the eigenstrain method by altering the linear system used to determine eigenstrain. The most obvious approach is to include σ_{fs} directly in the analysis. That is, we form a linear system relating stress to eigenstrain for the final section just as we did for the slice and the tube. Calling this system $\boldsymbol{M}_{fs}$, the following eigenstrain system results

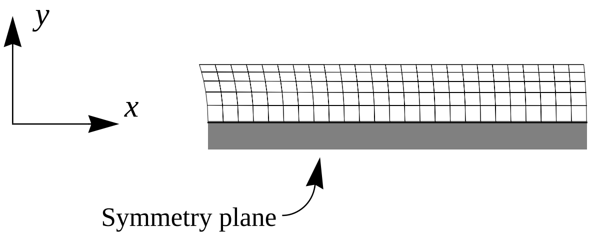

Figure 6.19 – Mesh used to model the final section. This model is three dimensional and has five layers of elements in the *z*-direction (out of the paper).

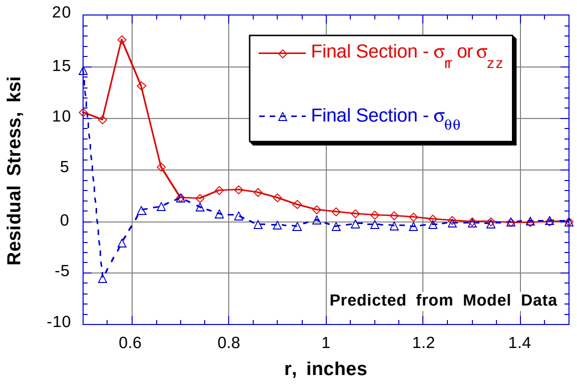

Figure 6.20 – Stress in the final section which exists when eigenstrain found from the elastic-plastic simulation is present.

$$\begin{Bmatrix} \sigma_s - \sigma_{fs} \\ \sigma_t - \sigma_{fs} \end{Bmatrix} = \begin{Bmatrix} \boldsymbol{M}_s - \boldsymbol{M}_{fs} \\ \boldsymbol{M}_t - \boldsymbol{M}_{fs} \end{Bmatrix} \{\varepsilon^*\} . \tag{6.8}$$

Now the left hand side of the equation represents what was measured experimentally: stress change from slice to final section and from tube to final section. Unfortunately, this linear system is poorly conditioned. The reason for the ill-conditioning has the physical interpretation that certain combinations of the interpolation functions for eigenstrain cause little stress change when the tube is sectioned. Accordingly, such variations cannot be estimated by the inversion of Equation 6.8.

We can illustrate the influence of stress remaining in the final section on the midtube stress estimates provided by the eigenstrain method by returning to the numerical verification detailed in Section 6.4.3. In this verification, we used stress determined directly from the slice and tube finite element models, assuming stress in the final section would be zero. With results from modeling of the final section, σ_{fs} can be subtracted from stresses in the slice and tube, and the resulting stress used to find the eigenstrain. The results of that procedure are shown in Figure 6.21. Here we see results similar to those provided by the experimental data. Residual stress at the inner diameter is not well predicted. Furthermore, there is similarity in the axial residual stress estimated by the

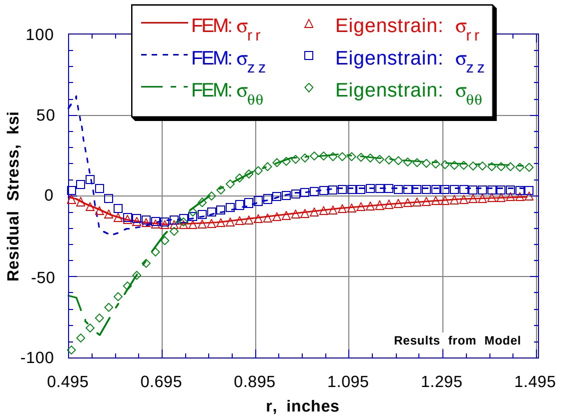

Figure 6.21 – Residual stress predicted when model data which account for stress in the final section are used in the eigenstrain method.

eigenstrain method when the data are taken from the experiment, Figure 6.17, or the model, Figure 6.21.

Examination of Figure 6.21 indicates that estimates of residual stress at the inner diameter are affected by the presence of stress in the final section. However, as shown in Figure 6.21, stress estimates more than 0.04 inch from the tube's inner surface are largely unaffected by ignoring σ_{fs}. From this, we expect that residual stress at the midlength estimated from the experimental data would also have good accuracy for radial positions greater than 0.54 inch. The results shown in Figure 6.17, however, indicate sizable differences between elastic-plastic modeling and experimental results for $r > 0.54$.

Differences in stress for $r > 0.54$ should not be attributed to systematic error in the eigenstrain method. To illustrate this point, we can compare the raw sectioning data with similar data from the elastic modeling of the tube, slice and final section. Examination of Figure 6.22 reveals that the stress change expected from modeling and that revealed in experiment are significantly different. In fact, at the inner diameter, the hoop stress change from slice to final section predicted from modeling is 40% larger than the experimental result. Since the data represented in these figures provide the input to the eigenstrain method, better agreement between elastic-plastic modeling and results of the eigenstrain method would be surprising.

Further, systematic errors in measured strains, from which stress change is computed, are fairly small. Taking the maximum standard deviation of any of the set of four strain measurements reported, 12 $\mu\varepsilon$, we compute an expected maximum standard deviation in stress release of 1.0 ksi. This expected error is much smaller than differences between the model and experiment. Apparently there is a sizeable difference between residual stress actually introduced by the swage and computed by simulation of the process with elastic-plastic finite element modeling.

To further investigate the difference between the actual swage and the elastic-plastic model, a simple experiment was conducted. A small arc specimen was removed from the tube, as shown in Figure 6.23. This specimen will have different residual stresses than those which exist in the tube, but these stresses are still determined by the swage-imposed eigenstrain. We determine residual stress near the inner diameter of this specimen by using the strain gage hole-drilling method, applying it in the same way we detailed in Chapter 4 and realizing that its accuracy will be on the order of ±5 ksi. These measurements indicate that residual stresses averaged over the first 0.004 inch from the surface of this specimen are +81 ksi in the axial direction and +50 ksi in the hoop direction.

Elastic finite element calculation, using the geometry of the removed specimen and eigenstrain from the elastic-plastic model, can also provide stress estimates. A finite element mesh was constructed to represent the geometry of the removed arc-shaped specimen. The negative of the elastic strain at the midtube predicted by the elastic-plastic simulation discussed earlier was then imposed on this model as eigenstrain, and residual stress in the specimen determined. Results of this analysis show that the elastic-plastic model predicts hoop and axial stresses in the arc specimen of +45 ksi and +7 ksi,

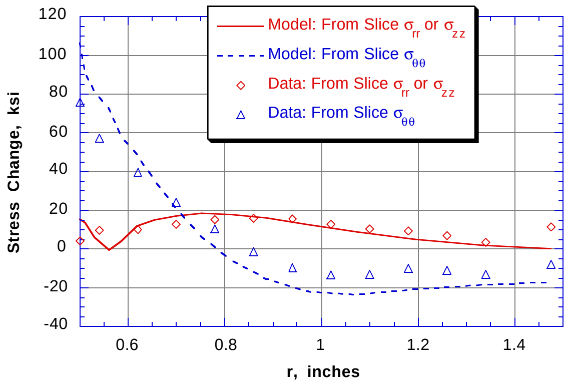

a) Slice to final section stress change.

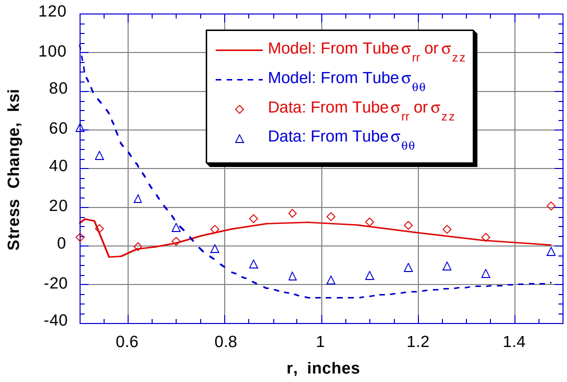

b) Tube to final section stress change.

Figure 6.22 – Measured and predicted stress change accompanying geometry change from (a) slice to final section, and (b) tube to final section.

respectively. These results are quite different from the results found by hole drilling, even given the uncertainty of that technique. This experiment shows, in another way, that the elastic-plastic modeling of the swage is less than perfect.

Possible sources of error in the elastic-plastic simulation which have not been specifically addressed here are errors due to modeling assumptions and mesh refinement. Errors caused by modeling assumptions were discussed at the end of Section 6.4.2. To further address the influence of mesh refinement on residual stresses estimated by the elastic-plastic simulation, two additional finite element meshes were created. The first additional mesh was obtained by scaling the length of the tube mesh shown in Figure 6.12 by one-half. The scaling in length changes the element size in the axial direction of the tube from 0.04 inch to 0.02 inch. The second additional mesh is shown in Figure 6.24 and has twenty elements in the radial direction. The axial element pitch in this mesh varies from 0.074 inches at the tube entrance to 0.018 inches at the tube midlength. The variation of element size with axial direction was included to reduce the total number of elements in the model (thus reducing the computational burden) while providing an approximately 0.02 inch element pitch near the midlength of the tube. Residual stresses computed on these three different meshes, the one used to provide stress estimates discussed in Section 6.4.2 and the two additional meshes just described, are shown in Figure 6.25. All of these analyses assume a 1.03% interference, a friction coefficient of 0.075, and the flow curve determined by Panontin (shown in Figure 6.4), so differences between models are due only to differing mesh refinement.

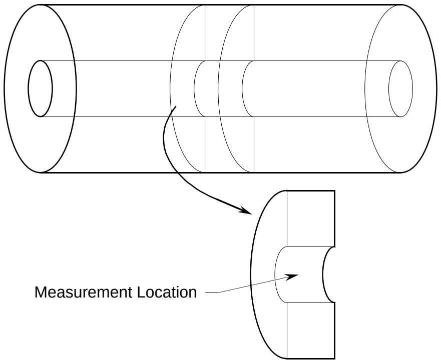

Figure 6.23 – Arc specimen removed from the tube to investigate residual stress near the inner diameter.

The results presented in Figure 6.25 indicate that additional mesh refinement greatly changes residual stress estimates at the inner diameter. The stress estimates discussed in Section 6.4.2 are denoted “15 elements” in Figure 6.25, reflecting the number of elements in the radial direction of the model used to produce them. Stress estimates from the axially-scaled model are denoted “15 elements (short)”, and those from the model shown in Figure 6.24 are denoted “20 elements”. Axial stress at the inner diameter of the tube is nearly doubled by increasing the level of refinement in the axial direction. This trend is shown by both refined models. Hoop stress at the inner diameter is also altered with mesh

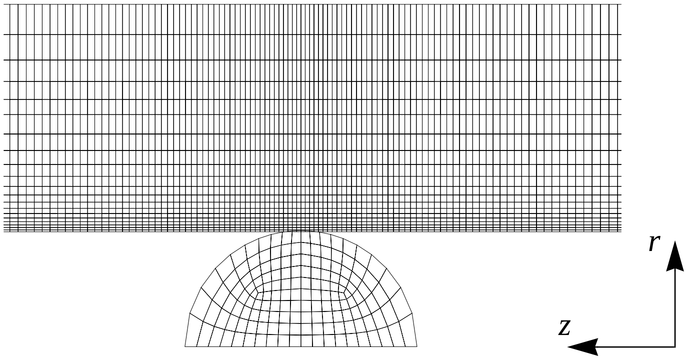

Figure 6.24 – Finite element mesh constructed to investigate mesh refinement. Mesh shown at the midlength of the tube.

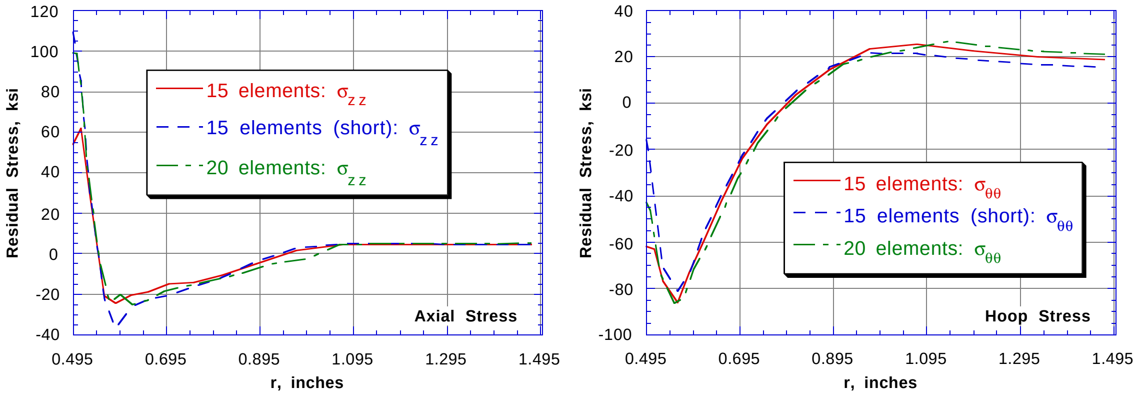

(a) (b)

Figure 6.25 – Influence of mesh refinement on residual stresses predicted at the midlength of the tube. (a) Axial component, and (b) hoop component of residual stress.

refinement. The axially-scaled model shows a larger shift in hoop stress predicted at the inner diameter than does the twenty-element model, but both indicate a sizable increase in hoop stress at the inner diameter. Away from the inner diameter neither the hoop stress nor the axial stress show a significant change. Residual stress estimates provided by these two additional models indicate that the results presented earlier, in Section 6.4.2, are relatively free of errors due to mesh refinement, except very close to the inner diameter.

6.6 Conclusions

This chapter illustrates several key features of the eigenstrain method and the procedures used in this thesis to investigate residual stress measurement techniques. The geometric extensibility of the eigenstrain method was demonstrated by adapting it to an axisymmetric geometry. The axisymmetric method was verified by *elastic* finite element based simulation of the measurement scheme, which proved valuable. When the experimental application of the eigenstrain method indicated that erroneous results were produced relative to an assumed residual stress state, again the finite element technique was applied to elucidate sources of error. Behind these efforts, the ability to impose eigenstrain in an elastic analysis and compute residual stress allowed the work to be performed. Furthermore, by understanding the nature of residual stress problems from the eigenstrain viewpoint, issues complicating residual stress determination by sectioning are elucidated.

Experimental efforts to verify the eigenstrain technique are hampered by the apparent inability of elastic-plastic finite element analysis to accurately simulate the swage process. This point is illustrated by examination of sectioning results for stress change that occurs when a small piece of material (the final section) is removed from a slice, which was in turn removed from the middle of an autofrettaged tube. Comparing the stress change predicted by modeling with experimental results reveals that stresses predicted by the swage simulation are significantly larger than those which actually exist in the tube.

Despite the divergence of experiment and elastic-plastic simulation, this experiment clearly demonstrates the inability of the eigenstrain method to resolve small scale variations in eigenstrain. Both the simulation and hole-drilling results indicate that a large tensile residual stress is present in the axial direction at the inner diameter of the swaged tube. The eigenstrain method fails to predict this stress. Further investigation reveals that stresses which remain in the final section hinder the ability of the method to predict the presence of the axial stress. By measuring stress release accompanying further sectioning of this small piece, the eigenstrain method should, in principle, be able to reveal the axial stress with better accuracy. This was not pursued due to the small scale on which sectioning would have to have been performed.

Chapter 7

Localization of the Eigenstrain Method

Chapter 3 suggests that the eigenstrain method is better than competing sectioning techniques. Chapter 4 presented a numerical study that illustrated that the method is capable of estimating residual stress in the middle of a welded plate with good accuracy. However, the eigenstrain method relies on extensive instrumentation and sectioning. In this chapter we develop a localization of the eigenstrain technique, which allows stress estimates to be made inside a small region of interest near the weld bead. For prediction of fatigue and fracture of welded structure, the weld bead is the most critical region since this is where defects and high tensile residual stresses exist. For fatigue and fracture prediction for a welded joint, then, residual stresses need only be determined near the bead. Typically, the transverse extent of the weld bead is on the order of the thickness of the welded plate. Hence, we set out to formulate a method capable of determining weld residual stress in the hexahedral region shown in Figure 7.1.

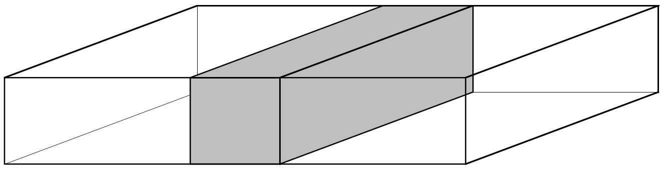

Figure 7.1 – Region of interest within a block of material where residual stress is to be determined by the localized eigenstrain method.

7.1 A one-dimensional example

The localization of the eigenstrain method can best be explained by examination of a simple example. Suppose we wish to determine the eigenstrain field which causes residual stress in a thin strip of material as shown in Figure 7.2. Let us further assume that the eigenstrain field present in this body is dependent only on the coordinate *x*, directed along the length of the strip. If the eigenstrain field is known, residual stress is found by solving a plane stress elasticity problem. This example is therefore a two-dimensional stress problem due to an eigenstrain field distributed in one-dimension.

For planar elasticity, the compatibility conditions reduce to

$$\frac{\partial^2 \varepsilon_{xx}}{\partial y^2} + \frac{\partial^2 \varepsilon_{yy}}{\partial x^2} = \frac{\partial^2 \varepsilon_{xy}}{\partial x \partial y}. \tag{7.1}$$

Restricting ourselves to an eigenstrain field which depends only on *x*, Equation 7.1 shows that any $\varepsilon^*_{xx}(x)$ or $\varepsilon^*_{xy}(x)$ will satisfy compatibility, therefore causing deformation but not stress. Accordingly, residual stress is caused only by $\varepsilon^*_{yy}(x)$.

Timoshenko (1970) presents the elasticity solution to the problem of a strip subject to a sinusoidal temperature variation in *x*. This solution can be used to solve for stress in the presence of $\varepsilon^*_{yy}(x)$ as follows. Stress due to thermal strain is an eigenstrain problem in which ε^* is the unit tensor multiplied by thermal expansion, α, and the temperature field, T, given by

$$\varepsilon^* = \begin{bmatrix} \varepsilon^*_{xx} & \varepsilon^*_{xy} \\ \varepsilon^*_{xy} & \varepsilon^*_{yy} \end{bmatrix} = \alpha T \begin{bmatrix} 1 & 0 \\ 0 & 1 \end{bmatrix}. \tag{7.2}$$

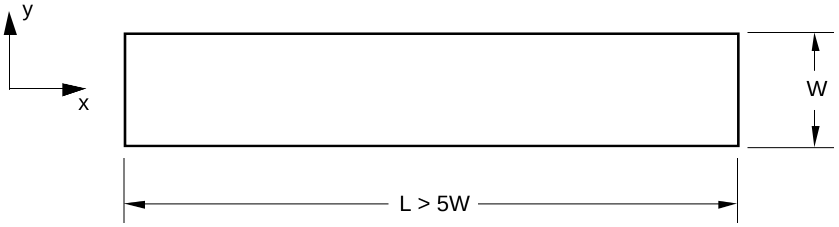

Figure 7.2 – Strip in which eigenstrain is distributed.

Since the temperature varies only with *x* in this problem, the presence of $\varepsilon^*_{xx}(x)$ will not give rise to stress. The solution discussed by Timoshenko, then, gives the stress due to a planar eigenstrain field in which

$$\varepsilon^*_{yy}(x) = \alpha T_o[\sin(\omega x)]. \tag{7.3}$$

where T_o and ω are the amplitude and frequency of the distribution, respectively. For a general distribution of eigenstrain with *x*, a Fourier series solution can be used to arrive at the stress. We will return to this simple problem later to assess the accuracy of the localized eigenstrain method.

We now discuss the task of *localizing* the eigenstrain method. The goal of the localized method is to provide stress results within a specific region of interest while only requiring measurements to be made within that region. If the localization is successful, the localized method will retain the ability of the eigenstrain method to estimate residual stress in regions where stress was not measured.

Consider the region of interest shown shaded in Figure 7.3(a) and suppose that the actual eigenstrain in the strip is distributed as shown in Figure 7.3(b). To determine the

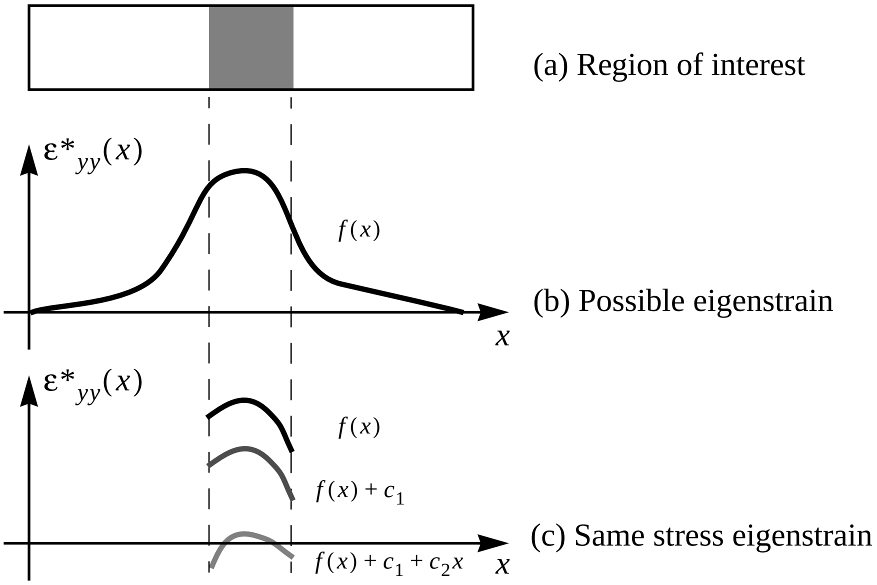

Figure 7.3 – Region of interest within a strip, a possible eigenstrain distribution, and different eigenstrain distributions which would cause the same stress in the chunk.

stress in the region of interest, the region of interest would be cut free and then diced to relieve all the stress, as shown in Figure 7.4. In this figure, the region of interest is lightly shaded and the region to be diced is shown darker. We refer to the removed region of interest as the “chunk”. The eigenstrain distribution in the chunk is that between the dashed lines in Figure 7.3(b). However, because compatibility allows for an arbitrary addition of a linear function of x without a change in stress, any of the distributions shown in Figure 7.3(c) will cause the same stress in the chunk. These three distributions will, however, cause different stress to arise in the slice, since material surrounding the chunk-region will restrict deformation corresponding to the arbitrary linear eigenstrain distribution. Eigenstrain found from stress in the chunk, then, is the eigenstrain present in the region of interest within the slice, up to an unknown linear function of x.

For the sake of notation, we refer to the slice as geometry “A”, and the chunk as geometry “B”. The part of the eigenstrain determined from stresses in the chunk is then referred to as ε^*_B. To find ε^*_B from stress present in the chunk, the discretization shown in Figure 7.5(b) is used. When each of the three shape functions shown are scaled by individual “nodal” values of eigenstrain, and these scaled functions summed, a three parameter piecewise-linear distribution results. Further, any combination of nodal values will result in a distribution which is zero at both edges of the chunk. This ensures that no constant or linear distribution of eigenstrain is present in the chunk, as the chosen shape functions specifically exclude them. We use a *three* parameter interpolation because there are *three* measurement locations along the x-direction. Having the same number of interpolation and measurement stations along the x-direction ensures a well condition linear system to be used to determined the interpolation parameters.

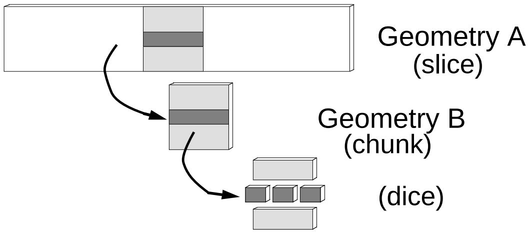

Figure 7.4 – Sectioning procedure for a strip containing a longitudinal variation of eigenstrain, showing the slice, chunk, and dice.

To achieve an estimate of residual stress in the region of interest prior to sectioning, the unknown linear function and an estimate of the eigenstrain lying outside of the region of interest must be determined. We combine both these parts of the eigenstrain into ε^*_A. The discretization of ε^*_A is shown in Figure 7.5(c). The linear function is recovered by the two shape functions within the region of interest, and the eigenstrain external to the region of interest is represented simply by the two sawtooth functions outside. Stress in the slice, σ_A, estimated from slice-to-chunk-to-dice strain release measurement, is used with stress in the slice caused by ε^*_B to find ε^*_A.

Since stress estimates outside of the region of interest are not required, the crude sawtooth functions used to represent eigenstrain there are satisfactory. These capture the misfit along the cutting planes between the slice and the chunk which allows stress in the region of interest to be adequately captured. The sawtooth does not give reasonable stress estimates outside of the region of interest, but the motivation for the method lies in the fact that those estimates are not required.

We now turn to the measurement system used to estimate residual stress caused by $\varepsilon^*_{yy}(x)$. Taken together, there are seven nodal values of eigenstrain to estimate, three in ε^*_B and four in ε^*_A (Figure 7.5). We place a biaxial strain gage at each of the nodal points x_1, x_2, and x_3 shown in Figure 7.5(b). These gages lie at the midwidth of the strip, and the sample is sectioned as shown in Figure 7.4. At each point, biaxial gages measure ε_{xx} and ε_{yy} released during each geometry change. We measure the strain change from

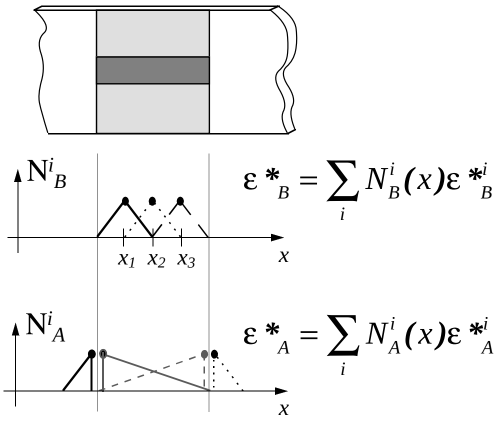
N^i_B
$\varepsilon^*_B = \sum_i N^i_B(x)\varepsilon^{*i}_B$
x_1 x_2 x_3
x
N^i_A
$\varepsilon^*_A = \sum_i N^i_A(x)\varepsilon^{*i}_A$
x

(a) Region of interest

(b) Shape functions for ε^*_B

(c) Shape functions for ε^*_A

Figure 7.5 – Shape functions used to discretize the eigenstrain.

slice to chunk and from chunk to dice. The strain changes allow calculation of biaxial residual stress at the three points in the chunk and in the slice by using the usual Hookean plane stress relation. We assume that the dice are small enough in relation to the variation of eigenstrain that they contain no stress. A discussion of how dice size impacts the stress release can be found below, in Section 7.1.2. In total, then, there are twelve known stress components, six in the chunk and six in the slice. The seven parameters of ε^*_B and ε^*_A can be determined from these twelve measured stress components by using a least squares solution.

The above procedure determines a system of eigenstrain which produces an estimate of residual stress at the node points within the slice and chunk. The distribution of residual stress with y is found in the slice by imposing ε^*_B and ε^*_A in a finite element model, as described in Section 4.2.2. Recovery of the y-distribution of residual stress at each nodal location in x makes the eigenstrain method attractive in this example. Strains are measured at one y-coordinate, the mid-width, and residual stress is estimated across the strip. (This is accomplished from knowledge that the eigenstrain is independent of the y-coordinate. In practice, such assumptions about the eigenstrain distribution must be made from knowledge of the manufacturing processes which introduced the residual stress, just as we have done for the case of continuous welding in Chapter 4.)

7.1.1 Localized eigenstrain method applied to the strip

Now that we have presented the localized eigenstrain method, we examine its accuracy for a strip with a sinusoidal axial variation of eigenstrain. Since we have the analytical solution for this problem (Timoshenko, 1970), we can compare the estimates of residual stress with that solution. Results for this example are presented in a non-dimensional form, so that material properties are not needed. (One could assume material properties typical of steel, $E=30\text{x}10^6$psi, $\nu=0.3$, and $\alpha=6\text{x}10^{-6}$in/in/°F.) The strip is shown in Figure 7.2, and the region of interest is shown in Figure 7.3(a). The width of the strip which is taken to be 1.5 inches and the length of the region of interest to be 1.2 inches. The region of interest is far enough from the ends of the strip that the strip may be assumed to have infinite length. The coordinates chosen are centered on the region of interest, both in length and width. Accordingly, stresses caused by the sinusoidal eigenstrain field will be symmetric in the *y*-coordinate and anti-symmetric in *x*.

Suppose that strain changes are measured at x=-0.4, x=0, and x=0.4 inches at the mid-width of the strip, giving a spacing between gages, h, of 0.4 inches. Spacing of these strain measurement locations was chosen as a physical constraint by considering the feasibility of dicing. Two-tenths of an inch is allowed from the center of the measurement location to the centerline of the cut. Cutting in such close proximity to strain gages is indeed possible, as demonstrated in Chapter 6, by using electric discharge machining (EDM). Nodal locations for the eigenstrain distribution within the region of interest (x_1, x_2, and x_3 in Figure 7.5(b)) are chosen to be at x=-0.3, x=0, and x=0.3. These locations provide equal spacing between nodes and from x_1 and x_3 to the chunk boundary. As will be shown in the next section, choosing node points in this way provides better results than choosing the nodes to be at the strain measurement locations. The sawtooth functions used to estimate the eigenstrain external to the region of interest each have a base width of 0.4 inch, the same as the spacing between strain measurement points, h.

The solution for eigenstrain depends on obtaining residual stress estimates at points in the chunk and in the slice. As was done in Chapter 4, we do not address the experimental uncertainties which would arise in obtaining these measurements, but rather obtain the values from a finite element simulation. In this way, we are merely trying to justify the approach to localization proposed here.

To investigate the accuracy of the localized method with respect to the amount of variation of eigenstrain, we vary the frequency of the sinusoidal distribution, ω, in Equation 7.3. Results for frequencies of $\omega=\pi/(0.67h)$, $\pi/(2h)$, $\pi/(3h)$, and $\pi/(4h)$ are shown in Figure 7.6 along the line x=0.4. Since the stresses in the slice and chunk are anti-symmetric about x=0, errors on the line x=-0.4 are the same as those shown in the figure, only of opposite sign and errors on the line x=0 are negligible. As can be seen, the localized technique produces good results when compared to the analytical solution provided by Timoshenko. Errors present are greatest at the point furthest from the measurement site, namely, the top and bottom edges of the strip. The case with the most error has the largest frequency, $\omega=\pi/(0.67h)$. The eigenstrain field cycles three-quarters of a period between measurement points at that frequency, so that the linear interpolation adopted is not capable of fully reproducing the eigenstrain present in the strip. Therefore, nearly 50% error in stress estimate is present for that case. Overall, however, the method does a good job at estimating the residual stresses produced by the eigenstrain field based on relatively few measurements.

Errors present in the stress estimates come from several sources, including the residual stress input to the eigenstrain method, the interpolation of the eigenstrain, and the refinement of the computational mesh used to determine the eigenstrain system. Stresses input into the linear system used to find eigenstrain are taken from a finite element model of the strip or the chunk. The finite element mesh used to find these stresses is shown in Figure 7.7(a). This mesh is adequately refined to give accurate stress estimates at the mid-width of the strip and chunk for cases in which $\omega<\pi/h$. For the case when $\omega=\pi/(0.67h)$, error is present in the stress computed by FEA, as shown in Figure 7.8.

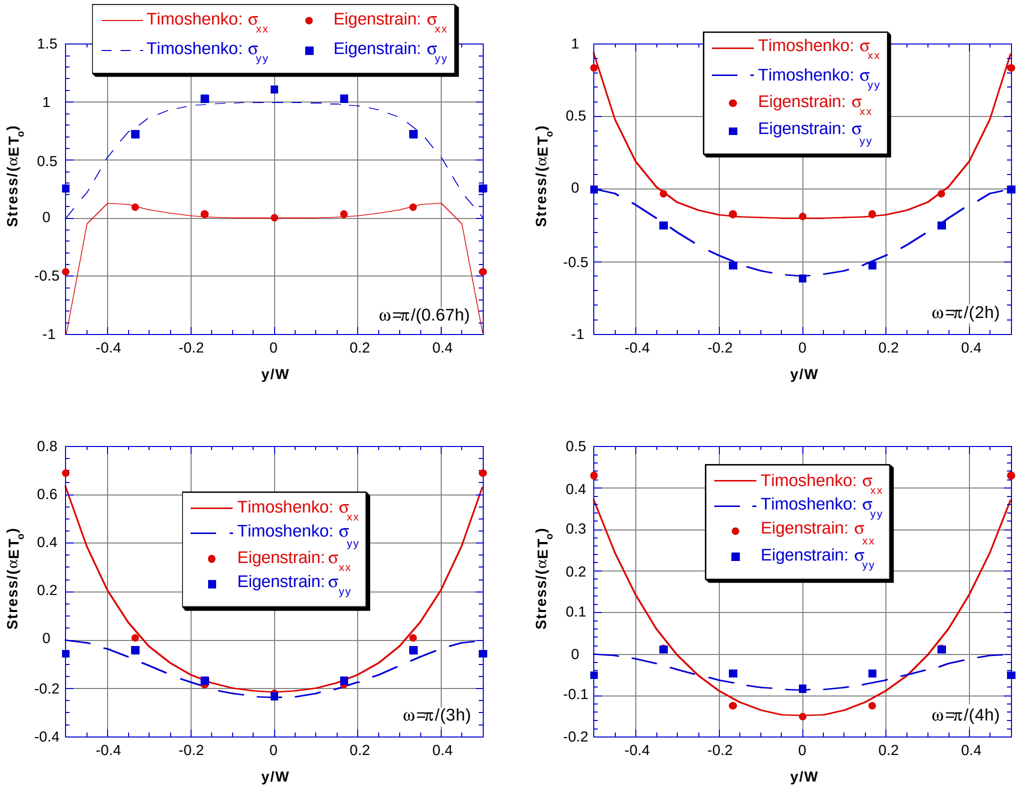

Figure 7.6 – Results of the localized eigenstrain method for a strip subject to a sinusoidal temperature variation $T(x) = \alpha T_o[\sin(\omega x)]$ of varying frequency.

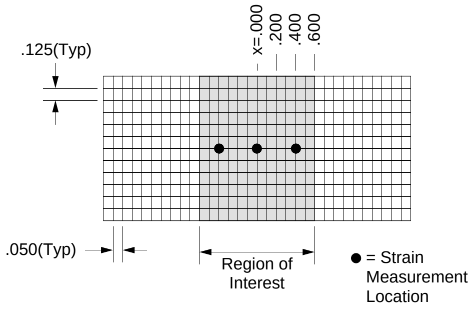
.125(Typ)
x=.000
.200
.400
.600
.050(Typ)
Region of Interest
● = Strain Measurement Location

a) Mesh used to obtain stress estimates.

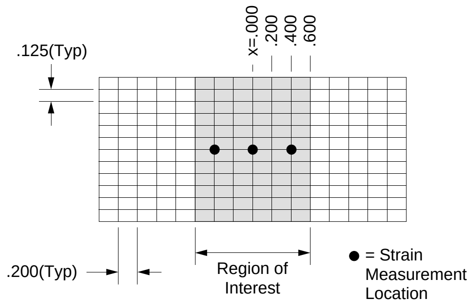
.125(Typ)
x=.000
.200
.400
.600
.200(Typ)
Region of Interest
● = Strain Measurement Location

b) Mesh used to form the eigenstrain linear system.

Figure 7.7 – Finite element meshes used to a) obtain stress estimates for input to the localized eigenstrain method, and b) form the linear system for eigenstrain estimation. For the strip, the meshes extend to the left and right, with the same mesh density, to x=±4. For the chunk geometry, elements outside the shaded region are deleted from the mesh.

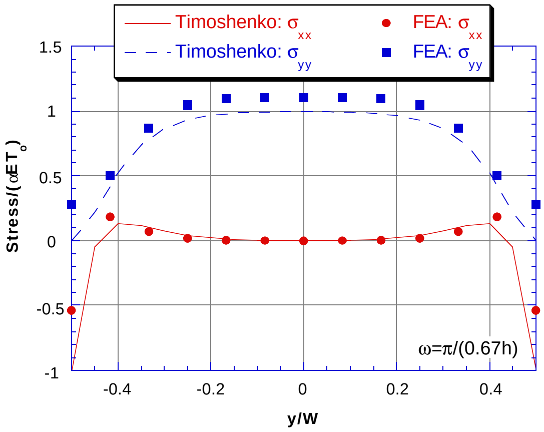

Figure 7.8 – Exact and FEA estimate of stress for the case $T(x) = \alpha T_o[\sin(\pi x/(0.67h))]$.

Naturally, these errors contribute to errors in stress estimates provided by the localized eigenstrain method.

Another source of error for the localized eigenstrain method is the spacing of the interpolation grids used for strain measurement and eigenstrain distribution. Because of this spacing, there is an upper limit to the frequency of oscillation which can be accurately captured. An excellent example of a distribution of eigenstrain which causes drastically incorrect estimates of stress is the case when $\omega=\pi/h$. At this frequency, there is no stress present at any of the strain measurement points in the slice. On the other hand, there is shear stress present on lines of constant x at x_1, x_2, and x_3 in the strip. The eigenstrain method fails to predict these shear stresses, as shown in Figure 7.9. This plot is similar to those in Figure 7.6, except that we have plotted shear stress, σ_{xy}, in place of σ_{xx}. The choice of strain measurement spacing has a large impact on the ability to measure stress with the eigenstrain method. However, such errors are not restricted to this method, and are the natural result of any measurement technique which uses discrete measurement locations. Some knowledge of the underlying residual stress field must be obtained in order for the measurement locations to be identified. In the absence of such knowledge, errors like those shown in Figure 7.9 must be expected.

Another way in which errors accumulate in the eigenstrain method is the refinement of the finite element mesh used in formulation of the eigenstrain system. The mesh used for

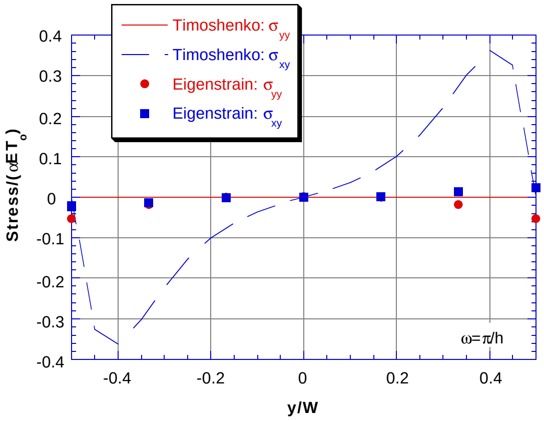

Figure 7.9 – Results of the localized eigenstrain method for a strip subject to a sinusoidal temperature variation $T(x) = \alpha T_o[\sin(\pi x/h)]$.

this example is shown in Figure 7.7(b). There are two elements between each strain measurement location, and twelve elements evenly spaced in the vertical direction. This mesh is not well-refined, so stresses near the top and bottom edges of the strip are not well estimated. The errors due to this lack of refinement show up in the estimates of residual stress for the cases $\omega=\pi/(3h)$ and $\omega=\pi/(4h)$. Specifically, σ_{yy} at the top and bottom edges of the strip should be zero, since the edge is traction-free, but as shown in the lower two plots in Figure 7.6, this is not the case. Such errors are typical of insufficient mesh refinement.

Despite all of these sources of error present in the eigenstrain method, the method is capable of producing good results, as demonstrated in Figure 7.6. And, most importantly, the quality of the results is relatively independent of the frequency of $\varepsilon^*_{yy}(x)$. This is especially important for the practical case where the underlying frequency of the distribution is unknown, or when the distribution is other than sinusoidal. Since a non-sinusoidal distribution can be constructed by a Fourier series, the ability to approximate the stress due to the sinusoidal variation is fundamental. As long as the frequency of the sinusoidal distribution is smaller than $\pi/(2h)$, where h is the spacing between measurement locations, the localized method works well. Accordingly, for non-sinusoidal distributions, only the frequency content below this value can be reliably estimated. As stated previously, the connection between measurement spacing and quality of estimated stress is fundamental to all measurement techniques that use discrete locations, not only the method examined here.

The overall concept of the localized eigenstrain method proves to be very valuable for several reasons. First the method allows one to obtain stress estimates only within a region of interest of a body. Also, because the method makes use of information about the process which induced the eigenstrain, it is capable of producing results with less experimental effort than other techniques. These principles were illustrated in an example. First, a region of interest was selected in which residual stresses were to be determined, the small rectangular region shown in Figure 7.3(a). Then, it was determined that the eigenstrain field present in this body is distributed only as a function of position down the strip. Under these conditions, an eigenstrain technique was developed that uses only six strain measurements taken at the mid-width of the strip, two measurements at each of three locations, and a second set of six measurements in the chunk. From these few measurements, the localized eigenstrain technique was used to determine the residual stress across the width of the strip at each of the three locations along the length of the region of interest.

7.1.2 Effect of dice size on stress release

The stress caused by a sinusoidal variation of eigenstrain in a strip can also be used to investigate the effect of finite dice-size on stress release. Consider the state of stress resulting from a temperature variation given by

$$T(x) = \alpha T_o \sin\left(\frac{\pi x}{b} + \frac{\pi}{2}\right). \tag{7.4}$$

This temperature variation differs from that given in Equation 7.3 only by a phase shift of $\pi/2$ and a different definition of frequency. These changes result in a temperature distribution that has a fundamental period of 2*b* and that causes maximum stress magnitude at $x = 0$. According to Timoshenko, stress at the center of the strip, $x = y = 0$, depends on the ratio of the half-period of the temperature distribution, *b*, to the width of the strip, *W*.

The relationship between stress at the center of the strip and *b/W* is shown by the curves in Figure 7.10 and was derived from the solution reported by Timoshenko. When the half-period is much smaller that the strip width $(b \ll W)$, σ_{xx} is zero and σ_{yy} is large and compressive. Conversely, when $b \gg W$, both stress components tend to zero. The symbols in Figure 7.10 show the relationship between stress at the center of a square geometry (with edge-length *W)* and *b/W*, which is not substantially different from the trend for the slice. The results for the square are found from finite element computation using the mesh shown in Figure 7.7(a) but scaled in *x* to obtain a square.

To release stress in the strip due to a particular frequency of eigenstrain variation, the width of the strip can be reduced by sectioning. Assume that the half-period of the temperature distribution, *b,* is held constant. Further assume that a small strip of width *d* in the *y*-direction, and length large compared to *d* in the *x*-direction, is removed from the center of the larger strip. To release stress, *d* must be small compared to *b*. According to the lines in Figure 7.10, if $d = b/3$, transverse stress in the strip will be small. Results for the square geometry show that if a square dice of size $d = b/3$ is cut from the center of the strip, both transverse and axial stress in the dice will be small. It is interesting to note that for a particular value of *b/W*, removing a square of size *W* from the strip does little to release stress in the transverse direction, but does change the axial stress.

Now, consider the more common situation where residual stress is relieved by sectioning without prior knowledge of the underlying eigenstrain distribution. From Fourier analysis, we know that a general distribution of temperature (or eigenstrain) is made up of a series of sinusoidal functions. The results presented in Figure 7.10 demonstrate that by cutting square dice of size *d*, stresses due to eigenstrain frequency content given by $b > 3d$ are (almost) completely released. But, stresses due to eigenstrain frequency content given by $b < (d/4)$ are not released at all. Stress due to eigenstrain with frequency content given by the range $(d/4) < b < 3d$ are partially released.

As an example, we return to the range of temperature distributions analyzed in Section 7.1.1. The frequency of the distribution was given in terms of the spacing between stress measurement locations, *h*, which was assumed to be 0.4 inch. If square dice cut from the strip are *d* = 0.4 inch on each side, we can discern the stress release achieved for each frequency investigated. These results are summarized in Table 7.1. Significant stress

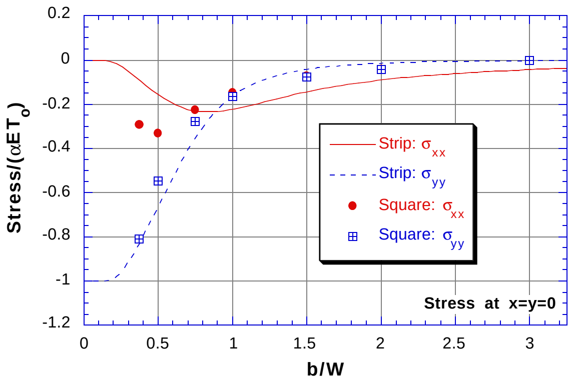

Figure 7.10 – Relation between *b/W* and stress at the center of the strip and the square. Stress components in the square are nearly equal for *b/W* > 1.5 and they cannot be distinguished in the plot.

remains in the dice only for the case when $b = 0.268$. When $b = 0.800$, a small amount of stress remains but the initial stress was also small.

ω	b (inch)	b/W	b/d	σ_{xx} released (%)	σ_{yy} released (%)
$\pi/(0.67h)$	0.268	0.179	0.67	$-5900^{\dagger}$	65
$\pi/(2h)$	0.800	0.533	2.0	79	93
$\pi/(3h)$	1.20	0.800	3.0	99.5	99.5
$\pi/(4h)$	1.60	1.07	4.0	100	100

Table 7.1 *– Stress release from strip to dice for various frequencies, h=d=0.4 and W=1.5.*

† Axial stress change as a percentage is extremely large for $b = 0.286$ because axial stress initially in the strip is very nearly zero.

Of course, when one performs an experiment, the critical thing to know is whether dice were cut small enough to fully release the residual stress. The frequency content of the released stress could be used as an indicator of the level of stress release, but a simpler approach is more helpful. Full stress release is assured if the compatibility relations of elasticity are satisfied within the dice. From a practical point of view, residual stress is released if compatibility is nearly satisfied. In the context of the current problem, compatibility is satisfied if $T_{,xx} = 0$ at every point in the dice. From calculus recall that the second derivative of a function $f(x)$ is related to the local radius of curvature, ρ, of that function by

$$\rho = \left| \frac{[1 + (df/dx)^2]^{3/2}}{d^2 f/dx^2} \right| . \tag{7.5}$$

The radius of curvature provides a physical vantage point from which to interpret stress release data. For the sinusoidal temperature variation given in Equation 7.4, the local radius of curvature of $T(x)$ at $x = 0$ is given by

$$\rho = \left(\frac{b}{\pi}\right)^2 . \tag{7.6}$$

Figure 7.11 shows the relationship between stress release and ratio of dice size to radius of curvature, d/ρ. Here we see that practically all stress is released if $d/\rho < 3.0$.

From these observations regarding stress release in the case of a sinusoidal variation of temperature, we can form a general criterion for the assurance of full stress release by dicing. These results suggest that if dice are smaller than three times the radius of curvature of the underlying eigenstrain field, nearly complete stress relief will be obtained. If the eigenstrain field has a smaller radius of curvature than one-third the dice size, only partial stress relief will be obtained. This partial stress relief is important, because it can reveal when incomplete stress release has taken place. To investigate the possibility of incomplete stress relief, one proceeds in the usual way. Measured stress change is used to determine the eigenstrain field which is then inspected to determine if the dice size is appropriate for the local radius of curvature of the eigenstrain field. If $d/\rho > 3.0$ at any point, incomplete stress relief should be suspected and further sectioning performed to release the remaining stress.

7.2 Generalization to three dimensions

The localized eigenstrain technique can be applied to the case of continuous welding, when four eigenstrain components are distributed in two dimensions. The procedure used to perform the localized measurements is similar to that just presented. The eigenstrain field is separated into the portions inside and outside of a region of interest and then obtained by sectioning.

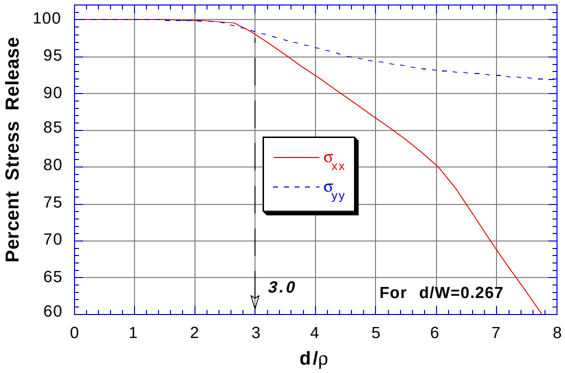

Figure 7.11 – Stress release versus *d*/ρ, where *d* is the dice size and ρ is the local radius of curvature of the temperature field.

Localization of the eigenstrain method for a continuous weld is based on a modification of the sectioning technique proposed by Ueda (Ueda, 1985) and evaluated in Chapter 4. This modified sectioning technique is shown schematically in Figure 7.12. The instrumented surface of the region of interest is shaded in the figure, and represents the location of the weld bead. The sectioning process differs from the one proposed by Ueda because an intermediate "chunk" geometry in created by removing the region of interest from the slice. This modified sectioning process allows for separation of the eigenstrain field into the portion inside and outside of the region of interest. Again, the division of eigenstrain into these two parts is fundamental to the success of the localized technique. The shape functions used to interpolate the eigenstrain must allow for this division. One set of functions is used to interpolate the eigenstrain that can be determined from stress in the chunk geometry, and another is used for eigenstrain to be determined from stresses in the slice. The problem is similar to the simpler one just examined, but now we must account for all four components of eigenstrain present and their distribution in two directions.

7.2.1 Model problem to illustrate the method

Description of the localized eigenstrain method is most easily performed with an example problem solidly in mind. So, we will be specific early on, and lay out a problem to be solved. In the end, we will evaluate the localized eigenstrain technique in exactly the same way as was done for Ueda's method. So, the problem to be solved is the same as described in Chapter 4. We have a block of material, which has presumably been removed from a welded joint, and has dimensions shown in Figure 7.13. A region of interest in the

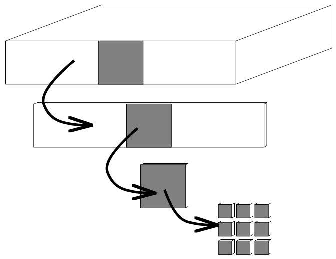

Figure 7.12 – Sectioning procedure used in the localized eigenstrain technique for continuous welds.

xy-plane of this block is identified, shown shaded in the figure. The free surface of this region is instrumented as shown in Figure 7.14. Following instrumentation, the block is sectioned as shown schematically in Figure 7.12. Strains changes are measured which accompany removal of the slice from the block, chunk from the slice, and finally from slice to dice. Assuming that the dice are small enough relative to the spatial gradients of

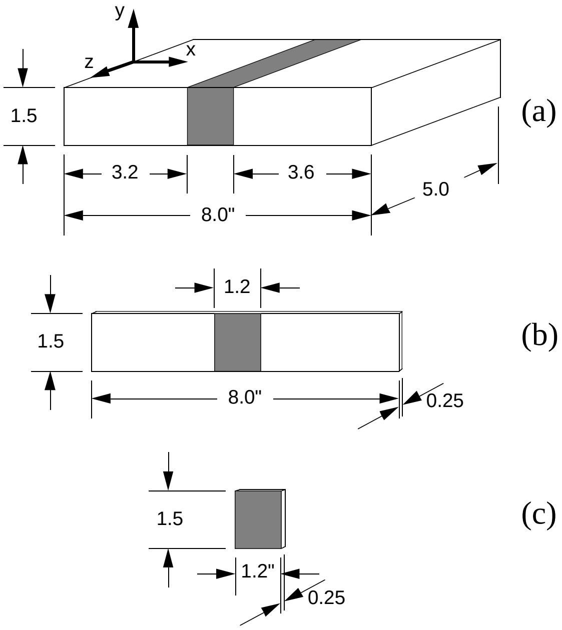
y
x
z
1.5
3.2
3.6
8.0"
5.0
(a)
1.2
1.5
8.0"
0.25
(b)
1.5
1.2"
0.25
(c)

Figure 7.13 – (a) Block of material in removed from a welded joint, (b) slice removed from the block, and (c) chunk removed from the slice.

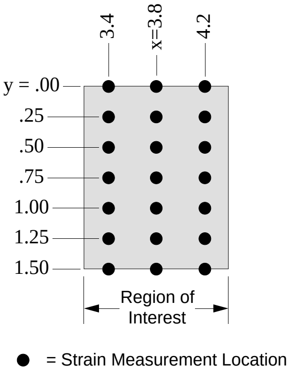
3.4
x=3.8
4.2
y = .00
.25
.50
.75
1.00
1.25
1.50
Region of Interest
● = Strain Measurement Location

Figure 7.14 – Measurement locations within the region of interest.

eigenstrain, the dice will be stress-free. Using Hookean stress-strain relations for plane stress, residual stress can then be computed at the measurement locations in the block, slice, and chunk geometries.

Now that residual stress has been determined experimentally at the measurement locations in these three geometries, the localized eigenstrain technique is used to find an eigenstrain system which will reproduce these residual stresses at the measurement locations (on the free-surface of the chunk, slice, and block). If the method is formulated properly, this eigenstrain distribution will also provide a good estimate of residual stress as a function of the longitudinal coordinate (i.e., as we move from the *xy*-free-surface of the block into the interior). The method which has been developed recovers residual stress away from the free-surface of the block with good accuracy, as will be shown toward the end of this chapter.

7.2.2 Division of eigenstrain into ε^*_A and ε^*_B

One of the crucial steps in assuring success in the case of the one-dimensional eigenstrain distribution was separating the eigenstrain. This division followed from consideration of those eigenstrain fields would cause unrestrained deformation in the chunk but cause stress in the slice. This led to the development of two separate portions of eigenstrain to be determined by the localized eigenstrain method. The first part, ε^*_B, is found from stress in the chunk, and the second part, ε^*_A, from stress in the slice. This second part of the eigenstrain is further divided into two distinct parts. The first is eigenstrain which lies within the region of the chunk, but does not cause stress once the chunk is cut free from the slice. The second part of ε^*_A is an approximate representation for eigenstrain which lies outside of the chunk region. The interpolation scheme for the first part of ε^*_A will vary for each component of eigenstrain, while that for the second part will be the same for each component.

For the case of $\varepsilon^*_{yy}(x)$, we showed in Section 7.1 that eigenstrain which causes stress-free deformation in the chunk but causes stress in the slice amounts to a linear and a constant field within the chunk region. We investigate this matter for the other eigenstrain components by looking at the compatibility relations for a plane stress geometry, which we repeat here for convenience

$$\frac{\partial^2 \varepsilon_{xx}}{\partial y^2} + \frac{\partial^2 \varepsilon_{yy}}{\partial x^2} = \frac{\partial^2 \varepsilon_{xy}}{\partial x \partial y}. \tag{7.7}$$

Now, however, we assume that each component of eigenstrain in the plane is a function of x and y, $\varepsilon^*_{ij} = \varepsilon^*_{ij}(x, y)$. Eigenstrain which satisfies Equation 7.7 will cause stress-free deformation. From this equation, the strain fields which satisfy compatibility in the chunk are

$$\varepsilon_{xx} = y f_1(x) + g_1(x) + c_1 \tag{7.8}$$

$$\varepsilon_{yy} = x f_2(y) + g_2(y) + c_2, \tag{7.9}$$

and

$$\varepsilon_{xy} = f_3(x) + g_3(y) + c_3. \tag{7.10}$$

where, $f_i(\bullet)$ and $g_i(\bullet)$ are arbitrary functions, and c_i are arbitrary constants. These are the same equations presented in Chapter 4 as strain fields which cause stress-free deformation in the slice. (We consider each strain component separately in looking at stress-free deformation modes. There are an infinite number of strain components which would satisfy Equation 7.7 when all components are considered together. However, since we are using linear interpolation, we can represent only a very few of these stress-free deformation modes exactly.)

We now need to look at which of these functions cause stress in the slice, if imposed only within the region of the chunk. For ε^*_{xx}, the strain represented by Equation 7.8 will cause no stress in the slice or in the chunk, just rigid body deformation. To illustrate this point, consider each term in Equation 7.8 imposed only in the chunk region of the slice. If $\varepsilon^*_{xx} = c_1$ then the chunk region will grow in the x-direction. Such growth is not restrained by the surrounding slice-material, therefore it will cause no stress. If $\varepsilon^*_{xx} = g_1(x)$ then the chunk region will grow in the x-direction, and the amount of growth at a specific location in x is dictated by the function $g_1(x)$. Such growth is also unrestricted by the material surrounding the chunk region. Finally, if $\varepsilon^*_{xx} = y f_1(x)$ the chunk region will grow in length as a function of x, and as a linear function of y. This field makes the chunk region deform into a rhomboid, with the top and bottom edges straight and flat, but the left and right boundaries of the chunk region straight and skewed relative to vertical. Again this deformation is stress-free. Accordingly, there is no part of ε^*_{xx} which causes stress-free deformation in the chunk but does cause stress in the slice.

To the contrary, for ε^*_{xy}, the strain represented by Equation 7.10 will cause stresses in the slice if imposed in the chunk region. Specifically, if $\varepsilon^*_{xy} = g_3(y)$ is imposed in the chunk region of the slice, it will give rise to stress. This eigenstrain field will cause the left and right edges of the chunk to deform into some curve dictated by the function $g_3(y)$. Such deformation will cause stress in the slice geometry, since material in the slice will restrict the deformation.

Turning to ε^*_{yy}, each term in Equation 7.9 will cause stress in the slice if imposed only in the chunk. If the field $\varepsilon^*_{yy} = c_2$ is imposed in the chunk region of the slice, that region would swell uniformly. The material surrounding the chunk region would restrict this deformation, causing stress in the material. The situation is similar when $\varepsilon_{yy} = g_2(y)$ or $\varepsilon_{yy} = xf_2(y)$, material surrounding the chunk region will restrict deformation and therefore stress will arise.

7.2.3 Scheme for interpolation of ε^*_B

Functions used to interpolate eigenstrain determined from stress in the chunk, ε^*_B, in the *x*-direction within the chunk are shown in Figure 7.15. These functions are the result of only a few considerations. First, eigenstrains which would cause stress-free deformation in

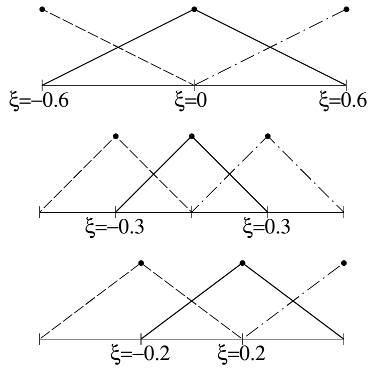

a) Interpolation of ε^*_{xx}

b) Interpolation of ε^*_{yy}

c) Interpolation of ε^*_{xy}

Figure 7.15 – Interpolation functions used to distribute ε^*_A in the chunk. $\xi = x - x_o$, where x_o is the center of the chunk. Measurements taken at ξ = -0.4, 0, 0.4.

the chunk are explicitly excluded by proper choice of the interpolation scheme. This consideration is discussed in detail below. Second, spacing between interpolation nodes of each component is constant. It was found that even spacing produces a linear system for eigenstrain determination which is as well conditioned as possible, and therefore produces superior results.

For each particular component of eigenstrain, suppression of stress-free deformation is assured by proper choice of the x-interpolation functions for that component. This approach ensures that as much x-interpolation as possible is performed while not having to eliminate parameters within the linear system used to solve for stress. In other words, we choose the shape functions such that the linear system maintains as many effective parameters as possible. For interpolation in the y-direction, however, this is not true. No effort is made to optimize the y-interpolation for each particular component. Non-optimized y-interpolation has a small effect on the system. As an example, consider the interpolation of ε^*_{xy}. Any $f(x)$ will give rise to stress-free deformation in the chunk. Elimination of this deformation mode from the interpolation entails setting ε^*_{xy} to zero along any line $y = \text{constant}$. This causes the loss of three equations in the linear system, since there are three nodal values of eigenstrain at any line $y = \text{constant}$. Now compare this with the effect of not optimizing the x-interpolation of ε^*_{xy}. Any $g(y)$ will cause stress-free deformation, and setting ε^*_{xy} to zero along any line $x = \text{constant}$ will eliminate that deformation. If the interpolation did not specifically eliminate this deformation mode, seven equations would have to be removed from the linear system, as there are seven eigenstrain nodes on any line $x = \text{constant}$. Accordingly, optimization of the x-interpolation is paramount to optimization of y-interpolation.

For ε^*_{xx}, the only stress-free deformation modes in the chunk are given by Equation 7.8. Neither a $x f(y)$ nor a $g(y)$ term, which can be excluded by optimizing the x-interpolation, are included in these functions, and therefore ε^*_{xx} can be interpolated to the edges of the chunk. On the other hand, ε^*_{yy} has zero-stress modes corresponding to both $x f(y)$ and $g(y)$. Accordingly, our interpolation scheme sets ε^*_{yy} to zero at the left and right free-edges of the chunk. The shear component of cross-sectional eigenstrain, ε^*_{xy}, also has a zero-stress mode corresponding to $g(y)$, so that ε^*_{xy} is zero at one of the free-edges of the chunk. Looking at Figure 7.15, these stress-free deformation modes for each component of eigenstrain are suppressed by the interpolation functions developed.

The eigenstrain field developed in Chapter 4 and used to investigate residual stress determination techniques can be used to investigate the performance of the interpolation of ε^*_B. Once the interpolation scheme was complete, a linear system was formed relating parameters in the interpolation of eigenstrain to residual stress at measurement locations in the chunk. Since there are twenty-one measurement locations on the chunk, at which three strain changes are measured, there are sixty-three measurements of stress. By counting the number of parameters in the interpolation scheme for all components of eigenstrain, as shown in Figure 7.15, and multiplying them by seven, the number of evenly spaced interpolation poles in the *y*-direction, it can be seen that there are sixty-three parameters to be determined. Since we have ignored zero-stress modes associated with the *y*-interpolation scheme, there are only fifty-four effective stress producing parameters available. Accordingly, a least squares solution is used to find the eigenstrain parameters from the sixty-three stress components. Once the eigenstrain parameters are determined, estimates of residual stress are obtained. Figure 7.16 shows a comparison of the exact distribution of stress, determined from a model of the chunk, and that resulting from the estimated eigenstrain. Extremely good agreement is obtained, which bodes well for the interpolation scheme adopted.

7.2.4 Scheme for interpolation of ε^*_A

Now that a set of interpolation functions have been developed to distribute ε^*_B within the chunk geometry, it is left to develop a set of functions to interpolate ε^*_A, the eigenstrain which needs to be determined from stresses in the slice. Again, we will discuss the interpolation in the *x*-direction, as *y*-interpolation is uniform. As with the one-dimensional example presented in the previous section, we need to account for the two types of eigenstrain which cause stresses in the slice which cannot be predicted by stresses in the chunk. The first part is the eigenstrain which causes stress when present in the chunk region of the slice geometry, but causes no stress when the chunk is cut free. The form of this portion of ε^*_A will vary for each component of eigenstrain. The second part of the eigenstrain to be determined by stress in the slice is the eigenstrain which lies outside of the chunk region.

The first part of ε^*_A is interpolated in a unique fashion for each component of eigenstrain as shown in Figure 7.17. For ε^*_{xx}, there are no stress-free modes of eigenstrain distribution which are not also stress-free in the slice. Therefore, there is no part of ε^*_{xx} which lies within the chunk region and is not determined by the stresses in the chunk. For ε^*_{yy}, there are two functions of eigenstrain that cannot be found from stresses in the chunk. These correspond to $x\,f(y)$ and $g(y)$. So, at each y-coordinate, we must be able to represent both a constant and a linear field within the chunk region. The functions shown in Figure 7.17(a) perform that task. When combined with the y-interpolation scheme, these shape functions are able to approximate both $x\,f(y)$ and $g(y)$. In the case of ε^*_{xy}, the distribution $g(y)$ cannot be determined from stresses in the chunk, and so the shape function shown in Figure 7.17(b) is used at each y-interpolation station.

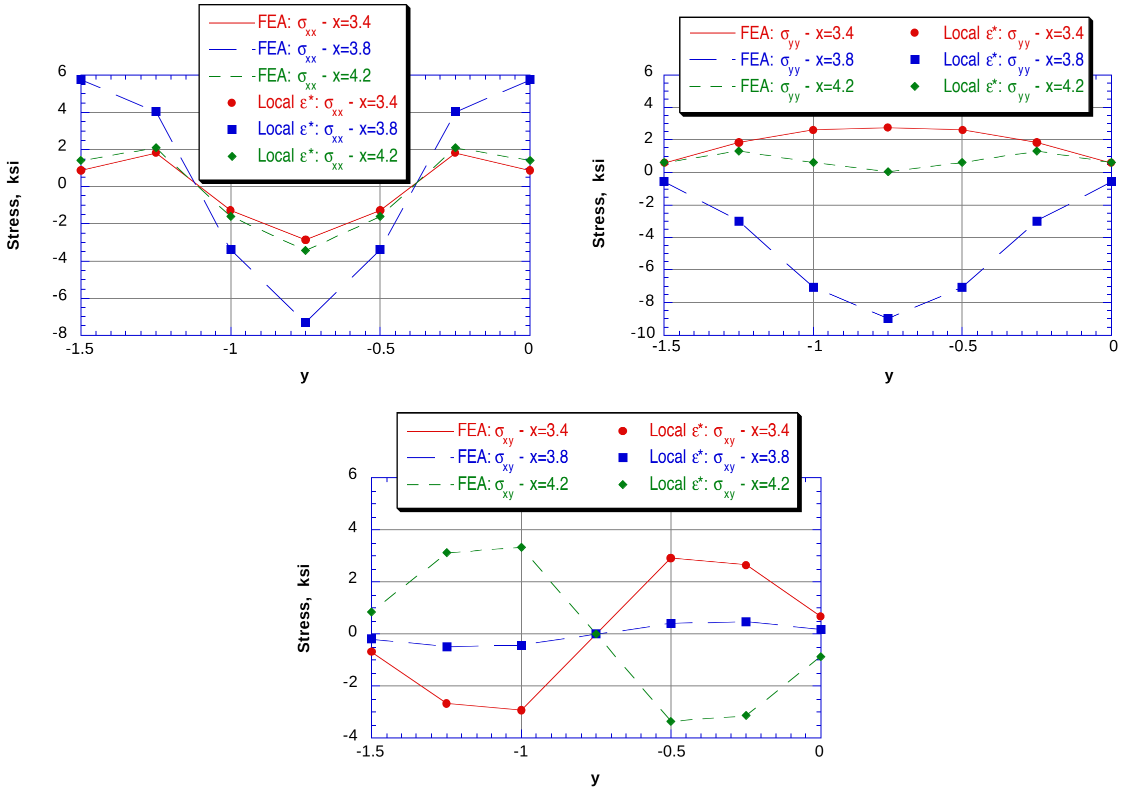

Figure 7.16 – Stresses in the chunk computed by FEA and the localized eigenstrain method. Each plot represents a separate stress component, as shown in each legend.

The second part of ε^*_A is that which lies outside of the chunk region. It has been found by trial and error that the shape of the function used to interpolate this part of the eigenstrain does not alter the results of the stress approximation within the region of interest. Therefore, the simple sawtooth functions shown in Figure 7.17(c) are used to interpolate each component of eigenstrain.

There are seven interpolation points in the *y*-direction and nine parameters of ε^*_A at each *y*-interpolation station (two for ε^*_{xx}, four for ε^*_{yy}, and three for ε^*_{xy}). Accordingly, there are sixty-three parameters to be determined from stresses in the slice. Since there are also sixty-three measurements taken, it is possible to determine ε^*_A from these measurements. Again, we can evaluate this system of eigenstrain interpolation by testing it computationally. Stresses in the slice are determined in the presence of the planar components of the test eigenstrain field by using finite element analysis. Stresses in the chunk are also determined from a model of that geometry. From stresses in the chunk, ε^*_B is determined, as described above. Then ε^*_B is imposed on a finite element model of the slice, and stresses obtained. Finally, ε^*_A is found by solving the system

$$\varepsilon^*_A = \boldsymbol{M}_A^{+}[\sigma_A - \sigma_A^{B}] \qquad (7.11)$$

where,

$\boldsymbol{M}_A^{+}$ = pseudo-inverse of $\boldsymbol{M}_A$, the eigenstrain system for ε^*_A

and,

σ_A^{B} = stress in the slice (geometry A) caused by ε^*_B.

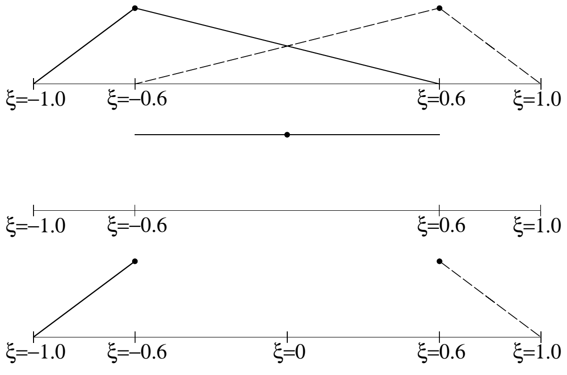

a) Interpolation of ε^*_{yy}

b) Interpolation of ε^*_{xy}

c) Sawtooth functions common to all components.

Figure 7.17 – Interpolation functions used to distribute eigenstrain determined from stress in the slice, ε^*_A. $\xi = x - x_o$, where x_o is the center of the chunk.

(The pseudo-inverse operator allows inversion of singular and near-singular linear systems and produces results equivalent to those of the least-squares method (Albert, 1972).) Finally, both ε^*_A and ε^*_B are imposed on a finite element model of the slice to find the predicted stresses in slice. Figure 7.18 shows stresses in the slice determined by finite element analysis and by the localized eigenstrain technique. Excellent agreement is obtained.

Thus far we have considered only the slice geometry. For this method to be useful for welded joints, however, we need to investigate whether the eigenstrain distribution represented by ε^*_A and ε^*_B, determined from stresses in the chunk and slice, will induce the correct stresses in the block geometry. To test this, a finite element model of the block

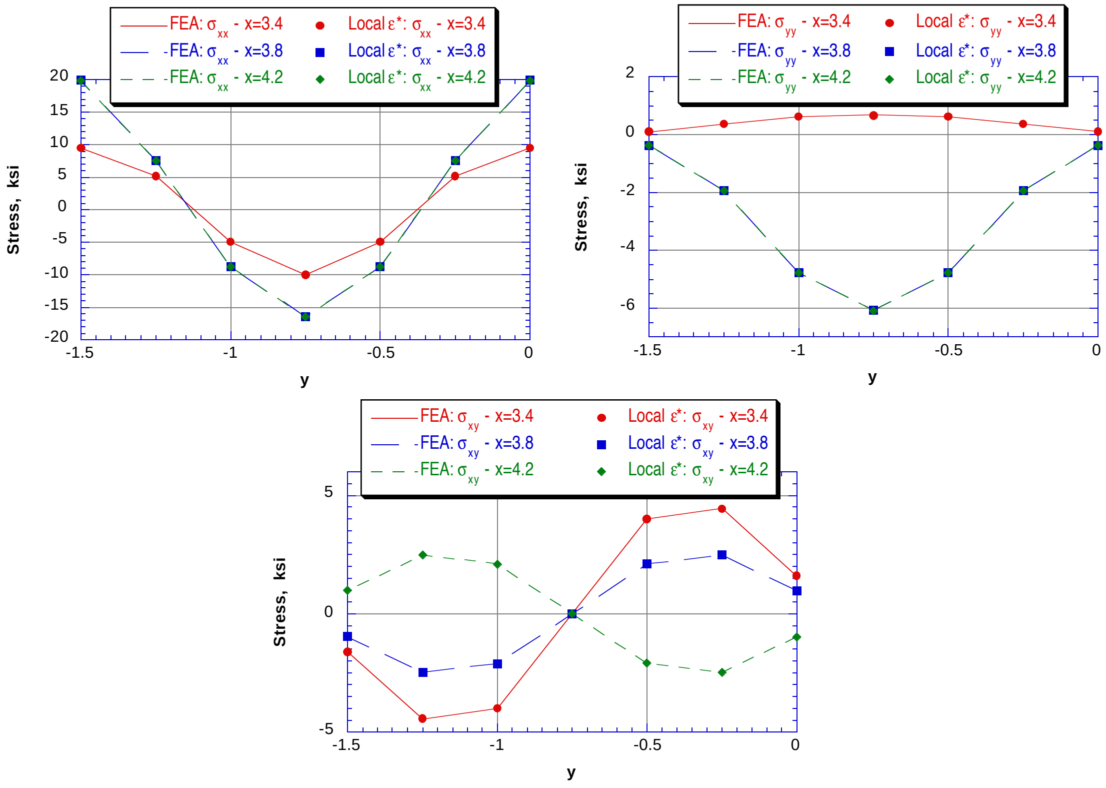

Figure 7.18 – Stresses in the slice computed by FEA and the localized eigenstrain method. Each plot represents a separate stress component, as shown in each legend. (Results for σ_{xx} and σ_{yy} on x=3.8 and x=4.2 are virtually identical, so they cannot be distinguished in the plots.)

geometry is constructed, the planar components of the test eigenstrain function are imposed on it, and stresses at the midplane of the block are obtained. Also, the interpolated system of ε^*_A and ε^*_B is imposed within the block, and these results obtained. As can be seen in Figure 7.19, there is agreement between computed and estimated stresses. (Actually, the agreement is remarkable.) It is also interesting to look at the contour of $y = -0.5$ at the midplane of the joint, as shown in Figure 7.20. Here there is excellent agreement for all stress components within the region where stresses were "measured", $3.4 \le x \le 4.2$, and estimated stresses quickly diverge from the finite element solution outside that region.

7.2.5 Interpolation for longitudinal eigenstrain, ε^*_{zz}

At this point, we have developed what appears to be an excellent method for obtaining an estimate of residual stress within a block of material subject to the planar components

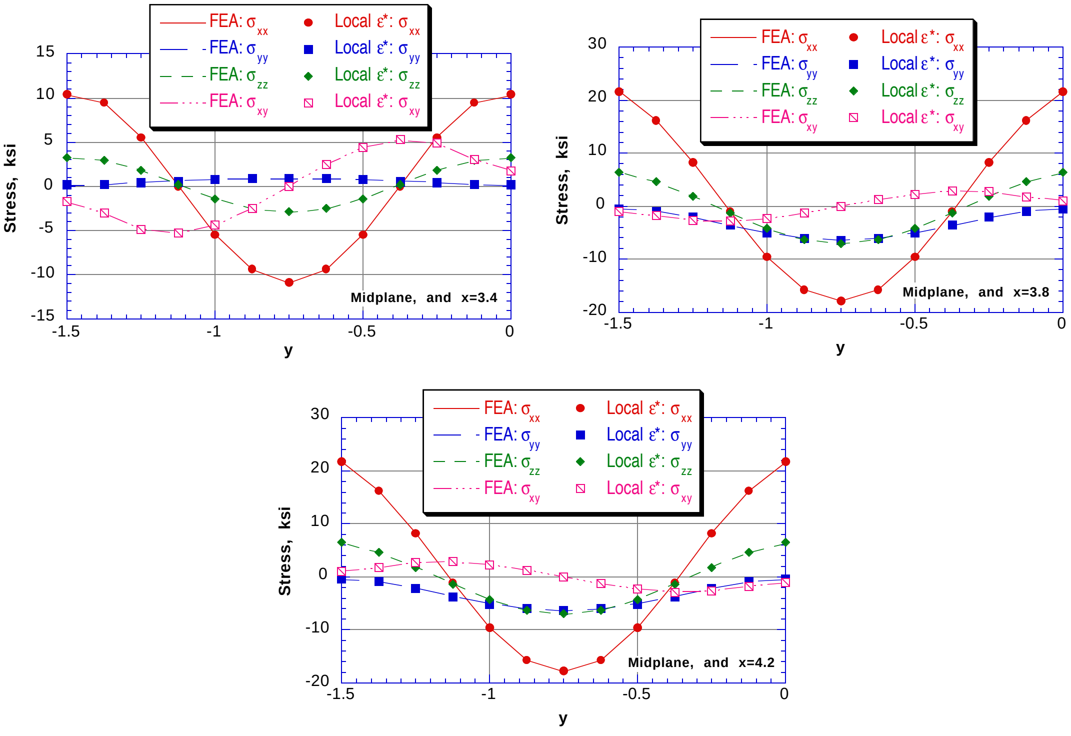

Figure 7.19 – Stresses on the block midplane computed by FEA and the localized eigenstrain method. Each plot is for a different *x*-location, as indicated at the bottom-right.

of eigenstrain. Now, we need to include the ability to estimate a localized representation of the longitudinal component of eigenstrain, ε^*_{zz}, from stresses measured on the free-surface of the block. To do this, we use the same interpolation scheme used to interpolate ε^*_{xx} in the chunk and slice, as shown in Figure 7.15(a) and Figure 7.17(c). We use the functions for ε^*_{xx} because they represent the proper compatibility for ε^*_{zz}. A constant and two linear functions, one each in *x* and *y*, of $\varepsilon^*_{zz}(x, y)$ are the only functions that will allow stress-free deformation to occur in the block. Since we are not imposing any eigenstrain outside of the vicinity of the region of interest in the block, there is no way that any stress-free deformation can be imposed by interpolating ε^*_{zz} within the region of interest (except for the trivial solution, $\varepsilon^*_{zz} = 0$). Both of the sets of shape functions previously used for ε^*_{xx}, taken together, comprise the interpolation scheme in the *x*-direction. Interpolation in the *y*-direction is uniform as for the other components, with seven rows of nodes down the *xy*-face of the block.

In estimating the longitudinal eigenstrain component, there is no distinction between the chunk and the slice, except in the discontinuity in the interpolation across the boundary of the region of interest. That is, the solution procedure for finding a parameterized version of ε^*_{zz} is that same as in the non-localized eigenstrain method. The planar components of eigenstrain are estimated as described above, then these are imposed in a finite element model of the block to find the stresses they cause on its free-surface. These stresses are

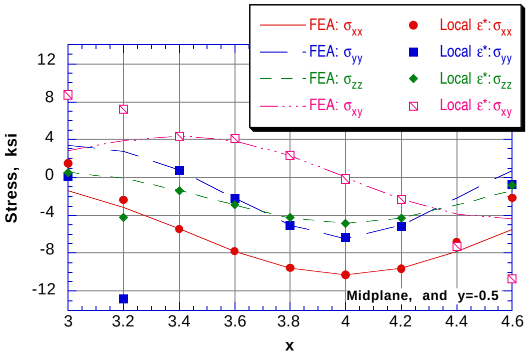

Figure 7.20 – Stresses in the block computed by FEA and the localized eigenstrain method, on the block midplane at $y = -0.5$.

subtracted from the experimental estimates of residual stress on the block free-surface, and the difference used to determine the parameters in the ε^*_{zz} interpolation.

We can assess this interpolation by imposing the ε^*_{zz} component of the test eigenstrain function on a finite element model of the block geometry to arrive at stresses on its free-surface. Stresses at the measurement locations are then input into an eigenstrain system formed using the interpolation functions for ε^*_{zz} just described. The parameters in the interpolation are then determined by solving this linear system. The resulting interpolated eigenstrain is then imposed on a finite element model of the block. Stresses at the middle of the block, within the region of interest, computed by the interpolated eigenstrain field can now be compared to the stresses computed by FEA, as shown in Figure 7.21. Agreement between the two sets of stresses is apparent. However, sizable errors are obtained in σ_{zz}, especially near the top and bottom of the block, y=0.0 and y=-1.5. The error is about 16% of the estimated σ_{zz}. Overall, the performance of the method is good, but the errors present call for further investigation of their source.

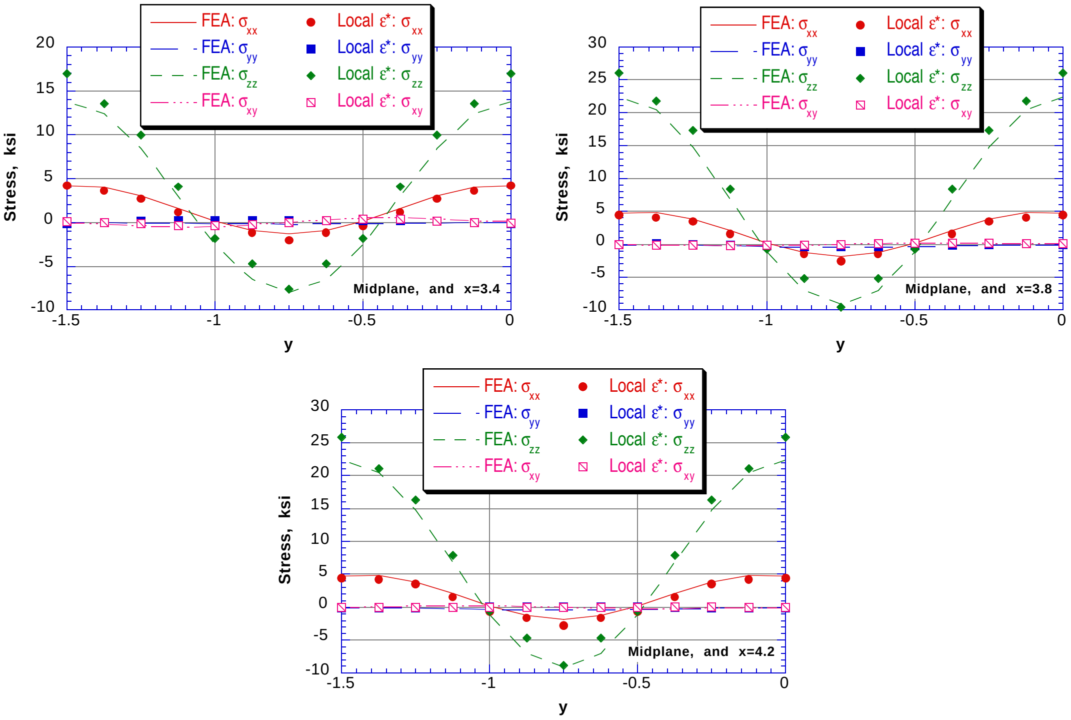

Figure 7.21 – Stresses due to ε^*_{zz} in the block computed by FEA and the localized eigenstrain method. Each plot is for a different *x*-location, as indicated at the bottom-right.

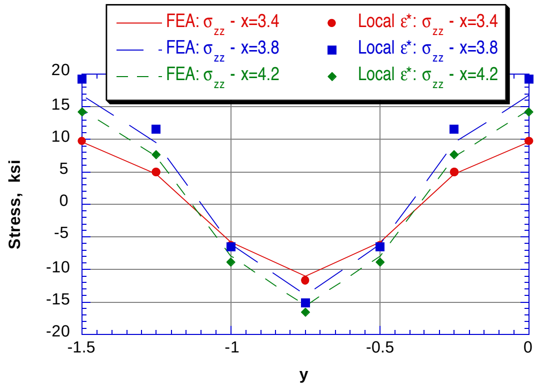

Figure 7.22 – Longitudinal stress at the midplane due to ε^*_{zz} in the abbreviated block computed by FEA and the localized eigenstrain method.

There are several possible sources of error. One is that the errors are the result of the interpolation spacing, which can be addressed by moving "measurement sites" closer together and adding interpolation nodes. Another possible source of error is that the method is not properly separating the eigenstrain into the internal and external parts. Both of these possible sources of error can be investigated.

In order to determine if the errors in estimated stress are the result of a lack of ability to distinguish between internal and external eigenstrain, a simple experiment was conducted. A finite element model was constructed of a block of material which had the same planar dimensions as the chunk, but had a depth in the *z*-direction of five inches. The block dimensions are then 1.2" wide, 1.5" thick, and 5.0" deep. This geometry embodies the whole region of interest where stresses are to be determined by the localized eigenstrain method, shown in Figure 7.1, including the depth in the *z*-direction. By investigating this problem, then, we eliminate the need for the method to distinguish between internal and external longitudinal eigenstrain.

The model eigenstrain function is imposed on a model of the region of interest and stresses computed on the free-surface and the midplane. The eigenstrain method is adopted to this geometry and applied, using free-surface stresses from the computation, to obtain estimates of midplane stress. These estimates of σ_{zz} are compared to the results of the FEA computation in Figure 7.22. As can be seen in the figure, the maximum error

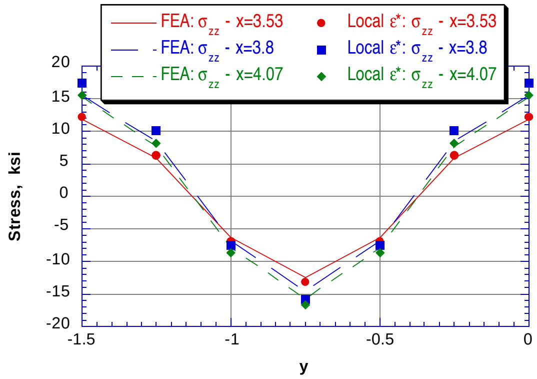

Figure 7.23 – Longitudinal stress due to ε^*_{zz} in the scaled abbreviated block computed by FEA and the localized eigenstrain method.

occurs on the line *x*=3.8, the center of the region of interest, and is 13% of the measured stress. This result indicates that knowing residual stress across the entire face of the block of material does not lead to significantly better stress estimates than were obtained for the localized method (Figure 7.21).

To investigate the error introduced into estimated stresses by the spacing of the measurement locations, we alter the previous computational experiment. The mesh used to represent the region of interest is scaled in the *x*-direction by two-thirds, yielding a block of material 0.8" wide, 1.5" thick, and 5.0" deep. This makes the spacing between measurement locations 0.27", or 50% closer than they were previously, and similarly changes the interpolation spacing. Since the geometry is different, stresses caused by the longitudinal component of the model eigenstrain distribution change, but only slightly. As can be seen in Figure 7.23, errors in estimated longitudinal stress are slightly smaller than those in the previous experiment (Figure 7.22). Specifically, the maximum error present decreases to 10% of the measured stress and occurs at *y*=-0.75, and *x*=3.8. Again, the reduction in error is small. Decreasing the spacing between both the measuring locations and the *x*-interpolation stations does not greatly improve the estimates of σ_{zz} at the midplane of the block. The interpolation for ε^*_{zz} which uses the same interpolation functions as used for ε^*_{xx}, shown in Figure 7.15 and Figure 7.17, apparently provides results as good as possible. All evidence leads to the conclusion that the error in stress estimates provided by the interpolated ε^*_{zz} must be fundamental to the eigenstrain method, as all efforts to reduce this error have met with only limited success.

7.3 Results of the localized eigenstrain method

We now test the localized eigenstrain method as we did Ueda's method in Chapter 4. Essentially the hard work has been performed. The linear systems formed for determination of ε^*_B, ε^*_A, and ε^*_{zz} can be used with stress on the free-surfaces of the chunk, slice, and block computed by FEA. Parameters determined from solution of these systems are then used to interpolate the total eigenstrain on a model of the block geometry, and residual stress estimates on the block midplane are obtained. These stress estimates are compared to their finite element counterparts in Figure 7.24. Good agreement between

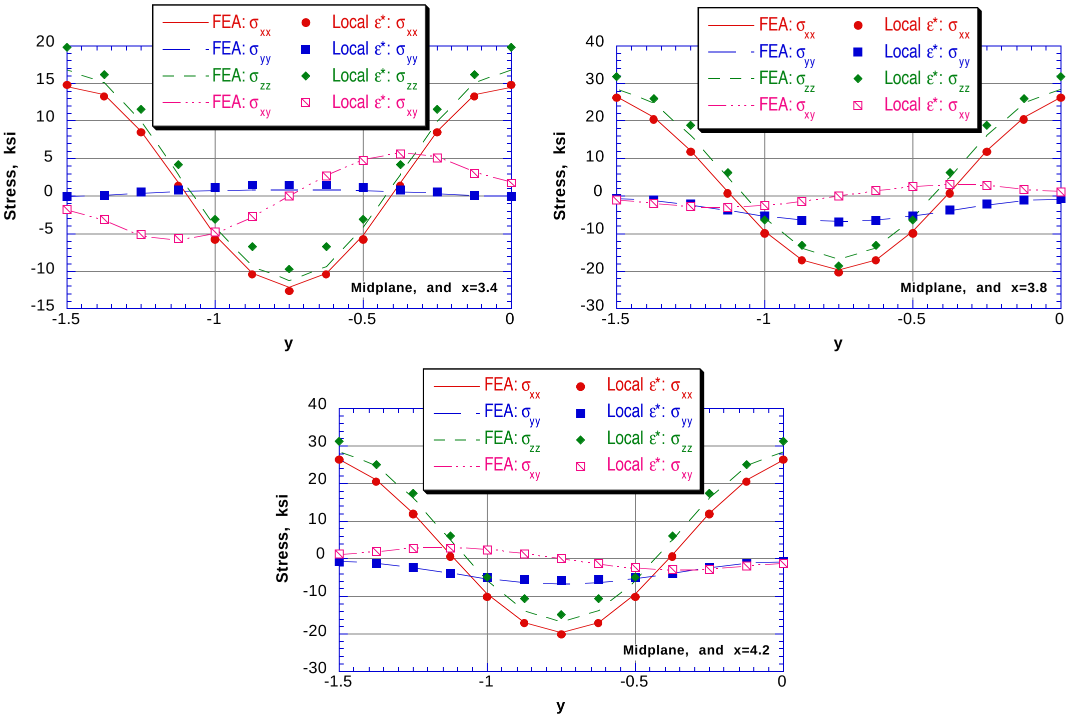

Figure 7.24 – Stress at the midplane of the block induced by the model eigenstrain function as computed by FEA, compared to those estimated by the localized eigenstrain method. Each plot is for a different *x*-location, as indicated at the bottom-right.

the two sets of results is obtained. Errors present in σ_{zz} are not a surprise in view of the forgoing discussion regarding errors introduced by the interpolation of ε^*_{zz}.

The localized eigenstrain method can be used to estimate residual stresses at the midplane of the block to a good degree of accuracy. The maximum difference between estimated and exact stress is smaller that obtained using the “non-localized” eigenstrain method, as shown in Figure 7.25(a). The improved accuracy is the result of the improved shape functions used to interpolate the eigenstrain. In developing these functions, an effort was made to keep small the number of eigenstrain components which are lost to modes of stress-free deformation. Overall, the difference between estimated and exact stress for either method is fairly small in relation to the levels of stress present in the block which are shown in Figure 7.25(b).

The development of the localized eigenstrain technique adds to the ability of the technique developed by Ueda. The localized method has the advantages of Ueda’s method, while being easier to implement. The experimental effort required for the two techniques varies greatly. Implementation of Ueda’s technique, as described in Chapter 4, would require one-hundred-forty three-element strain gage rosettes. The localized technique, on the other hand, would require only twenty-one. This is a huge reduction in effort, which makes use of the eigenstrain technique much more practical. Not only is the experimental effort reduced, but the computational burden as well. One finite element solution must be

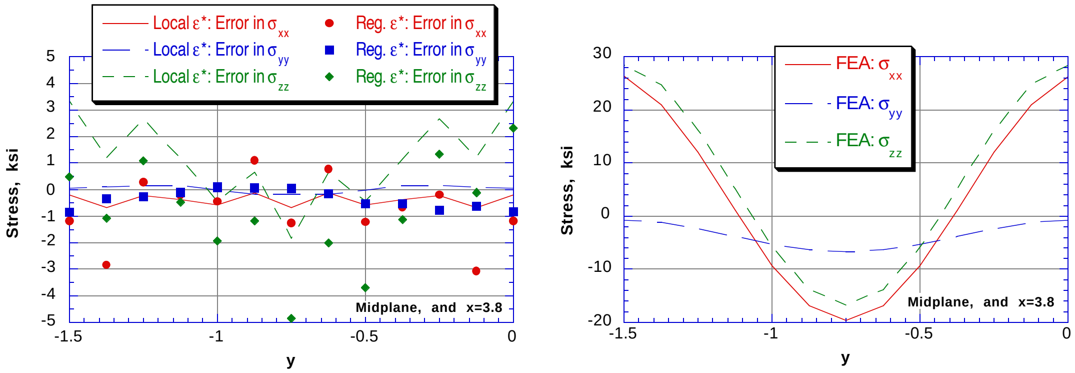

(a) (b)

Figure 7.25 – (a) Error in stress estimated by the regular and localized eigenstrain methods, and (b) nominal values of stress, both on the midplane of the block and the line *x*=3.8.

obtained for each eigenstrain parameter in the interpolation system. As described in Chapter 4, Ueda’s technique had five-hundred such parameters. The method presented here has only one-hundred-forty-seven. For these reasons, the localized eigenstrain method adds ease of execution to the previously existing method developed by Ueda.

Chapter 8

Conclusions

Structures are generally designed to be in service for a specified time or number of operations. As the end of this design lifetime draws near, organizations must examine the options of replacement and recertification. For expansive infrastructure, the daunting cost of replacement mandates recertification and possible repair. For aging welded structure, the recertification process involves acquiring information on the defect population present in the structure, and forthwith assessing the possibility of sub-critical crack growth from these defects to a size where fracture would occur. Weld residual stress plays an important role in both crack growth and fracture phenomena, and must be accounted for in the assessment process. Commonly, tensile residual stress of yield strength magnitude is assumed to be present throughout the thickness of a welded joint. This assumption ignores compressive residual stresses which are usually present in thick welded plates at the root of the joint, where crack-like defects commonly occur. The ability to include a more realistic residual stress profile in lifetime assessment has been hampered by the lack of experimental methods capable of revealing residual stress deep in welded components.

8.1 Summary of the thesis

This thesis has reviewed the fatigue of weldments, described the creation of intentionally defective welded joints, and examined techniques for subsurface residual stress determination. A summary of the major results are listed below.

1. A wealth of information on fatigue in the weld region was summarized. Comparison of fatigue crack growth experiments and analysis reveals that the use of linear elastic fracture mechanics provides a fairly accurate prediction of crack growth when residual stresses are known.
2. Experiments with welding demonstrate that it is possible to produce thick welded plates which contain a simulated buried weld defect of predetermined size and location. The availability of defective welded plates offers the possibility of performing experiments to investigate crack growth from a realistic internal weld defect. A non-defective weld fabricated using the same welding procedures allows possible comparison of residual stresses caused by welding in defective and non-defective welds.
3. A method for computer-based simulation of sectioning methods was developed. This simulation technique provides a way to investigate the assumptions of sectioning-based residual stress measurement methods.
4. The assumptions and benefits of three residual stress determination techniques for thick welded plates were investigated. This study found that Ueda’s assumption of longitudinal independence of the eigenstrain field imposed by continuous welding appears valid. On the other hand, the assumption of linear stress release made by Norton and Rosenthal was found to be erroneous. Gunnert’s technique was discussed and the technique was shown to be of value by Procter and Beaney.
5. The eigenstrain method for residual stress determination, proposed by Ueda, was shown to be a promising technique. The method was presented in its general form, and then its application to a welded plate was discussed in detail. A concerted effort was made to provide a significant amount of detail, so that a clear understanding of the eigenstrain technique can be obtained.
6. An experimental implementation of the eigenstrain method was performed to determine stress in a thick welded joint. The hole drilling method was used to find residual stress which would be used as input to the eigenstrain method. Results of the hole drilling experiments appeared unrealistic, possibly due to large uncertainties when applying the hole drilling method.

7. The eigenstrain method was also investigated for a swage-autofrettaged tube. Residual stress estimates obtained experimentally were compared to the results of an elastic-plastic simulation. This study found that the residual stress fields estimated by these two techniques agreed in spatial variation but differed in magnitude. Raw stress release data collected during the experiment were found to be significantly different from that expected based on the results of an elastic-plastic finite element simulation. Accordingly, the major difference between the simulation and the experiment appears to arise from inaccuracies in the simulation of the swage process.

8. The analytical and experimental demands of the eigenstrain method make its application expensive. A localized eigenstrain technique was developed to allow residual stress estimation at a lower cost. The experimental effort required by the localized technique is reduced by up to *five times*, relative to Ueda's method. This new method was verified by numerical simulation and shown to be just as accurate as the method developed by Ueda.

8.2 Directions for future research

This thesis makes strides toward the development of a verified technique for triaxial residual stress determination. Numerical simulation of sectioning-based methods proved a valuable tool in this task. However, the difficulties encountered in performing the experimental verification leave additional work to be performed. The application of an improved sectioning scheme to the swage-autofrettaged tube should allow the eigenstrain method to provide a better estimation of residual stress. Yet, as pointed out in Section 6.6, the modeling of the swage process also appears to contain significant error. To address the differences between swage-simulation and experiment, both the elastic-plastic modeling and the sectioning process need to be further refined.

The localized eigenstrain method can be applied to find residual stress in sound and defective welds. The use of this method on a defective weld relies on its adaptability to any geometry. Consider the defective joint described in Section 2.4 and shown in Figure 2.6 on page 93. In principle, the eigenstrain method can be applied to this geometry by merely including the defect in the finite element mesh used to form the eigenstrain linear system. However, the ability to actually perform these measurements has not been demonstrated in this thesis. To verify the ability to include the presence of a defect, a numerical study like that executed in Chapter 4 could be employed. If this numerical validation shows that the method can be applied to defective welds, residual stress which develops around a defect can be compared experimentally to that which is set up in defect-free conditions. Sound and defective welds made under similar conditions, like those described in Chapter 2, could be used to investigate this issue.

Some work might also be performed to package the eigenstrain technology, thereby facilitating its adoption by industry. The finite element modeling used to form the linear system used to find eigenstrain represents an elasticity solution. The solution for stress on the free surface of the sections cut from the welded joint depend only on the ratio of height to width and width to depth. As long as the proportions for the actual sections used in the process are in the same ratio as those shown in Chapter 7, the same linear systems can be used to execute the localized eigenstrain method. The compilation of the eigenstrain linear systems would eliminate the need for finite element modeling in estimating the eigenstrain distribution. However, linear elastic finite element analysis would still need to be performed to impose the estimated eigenstrain in a model of the structure from which the sample was removed.

The ability to cost-effectively and accurately determine triaxial residual stress offers the ability to examine its influence on the processes of fatigue and fracture. In all of the fatigue experiments reviewed in Section 1.5 the residual stress state existed in thin specimens and was assumed to be biaxial. Several of the LEFM methods described in Section 1.2 and Section 1.5 account for residual stress by including its influence on $\mathrm{R}^{\mathrm{eff}}$, given in Chapter 1 as

$$\mathrm{R}^{\mathrm{eff}} = \frac{K_{min}^{app} + K^{res}}{K_{max}^{app} + K^{res}}. \tag{8.1}$$

This approach includes only the residual stress acting to open the crack. This approach captures what may be the major influence of residual stress on fatigue crack growth. However, the triaxial state of stress in the vicinity of the crack tip is what determines the amount of plasticity that occurs there, and, as discussed in Section 1.2, it is plasticity that causes crack closure. A recent paper (Panontin and Hill, 1996) describes a computational study that demonstrates in detail how an assumed triaxial residual stress can significantly reduce the amount of plasticity occurring at the crack-tip under monotonic loading. If the amount of crack-tip plasticity is reduced similarly under cyclic loading, crack closure will not occur to the degree it would in the absence of the triaxial residual stress field. It would then be expected that the fatigue crack growth rate would be higher than that anticipated if the triaxial nature of the residual stress field was ignored. This effect of triaxial residual stress could be demonstrated experimentally by studying crack growth occurring in a well-characterized triaxial residual stress field. The eigenstrain method could be used to provide an estimate of triaxial residual stress in samples to be used in such a study.

Another area in which the eigenstrain method can be used is in the verification of computational weld mechanics. Numerous papers have been presented in the literature which recount triaxial residual stress results provided by computation. Verification of the modeling results is usually presented by comparing residual stresses computed on the surface of the joint with experimental measurements. If there is agreement on the surface, then the subsurface stresses are assumed to be accurate as well. Application of the eigenstrain method to fabricated welds which have been modeled would provide for a comparison of sub-surface residual stress.

As a final thought, the estimation of triaxial weld residual stress has a place in the larger context of lifetime assessment for welded structures. The body of work described here has the major result of potentially providing a cost-effective method for residual stress determination in thick welded joints. The availability of this technique allows the engineer to include experimental estimates of residual stress in the lifetime assessment process. Further, the eigenstrain method is a general one that can be applied to find residual stress induced by processes other than welding. Published examples of the application of the eigenstrain technique in other areas include the measurement of residual stresses in a cylinder due to quenching (Ueda, 1986d), at the bond-interface of a thermally sprayed coating (Kim, 1992), and through the thickness of a multi-layered plasma sprayed coating (Itoh, 1995).

References

Cited references

Albert, A. (1972). Regression and the Moore-Penrose Pseudoinverse. New York, Academic Press.

Adams, N. J. I. (1973). “Crack growth in the vicinity of welds.” Welding Journal, Research Supplement **52**(Nov): pp. 508-513.

Allen, D. R., W. H. B. Cooper, et al. (1982). “The use of ultrasonics to measure residual stresses.” Research Techniques in Nondestructive Testing (Vol. 6), R S. Sharpe, ed. London, Academic Press. pp. 151-209.

ASTM (1985). E 837: Determining residual stresses by the hole-drilling strain-gage method. Philadelphia, PA, American Society for Testing and Materials.

Bakioglu, M. and F. Erdogan (1977). “The Crack-Contact and the Free-End Problem For a Strip Under Residual Stress.” Journal of Applied Mechanics **44**: pp. 41-46.

Baldwin, Jr., William Marsh (1949). “Residual Stresses in Metals - Twenty-third Edward Marburg Lecture.” ASTM Proceedings **49**: pp. 539-583.

Bathias, C. and R. M. Pelloux (1973). “Fatigue crack propagation in martensitic and austenitic steels.” Met. Trans. **4**: pp. 1265-1273.

Beghini, M. and L. Bertini (1989). “Analytical and numerical evaluation of the residual stress effects on fatigue crack propagation.” Proceedings of the 4th International Conference on Computational Methods and Experimental Measurements. Southampton, Computational Mechanics Pub.

Beghini, M. and L. Bertini (1990). “Fatigue crack propagation through residual stress fields with closure phenomena.” Engineering Fracture Mechanics **36**(3) : pp. 379-387.

Bowie, O. L. and C. E. Freese (1981). “Cracked rectangular sheet with linearly varying end displacements.” Engineering Fracture Mechanics **14**: pp. 519-526.

Brand, P. C., T. T. DeKeijser, et al. (1993). "Residual Stresses and Plastic Deformation in GTA-Welded Steel." Welding Journal **1993**(March): pp. 93s-100s.

Bueckner, H. F. (1958). "The Propagation of Cracks and the Energy of Elastic Deformation." Transactions of the ASME, Series A-D **80**: pp. 1225-1230.

Cheng, W. and I. Finnie (1986). "Measurement of residual hoop stresses in cylinders using the compliance method." Journal of Engineering Materials and Technology **108**(2): pp. 87-92.

Cheng, W. and I. Finnie (1990). "The crack compliance method for residual stress management." Welding in the World **28**(5/6): pp. 103-110.

Cheng, W., I. Finnie, et al. (1991). "Measurement of residual stresses near the surface using the crack compliance method." Journal of Engineering Materials and Technology, Transactions of the ASME**113** (2) pp. 199-204.

Cheng, W., I. Finnie, et al. (1992a). "Deformation of an edge-cracked strip subjected to normal surface traction on the crack faces." Engineering Fracture Mechanics **42**(1) pp. 97-107.

Cheng, W., I. Finnie, et al. (1992b). "Estimation of axisymmetric residual stresses in a long cylinder." Journal of Engineering Materials and Technology, Transactions of the ASME **114**(2) pp. 137-140.

Cheng, W. and I. Finnie (1993). "Measurement of residual stress distributions near the toe of an attachment welded on a plate using the crack compliance method." Engineering Fracture Mechanics **46**(1): pp. 79-91.

Cook, R., D. Malkus, et al. (1989). Concepts and Applications of Finite Element Analysis. New York, John Wiley and Sons.

Dinsdale, W. O. and J. G. Young (1962). "Significance of Defects in Aluminium Alloy Fusion Welds; Part 1: Lack of Fusion in 1/4 in. and 1/2 in. NP5/6." British Welding Journal **9**(8): pp. 482-493.

Dinsdale, W. O. and J. G. Young (1964). "Significance of Defects in Aluminium Alloy Fusion Welds; Part 2: Double Operator Defects in 1/2 in. NP5/6 and Pure Aluminium." British Welding Journal **11**(5): pp. 482-493.

Elber, W. (1970). "Fatigue crack closure under cyclic tension." Engineering Fracture Mechanics **2**: pp. 37-45.

Elber, W. (1971). "The Significance of Fatigue Crack Closure." Damage Tolerance in Aircraft Structures, ASTM 486. Philadelphia, PA, American Society for Testing and Materials. 230-242.

Finnie, I. and G. Stevick (1982). "The stress intensity factor due to an internal circumferential crack at a butt weld between cylinders." ASME Paper No. 82–PVP–46 (Preprint of paper given at the 1982 PVP). New York, ASME.
(Published in a condensed form in Journal of Engineering Materials and Technology, Transactions of the ASME **106**(1): pp. 21-24.)

Forman, R. G., V. E. Kearney, et al. (1967). "Numerical analysis of crack propagation in cyclic-loaded a structure." Journal of Basic Engineering, Trans. ASME **89**: pp. 459-464.

Glinka, G. (1979). "Effect of residual stresses on fatigue crack growth in steel weldments under constant and variable amplitude loads." ASTM STP 677. Philadelphia, PA, ASTM. pp.198-214.

Glinka, G. (1987). "Residual stresses in fatigue and fracture: theoretical analyses and experiments." Advances in Surface Treatment: Technology-Application-Effects.v.4: Residual Stresses. New York, NY, Pergamon Press. pp. 413-454.

Glinka, G. and G. Shen (1991). "Universal features of weight functions for cracks in mode I." Engineering Fracture Mechanics **40**(6): pp. 1135-1146.

Goldak, J. A., B. Patel, et al. (1985). "Computational Weld Mechanics." Advanced Joining of Materials (AGARD CP-398) : pp. 1-1 - 1-32.

Graham, S. M. (1988). "Stress intensity factors for bodies containing initial stress", PhD Dissertation, University of Maryland, College Park.

Gray, T. G. F., J. Spence, et al. (1975). Rational Welding Design. London, Newes-Butterworths.

Gunnert, R. (1955). Residual Welding Stresses. Stockholm, Almquist & Wiksell.

Gunnert, R. (1961). "Residual Stresses." Proceedings of the Special Symposium on the Behavior of Welded Structures. Urbana, IL, University of Illinois Engineering Experiment Station. pp. 164-201.

Gurney, T. R. (1968). Fatigue of Welded Structures. London, Cambridge University Press.

Hampton, R. W. and D. V. Nelson (1989a). "Comparison of residual stress measurements in welded thin plates by X-ray and hole drilling methods." Symposium on Nondestructive Evaluation: NDE Planning and Application, Honolulu, HI, ASME.

Hampton, R. W. and D. V. Nelson (1989b). "On the use of the hole drilling technique for residual stress measurements in thin welded plate." Symposium on Nondestructive Evaluation: NDE Planning and Application, Honolulu, HI, ASME.

Hampton, R. W. 1991, HoleGage 1.0, COSMIC Program ARC-12807. Washington, D.C., NASA.

Harrison, J. D. (1969). "The Analysis of fatigue test results for butt welds with lack of penetration defects using a fracture mechanics approach." FRACTURE 1969. London, Chapman & Hall. pp. 777-789.

Hibbitt, Karlsson, et al. (1995). ABAQUS/Standard User's Manual, Version 5.5. Pawtucket, RI, Hibbitt, Karlsson, and Sorensen, Inc.

Hilley, M. E., Ed. (1971). SAE Handbook Supplement J784a: Residual stress measurement by X-ray diffraction. Warrendale, PA, SAE.

Honda, K., T. Torii, et al. (1987). “Effect of Residual Stress Field on Fatigue Crack Growth in Cracked Plates.” International Conference on the Role of Fracture Mechanics in Modern Technology, Fukuoka, Japan, North-Holland. pp. 875-888

Isida, M. (1971). “Effect of width and length on stress intensity factors of internally cracked plates under various boundary conditions.” International Journal of Fracture Mechanics **7**(3): pp. 301-316.

Itoh, Y., J. Fukakura, et al. (1986). “Proportional Extrapolation Techniques for Determining Stress Intensity Factors.” Nuclear Engineering and Design **94**: pp. 249-257.

Itoh, Y. Z., S. Suruga, et al. (1989). “Prediction of Fatigue Crack Growth Rate in Welding Residual Stress Field.” Engineering Fracture Mechanics **33**(3): pp. 397-407.

Itoh, Y., M. Saitoh, et al. (1995). “Microstructure and residual stress of low-pressure plasma-sprayed MCrAlY coatings.” Transactions of the Japan Society of Mechanical Engineers, Part A **61**(581): pp. 97-92.

Kanninen, M. F. and C. H. Popelar (1985). Advanced Fracture Mechanics. Oxford, England, Oxford University Press.

Kim, Y. C., T. Terasaki, et al. (1992). “A method of measuring the through-thickness residual stress in a thremally-sprayed coating.” Thermal Spray Coatings: Properties, Processes, and Applications. Proceedings of the Fourth National Thermal Spray Conference, 4-10 May 1991. Materials Park, Ohio, ASM International. pp. 221-227.

Lam, Y. C. and K. S. Lian (1989). “Effect of residual stress and its redistribution on fatigue crack growth.” Theoretical and Applied Fracture Mechanics **12**(1) pp. 59-66.

Leggatt, R. H. (1984). “Fracture Assessment in the Presence of Residual Stresses.” Advances in Fracture Research (Fracture 84). New York, Pergamon Press. pp. 1239-1246.

Masubuchi, K. (1980). Analysis of Welded Structures : Residual Stresses, Distortion, and Their Consequences. New York, Pergamon Press.

McClung (1991). “The influence of applied stress, crack length, and stress intensity factor on crack closure.” Metallurgical Transactions A **22A**(July): pp. 1559-1571.

Mills, W. J. and L. A. James (1987). “Residual stress effects on fatigue crack growth behavior in stainless steel welds.” Journal of Pressure Vessel Technology (Trans ASME) **109**(Aug): pp. 336-339.

Moftakhar, A. A. and G. Glinka (1992). “Calculation of stress intensity factors by efficient integration of weight functions.” Engineering Fracture Mechanics **43**(5) pp. 749-756.

Munse, W. H. (1964). Fatigue of Welded Steel Structures. New York, NY, Welding Research Council.

Mura, Toshio (1982). Micromechanics of Defects in Solids, 1st Edition. Lancaster, Nijhoff.

Mutoh, Y. and I. Sakamoto (1984). “Fatigue Crack Propagation in the weld bond region of a type 304 stainless steel weldment.” Advances in Fracture Research (Fracture 84). New York, NY, Pergamon Press. 1695-1702.

Nelson, D. V. (1982). “Effects of Residual Stress on Fatigue Crack Propagation.” Residual Stress Effects in Fatigue, ASTM STP 776. American Society for Testing and Materials. pp. 172-194.

Newman, J. C., Jr. (1981). “Prediction of fatigue-crack growth under variable-amplitude and spectrum loading using a closure model.” NASA Technical Memorandum 81942 .

Newman, R. P. (1956). Transactions of the Institute of Marine Engineering **68**: pp. 153-172.

Newman, R. P. (1959). “Effect on Fatigue Strength of Internal Defects in Welded Joints.” British Welding Journal **6**(2): pp. 59-64.

Noyan, I. C. and J. B. Cohen (1986). Residual Stress: Measurement By Diffraction and Interpretation. New York, Springer-Verlag.

O'Hara, G. P. (1991). “Analysis of the swage autofrettage process.” PVP v. 217. New York, ASME. pp. 193-196.

Ohta, A., I. Soya, et al. (1986). “Statistical evaluation of fatigue crack propagation properties including threshold stress intensity factor.” Engineering Fracture Mechanics **24**(6): pp. 789-802.

Ohta, A., M. Kosuge, et al. (1987). “Fatigue crack growth in welded joints under compressive applied stresses.” International Journal of Fracture **33**: pp. R17-R20.

Ohta, A., M. Kosuge, et al. (1988). “Fatigue crack propagation in tensile residual stress fields of welded joints under fully compressive cycling.” International Journal of Fatigue **10**(4): pp. 237-242.

Ojdrovic, R. P. and H. J. Petroski (1991). “Weight functions from multiple reference states and crack profile derivatives.” Engineering Fracture Mechanics **39**(1) pp. 105-111.

Panontin, T. L. (1994). The Relationship Between Constraint and Ductile Fracture Initiation as Defined by Micromechanical Analyses. Stanford University.

Panontin, T. L. and M. R. Hill (1996). “The effect of residual stresses on brittle and ductile fracture initiation predicted by micromechanical models,” accepted for publication in International Journal of Fracture.

Paris, P. C., M. P. Gomez, et al. (1961). “A rational analytic theory of fatigue.” The Trend in Engineering **13**: pp. 9-14.

Parker, A. P. (1982). “Stress Intensity Factors, Crack Profiles, and Fatigue Crack Growth Rates in Residual Stress Fields.” Residual Stress Effects in Fatigue, ASTM STP 776. Philadelphia, ASTM. pp. 13-31.

Parker, A. P. and O. L. Bowie (1983). “The weight function for various boundary condition problems.” Engineering Fracture Mechanics **18**(2): pp. 473-477.

Parry, M., H. Nordberg, et al. (1972). “Fatigue Crack Propagation in A514 Base Plate and Welded Joints.” Welding Journal **51**(10): pp. 485s-490s.

Petroski, H. J. and J. D. Achenbach (1978). “Computation of the weight functionfrom a stress intensity factor.” Engineering Fracture Mechanics **10**: pp. 257-266.

Procter, E. and E. M. Beaney (1987). “Trepan or ring core method, centre-hole method, Sach's method, blind hole methods, deep hole technique.” Adv in Sur Treat: Technol - Appl - Eff. Vol 4: Residual Stresses. New York, NY, Pergamon Press. pp. 165-198.

Radaj, D. (1990). Design and Analysis of Fatigue Resistant Welded Structures. New York, NY, Halsted Press.

Raju, I. S. and J. C. Newman, Jr. (1979). “Stress-intensity factors for a wide range of semi-elliptical surface cracks in finite thickness plates.” Engineering Fracture Mechanics **11**(4): pp. 817-829.

Reissner, H. (1931). “Eigenspannungen und Eigenspannungsquellen.” Zeitschrift für Angewandte Mathematik und Mechanik **11**(1): pp. 1-8.

Rice, J. R. (1972). “Some Remarks on Elastic Crack-Tip Stress Fields.” Int. J. Solids Structures **8**: pp. 751-758.

Ritchie, D. and R. H. Leggatt (1987). “Measurement of the distribution of residual stresses through the thickness of a welded joint.” Strain **23**(2): pp. 61-70.

Rosenthal, D. and J. T. Norton (1945). “A method of measuring triaxial residual stresses in plates.” Welding Journal **24**: pp. 295s-307s.

Rybicki, E. F. and J. R. Shadley (1986). “A three-dimensional finite element evaluation of a destructive experimental method of determining through-thickness residual stresses in girth welded pipes.” Journal of Engineering Materials and Technology **108**(2): pp. 99-106.

SAE (1965). Methods of Residual Stress Measurement: SAE Handbook Supplement J936. Warrendale, PA,

Schajer, G. S. (1988a). “Measurement of Non-Uniform Residual Stresses Using the Hole-Drilling Method. Part I Stress Calculation Procedures.” J. Engineering Materials and Technology **110**(4): pp. 338-343.

Schajer, G. S. (1988b). “Measurement of Non-Uniform Residual Stresses Using the Hole-Drilling Method. Part II Practical Application of The Integral Method.” J. Engineering Materials and Technology **110**(4): pp. 344-349.

Schajer, G. S. and E. Altus (1996). “Stress calculation error analysis for incremental hole-drilling residual stress measurements.” Journal of Eng Matls and Tech, Trans ASME **118**(1): pp. 120-126.

Shah, R. C. and A. S. Kobayashi (1971). “Stress intensity factor for an elliptical surface crack under arbitrary normal loading.” Engineering Fracture Mechanics **3**(1): pp. 71.

Shi, Y. W., B. Y. Chen, et al. (1990). “Effects of welding residual stresses on fatigue crack growth behaviour in butt welds of a pipeline steel.” Engineering Fracture Mechanics **36**(6): pp. 893-902.

Tada, H. and P. C. Paris (1983). “The stress intensity factor for a crack perpendicular to the welding bead.” International Journal of Fracture **21**: pp. 279-284.

Tada, H., P. C. Paris, et al. (1973). The stress analysis of cracks handbook. Hellertown, PA, Del Research Corp.

Terada, H. (1976). “An analysis of the stress intensity factor of a crack perpendicular to the welding bead.” Engineering Fracture Mechanics **8**: pp. 441-444.

Terada, H. (1987). “An Analysis of a Crack in the Residual Stress Field of Welding.” International Conference on the Role of Fracture Mechanics in Modern Technology. Fukuoka, Japan, North-Holland. pp. 899-910.

Timoshenko, S.P. and J.N. Goodier, 1970, Theory of Elasticity. New York, McGraw-Hill.

Torii, T., K. Honda, et al. (1989). “Surface Fatigue Crack Propagation Behavior in a Residual Stress Field.” JSME International Journal, Series I **32**(3): pp. 450-457.

Ueda, Y., K. Fukuda, et al. (1975). “A new measuring method of residual stresses with the aid of finite element method and reliability of estimated values.” Transaction of the JWRI **4**(2): pp. 123-131.

Ueda, Y., Y. C. Kim, et al. (1985). “Measuring Theory of Three-Dimensional Residual Stresses Using a Thinly Sliced Plate Perpendicular to Welded Line.” Transactions of the JWRI **14**(2): pp. 151-157.

Ueda, Y., Y. C. Kim, et al. (1986a). “Mechanical characteristics of repair welds in thick plate (report i) - distributions of three-dimensional welding residual stresses and plastic strains and their production mechanisms.” Transactions of JWRI (Japanese Welding Research Institute) **15**(2): pp. 359-368.

Ueda, Y., Y. C. Kim, et al. (1986b). “Measurement of three-dimensional welding residual stresses due to electron beam welding.” Transactions of JWRI (Japanese Welding Research Institute) **15**(1): pp. 125-131.

Ueda, Y. and K. Nakacho (1986c). “Distributions of welding residual stresses in various welded joints of thick plates.” Transactions of JWRI (Japanese Welding Research Institute) **15**(1): pp. 113-124.

Ueda, Y., K. Fukuda, et al. (1986d). “New measuring method of axisymmetric three-dimensional residual stresses using inherent strains as parameters.” Journal of Engineering Materials and Technology, Transactions of the ASME **108**(4): pp. 328-334.

Ueda, Y. and K. Fukuda (1989). “New measuring method of three-dimensional residual stresses in long welded joints using inherent strains as parameters-Lz method.” Journal of Engineering Materials and Technology, Transactions of the ASME **111**(1): pp. 1-8.

Ueda, Y., K. Nakacho, et al. (1991). “Application of FEM to theoretical analysis, measurement and prediction of welding residual stresses.” Transactions of JWRI (Japanese Welding Research Institute) **20**(1): pp. 97-107.

Unangst, K. D., T. T. Shih, et al. (1977). “Crack Closure in 2219-T851 Aluminum Alloy.” Engineering Fracture Mechanics **9**: pp. 725-734.

Underwood, J. H., L. P. Pook, et al. (1977). “Fatigue-crack propagation through a measured residual stress field in alloy steel.” Flaw Growth and Fracture, ASTM STP 631. Philadelphia, PA, American Society for Testing and Materials. pp. 402-415.

Warren, W. G. (1956). Welding Research **6**: pp. 112r-117r.

Weck, R. (1948). “Residual Stresses Due to Welding.” Symposium on Internal Stresses in Metals and Alloys. London, The Institute of Metals. pp. 119-129.

Wilson, W. M., W. H. Munse, et al. (1950). Illinois University Engineering Experiment Station Bulletin, 384.

Wu, X. R. and J. Carlsson (1983). “The generalized weight function method for crack problems with mixed boundary conditions.” Journal of the Mechanics and Physics of Solids **31**(6): pp. 485-497.

Zhang, X., S. L. Chan, et al. (1992). “Numerical simulation of fatigue crack growth under complex loading sequences.” Engineering Fracture Mechanics **42**(2): pp. 305-321.

Additional related references

Aaghaakouchak, A. A., S. Dharmavasan, et al. (1990). “Stress intensity factors for cracks in structures under different boundary conditions.” Engineering Fracture Mechanics **37**(5): pp. 1125-1137.

Aamodt, B. and P. G. Bergan (1976). “On the principle of superposition for stress intensity factors.” Engineering Fracture Mechanics **8**: pp. 437-440.

Ahmad, J. and M. F. Kanninen (1984). “An Assessment of Analysis Methods for Cracks in Welds.” International Conference on Numerical Methods in Engineering, Swansea, England,

A.S.M.E. (1989). Weld Residual Stresses and Plastic Deformation. New York, ASME.

Bertini, L. (1991). “Influence of seawater and residual stresses on fatigue crack growth in C-Mn steel weld joints.” Theoretical and Applied Fracture Mechanics **16**(2): pp. 135-144.

Carlsson, J. (1984). “Fracture mechanics for cracks in weldments.” Advances in Fracture Research, New Delhi, India. New York, Pergamon Press.

Cheng, W. and I. Finnie (1986). “Examination of the computational model for the layer removal method for residual-stress measurement.” Experimental Mechanics **26**(2): pp. 150-153.

Cheng, W. and I. Finnie (1990). “Kii solutions for an edge-cracked strip.” Engineering Fracture Mechanics **36**(2) pp. 355-360.

Dodds, R. H. J. and D. T. Read (1990). “Experimental and numerical studies of the J-integral for a surface flaw.” International Journal of Fracture **43**(1) pp. 47-67.

Fukuda, S. and Y. Tsuruta (1978). “An experimental study of redistribution of welding residual stress with fatigue crack propagation.” Transactions of the Welding Research Institute of Osaka University **7**: pp. 67-72.

Griffith, A. A. (1921). “The Phenomena of Rupture and Flow in Solids.” Philosophical Transactions of the Royal Society of London, Series A **221**: pp. 163-198.

Kemper, H., B. Weiss, et al. (1989). “Alternative presentation of the effects of the stress-ratio on the fatigue threshold.” Engineering Fracture Mechanics **32**(4) pp. 591-600.

Kobayashi, H., Y. Arai, et al. (1989). “Nondestructive measurement of welding residual stresses by acoustoelastic technique and prediction of fatigue crack growth.” American Society of Mechanical Engineers (Publication) NDE v. 5. New York, NY, ASME. pp. 185-189.

Kwun, H. (1986). “Nondestructive measurement of residual bulk stresses in welded steel specimens by use of magnetically induced velocity changes for ultrasonic waves.” Materials Evaluation **44**(13): pp. 1560-1566.

László, F. (1943-1945). “Tessalated Stresses, Parts I-IV.” Journal of the Iron and Steel Institute **147, 148, 150, 152**: p. 173, 137, 183, 207.

Lawrence, F. V. and E. P. Cox (1976). “Influence of Inadequate Joint Penetration on Tensile Behavior of A514 Welds.” Welding Journal **55**(5): pp. 113s-120s.

Lawrence, F. V. and W. H. Munse (1973). “Fatigue Crack Propagation in Butt Welds Containing Joint Penetration Defects.” The Welding Journal **52**(May 73): pp. 221s-225s, 232s.

Masubuchi, K. (1968). “Effects of Residual Stresses on Fracture Behavior of Weldments.” Weld Imperfections, Proceedings of a Symposium at Lockheed Palo Alto Research Laboratory. Menlo Park, CA, Addison-Wesley. pp. 567-589.

McClung, R. C. and H. Sehitoglu (1989). “On the finite element analysis of fatigue crack closure (2 Parts).” Engineering Fracture Mechanics **33**(2) : pp. 237-252, 253-272.

Nabarro, F. R. N. (1948). “László's papers on tessellated stresses: A review.” Symposium on Internal Stresses in Metals and Alloys. London, England, The Institute of Metals. 61-72.

Nordmark, G. E., et al. (1987). “Effect of Weld Discontinuities on fatigue of Aluminum Butt Joints.” The Welding Journal **66**(Jun 87): pp. 162s-173s.

Oddy, A. S., J. M. J. McDill, et al. (1990). “Consistent Strain Fields in 3D Finite Element Analysis of Welds.” Journal of Pressure Vessel Technology (Trans ASME) **112**(Aug): pp. 309-311.

Ohta, A., et al. (1985). “Significance of residual stresses in fatigue crack propagation behavior of welded joints.” Structural Safety and Reliability: Proceedings of ICOSSAR '85, Kobe, Japan, Int Assoc for Structural Safety & Reliability.

Pang, H. L. J. (1993). “Analysis of weld toe profiles and weld toe cracks.” International Journal of Fatigue **15**(1): pp. 31-36.

Pfluger, A. R. and R. E. Lewis, Ed. (1968). Weld Imperfections, Proceedings of a Symposium at Lockheed Palo Alto Research Laboratory. Menlo Park, CA, Addison-Wesley.

Read, D. T. (1989). “Measurement of applied j-integral produced by residual stress.” Engineering Fracture Mechanics **32**(1): pp. 147-153.

Read, D. T., H. I. McHenry, et al. (1989). “Elastic-plastic models of surface cracks in tensile panels.” Experimental Mechanics **29**(2) pp. 226-230.

Reemsnyder, H. S. (1978). Short Course On Fatigue Design of Welded Joints. Bethlehem Steel Corp., Bethlehem, PA, Unpublished.

Ritchie, R. O. (1987). “Mechanisms of fatigue crack propagation in metals, ceramics and composites: Role of crack tip shielding.” Mechanics and Physics of Crack Growth. New York, Elsevier Applied Science. pp. 15-28.

S.A.E. (1988). Fatigue Design Handbook (AE-10). Warrendale, PA, SAE.

Sih, G. C. (1987). “Role of Fracture Mechanics in Modern Technology.” International Conference on the Role of Fracture Mechanics in Modern Technology. Fukuoka, Japan, North-Holland. pp. 3-23.

Starkey, M. S. and R. P. Skelton (1982). “A comparison of the strain intensity and cyclic J approaches to crack growth.” Fatigue of Engineering Materials and Structures **5**(4): pp. 329-341.

Terada, H. (1976). “An analysis of the stress intensity factor of a crack perpendicular to the welding bead.” Engineering Fracture Mechanics **8**: pp. 441-444.

Tobe, Y. and F. V. Lawrence Jr. (1977). “Effect of Inadequate Joint Penetration on Fatigue Resistance of High-Strength Structural Steel Welds.” The Welding Journal **56**(Sept 77): pp. 259s-266s.

Tsai, C. L. and D. S. Kim (1990). “Analysis of fatigue crack propagation behavior in fillet welded t-joint.” Engineering Fracture Mechanics **36**(4) pp. 653-660.

Ueda, Y. and N. X. Ma (1993). “Expression of inherent strain in form of function and its estimation.” Yosetsu Gakkai Ronbunshu/Quarterly Journal of the Japan Welding Society **11**(1): pp. 189-198.

Wang, G. S. and A. F. Blom (1991). “A Strip Model for Fatigue Crack Growth Predictions Under General Load Conditions.” Engineering Fracture Mechanics **40**(3): pp. 507-533.

Wheeler, O. E. (1972). “Spectrum Loading and Crack Growth.” Journal of Basic Engineering, Transactions of the ASME **1972**(March): pp. 181-186.

Wu, S. and A. Abel (1992). Fatigue crack stress intensity factors: the influence of residual stresses. Proceedings of the Second International Offshore and Polar Engineering Conference. Golden, CO, Publ by Int Soc of Offshore and Polar Engineerns (ISOPE). pp. 312-317.

Zachary, L. W. and C. P. Burger (1976). “Stress Concentrations in Double Welded Partial Penetration Butt Welds.” The Welding Journal **55**(Mar 76): pp. 77s-82s.